Spectral variability of carbon stars: A comparison between theory and observations

Dissertation
eingereicht von
Mag. rer.nat. Rita Gautschy
zur Erlangung des akademischen Grades
Doctor rerum naturalium
an der Formal- und Naturwissenschaftlichen Fakultät
der Universität Wien
Wien, Februar 2001

Rita Gautschy
Institut für Astronomie
Türkenschanzstraße 17
A-1180 Wien, Austria
email: loidl@astro.univie.ac.at

February 2, 2001

Zusammenfassung

Um den Einfluss unterschiedlicher Modellparameter auf die atmosphärische Struktur zu untersuchen, haben wir Gitter plan paralleler und sphärischer hydrostatischer MARCS-Modelle für kohlenstoffreiche Sterne am Asymptotischen Riesenast erzeugt. Zusätzlich wurden synthetische Spektren im Wellenlängenbereich zwischen 0.5 und 25 μm berechnet, wodurch wir die Stärke der Molekülbanden als Funktion der stellaren Parameter studieren konnten. Es stellte sich heraus, dass die Molekülbanden im Wellenlängenbereich zwischen 0.5 und etwa 2.5 μm weniger sensitiv auf Änderungen der stellaren Parameter reagieren als solche bei längeren Wellenlängen. Das lässt sich damit verstehen, dass die Molekülbanden von C_2 und CN (die Banden zwischen 0.5 und 2.5 μm erzeugen) und jene von C_2H_2, C_3, und HCN (die Banden bei Wellenlängen länger als 2.5 μm erzeugen) in unterschiedlichen Regionen der Sternatmosphäre gebildet werden. Vereinfachend kann man sagen, dass Banden, die bei kühleren Temperaturen gebildet werden, stärker auf Änderungen der stellaren Parameter reagieren.

Wir zeigten dass man stellare Parameter wie Effektivtemperatur, C/O und $^{12}C/^{13}C$ Verhältnis eines Sterns im Prinzip aus Breitband- und Schmalband-Farbindizes bestimmen kann. Wir fanden Indizes für die keine oder nur geringe Unterschiede zwischen den Lagen der Beobachtungen und der Modelle in Zweifarbendiagrammen existieren.

Beobachtete Spektren relativ heisser (Effektivtemperaturen höher als etwa 3000 K), staubloser, nur mäßig variabler Kohlenstoffsterne mit niedrigem C/O Verhältnis können sehr gut mit den Spektren klassisch hydrostatischer Modellatmosphären beschrieben werden. Der irregulär variable Stern TX Psc ist das beste Beispiel für einen solchen Stern. In hydrostatischen Modellen können dynamische Effekte und Staub nicht berücksichtigt werden, daher ist eine Beschränkung auf nur mäßig variable Sterne ohne Staub notwendig. Die Beschränkung auf Sterne mit geringem C/O Verhältnis hat eine andere Ursache: Leider sind nach wie vor beträchtliche Unsicherheiten in den C_2 und C_3 Opazitäten vorhanden. Genau diese beiden Moleküle jedoch reagieren am stärksten auf eine Änderung des C/O Verhältnisses. Ihr Einfluss wird umso stärker je höher das C/O Verhältnis des Modells ist. Die meisten Kohlenstoffsterne jedoch erfüllen die

oben genannten Kriterien nicht, daher können ihre Spektren nicht mit Hilfe klassischer hydrostatischer Modellatmosphären erklärt werden. Daher untersuchten wir vier dynamische Modelle, die mit einem vollständigen frequenzabhängigen Strahlungstransport basierend auf 51 Frequenzpunkten gerechnet wurden. Die atmosphärische Struktur des hydrostatischen Anfangsmodells der dynamischen Rechnung zeigt kaum mehr Unterschiede zu einer Modellstruktur mit gleichen Parametern, die mit dem Programm MARCS basierend auf 10 000 Frequenzpunkten erstellt wurde. Die dynamischen Modelle reproduzieren eine Molekülbande bei 1.53 μm, die in kühlen Kohlenstoffsternen wie R Lep beobachtet wurde, mit hydrostatischen Modellspektren aber nicht beschrieben werden konnte. Zusätzlich beschreiben sie die Variationen der Molekülbanden mit der Pulsationsphase qualitativ richtig. Dynamische Modellspektren zeigen, dass die starken Absorptionsbanden im 7 und 14 μm Wellenlängenbereich, die in der Photosphäre entstehen, durch Beiträge aus der Sternhülle mit Emission aufgefüllt werden. Das wird auch tasächlich beobachtet. Jedoch ist es bisher nicht möglich, beobachtete Spektren mit dynamischen Modellspektren auch quantitativ zu beschreiben.

Wir diskutierten Probleme, die auftreten, wenn man AGB Sternen Radien und Pulsationsmoden zuweisen möchte. Es stellte sich heraus, dass bei den meisten bisher erfolgten Versuchen die Ausdehnung der Atmosphären systematisch überschätzt wurden. Daher wird die erste Obertonschwingung in den Interpretationen begünstigt. Basierend auf unseren Untersuchungen favorisieren wir die Fundamentalschwingung als vorherrschenden Pulsationsmode in Mira Sternen.

Abstract

We calculated grids of plane parallel and spherical hydrostatic MARCS model atmospheres for carbon-rich asymptotic giant branch stars to investigate the influence of various input parameters on the atmospheric structure. In addition, we produced synthetic spectra allowing us to study the intensity of the spectral features as a function of the stellar parameters. It turned out that the spectral signatures in the wavelength range between 0.5 and about 2.5 μm are less susceptible to changes of stellar parameters than spectral features longwards of 2.5 μm. This is due to the different atmospheric regions in which the spectral features of CN and C_2 (which have bands in the 0.5 to 2.5 μm region), and the ones of C_2H_2, C_3, and HCN (which have bands longwards of 2.5 μm) form. Generally, features which are formed at lower temperatures are more sensitive to changes of stellar parameters.

We showed that the effective temperature, the C/O ratio, and the $^{12}C/^{13}C$ ratio can in principle be determined from broad-band and narrow-band colour indices. We identified indices for which no or only small systematic differences exist between the loci of models and observations.

Observed spectra of relatively hot (effective temperatures above ≈ 3000 K) and moderately variable carbon stars with low C/O ratios and with only small amounts of dust can be fitted very well with classical hydrostatic model atmospheres. The irregular variable star TX Psc is the best example of such a star. In hydrostatic models, we cannot account for the dust and effects of dynamics; therefore, we must restrict ourselves currently to moderately variable stars without dust. The concentration on stars with low C/O ratios originates from considerable uncertainties in the opacities of C_2 and C_3 which are the molecules reacting strongest to changes of the C/O ratio. Their influence becomes increasingly pronounced with growing C/O ratio of the model. However, most of the carbon-stars do not fulfill the above mentioned criteria, thus we cannot explain their spectra with hydrostatic model atmospheres. We investigated four dynamical model atmospheres which were calculated with a full frequency-dependent radiative transfer based on 51 frequency points. The atmospheric structure of the hydrostatic initial model of the dynamic computation resembles already closely the one of a model with the same parameters calculated with the MARCS code

based on 10 000 frequency points. These dynamic models were able to reproduce a spectral feature around 1.53 μm which has been observed in very cool carbon Miras like R Lep and which could not be explained with pure hydrostatic models. Additionally, they described correctly the temporal variations of spectral features with pulsational phase in a qualitative manner. Dynamical model spectra predict that the strong photospheric absorption features in the 7 and 14 μm region of carbon stars is filled up with emission by contributions from a circumstellar shell. This is indeed what is observed. However, currently we are not able to describe observed spectra with dynamic model spectra quantitatively.

We discussed problems of assigning radii and eventually pulsation modes to AGB stars. It turned out that in most attempts to attribute radii to AGB stars, the dimensions seem to be systematically overestimated, the amount depends on the chosen filter passband. This naturally favours the first-overtone pulsation mode in the final interpretation. Based on our investigations we prefer the fundamental mode as the prevailing pulsation mode in Mira variables.

Contents

Chapter 1

Introduction

1.1 Stars on the Asymptotic Giant Branch

1.1.1 The Asymptotic Giant Branch

According to stellar evolution theory low and intermediate mass stars (about $1 \leq M/\mathrm{M}_\odot \leq 8$) evolve through hydrogen- and core helium burning and reach a part of the Hertzsprung-Russell diagram called the **A**symptotic **G**iant **B**ranch (AGB) where alternate burning of hydrogen and helium occurs in thin shells surrounding the electron-degenerate C/O core (e.g. Iben & Renzini 1983). The exact value of the upper and the lower mass limit and of the boundary between low and intermediate mass stars (about 2 $\mathrm{M}_\odot$) depend on the detailed input (e.g. chemical composition, overshooting, mass loss, and last but not least the stellar-evolution code).

The AGB phase sets in at central helium exhaustion and the formation of an electron degenerate C/O core. The evolution along the AGB itself is divided into two phases. In the first phase, the star burns helium in a shell quiescently. This phase is terminated when hydrogen reignites in a thin shell and as a consequence thermal pulses commence. Near the peak of a thermal pulse the convective transport near the helium burning zone is very efficient. For stars with sufficiently large mass, the base of the convective envelope may extend into the region containing nuclearly processed material and mixing thereby material to the surface. This process is called the third dredge-up; it is responsible for the existence of carbon-rich stars. The burning and mixing along the AGB is linked with the so-called carbon star mystery (Iben 1981): observations of the Large and the Small Magellanic Cloud prove that most of the carbon (and s-process element) enriched AGB stars are found at rather low luminosities indicating that they are lower-mass stars (cf. Smith et al. 1987, Frogel et al. 1990). On the other hand, AGB models predict the third dredge-up for much higher luminosities and/or higher masses only. One possible solution to this mystery might be that convection is more efficient than previously thought. Overshooting at the bottom of the pulse-driven convective zone leads to more efficient dredge-up (Herwig et al. 1997).

1.1.2 Basic properties of AGB stars

AGB stars are very extended objects with radii of a few hundred $R_\odot$, low effective temperatures (typically $< 3500\,K$), and high luminosities of a few 10^3 to $10^4\,L_\odot$. A considerable fraction of the AGB stars shows variability with periods between about 80 and 1000 days, they are referred to as **L**ong **P**eriod **V**ariables (LPVs). The LPVs are divided into several groups according to the regularity of the light curves: Miras (M), semi-regular (SRa and SRb) and irregular (Lb) variables. Their location in a Hertzsprung-Russell diagram is shown in Fig. 1.1, where they are labeled "M, Sr".

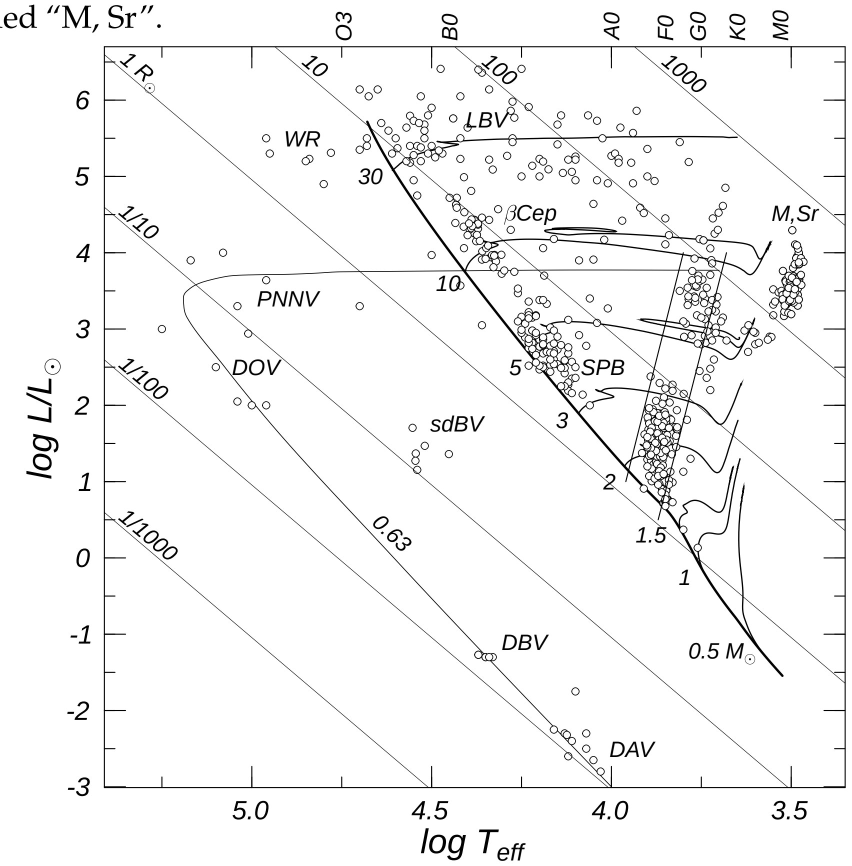

Figure 1.1: Theoretical Hertzsprung-Russell diagram. The thick full line denotes the zero age main sequence, the thin lines departing from it are evolutionary tracks of stars with different masses as labeled in the plot. Slanted lines mark lines of constant radii. AGB stars are labeled by "M, Sr" here. Viewgraph adopted from Gautschy & Saio (1995).

Another important mechanism taking place along the AGB is mass loss. AGB stars lose mass at relatively high rates, typical values lie between 10^{-4} and $10^{-8}\,M_{\odot}/yr$.

1.2 Models of Stellar Atmospheres

The so-called atmosphere represents our main source of information about the stars. Most of the line spectrum of a star originates from this region. Any interpretation of astronomical measurements concerning stellar structure and evolution requires detailed atmospheric models. In the case of cool, extended giants the modelling is severly complicated by three properties characterising the atmospheres of these stars: First, the temperatures are low enough to form molecules. Due to their huge number of absorption lines they produce a high opacity and dominate the atmospheric structure in the corresponding regions. As a consequence, any model calculation has to include the formation and the reactions of the appropriate molecular species. Secondly, stars on the AGB are extended and variable; one is confronted with dynamical phenomena such as shock waves, mass loss and dust formation which can only be simulated by time-dependent models. Finally, sphericity effects can be very important.

In the major part of a cool stellar atmosphere, almost all available carbon and oxygen is bound in CO. As a consequence, there exist three groups of AGB stars with different properties. If the abundance ratio C/O (by number) is less than one, then oxygen compounds dominate the chemical reactions and almost no molecules containing carbon are formed besides CO. In this case we observe a typical M type star with TiO, VO, SiO, CO, and H_2O absorption bands (e.g. Turnshek et al. 1985 for optical spectra; Aringer 2000). If the abundance ratio C/O is greater than one, then we observe a carbon star where apart from CO almost no molecular species including oxygen atoms can be found. The chemistry is dominated by various carbon compounds and the spectra are characterised by absorption bands of C_2, CN, CO, C_3, C_2H_2, CS and HCN (e.g. Turnshek et al. 1985 for optical spectra; Loidl et al. 1999a). A small third group of stars is defined by an abundance ratio of about unity, they are called S stars. Their spectra are dominated by absorption features of molecules like ZrO, VO or LaO (Turnshek et al. 1985).

In the construction of model atmospheres for stars in which line blanketing is important, it is necessary, for reasons of computational economy to adopt a statistical description of the opacity. Commonly used sampling methods of extensive molecular and atomic line data are the **O**pacity **D**istribution **F**unction (ODF) and the **O**pacity **S**ampling (OS) technique. Both methods are based on detailed monochromatic absorption coefficients that are assumed to be well known at a sufficient number of frequency points. The difference between the two methods lies only in the way they use the data to solve the radiative transfer equation. The goal of any opacity treatment is to reproduce the true value of the opacity at every optical depth in any given spectral interval. The calculation of ODF-based model atmospheres proceeds as for the OS models (see below), except that the opacity tables used are not samples of actual opacity, but represent the sampling of opacity distribution functions. In the ODF case, the spectrum is divided into a set of frequency intervals and the absorption coefficient is transformed to a smoothly varying function (the ODF) in each of the spectral intervals. Inside each interval, the absorption coefficient is taken at a limited number of frequency points to solve the radiative transfer equation, i.e. each such ODF function is the result of a sampling procedure within a frequency interval (see Fig 1.2). The most important approximation in this method is made in the calculation of the radiation field, where it is assumed that the monochromatic line opacities for two optical depths τ_1 and τ_2 are identical; the relative strengths of the lines between these two optical depths should not change with depth. It does not matter if the overall absolute strength of the line spectrum changes with depth; it is only important that there are no significant changes in relative strengths (Carbon 1984). To summarise, the ODF method assumes implicitly that the position of the lines does not change markedly as a function of depth, independent of temperature and pressure at which the opacity is evaluated in the atmosphere. This is a consequence of the fact that the information about the exact frequency distribution of the absorption coefficients gets lost after the calculation of the ODF. The position of the lines with depth can change if: (1) molecular lines of two species overlap, (2) velocity shifts in expanding atmospheres occur, (3) a shock is propagating through the atmosphere.

In the OS technique opacities and fluxes are sampled at a limited number of frequencies which are distributed over the spectrum. Subsequently, the equation of radiative transfer is solved for each chosen frequency point. In principle, the method can be used for any choice of frequency interval and with any desired spacing of frequency points. The approximations occur when the total flux and radiative pressure gradient are approximated by sums. Peytremann (1974) used a trapezoidal rule between adjacent quadrature points for the integration; these points were smoothly spread through the spectrum in such a way that the frequency distribution of the points matched the intensity distribution of a Planck function with 8500 K. Contrary to that, Johnson (1982) used equally spaced frequency points together with Kurucz's (1970) parabolic interpolation integration weights in order to compute frequency intervals. In practice, the mean distance between frequency points has to be much greater than the characteristic line width; hence the true monochromatic flux and its contribution to the radiative pressure gradient may vary drastically between consecutive sampling points and

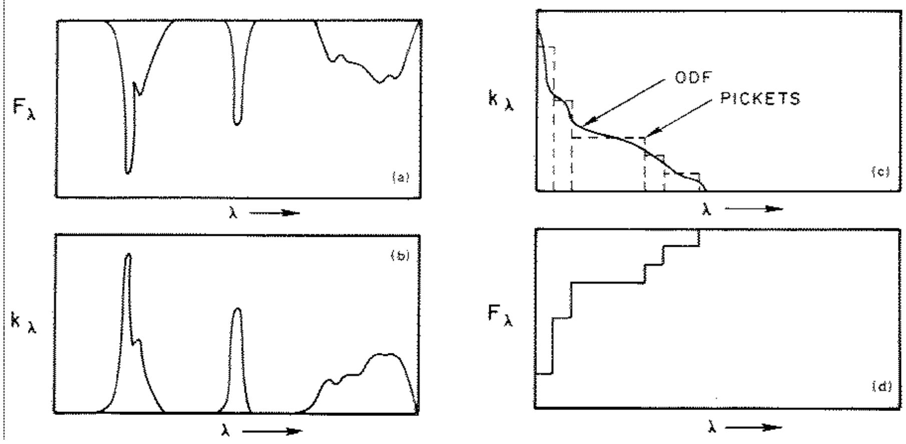

Figure 1.2: a) Hypothetical spectrum over a spectral interval. b) Hypothetical line absorption coefficient over this interval. c) The information in b) rearranged by strength of absorption to form an ODF. A possible six-picket representation is shown by the dashed line. d) The flux emitted by the picket representation of the opacities in c). Figure taken from Johnson & Querci (1986).

as a consequence these quantities are always under-sampled. The atmospheric model structure can be expected to converge slowly towards the true model when the number of frequency points is increased (Ekberg et al. 1986).

1.2.1 History of Hydrostatic Models

Classical models are usually based on the classical assumptions of **L**ocal **T**hermal **E**quilibrium (LTE) and hydrostatic equilibrium where horizontally homogeneous plane-parallel layers and steady state are assumed. The models take into account radiative and turbulent pressures. Querci et al. (1974) have been the first who included the molecular line-blanketing effect by CO, CN and C_2 through opacity probability distribution functions in the models, this statistical method was applied to 10^6 lines. For solving the ionisation and dissociation equilibria equations, 26 atoms (neutral and singly ionized) have been used together with 200 molecules. Opacity sources included also absorption and/or scattering due to H^-, H_2, H_2^-, H, He^-, C^-, C, e^- together with some metallic absorption and the pressure induced opacities due to H_2-H_2 and H_2-He collisions.

The structure of a plane parallel model atmosphere is completely defined by the effective temperature and the gravity. Assuming flux constancy with depth, the phenomenon of line blanketing in the atmosphere is thought to take place in the following manner: The middle part of the atmosphere is relatively opaque, in this region the many weak and strong lines absorb a significant amount of the radiation which would have been transmitted. As a consequence, the temperature of the region rises and creates a backwarming effect such that the radiation is able to leave the atmosphere. Closer to the surface, many spectral regions become more transparent, because the intensity of the strong lines decreases and weak lines disappear. So the energy subtracted by the lines drops, the emissivity drops and the temperature drops also, this is the surface cooling effect (Querci & Querci 1975).

In cool stars, molecules can exist even deep in the atmosphere, therefore molecular blanketing is an important process in atmospheres of AGB stars. The molecular blanketing leads to a surface cooling and a deep backwarming effect. When comparing models with and without molecular blanketing, the differences are more marked for atmospheres with lower temperatures, so molecular lines become increasingly important towards lower temperatures (Querci et al. 1974).

Gustafsson et al. (1975) wrote a first version of the MARCS code. The version of 1975 can be described as follows: For the models the assumptions of hydrostatic equilibrium, LTE, and plane-parallel geometry were made. Therefore it is not possible to describe dynamic phenomena, nevertheless some modifications to the static structure due to dynamical processes were included: the non-thermal contribution to the Doppler broadening velocity, the so-called microturbulent velocity, was added, the energy transport due to convection was roughly considered in the energy transfer balance and in the source function the contribution of scattering was included. The turbulent pressure, however, was neglected. Ionisation stages of H(I-II), He(I-II), C(I-III), N(I-III), O(I-II), Ne(I-II), Na(I-II), Mg(I-III), Al(I-IV), Si(I-III), S(I-III), K(I-II), Ca(I-III), Cr(I-III), Fe(I-III) and Ni(I-III) were considered in the pressure calculations. Partition functions of atoms are computed following Traving et al. (1966) and for the asymptotic part, which gives the contributions from levels close to the continuum, from Fischel & Sparks (1971). The contributions from H_2, H_2^+ and H^- to the pressure and to the internal energy of the gas were considered. Abundances of all diatomic molecules from H, C, N, and O at each depth were taken into account. The used equilibrium constants are from Tsuji (1973) for the molecules and from Vardya (1965) for H_2^+. The continuous absorption coefficients were obtained following Gustafsson (1973). The continuum opacity sources considered are H^-, H I, H_2^-, C I, Mg I, Al I, Si I, Rayleigh scattering and electron scattering.

The equation of radiative transfer, the condition of a constant total flux, and the equation of hydrostatic equilibrium are solved simultaneously. The radiative transfer part is solved with a Feautrier-type method. In the surface layers of the models, the temperature is determined by the condition of radiative equilibrium which describes the balance between the heating and the cooling in the low-absorption wavelength regions and the cooling from the high-absorption regions (Gustafsson et al. 1975).

Molecular opacities are treated in the ODF approximation. Opacity from continuum sources and the molecules CO, CN and C_2 are considered. The models are converged toward constant total luminosity with a Newton-Raphson scheme. The iteration requires a forward solution of the radiative transfer equation for each frequency and a linearization of the result with respect to temperature and electron pressure.

Lateron, Eriksson et al. (1984) calculated opacity distribution functions for HCN and constructed model atmospheres including this opacity. The effects of HCN turned out to be remarkably great. When HCN opacity is included the total opacity raises dramatically in the outer layers. As a consequence, the models become so much more extended that the assumption of a plane-parallel stratification is no longer very realistic (Eriksson et al. 1984). For models with $T_{\text{eff}} > 2900$ K however the HCN effects are small.

Jørgensen et al. (1992) calculated models, where opacity from continuum sources and the molecules CO, CN, C_2, HCN, C_2H_2 and C_3 were considered in the OS approximation, also spherical geometry was incorporated. Spherical geometry is handled by solving the radiative transfer equation on a set of parallel rays. Based on a radial optical depth scale, τ_{r}, a depth has to be selected which is sufficient for the radiation to be effectively thermalized. Below this depth the surface does not significantly influence the radiation field anymore. A reasonable criterion for this is to require the continuum absorption optical depth to be large compared to unity (Nordlund 1984). Rays are then suitably distributed to cover the region inside the selected thermalization depth to allow for accurate integrations. An approximately equidistant spacing in the cosine of the angle towards the normal, μ, was found to be a good choice (Nordlund 1984). In the remaining part of the atmosphere the rays are selected approximately equidistant in the logarithm of optical depth, but with a decreased ($\approx$ halfed) density. The last ray must have at least three intersections with the radial mesh (Nordlund 1984).

In contrast to plane-parallel model atmospheres, in spherical geometry one more parameter such as mass, luminosity or radius is needed. Models of high gravity are less sensitive to sphericity effects than models of low gravity. The spherical models cool additionally in the uppermost layers, therefore the molecular balance is shifted and this leads to changes in spectral features. Due to this cooling in the surface layers, the pressure of the polyatomic molecules is increased with a corresponding decrease in the partial pressure of the 'donor' molecules.

Basic uncertainties of the MARCS code

1. Errors introduced by the OS approximation
   A major problem are the missing molecular opacity sampling data. The

true monochromatic flux and the contribution to the radiative pressure gradient in the calculations is always under-sampled. This is due to the finite number of sampling points. As a result an error occurs in the temperature structure. This error is proportional to $N^{-1/2}$, where N denotes the number of frequency points (Gustafsson et al. 1975). This is consistent with the results of Helling & Jørgensen (1998).

2. NLTE effects
The radiation field interacts strongly with the matter of the stellar atmosphere via absorption and scattering. Hence, the radiation field has a strong influence on the occupation number of states of the gas. LTE will only be valid if thermodynamical collisions dominate the occupation number of states. Deep in the atmosphere the densities and the collisional rates are high. Under this conditions, one expects LTE to be an excellent approximation. In the outer atmosphere particle densities and electron densities are far lower. There, effects of NLTE are to be expected.

3. Neglection of metal lines
Metal lines are not included in our calculations. However, we expect the influence of the metal lines on the atmospheric structure to be small due to the limited wavelength range where they play an important role. Additionally, these lines are formed at high temperatures, in a region where the uncertainties due to the treatment of convection have to be expected to be more important. In the spectra metal lines become very important at wavelengths shorter than $0.7\,\mu$m.

4. Neglection of dynamic phenomena
It is not possible to take into account dynamic phenomena as pulsation or mass loss.

5. Chemical equilibrium assumption
We use an equilibrium chemistry for the computation of the model structures. The assumption of chemical equilibrium will be justified in the deep layers, but might be problematic in the outermost layers.

6. Opacity data
For some of the molecules (C_2, C_3, HCN and C_2H_2) the absorption coefficients are considerably uncertain. These uncertainties will be discussed in detail in Sect. 2.2.

Other approaches to atmospheric modelling treated the opacities in the opacity distribution function technique or through simple mean opacities. Tsuji (1973) focused on the chemical equilibrium of more than 200 compounds for a range of temperatures and pressures which might exist in cool stars, but without the use of model atmospheres. Johnson et al. (1988) computed models where they used OS for the opacity treatment but the opacity of H_2O was added as a straight mean. For oxygen rich LPVs, model atmospheres were constructed by e.g. Scholz & Tsuji (1984). Their models are based on the standard assumptions, the LTE approximation and the mean-opacity technique.

Molecular opacity data

The basic data necessary to evaluate molecular opacity are line-positions, line-intensities, lower energy levels of the transitions and line-broadening parameters for a large number of lines originating from various molecules. It is not yet completely clear which molecules need to be included to get a sufficient accurate description of the opacity, and to which degree of completeness and accuracy the corresponding data must be known. However, it is certain that molecules showing broad spectral features in regions not too far from the Planck maximum must be important for the stellar structure. For example, the molecule C_2H is among the most abundant molecules in some model atmospheres but no certain identification exists in observed stellar spectra. In molecular equilibrium computations H_2 is the molecule with the highest partial pressure. But it has no dipole transitions and therefore molecules many orders of magnitudes less abundant can easily compete with H_2 in dominating the opacity. The second most abundant molecule in most cool stars is CO. Although this molecule is infrared active and its integrated absorption coefficient is large, it has transitions in wavelengths shorter and larger than where the bulk of the flux is transmitted. Together with the fact that CO has only very few strong lines which become saturated easily, this is the reason that it has no large effect on the model structure. One has to seek the dominant opacity sources not only among the most abundant molecules, but also among some very rare ones (e.g. TiO in an oxygen-rich chemistry). Dominant molecules for the opacity are those which fulfill the following criteria (Jørgensen 1995):

- the integrated absorption coefficient should be high
- a reasonable fraction of the absorption should be in a region of the maximum flux emission and at the right temperatures in those layers of the photosphere where the molecule forms
- the number of transition states involved should be high
- the dissociation energy should be high relative to other molecules

The third point is important, because a molecule with a large integrated absorption coefficient arising from few strong transitions (e.g. SiO, CO) will absorb less than a molecule with the same coefficient but distributed over many weak or medium strong lines.

1.2.2 History of time-dependent models

Among others, pioneering work in the field of time-dependent model calculations of Long Period Variables atmospheres has been done by Wood (1979). He solved the hydrodynamical equations for two limiting cases of energy exchange between matter and radiation, the adiabatic and the isothermal limits. Pulsation of the star is simulated by varying the pressure applied at the inner boundary. A shock wave propagates outward once per period. In the adiabatic case, mass loss was produced in the form of a steady stellar wind. But the resulting mass loss rates were far too high. In the isothermal case no continuous mass loss was produced but occasional ejection of shells occured. The time-averaged mass loss rates resulting from this process are far too low. Therefore, a different or an additional mass loss mechanism such as the action of radiation pressure on grains probably exist.

The models of Bowen (1988) introduced a finite temperature relaxation rate to describe cooling behind shock waves and included radiation pressure on dust where a parameterized description of the dust opacity was used. Pulsation was simulated by a variation of the position of the inner boundary. Bowen showed that both, shocks and dust are important for efficient mass loss. The obtained mass loss rates were of the same order of magnitude as the observed values.

Mass loss from LPVs is now thought to be a two-step process involving the lifting of the atmosphere by shock waves which are caused by the stellar pulsation and then radiative acceleration of dust grains which form efficiently in the cool extended circumstellar envelope. Fleischer et al. (1992) constructed self-consistent dynamical models for C-stars which include a time-dependent description of the dust component of circumstellar dust shells. Thermal relaxation of the gas after the passage of the shocks was treated in the isothermal limit case. The interplay of dust, hydrodynamics and thermodynamics led to the formation of a discrete radial structure of the circumstellar dust shells, to the generation of shocks due to radiation pressure on dust, and to a significant backwarming effect. Shocks were not solely caused by the pulsation but were a product of the interaction between dust and hydrodynamics.

Contrary to the carbon-rich situation, for which consistent dust shell models exist, a systematic investigation with a consistent physical description is still lacking for oxygen-rich LPVs. This is mainly due to the more complex problem of inorganic dust formation in an oxygen-rich environment. In contrast to the carbon-rich situation, where mainly homogeneous amorphous carbon grains are formed, in the case of an oxygen-rich composition of the gas almost all carbon is locked up in the chemically inert CO molecule. Therefore, grains can only be formed from molecules containing the remaining oxygen and those abundant heavy elements (Fe, Si, Mg, S, Al and Ti) which are contained in reactive gas phase species (Jeong et al. 1999). In this case a heterogeneous composition of the emerging dust component has to be expected.

In the above described calculations (e.g. Höfner & Dorfi 1997) a constant gas opacity, independent of thermodynamical conditions and chemical composition, has been adopted as it was introduced by Bowen (1988). However, it turned out that this assumption generally produces unrealistic molecular spectra as the overall density of the atmospheres is much too high. As a consequence, the atmospheres have then been calculated using Planck mean absorption coefficients for the gas opacity (Höfner et al. 1998), which allows a self-consistent treatment of changes in chemical composition or the thermodynamical conditions. Recently, it became possible for the first time to calculate the dynamic atmospheric structure with frequency-dependent radiative transfer (Höfner 1999). For computational reasons, the number of frequency points which can be handled is still very low (51). However, as demonstrated by Helling & Jørgensen (1998) for hydrostatic model atmospheres, even as few as 50 points can be sufficient to obtain very realistic structures in contrast to grey models.

For the spectral synthesis we will mainly use the time-dependent models of Höfner (1999). Therefore, a brief description of these models is given in the following:

Gas and radiation are described as two interacting fluids. The conservation laws for the two components form a set of partial differential equations consisting of the equation of continuity, the equation of motion, the internal energy equation for the gas and the zeroth and first-order moment equation of the radiative transfer equation. The zeroth-order moment equation represents radiation energy conservation and the first-order moment equation the radiation momentum conservation. The gravitational field is described by the Poisson equation. The dust has to be treated time-dependently as a third component in addition to gas and radiation. The information about the dust component which is required for the construction of self-consistent models of LPV atmospheres is contained in the moments of the grain size distribution function (Gail & Sedlmayr 1988). Their time-evolution is described by moment equations which describe formation, growth and evaporation of the dust grains (Gauger et al. 1990).

To close the system of equations describing gas and dust, additional relations are needed. This involves the microphysics of the gas and dust (equation of state, opacity, source function, nucleation rate, etc.) and the geometry of the radiation field (the Eddington factor).

The calculations extend only over the circumstellar envelope and the outermost parts of the star. Therefore, a perfect gas law is used as an equation of state to determine the gas temperature and the gas pressure.

The source function represents the radiation emitted by the matter. In LTE, the frequency dependent source function is equal to the Planck function.

The Eddington factor contains information about the angular dependence of the intensity of the radiation field and it depends on the optical depth of the layer. It has to be determined by solving the radiative transfer equation after each timestep.

The inner boundary of the spherical shell is located above the driving zone for the pulsation and consequently the oscillations have to be simulated by variations of physical quantities at R_{int}. In state-of-the-art models of circumstellar envelopes, stellar pulsation is simulated by a "piston" below the photosphere, i.e. a temporally varying location of the inner boundary is employed (Höfner et al. 1995). The motion of the piston is described by two free parameters, the pulsation period and the velocity amplitude, and is assumed to be sinusoidal at the inner boundary. The flux at the inner boundary is kept constant, therefore the luminosity at the inner boundary varies proportional to the square of the radius at the inner boundary.

The initial models are in hydrostatic equilibrium and dust-free, and therefore completely determined by the stellar parameters mass, luminosity, effective temperature, and the elemental abundances.

For more details about the models employed in the following see Höfner et al. (1995), Höfner & Dorfi (1997), Höfner et al. (1998) and Höfner (1999).

1.3 Molecular Spectra

The spectra of cool giant stars are dominated by molecular bands in the optical and infrared range. Metal lines contribute significantly at wavelengths below $\approx 0.7\,\mu$m. Therefore, we will recall briefly the most important facts concerning molecular spectra which are needed to understand the nomenclature used. A detailed discussion can be found e.g. in the book of Herzberg (1988).

In a first approximation, the energy of a molecule can be represented as the sum of three contributions, the electronic, vibrational, and rotational energy. In Fig. 1.3 the vibrational and rotational levels in two electronic states are represented schematically. Corresponding to the three sources of energy, three kinds of spectra can occur:

- Rotation spectra, where transitions take place between the rotational levels of a given vibrational level in a given electronic state.

- Rotation – vibration spectra, in which transitions take place from the rotational levels of a given vibrational level to the rotational levels of another vibrational level of the same electronic state

- Electronic spectra, in which transitions from the rotational levels of the various vibrational levels of one electronic state take place to the rotational and vibrational levels of another electronic state

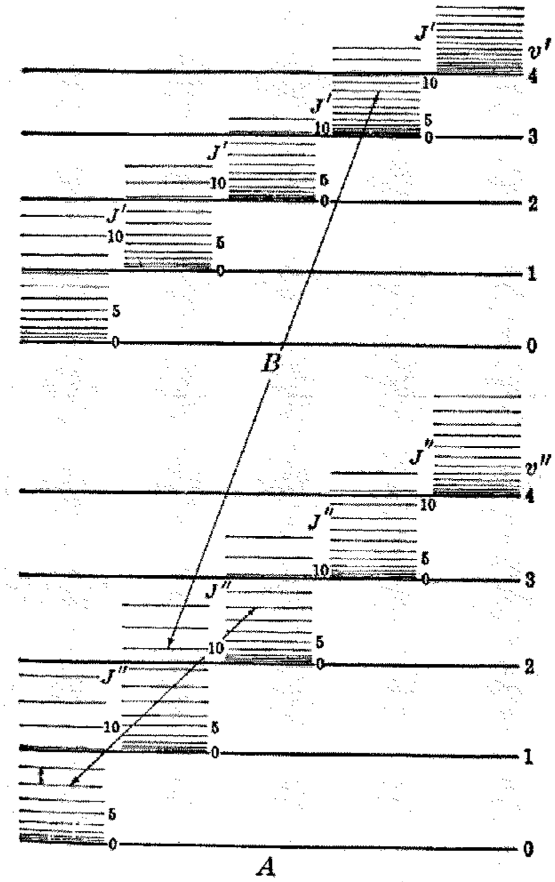

Figure 1.3: Vibrational and rotational levels of two electronic states A and B of a molecule (schematic). The three double arrows indicate examples of transitions in the pure rotation spectrum, the rotation – vibration spectrum, and the electronic spectrum of the molecule. Viewgraph taken from Herzberg (1988).

1.3.1 Diatomic Molecules

Rotation

The simplest model for the rotations of a diatomic molecule is the so-called dumbbell model: A system consisting of two mass points connected by a massless rod of a certain length. In wave mechanics, only certain discrete energy levels are possible, which are obtained by solving the Schrödinger equation of the rigid rotator. The result is

$$E_{\mathrm{r}} = \frac{h^2}{8\pi^2 \mu r^2} J(J+1),$$

where μ is the reduced mass, r the length of the massless rod, h the Planck constant, and J the *rotational quantum number.* J assumes the values $0, 1, 2, ...$

If the molecule is not completely rigid, there will be, on account of the centrifugal force, a slight increase in the internuclear distance when the molecule is rotating. As a result the rotational term-value is somewhat modified.

Vibration

In a first approximation, the vibrations of a diatomic molecule can be represented by a harmonic oscillator. When substituting its potential energy into the wave equation, one finds for the energy levels of the harmonic oscillator

$$E_{\mathrm{v}} = h\,\nu\,(v + \tfrac{1}{2}),$$

where the *vibrational quantum number* v can take the values $0, 1, 2,$ .... Actually, molecules are not strictly harmonic oscillators. As a consequence the spacing between the levels, instead of being constant as in a harmonic oscillator, gradually decrease until it reaches a value close to zero near the dissociation limit.

In general, rotation and vibration of the molecule will take place simultaneously, and therefore the interaction between these two motions must be considered. If the molecule is vibrating the internuclear distance is changing. As a consequence the rotational constant for a given vibrational level v is different from the rotational constant for the equilibrium position.

Electronic States

In atoms the state of an electron is characterised by the quantum numbers n and l, the principal quantum number and the azimuthal quantum number. The latter indicates the orbital angular momentum. Relative to an electric field, the orbital angular momentum vector can only have discrete orientation levels whose component in the field direction is $m_l h/2\pi$, where $m_l = l, l-1, l-2, ..., -l$. To distinguish different states of the electron of given n, l and different m_l one uses the quantum number

$$\lambda = |m_l| = l, l-1, ..., 0.$$

The orbital wave functions of one–electron states with $\lambda = 0, 1, 2, ...$ are called σ, π, δ, ... orbitals. Molecular orbits with $\lambda \neq 0$ have two components; they are *double degenerate.* Orbitals with $\lambda = 0$ have only one component; they are *nondegenerate.*

If the two nuclei in a molecule have the same charge (*homonuclear* molecule), the orbital wave functions can be symmetric (even) or antisymmetric (odd) with respect to the centre of symmetry in the molecule. This symmetry property is indicated by a subscript g for even or u for odd. For even l, the molecular orbital is even, and for odd l it is odd. For a given electron configuration several different electronic states are obtained in general. Each of these states is characterised by a *total orbital angular momentum* Λ which is simply the sum of all λ_i. The state is denoted by Σ, Π, Δ, ... (for $\Lambda = 0, 1, 2, ...$), of which Π, Δ, ... are doubly degenerate.

Rotation – Vibration Spectra

The various possible rotational transitions for a given vibrational transition form a rotation – vibration band. The wave numbers of the lines of such a band are the sum of the rotational and the vibrational contributions. Due to the selection rule that ΔJ can only be -1, 0 or $+1$, three series of lines arise in the case that the ground state of the molecule is a Π state, the so called R ($\Delta J = +1$), Q ($\Delta J = 0$) and P ($\Delta J = -1$) branch. If the ground state is a Σ state, no Q branch exists, because $\Delta J = 0$ does not occur.

1.3.2 Polyatomic Molecules

In polyatomic molecules, the vibrational motion is much more complex than in diatomic molecules.

For a linear triatomic XY_2 molecule there are three so-called normal vibrations, which are represented in Fig. 1.4. The vibrations designated by ν_1 and ν_3 are stretching vibrations along the line of the internuclear axis, while ν_2 is a bending vibration in which the nuclei oscillate perpendicular to the internuclear axis. This vibration has two degrees of freedom, it is doubly degenerate because it may occur in the plane or perpendicular to it. The vibrations ν_1 and ν_3 have different symmetry. The first is totally symmetric, the second one is antisymmetric with respect to the centre of symmetry.

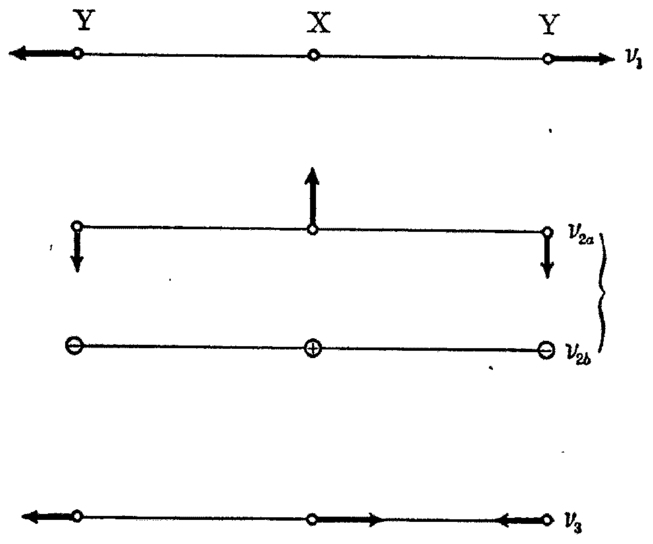

Figure 1.4: Normal vibrations of a linear XY_2 molecule (schematic). The displacements of the nuclei during the vibrations are indicated by the heavy arrows (not to scale). Viewgraph taken from Herzberg (1988).

In an unsymmetric linear triatomic molecule of the form XYZ like HCN there are also three normal vibrations, but the two stretching vibrations ν_1 and ν_3 are no longer distinguished by symmetry because there is no longer a centre of symmetry.

For a four-atomic linear molecule three stretching vibrations and two bending vibrations are found.

The nomenclature used in this work will be $(\nu_{11}\,\nu_{21}\,\nu_{31}\;-\;\nu_{12}\,\nu_{22}\,\nu_{32})$ for triatomic molecules and $(\nu_{11}\,\nu_{21}\,\nu_{31}\,\nu_{41}\,\nu_{51}\;-\;\nu_{12}\,\nu_{22}\,\nu_{32}\,\nu_{42}\,\nu_{52})$ for four-atomic molecules.

1.4 Molecular Features

Molecular lines are the dominating spectral features throughout the visible and infrared spectral range of late-type stars. In contrast to atomic lines of one species, which are arranged in series and clearly separated from each other, molecular lines lie very close to each other giving rise to molecular bands. The numerous molecular lines are caused by rotational, vibrational, and electronic transitions. The wavenumber of a particular line is given by the sum of the electronic, the vibrational and the rotational components.

In carbon-rich AGB stars the main molecular features are due to CN, C_2, CO, CS, CH, HCN, C_2H_2 and C_3. CN and C_2 are dominating the visual spectrum and extend to about 2 μm. They are caused mainly by electronic transitions. The other molecules which give rise to rotational and vibrational transitions dominate the infrared region. Figure 1.5 shows the contributions of different molecules to the spectrum of a carbon-rich model with $T_{\rm eff} = 3100$ K, $\log(g) = -0.40$, C/O = 1.40, $M = 1{\rm M}_\odot$, $\log(Z/{\rm Z}_\odot) = 0.0$ and $^{12}{\rm C}/^{13}{\rm C} = 89$. In the following, we describe the main features between 0.5 and 25 μm of each molecule:

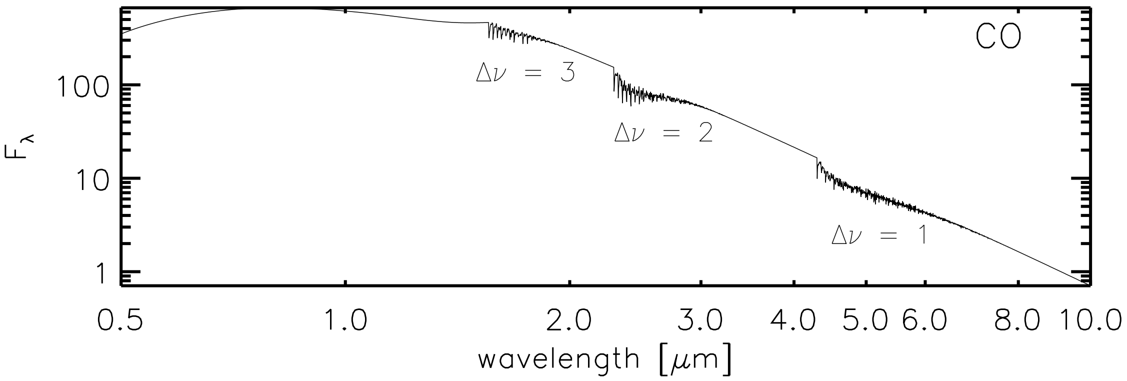

CO: Three molecular bands in the wavelength range between 0.5 and 25 μm are due to CO, at 1.57 ($\Delta\nu = 3$), 2.35 ($\Delta\nu = 2$), and 4.66 μm ($\Delta\nu = 1$).

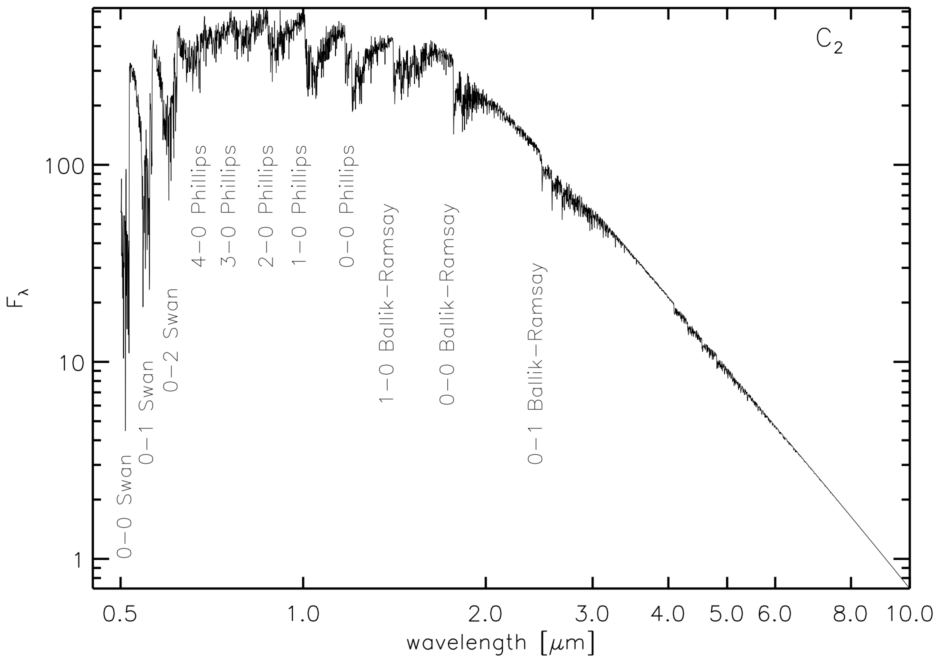

C_2: The Swan (0−0 at 0.52 μm), the Phillips (0−0 at 1.21 μm), and the Ballik-Ramsay (0−0 at 1.77 μm) band systems are the most prominent electronic transitions of C_2.

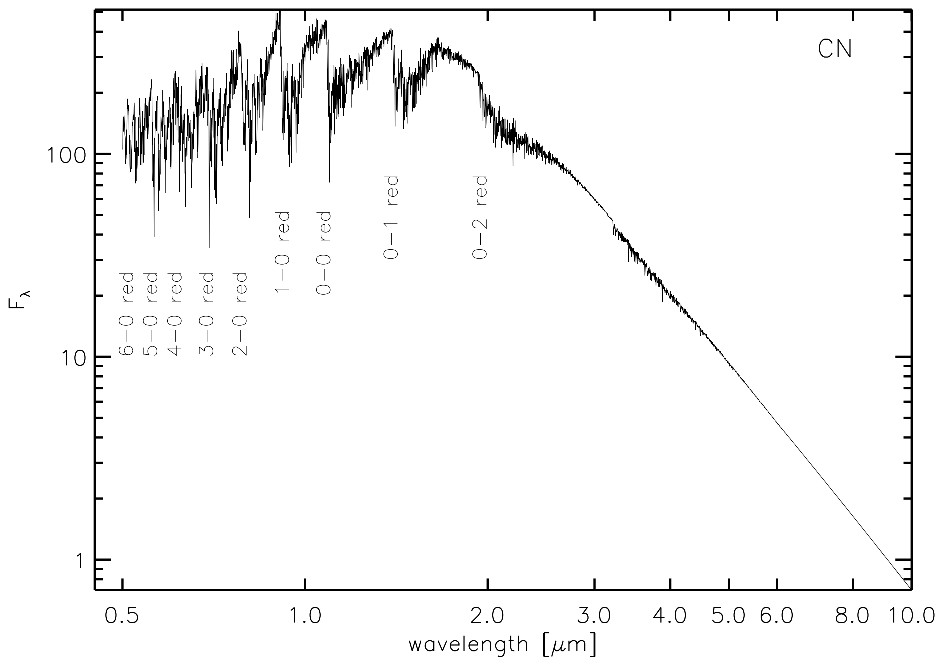

CN: The violet system (0−0 at 0.39 μm) and the red system (0−0 at 1.10 μm) are the most important electronic transitions of CN.

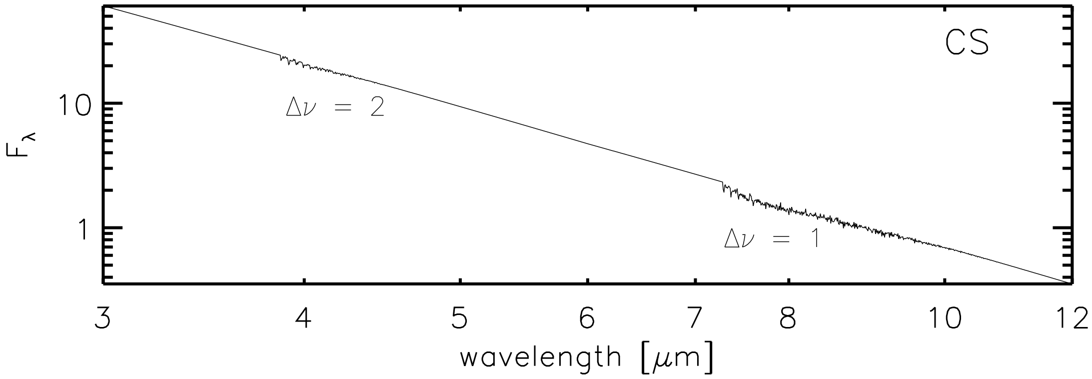

CS: Signatures at 3.85 ($\Delta\nu = 2$) and 7.2 μm ($\Delta\nu = 1$) are due to CS.

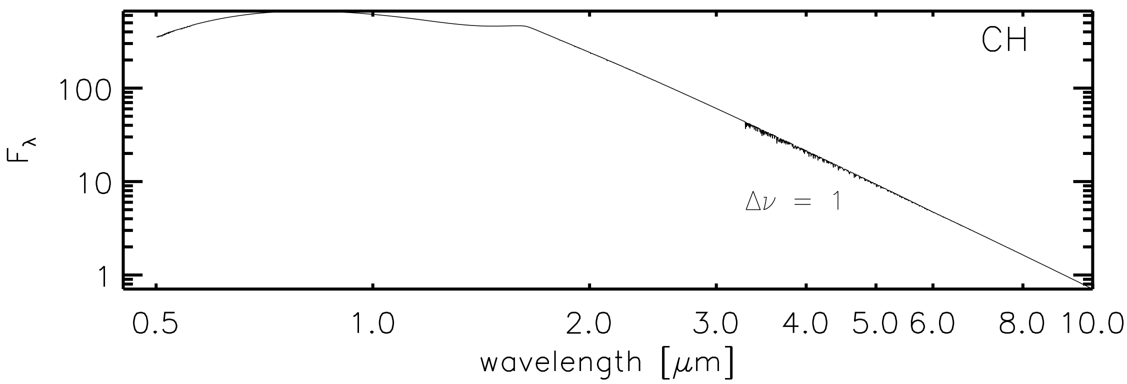

CH: A band around 3.65 μm ($\Delta\nu = 1$) originates from CH.

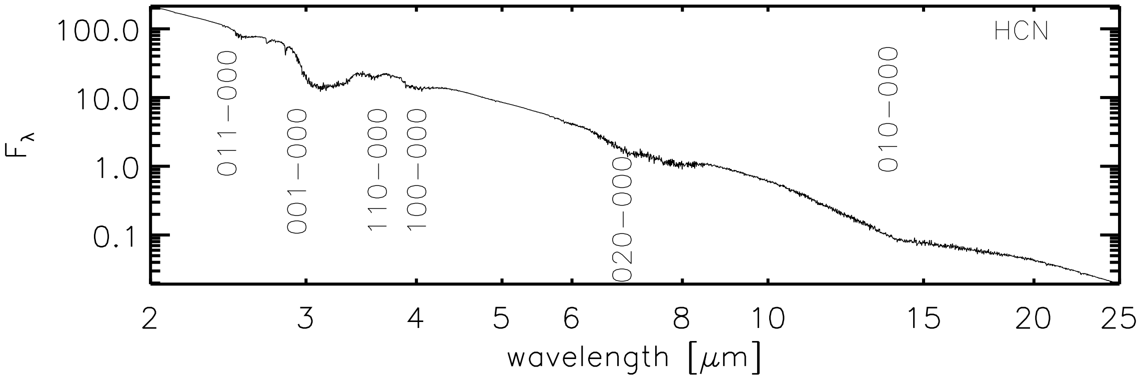

HCN: Prominent features at 2.50 (011−000; perpendicular band), 3.02 (001−000; CH stretch, parallel band), 3.57 (110−000), around 4 (100−000), around 7 (020−000; parallel band), and around 14 μm (010−000; bending mode, perpendicular band) originate from transitions of HCN.

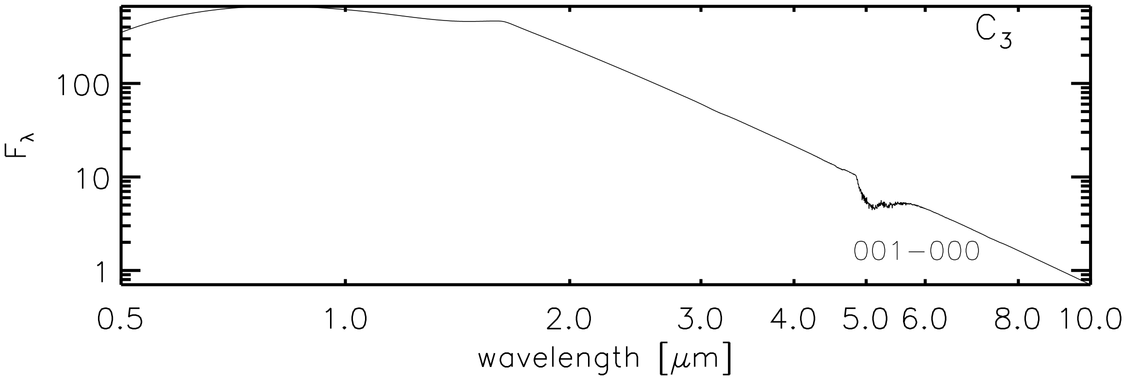

C_3: A band at 4.9 μm (001−000) is due to C_3.

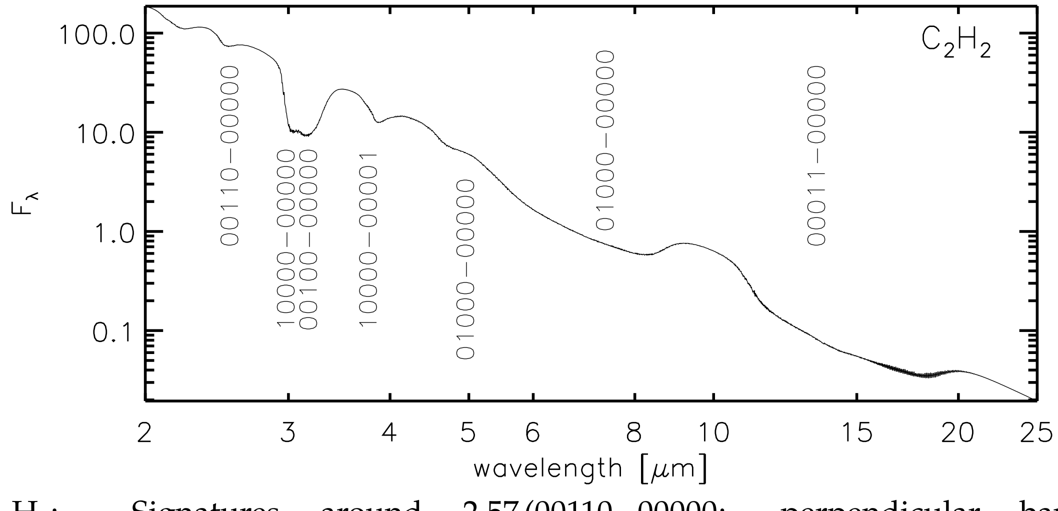

C_2H_2: Signatures around 2.57 (00110−00000; perpendicular band), 2.96 (10000−00000; CH stretch), 3.04 (00100−00000; CH stretch, parallel band), 3.78 (10000−00001; perpendicular band), 5.07 (01000−00000; CC stretch), 7.53 (00011−00000), and 13.71 μm (00010−00000; CH bend) are due to C_2H_2.

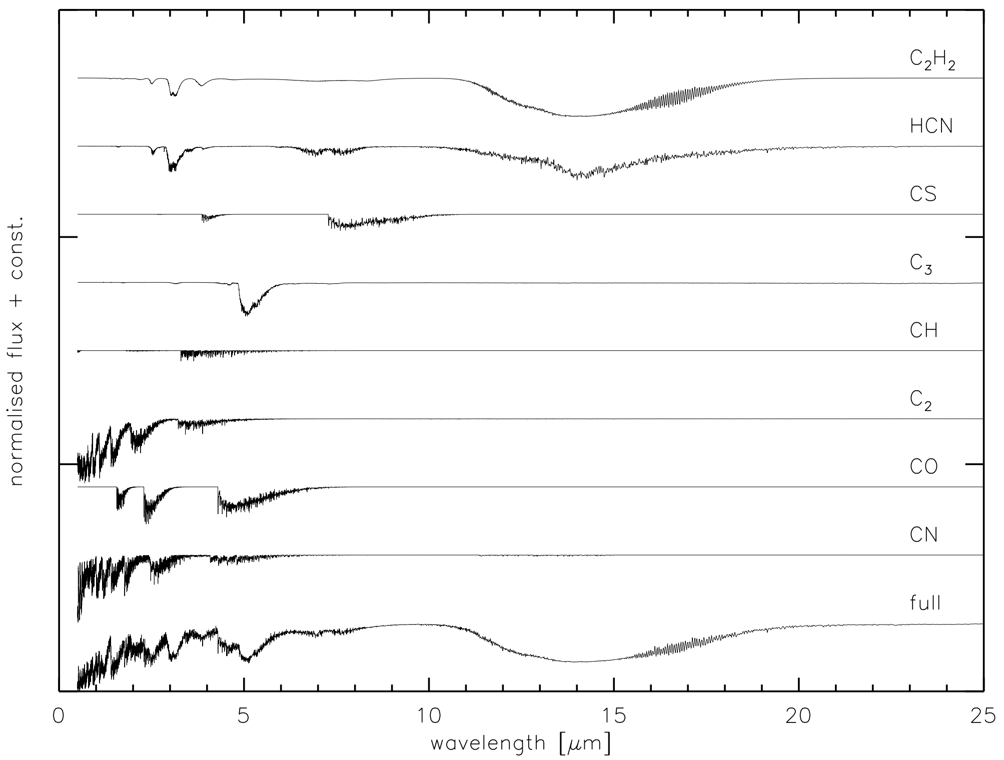

Figure 1.5: Identification of molecular bands of carbon stars in the wavelength region between 0.5 and 25 μm.

1.4.1 Regions of Line Formation

The range in temperature and radius where a molecular feature is formed in cool star atmospheres depends on the relative abundance of the species being involved, the strength of the transition, the local continuous opacity, and the atmospheric structure. In AGB stars, the observed lines usually do not originate from a narrow region. Especially CO is formed over a significant part of the star's atmosphere. The weak lines which have a high rotational excitation are formed in layers with temperatures between 3500 and 5000 K. The strong low excitation lines originate mainly from the outermost atmospheric layers and even from the circumstellar envelope of the star in objects with heavy mass loss. To illustrate the abundances of the various species, the partial pressures of the most important molecules are plotted versus temperature for a dynamical model in Figure 1.6.

The temperature and radial depth range over which molecular features are formed can be obtained in two ways: First, by removing successively layers from the inner or outer edges of the models, secondly we can calculate for each wave-

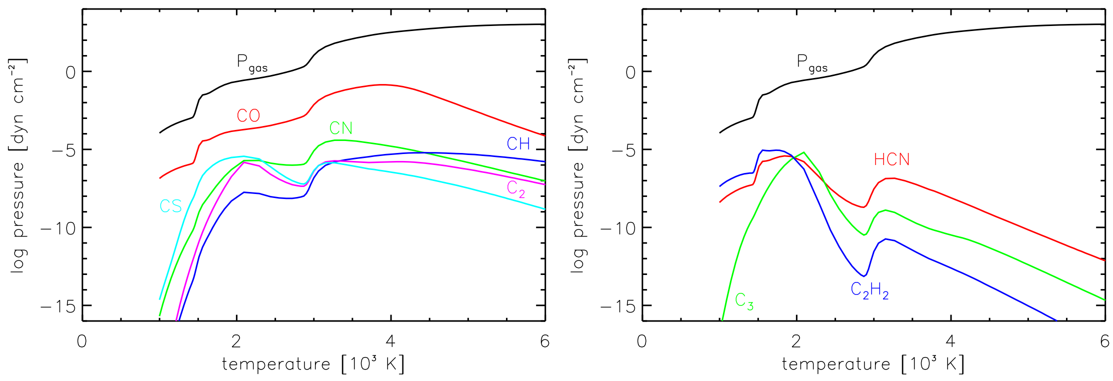

Figure 1.6: Partial pressures of various molecular species versus temperature of a dynamical model.

length and molecule at which temperature and radius an optical depth (τ) of 1 is reached. Both methods give identical results within 100 K for hydrostatic as well as for dynamic models. Using these two methods we derived the following:

- CO is one of the first molecules that forms in the hot inner parts of the atmosphere. The weak lines with a high rotational excitation come from layers with temperatures of up to 5000 K. The strong low excitation lines of CO form mostly in regions hotter than about 2400 K.

- CN forms deep in the atmosphere, at temperatures between 2400 and 5000 K.

- C_2 forms at temperatures between 2200 and 5000 K. Its partial pressure increases rapidly at temperatures above 2000 K.

- CS forms at temperatures between 2000 and 3500 K.

- CH forms mainly deep in the atmosphere, at temperatures between 2400 and 5000 K.

- The formation of C_3 requires a combination of relatively high partial pressure (in order for the collision probability to be high enough) and low temperature (in order not to dissociate). Its partial pressure has therefore a rather narrow peak around 2000 K. All C_3 features are formed at temperatures between 1700 and 2500 K.

- In a hydrogen dominated atmosphere, the formation of C_2H_2 is much less sensitive to the density than that of C_3 since only two non-hydrogen atoms participate in the formation. On the other hand C_2H_2 is much more sensitive to temperature (being four-atomic). As a result, C_2H_2 has a very broad distribution extending to much lower temperatures than C_3. This is the reason why C_2H_2 is more important in the grain formation process than C_3. All features of C_2H_2 originate between the outermost layers (typically 1400 K in hydrostatic models; about 500 K in dynamical models) and layers with temperatures of 2400 K.

- In the deeper layers of the atmosphere HCN is more abundant than C_2H_2 and C_3 because it is three-atomic and consists of only 2 non-hydrogen atoms, but its abundance resembles closely that of C_2H_2 in the upper layers. The HCN features are formed at temperatures between 1700 and 3000 K.

Chapter 2

A grid of hydrostatic model spectra

2.1 Hydrostatic model atmospheres

In order to study the behaviour of different model input parameters we calculated a grid of 500 plane parallel and spherical hydrostatic models for carbon-rich stars using an updated version of the MARCS code (Gustafsson et al. 1975) with spherical radiative transfer routines from Nordlund (1984). The improvements in the present version have been described by Jørgensen et al. (1992), Helling et al. (1996), and Jørgensen (1997).

The energy balance is treated in the opacity sampling scheme. Approximately 10,000 frequency points have been adopted for the radiative transfer computation. The models are fully self-consistent, thermodynamic quantities are computed in local thermal equilibrium (LTE) at approximately 50 depth layers from $\tau_{\rm Ross} \approx 10^{-6}$ to $\tau_{\rm Ross} \approx 100$. The molecules CO (from Goorvitch & Chackerian 1994), CN (from Jørgensen & Larsson 1990), C_2 (from Querci et al. 1974), CH (from Jørgensen et al. 1996), CS (from Chandra et al. 1995), HCN, C_2H_2, and C_3 (as described in Jørgensen 1997) are included in the opacity, together with continuum sources as described in Gustafsson et al. (1975). Elemental abundances for C, N and O were taken from Grevesse & Sauval (1994) and from Anders & Grevesse (1989) for all other species.

Hydrostatic model atmospheres are determined by the effective temperature $T_{\rm eff}$, the surface gravity $\log(g)$, the mass M and the chemical composition. First, we have produced a systematic grid of 250 plane parallel atmospheres by changing the effective temperatures, C/O ratios and gravitational acceleration in the range $2600\,{\rm K} \leq T_{\rm eff} \leq 3600\,{\rm K}$, $1.01 \leq {\rm C/O} \leq 1.80$ and $-0.8 \leq \log(g)\,[{\rm cm/s^2}]) \leq 0.0$, respectively; concentrating on objects with one solar mass and solar chemical abundances (except for C). The rest of the models were designed to show the effects of different masses, metallicities, $^{12}C/^{13}C$ ratios and sphericity. Additionally, most of these models have parameters corresponding to stellar evolution tracks

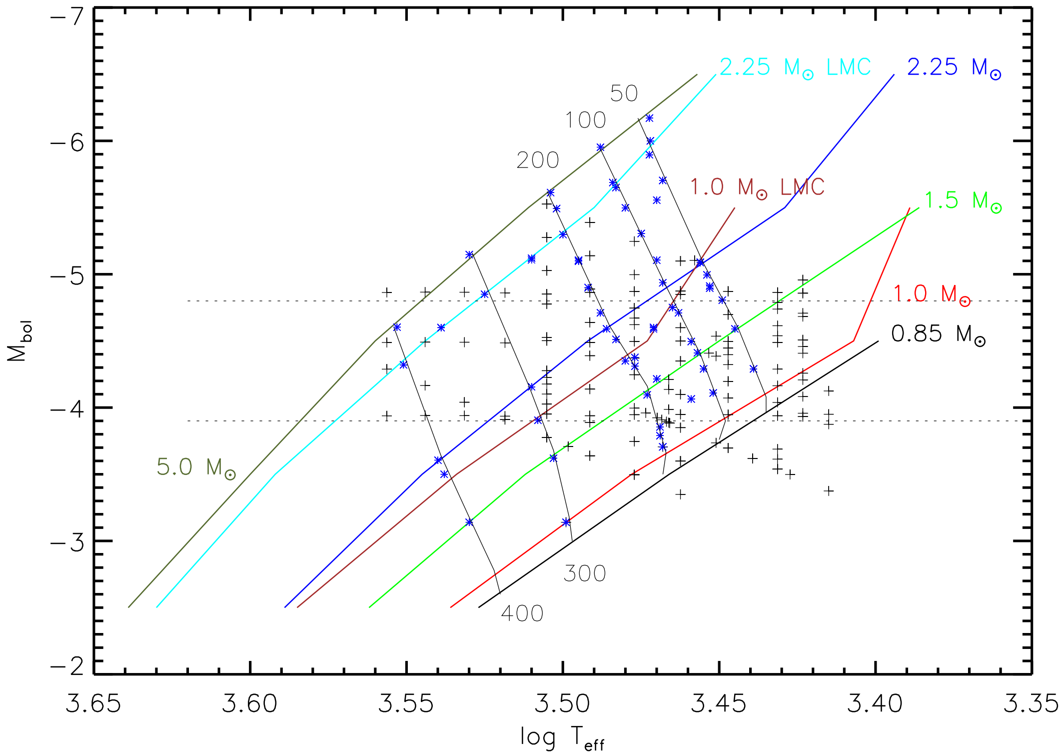

Figure 2.1: Stellar evolution tracks for stars with 0.85, 1, 1.5, 2.25 and 5 $M_\odot$ and solar composition as well as the tracks for 1 and 2.25 $M_\odot$ and LMC abundances are plotted. The black crosses denote models for which one model parameter was changed systematically, the blue asterisks are models which are consistent with stellar evolutionary tracks. The dotted lines mark the luminosity range expected for a core mass of 0.58 $M_\odot$ which is a probable minimum mass for the occurence of the third dredge-up (Mowlavi 1999). The slanted lines denote lines of constant periods, the periods are indicated on their top and bottom, respectively.

of Bessell et al. (1989). All these models are shown in Figure 2.1 where $M_{\rm bol}$ versus log $T_{\rm eff}$ is plotted. For the calculation of $M_{\rm bol}$

$$M_{\rm bol} = 4.75 - 2.5 \log L/\mathrm{L}_\odot$$

was used. The models for which one parameter was changed systematically are denoted by crosses, the ones consistent with the stellar evolution tracks by asterisks. Additionally, evolutionary tracks for 0.85, 1, 1.5, 2.25 and 5 $M_\odot$ stars with solar composition, as well as the tracks for 1 and 2.25 $M_\odot$ with LMC abundances are plotted. The slanted lines show the loci of constant periods. The dotted lines mark the luminosity range expected for a core mass of 0.58 $M_\odot$ which is a probable minimum mass for the occurence of the third dredge-up (Mowlavi 1999). A list of selected models and their parameters is given in Appendix A.

2.2 Molecular input data

While the molecular input data of CO and CN are well known, the situation is less satisfactory for other molecules. Therefore the OS absorption coefficients used for the model constructions and the synthetic spectrum computations have been improved recently (Jørgensen et al. 2000).

2.2.1 HCN

The original data of HCN were computed *ab initio* with the CASSCF method (Jørgensen et al. 1985). However, some of the stronger bands which appear in the low resolution stellar spectra are measured with higher accuracy in the laboratory than what can be achieved *ab initio*. Therefore, the opacities have been improved by scaling the stronger bands to the laboratory values.

2.2.2 C_3

The original data of C_3 were computed *ab initio* using the CASSCF method (Jørgensen et al. 1989).

One of the important input parameters in the construction of models and synthetic spectra of stars is the so called $K_p(C_3)$ value, which is unfortunately known with large uncertainty only. The $K_p(C_3)$ value expresses the equilibrium between atomic carbon, C_2 and C_3. $K_p(C_3)$ is a function of temperature T, usually expressed as a polynomial in $\Theta = 5040/T$. Two different polynomials for $K_p(C_3)$ were tested by Jørgensen et al. (2000). One is due to a widely used computation by Tsuji (1973 and private communication 1998), and one is a recent polynomial fit to the JANAF table data due to Helling (private communication 1998). Unfortunately, both values are rather uncertain compared to K_p for other molecules, the JANAF table data do not rely purely on experimental values in the case of C_3.

Following Jørgensen et al. (2000) all our models are calculated with the $K_p(C_3)$ value of Helling. Figure 2.2 illustrates the strong influence of the $K_p(C_3)$ value on the synthetic spectra. The black line shows a spectrum with $T_{\rm eff} = 3000\,$K, $\log(g) = 0.0$, C/O = 1.10 and the $K_p(C_3)$ value of Helling, the red line a spectrum with $T_{\rm eff} = 3000\,$K, $\log(g) = -0.5$, C/O = 1.02 and the $K_p(C_3)$ value of Helling. The green line shows a spectrum with $T_{\rm eff} = 3000\,$K, $\log(g) = 0.0$, C/O = 1.10 and the $K_p(C_3)$ value of Tsuji. The influence of the $K_p(C_3)$ value is much stronger than changing the C/O ratio or $\log(g)$ within acceptable limits. We notice that Tsuji's $K_p(C_3)$ value results in a much stronger C_3 feature around 5.1 μm and a weaker C_2H_2 and HCN feature around 3 μm.

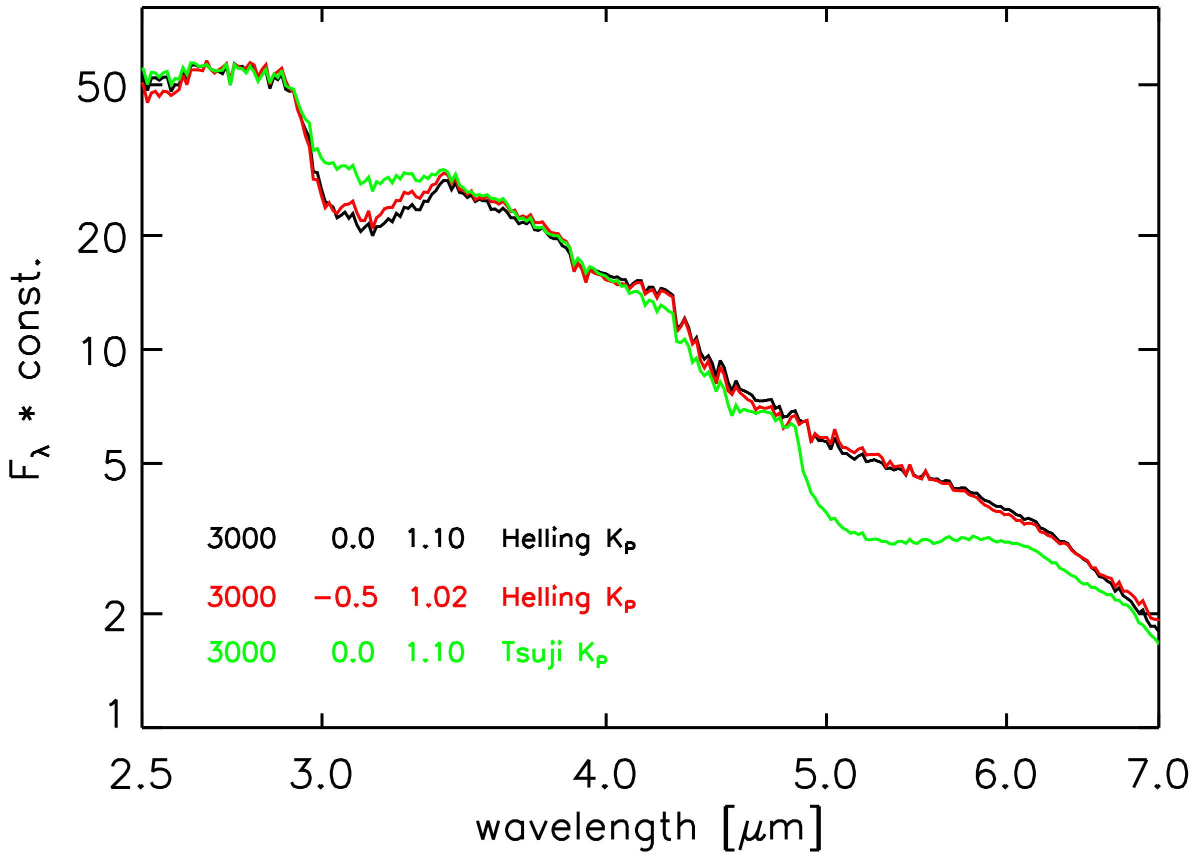

Figure 2.2: Illustration of the strong influence of the $K_p(C_3)$ value on the synthetic spectra. For details see text. Adopted from Jørgensen et al. (2000).

2.2.3 C_2H_2

For C_2H_2 which is not computed *ab initio*, the scaling to laboratory data is even more important than for HCN and C_3. The method for computing the bands is based on the theory described in Jørgensen (1990) and Sørensen & Jørgensen (1992). This method makes it possible to keep the correctly calculated high-temperature form of the bands (i.e., to include the contribution from many hot bands and adopt the right individual anharmonic frequencies of the contributing hot bands), while still taking advantage of the ground-state intensities measured in the laboratory at room temperature.

2.2.4 C_2

Three line lists for C_2 are described in the literature: One is due to Querci et al. (1971). Another is due to Kurucz (e.g. Kurucz 1994). The third and newest list is the compilation by Goorvitch (1990).

The lists of Querci and Kurucz are both quite complete in their wavelength coverage, and they agree well with each other in the visual region. Goorvitch's compilation is only for the Ballik-Ramsay system around 2 μm. This list seems to be the most complete in the spectral region it covers, but its integrated band strength is approximately a factor 20 smaller than the corresponding one derived from Querci's list in the same region. The Kurucz result lies somewhere between the other two lists in this region, although closer to the results of Goorvitch than to the Querci results.

Goorvitch (1990) found his results for the 2.5μm band to be in good agreement with ground based spectra of this band in WZ Cas. Whereas the results by Querci et al. (1974) and the corresponding results by Kurucz (1994) are in reasonable good agreement short-ward of 1.1μm, all three sources of C_2 data disagree substantially with one another in the long-wavelength region. Therefore, the line strengths of the lines in Querci's list were divided by a factor 10 above 1.5 μm, while the original values were kept below 1.15 μm where Querci's and Kurucz' list are in good mutual agreement. In the region between 1.15 and 1.5 μm we divided the line strengths with a factor linearly increasing from 1 to 10. The resulting band strengths may of course be uncertain by a factor of 3 or more.

2.2.5 Implications of the scaling

The introduced scalings for the above molecules have substantial implications for details in the spectra, but they affect the model structure only marginally because the changes apply only to limited frequency ranges. Compared to previous synthetic spectra and analyses of molecular features (e.g., Hron et al. 1998, Loidl et al. 1999), we find (1) the contribution of C_2H_2 to be weaker around 2.5μm and 3.8μm and stronger around 7μm (on the short-wavelength wing of the 8μm CS band), (2) the contribution of HCN to be weaker around 2.5μm, and stronger around 3.8μm and 8μm, and (3) the contribution of C_2 to be weaker in the 2.5μm region in the new computations.

2.3 Synthetic spectra

Based on a model structure, the synthetic spectra are computed by evaluating (1) the chemical abundances using an equilibrium chemistry, (2) the continuum absorption using routines from the MARCS code (Gustafsson et al. 1975), and

(3) the molecular opacities as a function of wavelength using the opacity sampling method. The chemistry routines are those of Tsuji (1973), with updated data as described in Helling et al. (1996) except for data for C_3 which are from Irwin (1981). For the computation of the synthetic spectra, a larger frequency set of the opacity samplings is used than what entered the model construction. The spectral sampling density corresponds to approximately 30 000 frequencies through the interval from 0.5 to 25 μm, or a resolution of approximately 20 000. Due to the statistical character of the opacity sampling technique, it is necessary to average the OS spectrum over a number of frequencies before it can be compared to an observed spectrum. When the line density is large, the OS spectrum technique tends to overestimate the absorption, and vice versa when the line density is small. The higher the frequency density in the sampling, the more accurate is the final spectrum.

We have computed synthetic opacity sampling spectra including the molecules CO, CH, C_2, CN, CS, HCN, C_2H_2 and C_3 in the wavelength range between 0.5 and 25 μm with a resolution of 20 000.

2.4 Influence of model parameters on atmospheres and synthetic spectra

Spherical hydrostatic model atmospheres are uniquely determined by the effective temperature $T_{\rm eff}$, the surface gravity $\log(g)$, the mass M and the chemical composition. Varying one model parameter allows to investigate its influence on the atmospheric structure, on the partial pressures of various molecules and as a consequence the appearance of the synthetic spectra. Figures 2.3, 2.4 and 2.5 illustrate the influences of various model parameters on the temperature - gas pressure (T - $P_{\rm g}$) structures and the partial pressures of various molecular species. In Fig. 2.6 and 2.7 the corresponding synthetic spectra are shown. The following statements are valid all over the investigated parameter space. For illustration purposes we chose models for Figs. 2.3 to 2.7 where the discussed effects are clearly visible. This implies that the reference model is not the same in all cases.

Increasing the effective temperature of a model results in a hotter T - $P_{\rm g}$ structure, which means that at a fixed gas pressure the model with the higher effective temperature (dotted line in Fig. 2.3) has a higher temperature. The effect becomes pronounced at temperatures around and below 4000 K. For the partial pressures of the molecules (upper panels in Fig. 2.4) this means that below about 4000 K they are considerably lower than in the cooler reference model (full lines), especially the partial pressures of temperature sensitive molecules like C_2H_2. In the upper panels of Fig. 2.6 the corresponding unnormalised and normalised synthetic spectra are shown, where the black curves correspond to the reference model (full line in the structure plots) and the red ones to the model with the higher effective temperature (dotted line in the structure plots). A higher effective temperature leads to a shift of the maximum of the energy distribution to the blue and generally to weaker features as expected from the considerably lower partial pressures of all relevant molecules. Fig. 2.6 shows the continua superimposed. Note that the fluxes of the hotter model were scaled for clearer illustration. The model parameters of the reference model (black full lines) are: $T_{\rm eff} = 2700$ K, $\log(g) = -0.58$, C/O = 1.10, $M = 1\,{\rm M}_\odot$, $\log(Z/{\rm Z}_\odot) = 0.0$, $^{12}{\rm C}/^{13}{\rm C} = 89$ (solar value). The comparison model (dotted lines) has the following parameters: $T_{\rm eff} = 3200$ K, $\log(g) = -0.29$, C/O = 1.10, $M = 1\,{\rm M}_\odot$, $\log(Z/{\rm Z}_\odot) = 0.0$, $^{12}{\rm C}/^{13}{\rm C} = 89$. Both models have a luminosity of 5000 $L_\odot$.

Increasing the C/O ratio of a model results in a hotter T - $P_{\rm g}$ structure, which means that at a fixed gas pressure the model with the higher C/O ratio (dotted line in Fig. 2.3) has a higher temperature. The effect becomes most pronounced between temperatures of 4500 and 2000 K. The partial pressures of several species are responding differently to this change in atmospheric structure. The one of CO is unaffected by this change, the ones of C_2 and C_3 increase while the ones of HCN and C_2H_2 decrease. The on first sight astonishing decrease of the C_2H_2 partial pressure is due to the fact that with an increase of the C/O ratio in the model, the balance between C_3, C_2H_2, and HCN shifts such that relatively more C_3 and less C_2H_2 and HCN is formed. The spectra (upper middle panel in Fig. 2.6) are affected by a higher C/O ratio in such a way that the maximum of the energy distribution is shifted to the blue. The CO, C_2H_2, and HCN features become slightly weaker, the CN, C_2 and C_3 features grow stronger. The model parameters of the reference model (black full lines) are: $T_{\rm eff} = 2700$ K, $\log(g) = -0.58$, C/O = 1.10, $M = 1\,{\rm M}_\odot$, $\log(Z/{\rm Z}_\odot) = 0.0$, $^{12}{\rm C}/^{13}{\rm C} = 89$. The comparison model (dotted lines) has the following parameters: $T_{\rm eff} = 2700$ K, $\log(g) = -0.58$, C/O = 1.40, $M = 1\,{\rm M}_\odot$, $\log(Z/{\rm Z}_\odot) = 0.0$, $^{12}{\rm C}/^{13}{\rm C} = 89$.

Compared to a plane parallel model structure, a *spherical structure* with the same model parameters is cooler. The effects of sphericity start below temperatures of about 2500 K (dotted line in Fig. 2.3). This implies that only the partial pressures and features of those molecules are affected by sphericity effects which are formed mainly below 2500 K (see Sect. 1.4.1). A lower gas pressure generally favours smaller molecules and lower temperatures favour larger molecules. In the case of sphericity, we have lower temperatures and higher gas pressures, thus the partial pressures of polyatomic molecules are higher than in the plane parallel case (see lower middle panel of Fig. 2.4), while the partial pressures of the smaller diatomic molecules remain essentially constant. The parameters of both models are: $T_{\rm eff} = 2700$ K, $\log(g) = -0.58$, C/O = 1.10, $M = 1\,{\rm M}_\odot$, $\log(Z/{\rm Z}_\odot) = 0.0$, $^{12}{\rm C}/^{13}{\rm C} = 89$. The direct comparison of the spectra of plane parallel and spherical models is hampered by the fact that the plane parallel spectra were calculated

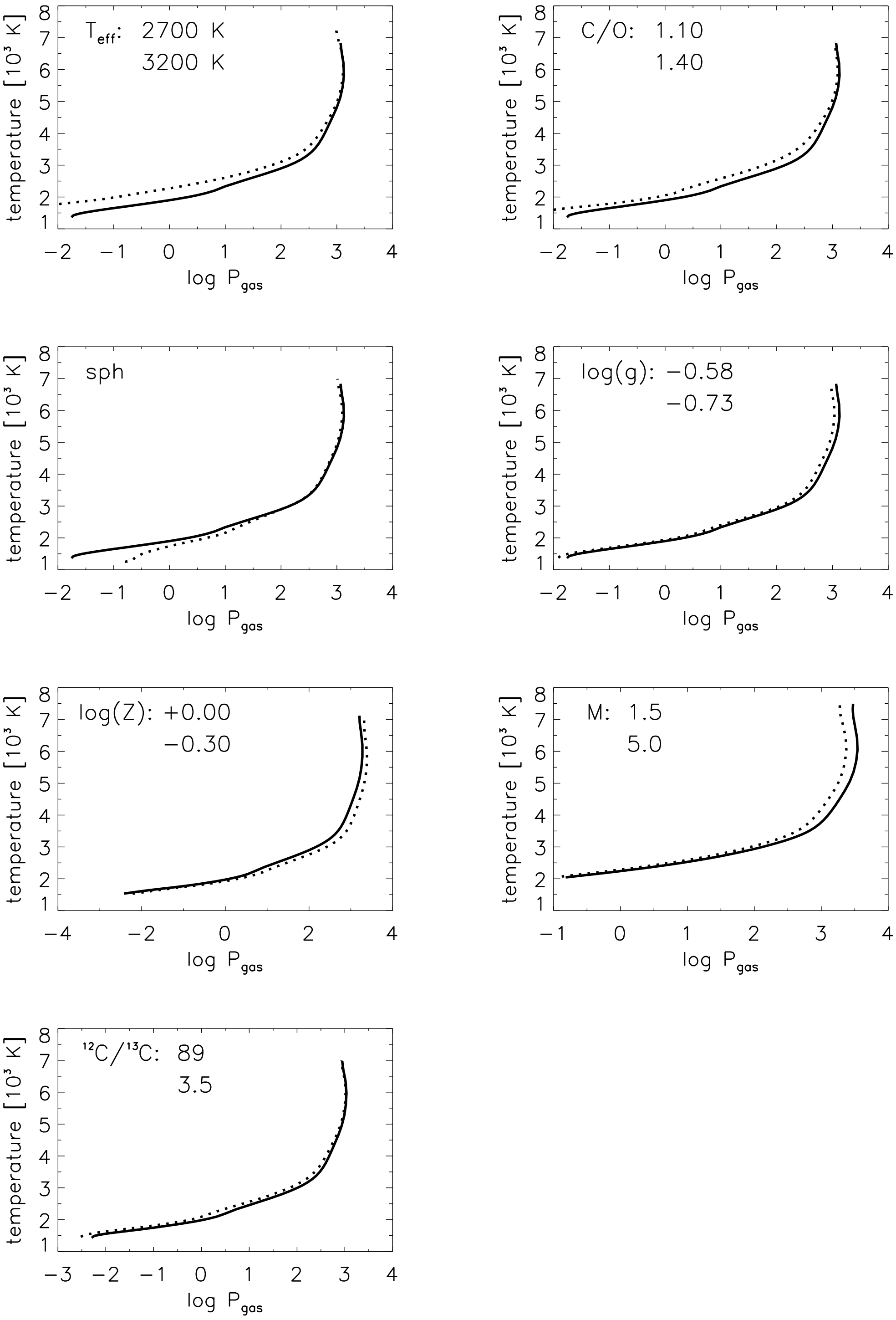

Figure 2.3: Gas pressure versus temperature of hydrostatic models where the parameter labeled in the figure has been varied compared to the reference model (full line), while all other parameters were kept constant. For details see text.

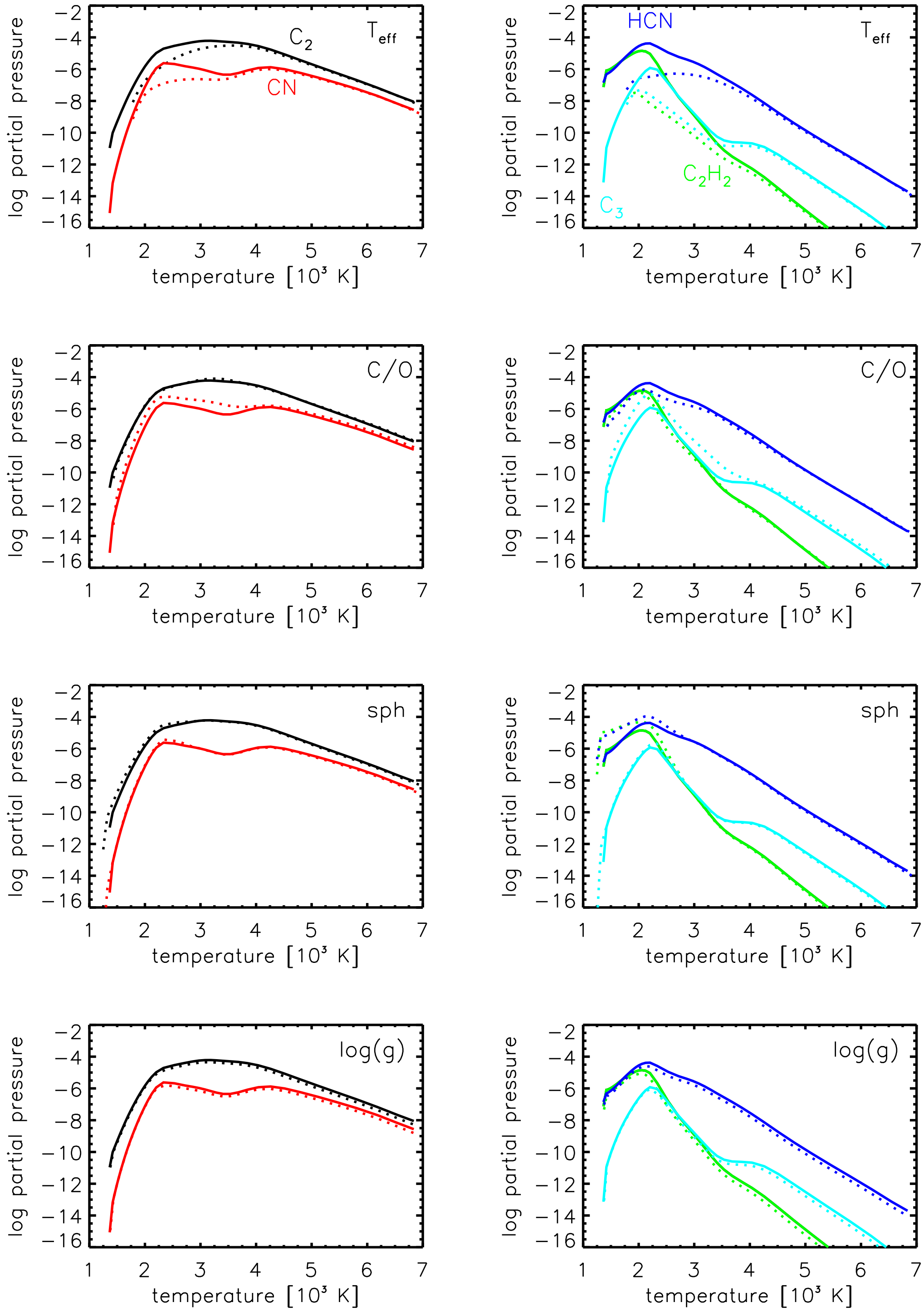

Figure 2.4: Partial pressures of various species versus temperature of hydrostatic models where the parameter labeled in the figure has been varied compared to the reference model (full line), while all other parameters were kept constant. For details see text.

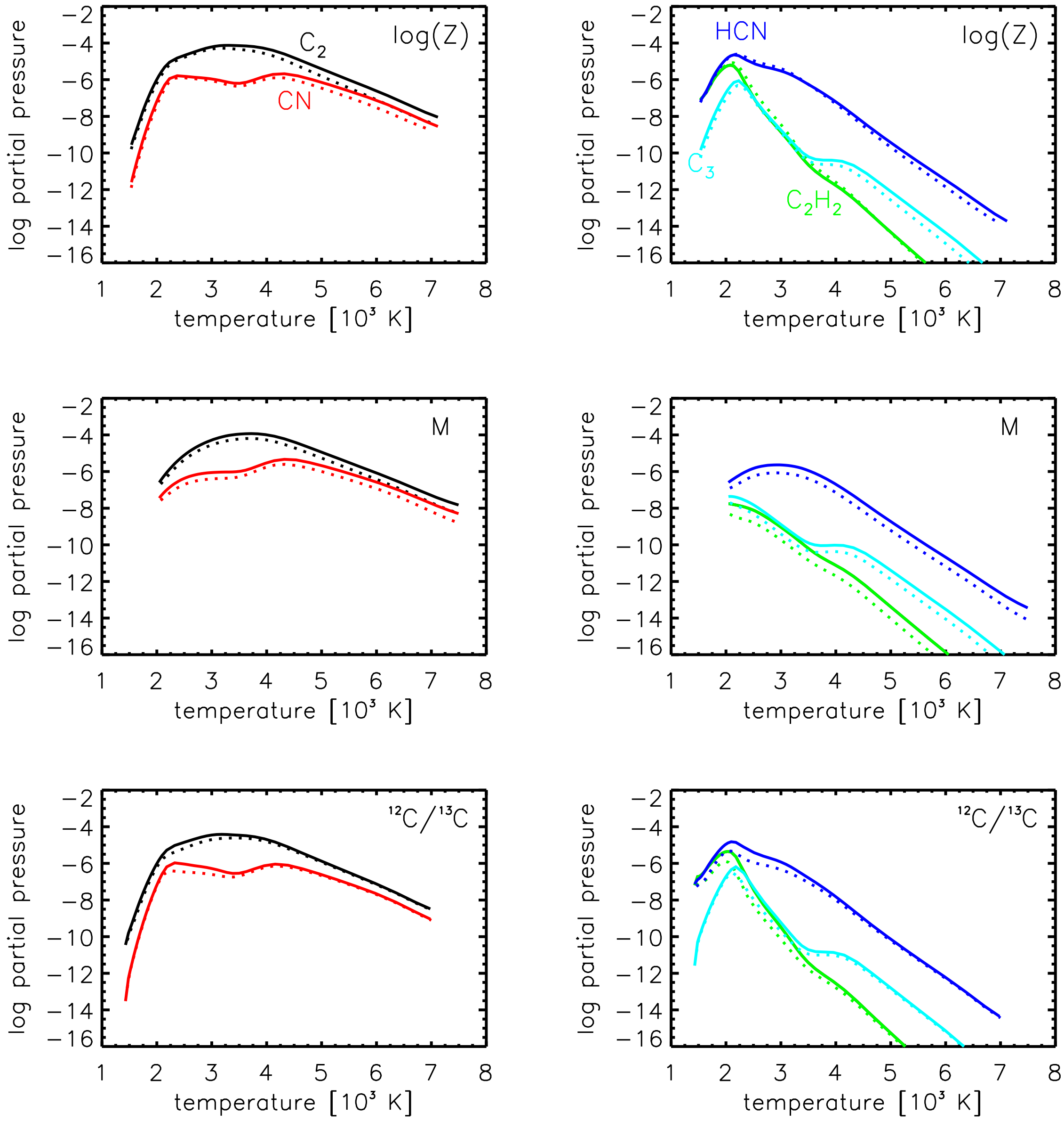

Figure 2.5: Partial pressures of various species versus temperature of hydrostatic models where the parameter labeled in the figure has been varied compared to the reference model (full line), while all other parameters were kept constant. For details see text.

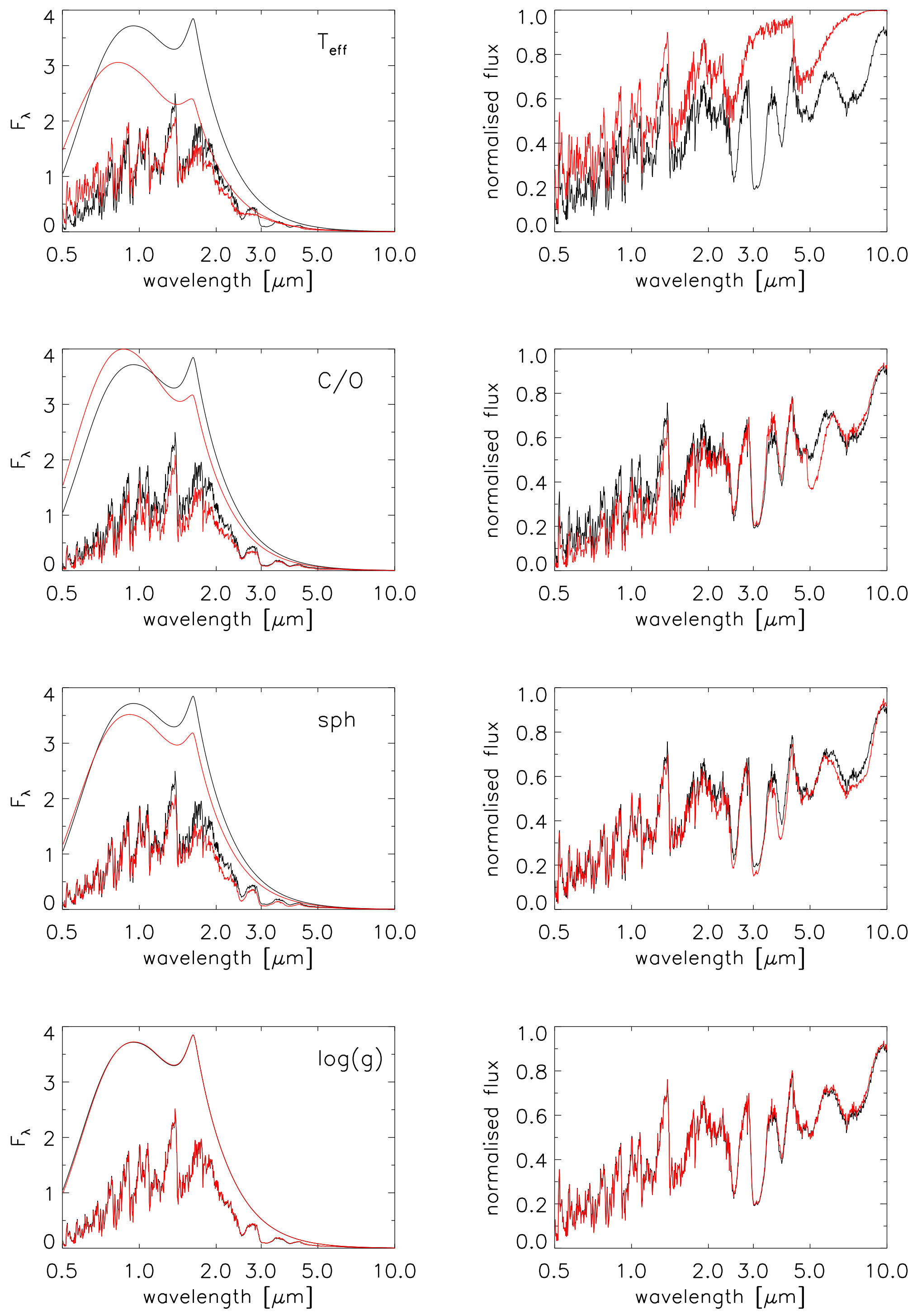

Figure 2.6: Synthetic spectra of hydrostatic models where the parameter labeled in the figure has been varied compared to the reference model (black line), while all other parameters were kept constant. Additionally, the model continua are shown. For details see text.

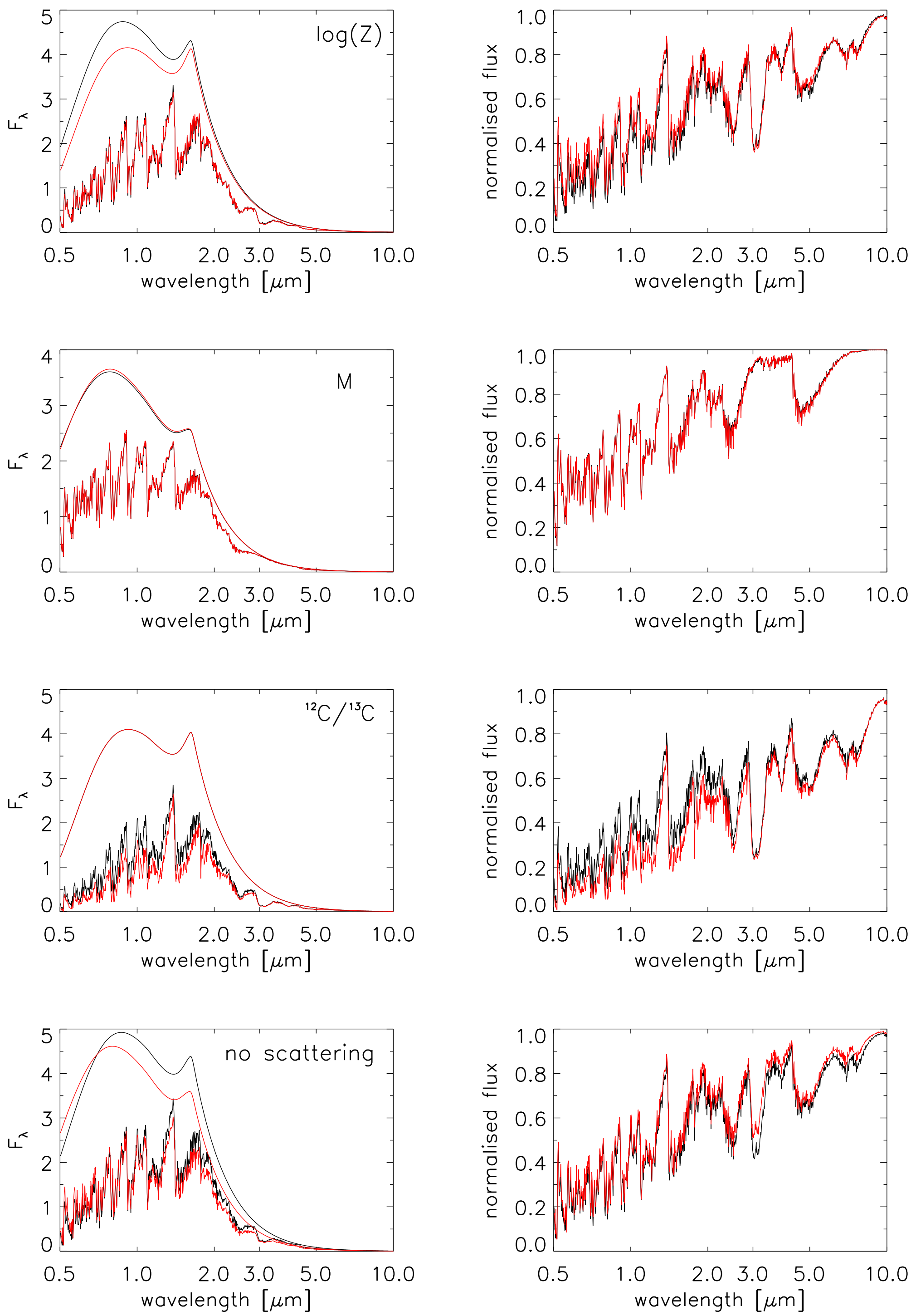

Figure 2.7: Synthetic spectra of hydrostatic models where the parameter labeled in the figure has been varied compared to the reference model (black line), while all other parameters were kept constant. Additionally, the model continua are shown. For details see text.

with scattering whereas the spherical ones neglected it. The influence of scattering on the spectra will be further discussed below. The maximum of the energy distribution of the spherical spectra is shifted to the blue (lower middle panel of Fig. 2.6). As expected from the behaviour of the partial pressures, the CO, CN, and C_2 features are unaffected, while the features of C_2H_2 HCN and C_3 become stronger.

A *lower surface gravity* (equivalent to a higher luminosity) results in a slightly hotter and more extended T - P_g structure (dotted line in Fig. 2.3). The partial pressures of all molecules decrease by approximately the same amount (lower panel of Fig. 2.4). Therefore, also the synthetic spectra of the two models with different surface gravity are more or less identical (lower panel of Fig. 2.6). The CO features become slightly stronger, while C_2, CN, C_2H_2 HCN and C_3 features behave in the opposite way. The model parameters of the reference model (black full lines) are: $T_\mathrm{eff} = 2700\,\mathrm{K}$, $\log(g) = -0.58$, $\mathrm{C/O} = 1.10$, $M = 1\,\mathrm{M}_\odot$, $\log(Z/\mathrm{Z}_\odot) = 0.0$, $^{12}\mathrm{C}/^{13}\mathrm{C} = 89$. The comparison model (dotted lines) has the following parameters: $T_\mathrm{eff} = 2700\,\mathrm{K}$, $\log(g) = -0.73$, $\mathrm{C/O} = 1.10$, $M = 1\,\mathrm{M}_\odot$, $\log(Z/\mathrm{Z}_\odot) = 0.0$, $^{12}\mathrm{C}/^{13}\mathrm{C} = 89$. The reference model has a luminosity of 5000 $\mathrm{L}_\odot$, the comparison model 7000 $\mathrm{L}_\odot$.

Lower metallicity results in a cooler T - P_g structure (dotted line in Fig. 2.3). The effect is most pronounced between 2000 and 7000 K. The partial pressures of various species respond differently to a change of metallicity. The ones of C_2, CN, and C_3 decrease; the partial pressure of HCN decreases above 3500 K while it increases below that value, and the one of C_2H_2 increases below 4500 K when compared to the model with solar metallicity (see upper panel of Fig. 2.5). The spectra (upper panel in Fig. 2.7) are affected by a lower metallicity in such a way that the maximum of the energy distribution is shifted to the red. The CO, CN, C_2, and C_3 features become weaker, while the C_2H_2 and HCN features strengthen. Note that the fluxes of the model with lower metallicity were scaled for clearer illustration. The model parameters of the reference model (black full lines) are: $T_\mathrm{eff} = 2958\,\mathrm{K}$, $\log(g) = +0.16$, $\mathrm{C/O} = 1.10$, $M = 2\,\mathrm{M}_\odot$, $\log(Z/\mathrm{Z}_\odot) = 0.0$, $^{12}\mathrm{C}/^{13}\mathrm{C} = 89$. The comparison model (dotted lines) has the parameters: $T_\mathrm{eff} = 2958\,\mathrm{K}$, $\log(g) = +0.16$, $\mathrm{C/O} = 1.10$, $M = 2\,\mathrm{M}_\odot$, $\log(Z/\mathrm{Z}_\odot) = -0.3$, $^{12}\mathrm{C}/^{13}\mathrm{C} = 89$.

Increasing mass leads to hotter T - P_g structures (dotted line in Fig. 2.3). The effects are most pronounced between temperatures of 3000 and 7500 K. The partial pressures of all molecules decrease by approximately the same amount (middle panel in Fig. 2.5). Therefore, the resulting synthetic spectra (upper middle panel of Fig. 2.7) look almost identical. The model parameters of the reference model (black full lines) are: $T_\mathrm{eff} = 3388\,\mathrm{K}$, $\log(g) = +0.53$, $\mathrm{C/O} = 1.10$, $M = 1.5\,\mathrm{M}_\odot$, $\log(Z/\mathrm{Z}_\odot) = 0.0$, $^{12}\mathrm{C}/^{13}\mathrm{C} = 89$. The comparison model (dotted lines) has the following parameters: $T_\mathrm{eff} = 3388\,\mathrm{K}$, $\log(g) = +0.25$, $\mathrm{C/O} = 1.10$, $M = 5\,\mathrm{M}_\odot$, $\log(Z/\mathrm{Z}_\odot) = -0.3$, $^{12}\mathrm{C}/^{13}\mathrm{C} = 89$.

A *lower* $^{12}C/^{13}C$ *ratio* results in a slightly hotter T - P_g structure (dotted line

Table 2.1: Effects on the synthetic spectra if model parameter(s) are varied

varied parameter(s)	effects on features	effects on energy distribution
higher L	C_2H_2 weaker; C_2, CN and C_3 stronger	–
higher T_{eff}	all stronger	bluer
higher M	all weaker	bluer
higher Z	CO, CN, C_2, C_3 stronger; C_2H_2 HCN weaker	bluer
higher C/O	CO, CN, C_2, C_3 stronger; C_2H_2 HCN weaker	bluer
higher T_{eff} + M	all weaker	bluer
higher T_{eff} + lower Z	all weaker	bluer
higher M + Z	all stronger	bluer
higher M + Z + T_{eff}	all weaker	bluer
lower M + T_{eff} + higher Z	all stronger	redder
lower M + Z + higher T_{eff}	all weaker	redder

in Fig. 2.3). The effect is most pronounced at temperatures between 2000 and 4000 K. We have calculated opacity sampling data for all included molecules with $^{12}C/^{13}C$ ratios of 89 (the solar value), 3.5 (the CNO cycle equilibrium, which is the theoretical minimum value) and 40 (an intermediate value). The partial pressures of C_2, CN and C_3 decrease slightly, the ones of C_2H_2 and HCN decrease too but stronger (lower panel of Fig. 2.5). The C_2, CN, and C_3 features become stronger while the C_2H_2 and HCN features remain unchanged compared to the reference model (lower middle panel of Fig. 2.7). The model parameters of the reference model (black full lines) are: $T_{\text{eff}} = 2800$ K, $\log(g) = -0.67$, C/O = 1.10, $M = 1\,M_\odot$, $\log(Z/Z_\odot) = 0.0$, $^{12}C/^{13}C = 89$. The comparison model (dotted lines) has the following parameters: $T_{\text{eff}} = 2800$ K, $\log(g) = -0.67$, C/O = 1.10, $M = 1\,M_\odot$, $\log(Z/Z_\odot) = 0.0$, $^{12}C/^{13}C = 3.5$.

The lower panel of Fig. 2.7 shows a comparison of the synthetic spectra of a plane parallel model calculated with and without scattering. The omission of scattering results in a shift of the maximum of the energy distribution to the blue and in weaker C_3, HCN and C_2H_2 features.

Different model parameters influence the synthetic spectra to different extents. Changes of effective temperature, the C/O ratio and the $^{12}C/^{13}C$ ratio have strong influences, while changing the surface gravity and mass induce rather small effects. If more than one model parameter is varied, it is not always clear how the spectra will change, especially if the effects of the varied parameters go into opposite directions. Then, the result will depend on how much the parameters have been changed. Nevertheless, if the luminosity of the two models that are to be compared is kept constant (i.e. the surface gravity and/or the mass is adjusted), clear trends of changes are visible; they are summarised in Table 2.1.

2.5 Sensitivity of spectral features to fundamental stellar parameters

Obtaining spectra simultaneously covering the optical and infrared range is not practical. Therefore, it is desirable to find spectral features and spectrophotometric indices over smaller wavelength ranges being sensitive to fundamental stellar parameters. With this purpose in mind we have, in a first attempt, searched for spectral features which can be observed from the ground and which are sensitive to effective temperature, the C/O ratio, log(g), mass, the ^{12}C/^{13}C ratio, and metallicity. We compare our results with data from Baumert (1972) and data from the Infrared Space Observatory. In a second step, we have calculated a large number of colour indices from our plane parallel hydrostatic models and compared them with data from Lançon & Wood (2000).

2.5.1 Spectral features in the Near Infrared

It would be interesting to determine effective temperature and abundance parameters from low resolution spectra rather than from high resolution data, since it will have a wide application to carbon stars in remote stellar systems. Unfortunately we were not able to find any molecular feature being sensitive enough to derive log(g), mass, and metallicity of the star for spectra with a resolution of 1000. As Figures 2.8 and 2.9 illustrate, the 3 μm C_2H_2 and HCN feature and the 5.1 μm C_3 feature proved to be good indicators for $T_{\rm eff}$ and the C/O ratio at least for stars with no or only small amounts of dust, respectively. Figure 2.8 shows normalised synthetic spectra in three wavelength ranges of spherical hydrostatic models with different effective temperatures, all other model parameters were kept constant (C/O = 1.10, $L = 5000\,L_\odot$, $M = 1\,M_\odot$, $\log(Z/Z_\odot) = 0.0$, $^{12}C/^{13}C = 89$). The dotted lines denote the continuum, the effective temperatures of the different model spectra are given in the plot. One can easily recognise that the lower the effective temperature is, the stronger are all bands and the further off the intensity is from the continuum. However, this is only obvious in the case of normalised spectra. But the increasing strength of the 3 μm (and the 2.5 and 3.8 μm) feature can be easily recognised also in unnormalised spectra. The lower the effective temperature, the stronger and broader is the 3 μm feature; the broadening is due

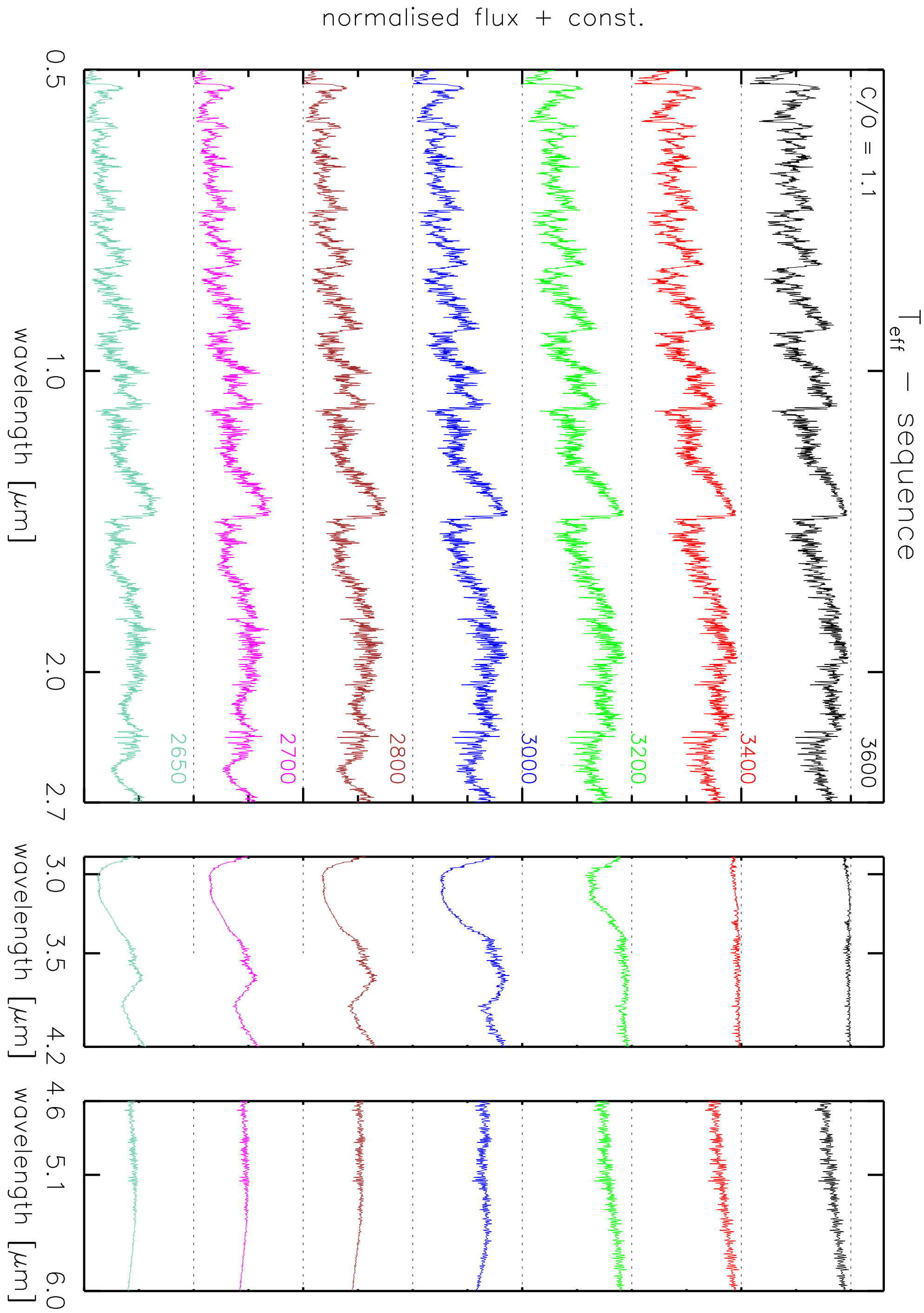

Figure 2.8: Normalised synthetic spectra of spherical hydrostatic models with different effective temperatures, where all other model parameters were kept constant (C/O = 1.1, $L = 5000\,\mathrm{L}_{\odot}$, $M = 1\,\mathrm{M}_{\odot}$, $\log(Z/\mathrm{Z}_{\odot}) = 0.0$, $^{12}\mathrm{C}/^{13}\mathrm{C} = 89$). For details see text.

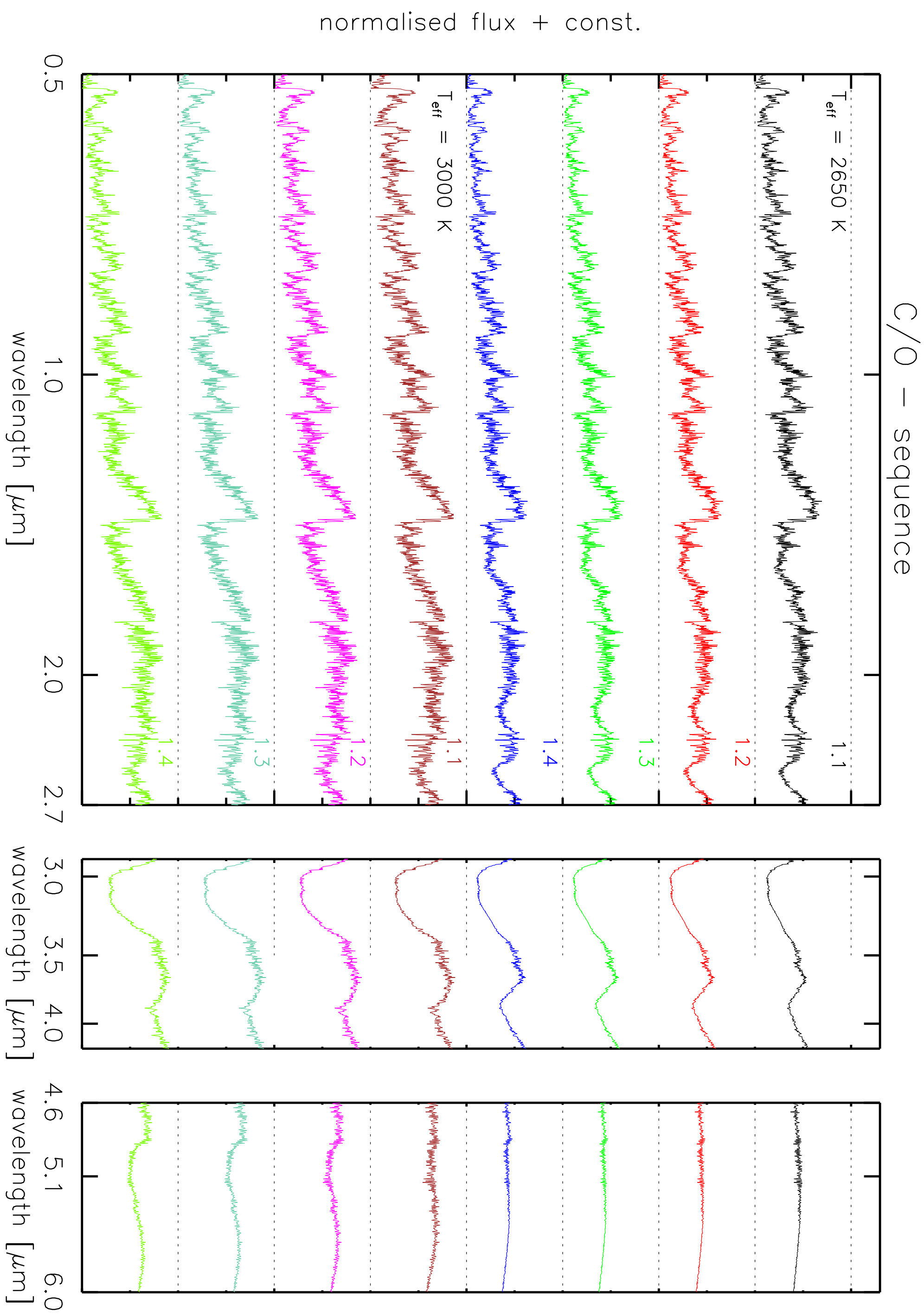

Figure 2.9: Normalised synthetic spectra of spherical hydrostatic models with different C/O ratios for two different effective temperatures, where all other model parameters were kept constant ($L = 5000\,L_\odot$, $M = 1\,M_\odot$, $\log(Z/Z_\odot) = 0.0$, $^{12}C/^{13}C = 89$). For details see text.

to the increasing contribution of hot bands of C_2H_2 and of HCN at lower temperatures. In models with effective temperatures around 2800 K the 3 μm feature becomes saturated, at such low effective temperatures the 3.8 μm feature is a slightly better indicator. All other model parameters have only a moderate influence on the strength of the 3μm feature, therefore it is suitable to determine the effective temperature of a star if the contribution of dust is negligible. Hot dust around a star can considerably weaken the strength of the 3 μm feature. On the contrary, a lower effective temperature has almost no other influence in the 5 μm region than departing more and more from the continuum flux while the shape and the slope of this spectral region stays almost constant. Figure 2.9 shows normalised synthetic spectra of spherical hydrostatic models with different C/O ratios for two different effective temperatures, all other model parameters have been kept constant ($L = 5000\,\mathrm{L}_\odot$, $M = 1\,\mathrm{M}_\odot$, $\log(Z/\mathrm{Z}_\odot) = 0.0$, $^{12}\mathrm{C}/^{13}\mathrm{C} = 89$). We see that in the wavelength region between 0.5 and 2.7 μm, the bands due to C_2 become slightly stronger if the C/O ratio increases. A high C/O ratio of a star is much easier to recognise in the 5 μm region, where the C_3 feature becomes considerably stronger the higher the C/O ratio. On the contrary, the 3 μm C_2H_2 and HCN feature weakens a bit. This weakening is due to a pressure balance shift between C_3, C_2H_2 and HCN such that relatively more C_3 and less C_2H_2 and HCN is formed if the C/O ratio in a model is increased.

Figure 2.10 displays a few spectra obtained with the Infrared Space Observatory (see Sect. 4.7). They are arranged in a sequence of decreasing effective temperature (upper left panel) and in a sequence of increasing C/O ratio (upper right panel). Below, sequences of spherical hydrostatic model spectra (lower left panel) with decreasing effective temperature and of increasing C/O ratio for two different effective temperatures (lower right panel) are shown for comparison.

Both features which are proposed here as powerful tool for determinations of $T_{\rm eff}$ and the C/O ratio of a star have the advantage that they are accessible to observations from the ground. The Earth's atmosphere is transparent for the long-wavelength part of the 3 μm feature (L filter; $3.04-3.80\,\mu$m) and, with limitations, for the short-wavelength part of the 5 μm feature (M filter; $4.44-5.08\,\mu$m).

2.5.2 Colour indices in the 0.5 to 2.5 μm region

Optical and near-infrared spectra and colours have been obtained continuously for at least the last 25 years. Therefore, it is desirable to use this information and investigate the wavelength region between 0.5 and 2.5 μm for potentially useful colour indices.

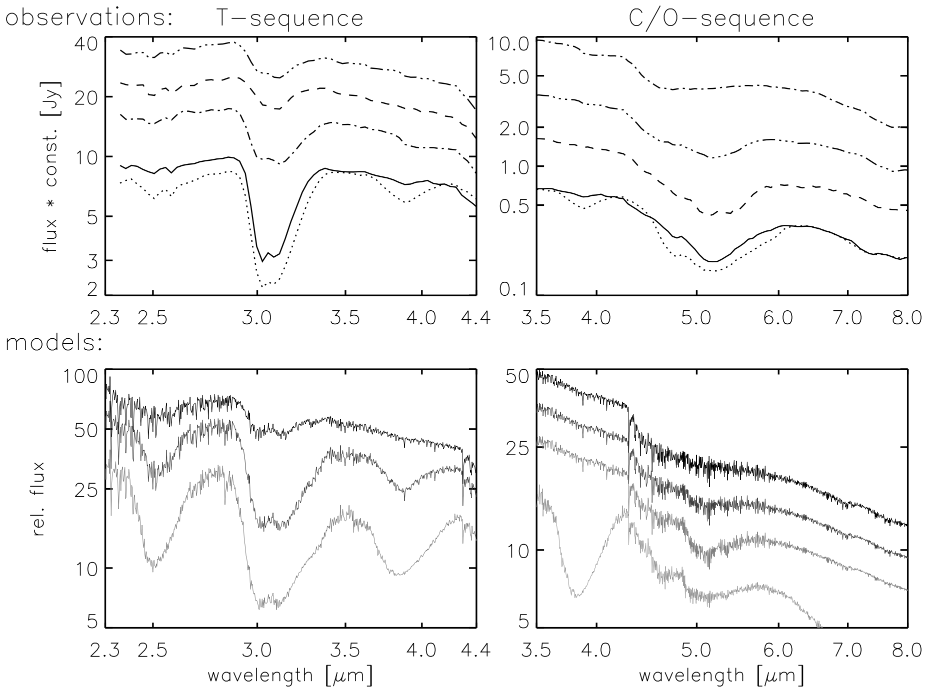

Figure 2.10: Spectra obtained with the Infrared Space Observatory arranged in a sequence of decreasing effective temperature (upper left panel) and in a sequence of increasing C/O ratio (upper right panel). The full line denotes a maximum light spectrum of R Scl, the dotted line a minimum spectrum of R Scl, the dashed line one of TT Cyg, the dash-dot line stands for TX Psc and the dash-triple-dot line for V460 Cyg. Spherical hydrostatic model spectra are shown for comparison in the lower panels. Lower left panel (top to bottom): $T_{\rm eff} = 3200\,{\rm K}$, $T_{\rm eff} = 3000\,{\rm K}$, $T_{\rm eff} = 2650\,{\rm K}$. Lower right panel (top to bottom): C/O = 1.10, C/O = 1.20, C/O = 1.40 (all for $T_{\rm eff} = 3200\,{\rm K}$) and C/O = 1.40 ($T_{\rm eff} = 2650\,{\rm K}$). Adopted from Loidl et al. (1999b).

Wing colours

For a small set of models which are consistent with the stellar evolution tracks of Bessell et al. (1989) we calculated "Wing colours" (see Sect. 4.1 for details) and compared our results with some of the measurements of Baumert (1972). Figure 2.11 shows the colour index 8122−7809 which measures the CN ($\Delta\,{\rm v} = +2$) transition strength versus the 7117−7809 index measuring the CN ($\Delta\,{\rm v} = +3$) transition strength. Full symbols denote multiple observations of the stars labeled in the plot. It is obvious that Miras (V CrB and V Cyg) are clearly separated from semiregular stars of type b (TT Cyg) and from irregular variables (TX Psc and V460 Cyg). Open symbols label the models, crosses stand for plane paral-

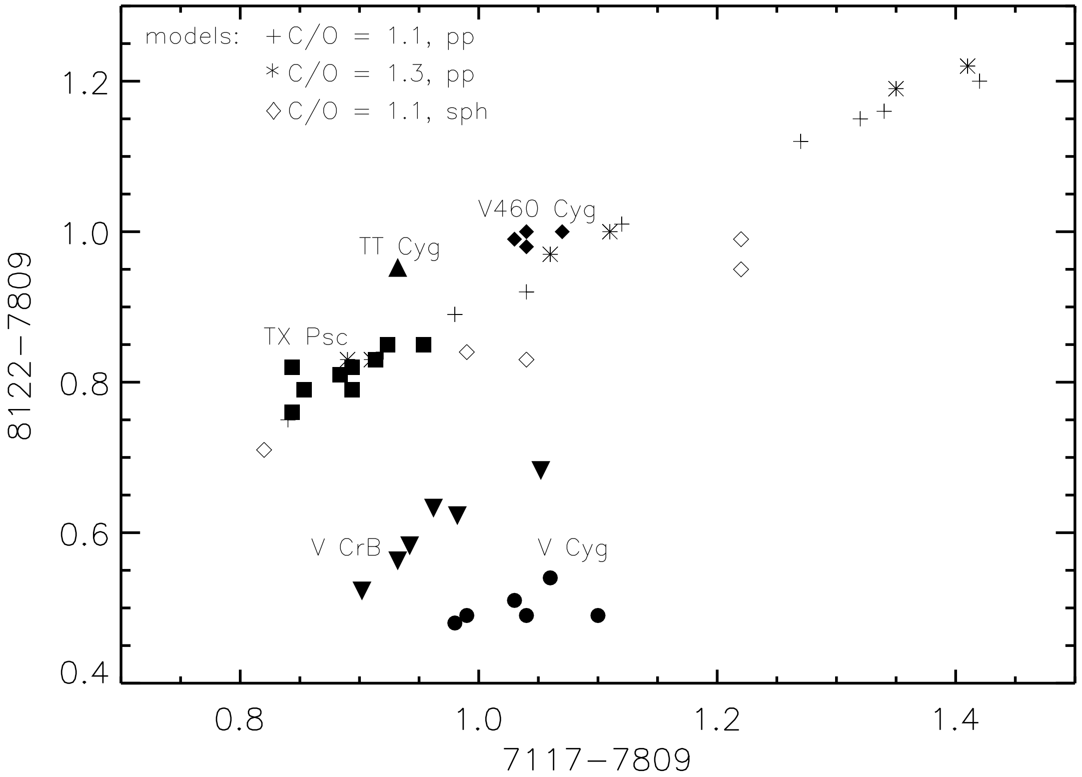

Figure 2.11: Plot of the colour index 8122−7809 which measures the CN (Δ v = + 2) transition strength versus 7117−7809 which measures the CN (Δ v = + 3) transition strength. Full symbols denote multiple observations of the same stars which are labeled in the appropriate region of the plot. Open symbols denote model results, crosses stand for plane parallel hydrostatic models with C/O = 1.10, asterisks for plane parallel models with C/O = 1.30, and diamonds for spherical models with C/O = 1.10.

lel hydrostatic models with C/O = 1.10, asterisks for plane parallel models with C/O = 1.30, and diamonds for spherical models with C/O = 1.10. The models can cover the observed ranges of band intensities of the moderately variable stars (for adjustion of the zero point see Sect. 4.1). Such a two-colour plot allows in principle to arrange stars in a sequence of decreasing/increasing effective temperature ($T_{\rm eff}$ of models and stars decreases from bottom left to top right) and to estimate whether the star is surrounded by a dust shell or not. The effects of the C/O ratio, luminosity, mass, and metallicity are negligible.

Other broad- and narrow-band indices

We calculated a large number of colour indices from our plane parallel hydrostatic models and, as an example, compared the results with data from Lançon &

Wood (2000). The spectra of Lançon & Wood (2000) cover the wavelength range between 0.5 and 2.5 μm, the near-infrared spectra were obtained with the 2.3 m telescope at the Siding Spring Observatory and the optical spetra were acquired simultaneously at the 1.88 m telescope on Mount Stromlo. These data will be discussed in detail in Sect. 4.2. The filter zero points were calculated from a Vega model of Dreiling & Bell (1980), we assumed that the Vega model has 0.0 mag in all filters.

Table 2.2: Filter names, positions and widths

name	central wavelength [μm]	filter width [μm]
V	0.545	0.230
R	0.600	0.350
I	0.805	0.220
J	1.220	0.300
H	1.630	0.380
K	2.190	0.540
W710	0.710	0.006
W883	0.883	0.0045
W888	0.888	0.0045
W110	1.100	0.006
W123	1.236	0.012
F108	1.083	0.0108
F110	1.100	0.06
F171	1.715	0.07
F180	1.800	0.07
F222	2.150	0.15

The investigated indices include possible combinations of filters chosen inside the commonly used sets of:
(i) VRIJHK broad band filters as defined in Bessell (1990), except that the V and K band have been truncated at 5 100 and 24 500 Å, respectively, to match the wavelength range available in the data of Lançon & Wood (2000).
(ii) Intermediate filters that we call "Wing filters" for brevity. They were initially defined by Wing (1967) and were summarised by Bessell et al. (1989).
(iii) Hubble Space Telescope NICMOS filters, whose transmission curves were obtained from the Space Telescope Science Institute (1997). The narrow filter transmissions were modelled as rectangles with appropriate central wavelengths and bandwidths, F108 (see Tab. 2.2) is on Camera 1, all others are on Camera 2.
(iv) Two narrow-band CO measurements as explained by Kleinmann & Hall (1986).

We call the index measuring the equivalent width of the CO 2-0 band head at 2.29 μm CO1. The second index, COH, measures the ratio of the flux density between 16 182 and 16 262 Å to the average of the flux densities in two narrow windows on either side of the CO feature; one between 16 145 and 16 175 Å, the other between 16 270 and 16 300 Å.
Figure 2.12 shows the narrow-band filters which proved to be useful plotted over a synthetic spectrum.

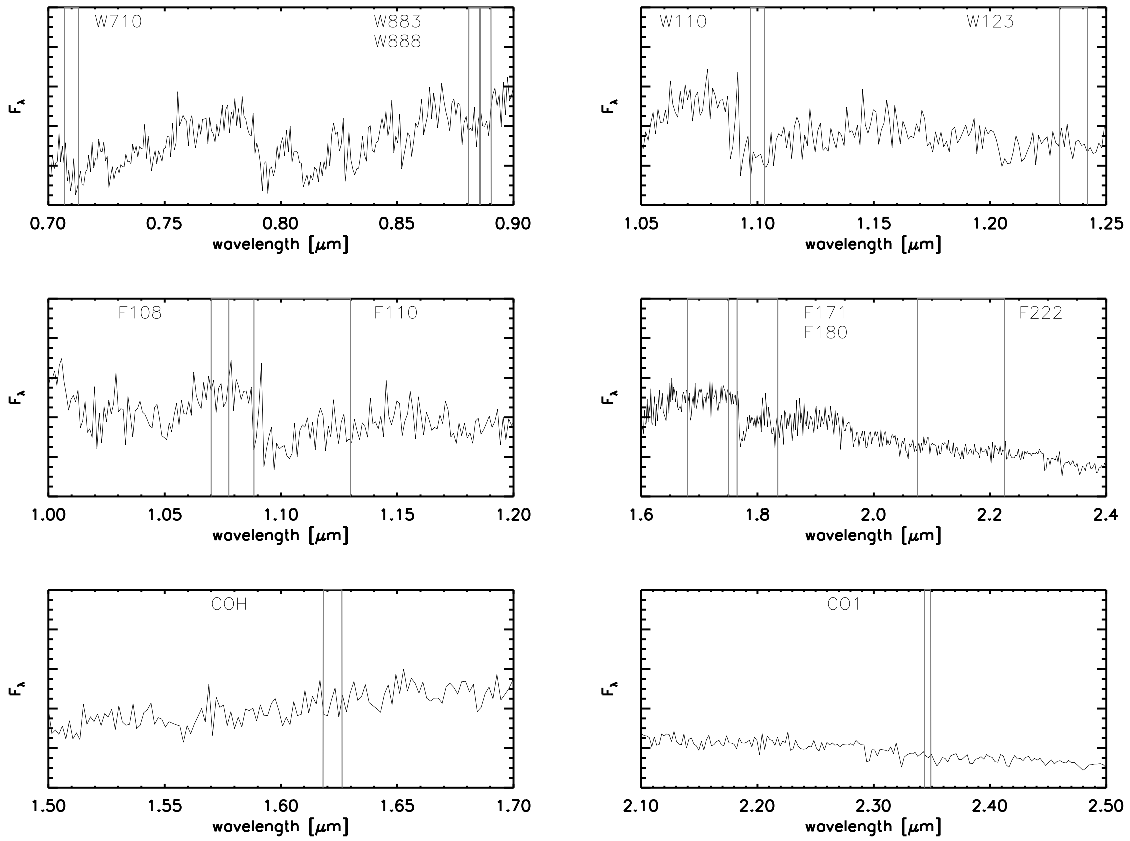

Figure 2.12: Various filters which proved to be useful plotted over a synthetic spectrum.

Effective-temperature indicators
The range of temperatures relevant for carbon-rich AGB stars is large, and the effect of this parameter on the energy distribution is strong. In the sample of theoretical spectra, linear correlation coefficients exceeding 0.975 (absolute value) were obtained between $T_{\rm eff}$ and V–K, R–K, R–H, R–J, W710–W123 (and colour indices combining filters from two different filter subsets). The correlations obtained with R–J, R–H and W710–W123 are the strongest. The correlations are shown in Figs. 2.13, 2.14 and 2.15. In similar plots for colours including V or K

band measurements, there is a stronger systematic shift between the loci of the data and the models. This shift is due to the lack of the inclusion of atomic lines in our models in the V filter.

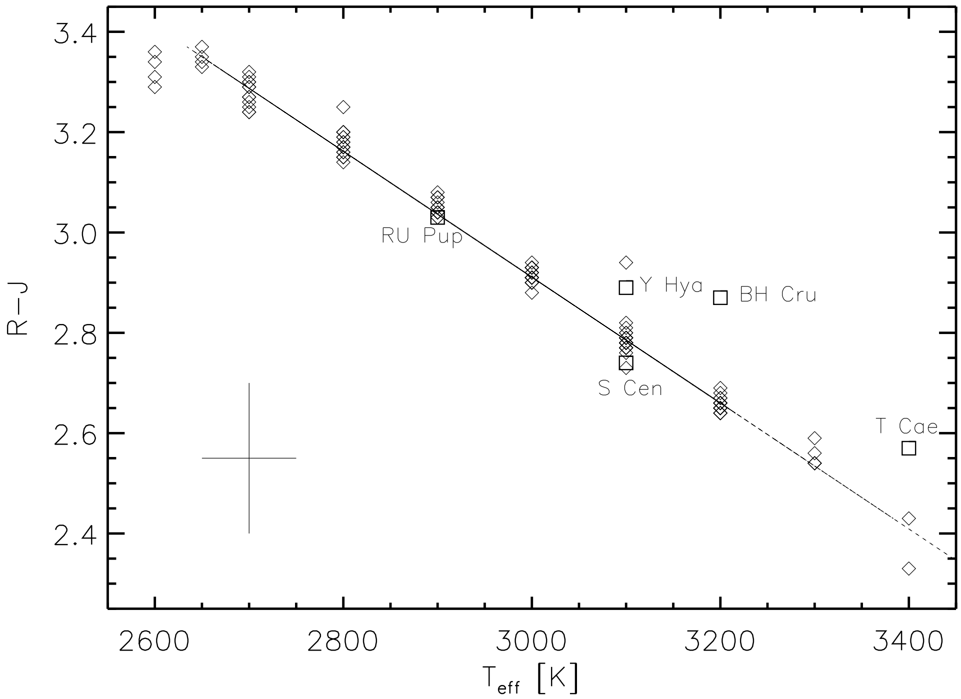

Figure 2.13: R–J as an effective temperature indicator for carbon rich stars. Each diamond represents a model spectrum. The dashed line shows the linear least squares regression: $T_{\rm eff}$ (K) = 5320 − 797 (R–J). The squares represent the January 1996 spectra of Lançon & Wood (2000); they are located at the effective temperature resulting from a fit to the spectra (see Sect. 4.2 for details). The vertical bar indicates the $2\,\sigma$ uncertainty on the colours of the data points. The horizontal bar accounts for the range of effective temperatures allowed with equally satisfactory fits.

$^{12}C/^{13}C$ indicators

In the sample of model spectra, the spread around the mean relations between $T_{\rm eff}$ and the temperature sensitive colours is too small to be useful to constrain other stellar parameters. Additional indices have to be selected. The tightest linear correlation with ^{12}C/^{13}C was obtained for W888–W883. The W888 filter measures mainly a ^{12}C band head of C_2 while the 883 filter measures mainly the ^{13}C band head of the same C_2 band. The two colour plot obtained by combining the W888–W883 index with, for instance, R–J in principle allows us to determine simultaneously $T_{\rm eff}$ and to constrain therewith the value of ^{12}C/^{13}C. The left part of Fig. 2.16 shows that the locus of the models and the data agree well in the

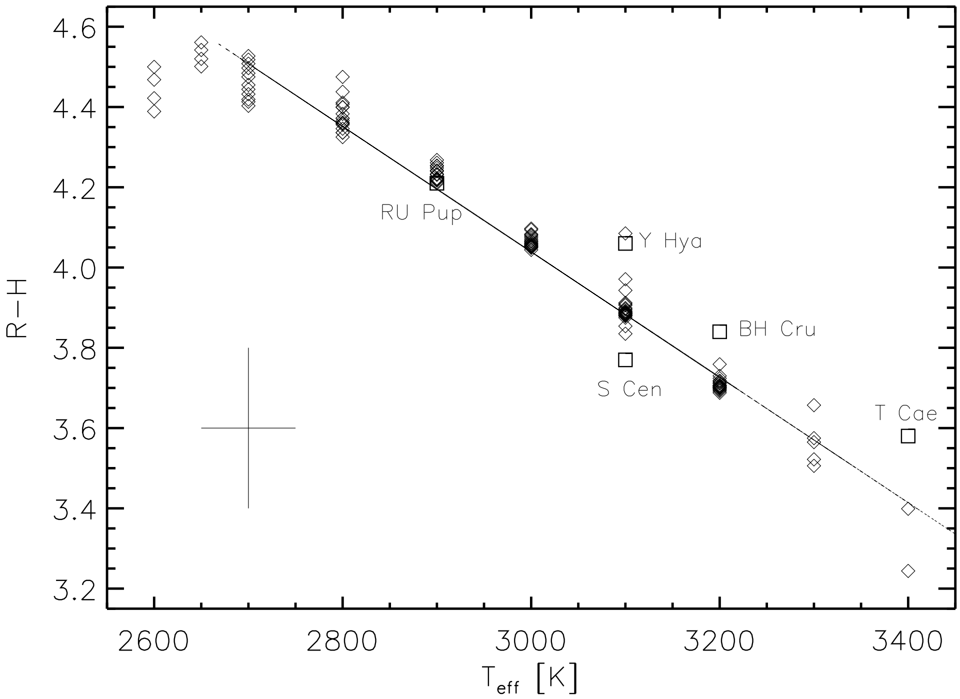

Figure 2.14: R–H as an effective temperature indicator. The linear regression line writes: T_{eff} (K) = 5585 − 640 (R–H).

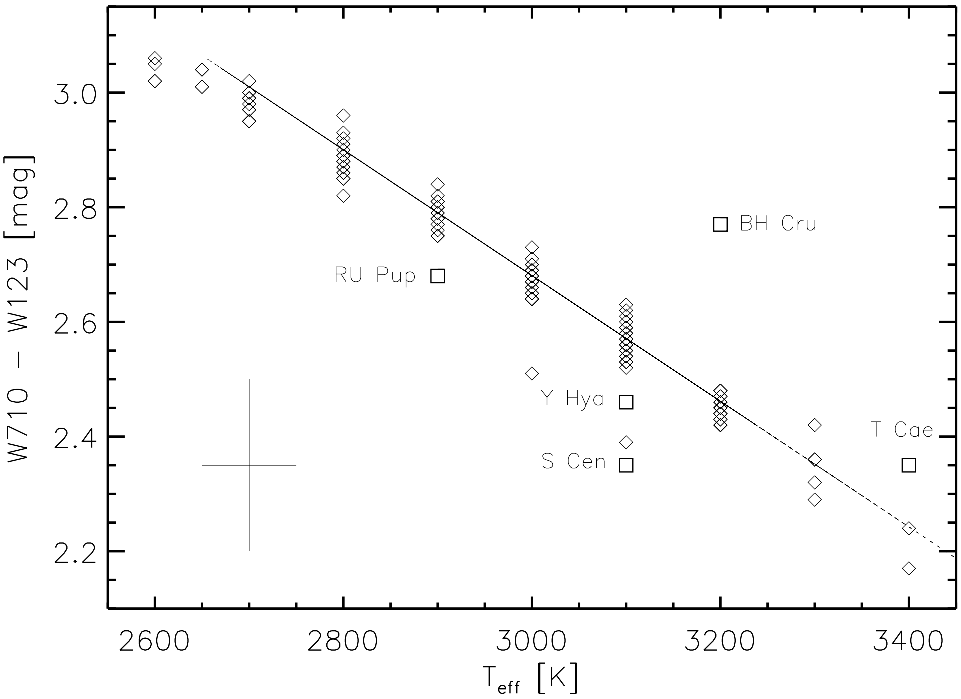

Figure 2.15: The intermediate band colour index W710–W123 as a T_{eff} indicator. The linear regression line writes: T_{eff} (K) = 5445 − 912 (W710–W123).

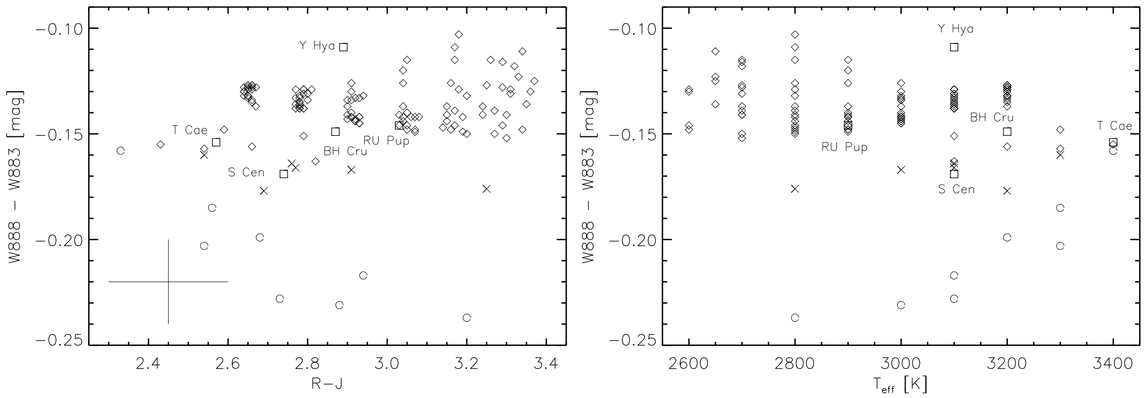

Figure 2.16: Left panel: The $^{12}C/^{13}C$ indicator W888–W883 versus $T_{\rm eff}$, as measured by R–J. Small symbols are models, computed respectively with $^{12}C/^{13}C = 89$ (diamonds), 40 (crosses) and 3.5 (circles). Large squares are the observational January 1996 data of Lançon & Wood (2000), for which a spectral fit was performed. 2 σ uncertainties of the observations are shown. Rigth panel: The $^{12}C/^{13}C$ indicator W888–W883 versus $T_{\rm eff}$ of the models.

two colour diagram, in the right part W888–W883 is plotted versus the effective temperature of the model.

C/O indicators
The best linear correlation with the C/O ratio is obtained for the intermediate band colour index W110–W123. The W110 filter measures mainly a CN band while in the W123 filter a C_2 band contributes significantly to the absorption of CN. Other potentially useful indices include the HST NICMOS colours F180–F171, F180–F222 and F108–F110.

The two colour plot of Fig. 2.17 allows us to simultaneously determine the effective temperature and the C/O ratio. Although there seems to be a systematic offset between the loci of the empirical and the model indices, in the sense that empirical values of W110–W123 are larger by about 0.1 magnitude than those of the models, there is a large region of overlap.

Surface gravity indicators
The effect of gravity variation over the range of parameters explored is small compared to the changes introduced by varying C/O or $^{12}C/^{13}C$. The reason for the low sensitivity of the near-IR spectral range to surface gravity lies in the relatively high temperatures (i.e. deep stellar layers) at which the relevant molecules form. No spectrophotometric index capable of directly constraining $\log(g)$ could be found.

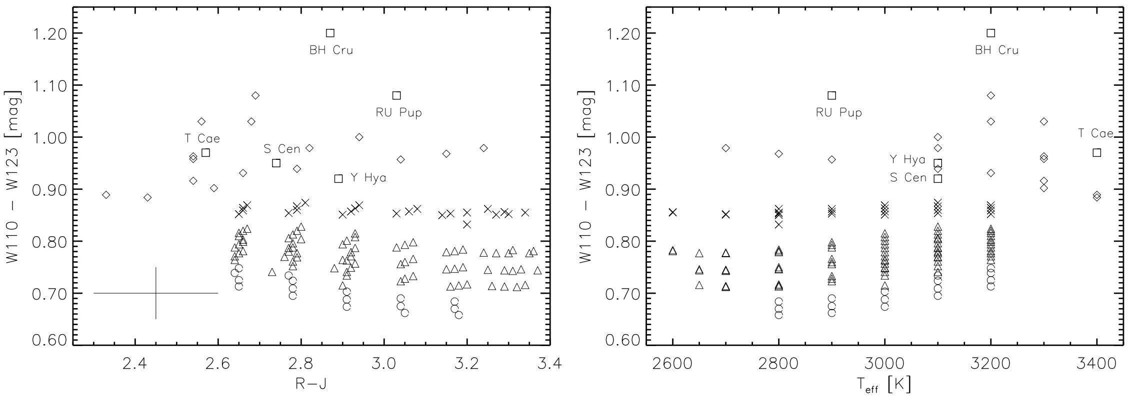

Figure 2.17: Left panel: The C/O indicator W110–W123 versus $T_{\rm eff}$, as measured by R–J. Small symbols are models, computed respectively with $C/O < 1.1$ (diamonds), $1.1 \leq C/O \leq 1.2$ (crosses), $1.2 < C/O \leq 1.4$ (triangles) and $1.4 < C/O \leq 1.8$ (circles). Large squares are observational January 1996 data of Lançon & Wood (2000), for which a spectral fit was performed. $2\,\sigma$ uncertainties of the observations are shown. Right panel: The C/O indicator W110–W123 versus $T_{\rm eff}$ for the models.

Conclusions

The stellar parameters $T_{\rm eff}$, $^{12}C/^{13}C$ and C/O can in principle be determined from broad- and narrow-band colour indices. We have been able to find indices for which no or small systematic differences exist between the loci of models and observations. We stress that very good photometry is needed to actually use any of these diagnostic plots. Spectrophotometry in the 3 and 5 μm region (L and M band) appear to be the most promising tool to determine $T_{\rm eff}$ and C/O of an AGB star. These results are consistent with what has been said in Sect. 2.4. Due to the facts that C_2H_2 is the most temperature sensitive molecule which we account for in the present calculations, and in addition the one which is formed at the lowest temperatures of all molecules, it has to be expected that its features are good tools for a determination of the effective temperature. On the contrary, the C_2 and CN features which dominate the optical and infrared region up to 2.5 μm, are formed much deeper inside the star where the structure is affected only very little if the effective temperature changes, hence the C_2 and CN features are a less sensitive tool for a determination of the effective temperature of a star. The same applies for the C/O ratio. The molecule most sensitive to the C/O ratio is C_3 which again forms further out in the atmosphere than C_2. Stellar parameters like mass and $\log(g)$ have minor (but non negligible) influences on the intensities of the 3 and 5 μm features; a higher mass weakens both features, a higher luminosity strengthens them.

Chapter 3

Dynamic model spectra

3.1 Dynamic models and spectrum synthesis

3.1.1 Dynamic model atmospheres

The hydrostatic initial models of dynamic model atmospheres are determined by the effective temperature $T_{\rm eff}$, the luminosity L, the mass M and the chemical composition. The structure of these initial models can be compared directly to models calculated with the MARCS code because both use the same molecular data (see Sect. 2.1). Figure 3.1 (upper panel) shows a comparison of the temperature-pressure stratification computed with the MARCS code with about 10000 frequency points (red) and a hydrostatic initial model calculated with 51 frequency points (black). Both structures have the following parameters: $T_{\rm eff} = 3000\,{\rm K}$, $M = 1\,{\rm M}_{\odot}$, $L = 5200\,{\rm L}_{\odot}$ and C/O = 1.10. The discrepancy at temperatures above about 6000 K is due to the fact that the black structure is calculated without convection and the red one with convection. The lower panel of Fig. 3.1 shows the corresponding synthetic spectra. For the dynamical calculation, two more parameters have to be specified, the piston velocity $\Delta u_{\rm p}$ and the piston period P. Table 3.1 summarises the models which were used in this thesis.

3.1.2 Synthetic spectra

A dynamical calculation yields the structure of the atmosphere and circumstellar envelope (density, temperature, degree of condensation, etc.) as a function of time. Additionally, the models provided by Susanne Höfner were extended inwards by solving the static stellar structure equations (Gautschy et al. 1996). This was necessary because it turned out that the models were not sufficiently optically thick at the inner boundary at all wavelengths of interest, especially in the continuum. However, the effect of dynamical phenomena on the spectra is

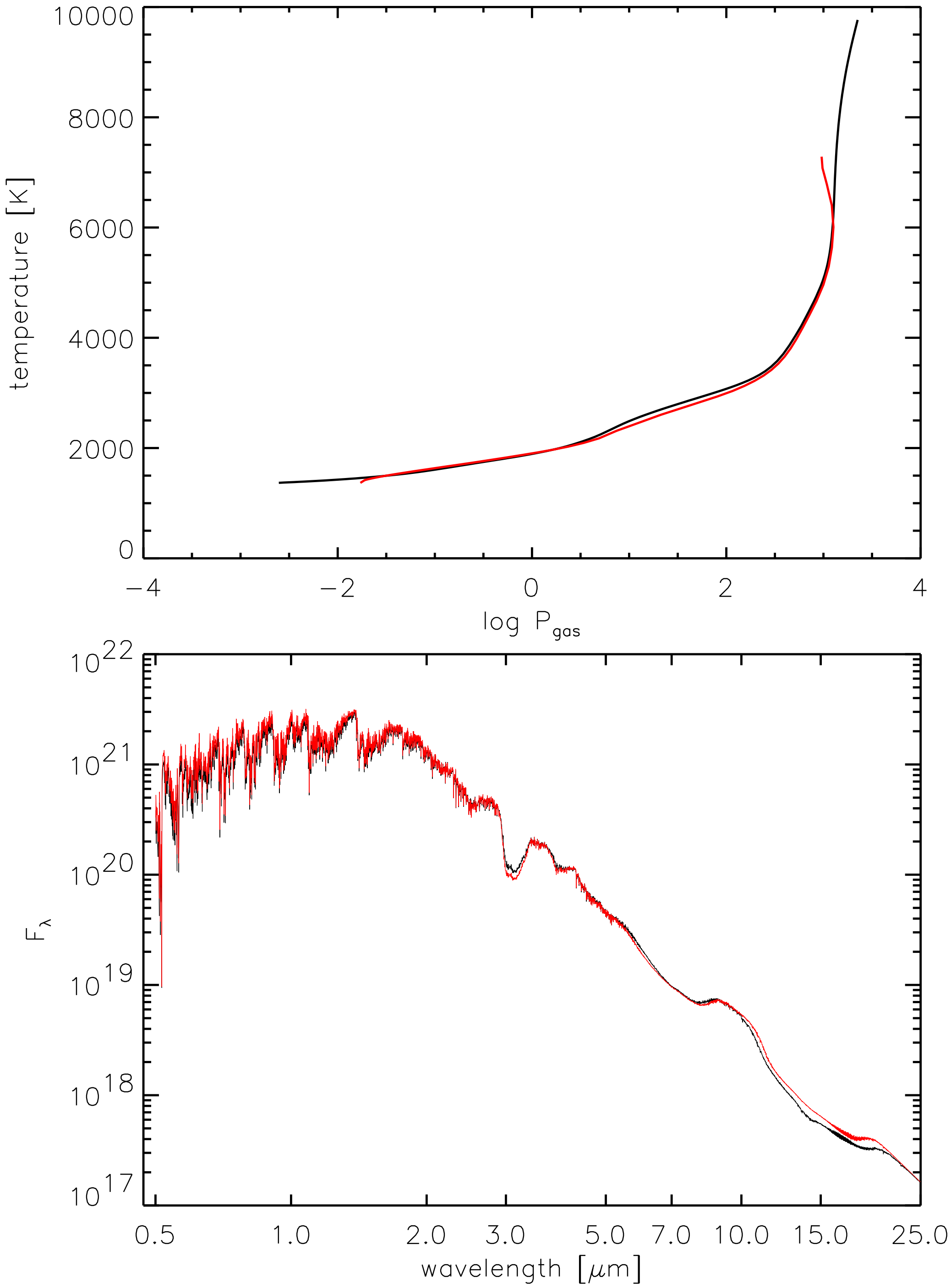

Figure 3.1: Temperature versus gas pressure (upper panel) and the corresponding synthetic spectra (lower panel) of a hydrostatic initial model calculated with 51 frequency points (black) and of a MARCS structure computed with 10000 frequency points. Both structures have the following parameters: $T_{\rm eff} = 3000\,\rm K$, $M = 1\,\rm M_{\odot}$, $L = 5200\,\rm L_{\odot}$ and $\rm C/O = 1.10$.

Table 3.1: Model parameters (L, M, T, R, C/O, P, $\Delta u_{\rm p}$, opacity treatment, dust data (see Table 3.2)) and results: mass-loss rate $\dot{M}$ and mean degree of condensation at the outer boundary $f_{\rm cond}$. A "P" denotes model structures which have been calculated using Planck mean opacities, and "F" model structures which have been calculated with a frequency-dependent radiative transfer. A "-" means that the model did not show mass loss by a stellar wind.

model	L_* [$L_\odot$]	M_* [$M_\odot$]	T_* [K]	R_* [$R_\odot$]	C/O	P [d]	$\Delta u_{\rm p}$ [km/s]	opa	dust	$\dot{M}$ [$M_\odot/yr$]	$f_{\rm cond}$
D13C14U4JT	13000	1.0	2700	521	1.40	650	4.0	P	*Jäger1000*	$3.1 \cdot 10^{-6}$	0.17
D13C14U4ZU	13000	1.0	2700	521	1.40	650	4.0	P	*Zubko*	$3.3 \cdot 10^{-6}$	0.21
D13C14U4MA	13000	1.0	2700	521	1.40	650	4.0	P	*Maron*	$2.9 \cdot 10^{-6}$	0.25
D13C14U4RO	13000	1.0	2700	521	1.40	650	4.0	P	*Rouleau*	$2.7 \cdot 10^{-6}$	0.28
D13C14U4JF	13000	1.0	2700	521	1.40	650	4.0	P	*Jäger400*	$2.8 \cdot 10^{-6}$	0.35
L52C11U2RO	5200	1.0	3000	264	1.10	295	2.0	F	*Rouleau*	–	–
L7TC14U5RO	7000	1.0	2800	359	1.40	390	5.0	F	*Rouleau*	$3.3 \cdot 10^{-6}$	0.35
L7C14U6RO	7000	1.0	2880	336	1.40	390	6.0	F	*Rouleau*	$3.0 \cdot 10^{-6}$	0.29
L7C18U4RO	7000	1.0	2880	336	1.80	390	4.0	F	*Rouleau*	$2.6 \cdot 10^{-7}$	0.26

not important in those parts of the atmosphere which are concerned by this extension, therefore the hydrostatic equations are sufficient for the description as a first order approximation.

To determine opacities at different layers of a given atmospheric temperature-pressure structure the program COMA was developed by B. Aringer, S. Höfner and R. Loidl. The result can be used as an input for a radiative transfer code making it possible to compute synthetic spectra at any desired resolution for any given wavelength range. First, the chemical abundances are calculated using an equilibrium chemistry, secondly the continuum absorption using routines from the MARCS code (Gustafsson et al. 1975), and finally the molecular opacities as a function of wavelength using the opacity sampling (OS) method. The chemistry routines are those of Tsuji (1973) with updated data as described in Helling et al. (1996) except for data for C_3 which are from Irwin (1981). The code is described in detail in Aringer (2000).

In the spectral synthesis code, the time-independent radiative transfer equation is solved for each frequency separately along parallel rays to obtain the spectral energy distributions (Windsteig et al. 1997 and references therein). Dust formation is accounted for, both by considering the depletion of condensible material when calculating the chemical equilibrium and by including the dust opacity of the dust grains in the radiative transfer. The dust temperature is higher than the radiation temperature and the gas temperature in all our models. This is due to the fact that the radiation temperature is an "artificial" temperature and its Planck function does not correspond to the "real" energy distribution of the radiation field. The mass absorption coefficient of amorphous carbon is higher at short wavelengths. To get rid of a certain amount of energy the emitted intensity of the dust grains has to be concentrated at shorter wavelengths than in the case of a grey opacity. This corresponds to a higher dust temperature. For other materials this needs not to be the case.

3.2 Pure dust spectra

3.2.1 Carbon grains

While carbon grains are expected to constitute a major fraction of the circumstellar dust in carbon stars, their exact form is still unclear. Carbon has the unique property that the atoms can form three different types of bonds through sp^1, sp^2 (graphite) and sp^3 (diamond) hybridisation.

Numerous observations of late-type stars do not support that graphite is the dominant dust type (e.g. Campbell et al. 1976; Sopka et al. 1985; Martin & Rogers 1987; Gürtler et al. 1996). The far-infrared (FIR) data of late-type stars generally show a dust emissivity law of $Q(\lambda) \sim \lambda^{-\beta}$ with a spectral index of $\beta \approx 1$. While graphite grains have a FIR emission proportional to λ^{-2} (Draine & Lee 1984), a behaviour such as λ^{-1} can be expected in a very disordered two-dimensional material like amorphous material (Huffman 1988; Jäger et al. 1998).

Amorphous carbon grains seem therefore to be very good candidates for the common type of carbon grains that are present in circumstellar envelopes. Another possibility could be small diamond grains. Presolar diamond grains have been identified in primitive unaltered meteorites (carbonaceous chondrites) and they are the most abundant of the presolar grains discovered so far (Lewis et al. 1987). The place of origin of the presolar diamonds is still unknown, but since they can only have formed under reducing conditions, Jørgensen (1988) suggested C-rich AGB stars as the place of formation of the majority of these grains.

A wide variety of possible amorphous carbon grain types exists, most of them fall in between the categories "diamond-like" and "graphite-like" amorphous carbon. The various laboratory data used in this investigation (see Fig. 3.2) have been discussed in detail in Andersen et al. (1999a), the most important properties are recalled briefly in Table 3.2. Andersen et al. (1999a) presented dynamic models (with Planck mean opacities; Höfner et al. 1998) using various laboratory optical constants of amorphous carbon to determine the influence of the different grain types on the structure and the wind properties of C-rich AGB star models. The resulting synthetic dust spectra and colours will be discussed in detail in Sect. 3.2.3.

Table 3.2: A list of authors who obtained optical constants from laboratory data of amorphous carbon.

Reference name	Wavelength interval (μm)	Designation in this work	Data from
Maron (1990)	0.2 – 300	*Maron*	Bussoletti et al. (1987)
Rouleau & Martin (1991)	0.1 – 300	*Rouleau*	Bussoletti et al. (1987)
Preibisch et al. (1993)	0.1 – 300	*Preibisch*	Bussoletti et al. (1987)
Zubko et al. (1996)	0.04 – 2000	*Zubko*	Colangeli et al. (1995)
Jäger et al. (1998)	0.02 – 500	*Jäger400*	Jäger et al. (1998)
Jäger et al. (1998)	0.02 – 500	*Jäger1000*	Jäger et al. (1998)

3.2.2 The nature of silicon carbide

Thermodynamic equilibrium calculations performed by Friedemann (1969a,b) and Gilman (1969) suggested that SiC particles can form in the mass outflow of C-rich AGB stars. The observations performed by Hackwell (1972) and Treffers & Cohen (1974) presented the first empirical evidence for the presence of SiC particles in stellar atmospheres. A broad infrared emission feature seen in the spectra of many carbon stars, peaking between 11.0 and 11.5 μm, is therefore attributed to solid SiC particles and SiC is believed to be a significant constituent of the dust around carbon stars.

One of the difficulties in interpreting laboratory data lies in disentangling the combination of several effects due to size, shape, physical state (amorphous or crystalline), purity of the sample, and possible matrix effects if a matrix is used. There is a general agreement that grain size and grain shape has a crucial influence on the absorption feature of SiC particles. Another issue considered is the effect of the crystal type. Silicon carbide shows pronounced polytypism which means that there exist a number of crystal types differing in only one spatial direction. All these polytypes are variants of the same basic structure and can therefore be divided into two basic groups: α-SiC (the hexagonal polytypes) and β-SiC (the cubic polytype). It was found by Spitzer et al. (1959b, 1959a), Papoular et al. (1998), Andersen et al. (1999b) and Mutschke et al. (1999) that the crystal structure of SiC cannot be determined from IR spectra, because of the lack of systematic dependence of the band profile on the crystal type. Borghesi et al. (1985) and Speck et al. (1999) find, however, the contrary result.

In our investigation we have used β-SiC data from Mutschke et al. (1999) to calculate the real parts (n) and the imaginary parts (k) of the complex refractive index, using the one-oscillator model. The damping constant γ is an "ad hoc"

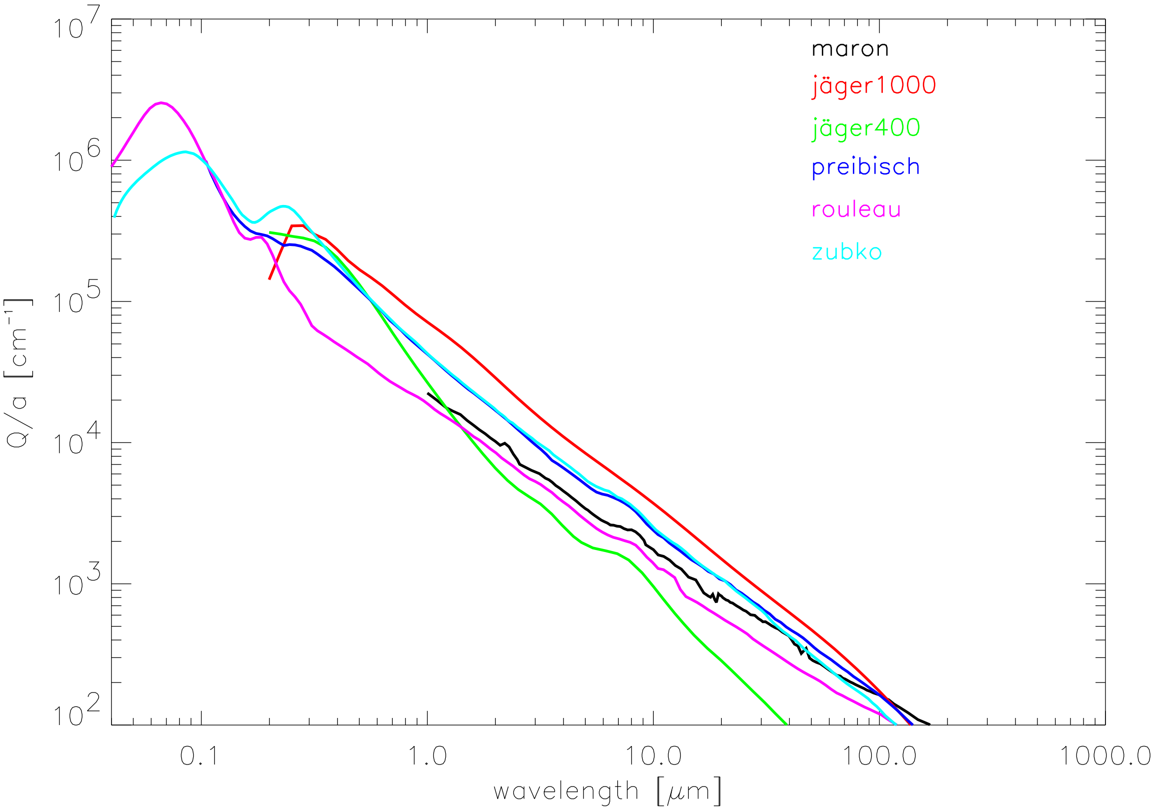

Figure 3.2: Calculated extinction efficiency of amorphous carbon from optical constants published by Maron (1990), Rouleau & Martin (1991), Preibisch et al. (1993), Zubko et al. (1996) and Jäger et al. (1998). The extinction efficiency factors were calculated from the optical constants (n and k) in the Rayleigh approximation for spheres.

parameter which, in a perfect crystal, reflects the anharmonicity of the potential curve. A damping constant of $\gamma = 10$ characterises crystals which are not structurally perfect but still far from amorphousness.

Due to the lack of systematic dependence of the band profile on the crystal type in the data from Mutschke et al. (1999), we could just as well have used the data from one of their α-SiC samples and would have obtained a similar result.

3.2.3 Spectral energy distributions

To investigate how the different dust data influence the resulting spectral energy distributions (SEDs), spectra were calculated using the optical constants of amorphous carbon of *Rouleau*, *Zubko*, *Jäger400* and *Jäger1000* on top of a fixed atmospheric structure. Two different kinds of SEDs were calculated; (1) fully consistent ones for which the same amorphous carbon data were used in the dynamical model and in the SED calculations and (2) "inconsistent" ones for which we used different dust opacity data for the detailed radiative transfer on top of the same dynamical model structure (fixed spatial distribution of density, temperature, degree of condensation). The latter spectra enable us to distinguish between the effect of the various dust data in the radiative transfer calculation and the effect on the model structure.

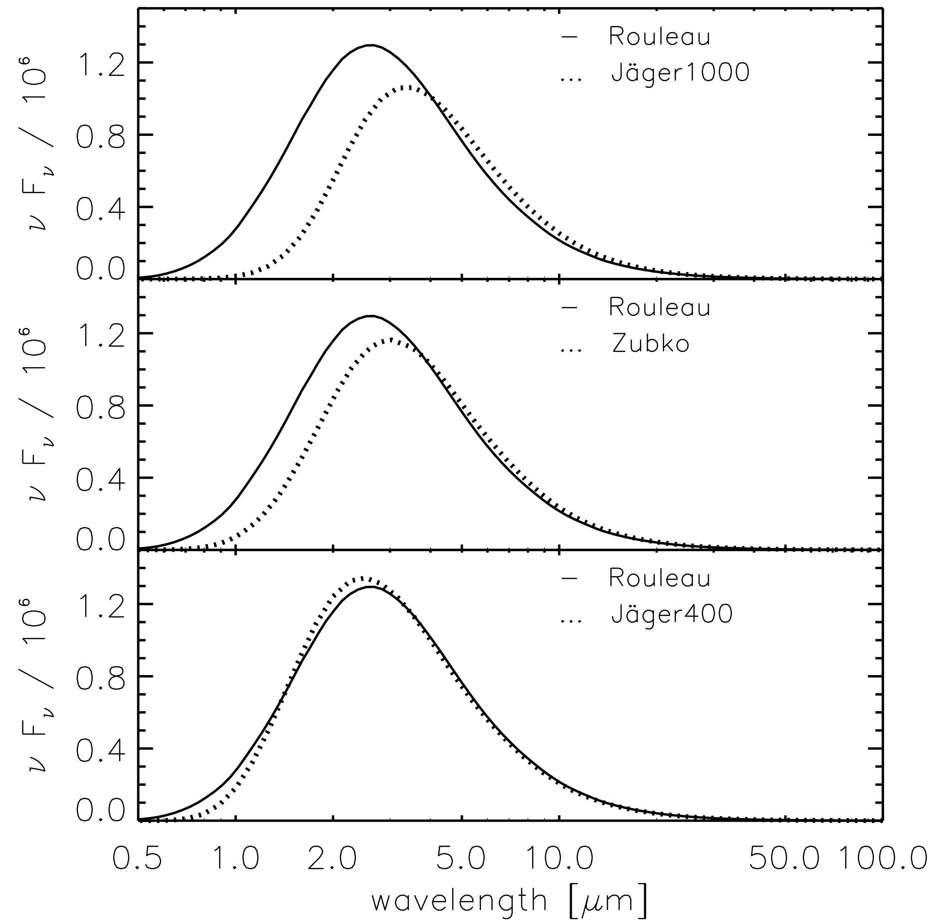

Figure 3.3: Spectral energy distributions of a minimum phase model where the spectra have been calculated with different dust data: we compare *Rouleau* (consistent calculation) with *Jäger1000* (upper), with *Zubko* (middle) and *Jäger400* (lower). For details, see the text.

Figure 3.3 shows the result for the SEDs based on a model at minimum phase of luminosity. The full line denotes always the SED of the consistent model where the *Rouleau* data were used for the underlying dynamical model as well as for the calculation of the spectrum. In the upper panel the (inconsistent) *Jäger1000* spectrum (dotted) calculated on top of the same *Rouleau* model is shown in addition to the consistent *Rouleau* spectrum. The middle panel shows the same for *Zubko* and the lower panel for *Jäger400*. The effects of the different dust data for a given structure compared to a consistent model using the *Rouleau* data can be summarised as follows:

- *Jäger1000*: the spectrum has a much lower flux in the short-wavelength region (0.5 to 5 μm) and the maximum at longer wavelengths. The lower flux level in this region is due to the fact that $Q_{\rm ext}/a$ for the *Jäger1000* data is higher than for the *Rouleau* data, therefore we have a higher total dust opacity which results in less flux emerging. The shift of the maximum is also due to the higher dust opacity in the *Jäger1000* case.

- *Zubko*: the spectrum has a lower flux level in the short-wavelength region and the maximum is shifted to longer wavelengths, but not as far as found for the *Jäger1000* spectrum. This is due to the fact that *Jäger1000* is a more "graphite-like" amorphous carbon dust than the *Zubko* material.

- *Jäger400*: the spectrum has a comparable flux all over the spectrum and the maximum at slightly shorter wavelengths. The slightly higher flux level around the maximum results from the lower $Q_{\rm ext}/a$ of the *Jäger400* data which is due to its more "diamond-like" nature compared to the *Rouleau* data. In the wavelength region where the maxima of the spectra lie, the two data sets are very similar, therefore the maxima of the SEDs do not differ significantly in wavelength.

Note that for the "inconsistent" SEDs the total flux may differ from the value of the consistent models due to the different model structures on top of which the SEDs are calculated.

3.2.4 Spectral energy distributions including SiC

The analysis of mid-IR carbon star spectra indicates that SiC is the best candidate to explain the observed emission-like feature around the 11 μm region. We have therefore considered SiC as an additional dust component (see Sect. 3.2.2 for details). The formation of SiC is not included in the self-consistent model calculations because (1) little is known about the condensation process (see Kozasa et al. 1996 for first attempts) and (2) we do not expect SiC to have a significant influence on the model structures. We use Planck means for the gas opacity and either Planck or Rosseland means for the dust opacity for the model computations. SiC will contribute only in a very narrow wavelength region, with small amounts to these mean opacities compared to amorphous carbon.

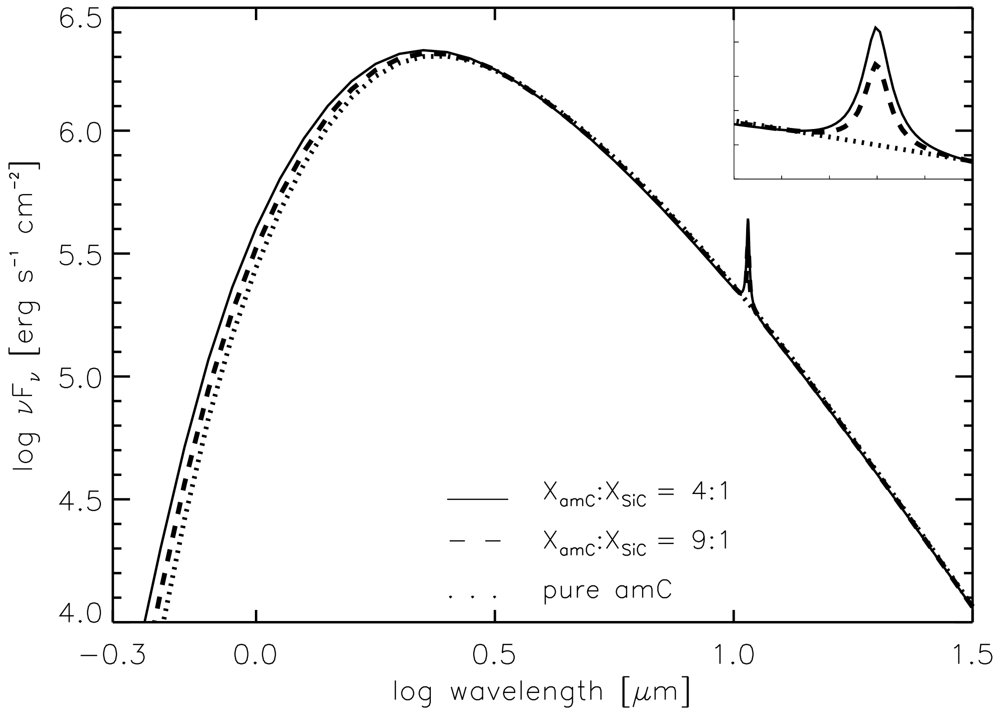

Figure 3.4: Spectral energy distributions of a minimum phase model with amorphous carbon data of *Jäger1000* alone (dotted), with a ratio X_{amC}:X_{SiC} of 9:1 (dashed) and a ratio of X_{amC}:X_{SiC} of 4:1 (full).

The effect of SiC as an additional dust component is described in the following qualitative manner: The dust opacity κ_d is calculated for each wavelength as

$$\kappa_d = \frac{\kappa_{amC} X_{amC} + \kappa_{SiC} X_{SiC}}{X_{amC} + X_{SiC}}$$

where X_i are the fractional parts of amorphous carbon and SiC, respectively, and where κ_{amC} and κ_{SiC} are the opacities of carbon and SiC. Figure 3.4 shows how a mixture of dust grains consisting of amorphous carbon (*Jäger1000* data) and SiC modifies the SED around 11.3 μm. Two different ratios of X_{amC} : X_{SiC}, 4:1 and 9:1 were adopted. The higher the amount of SiC, the stronger is the 11.3 μm feature (see inset of Fig. 3.4). Another choice than spherical for the grain shape of the SiC particles would result in a broader and weaker feature.

3.2.5 Synthetic colours

For the consistent spectra (model structure and spectra computed with the same dust data) we have calculated synthetic J, H and L colours as well as the IRAS 12 μm colour. We want to stress that we did not include molecular opacities and that we did not extend our models to lower temperatures as it was done in Windsteig et al. (1997). Such an outward extension has non negligible effects on especially the IRAS 12 μm flux. Therefore, these plots are suited for a comparison of the different models, but *not* for a direct comparison with observations. In a (J−H) versus (H−L) diagram (Fig. 3.5a) the models based on different amorphous dust data fall into distinct regions.

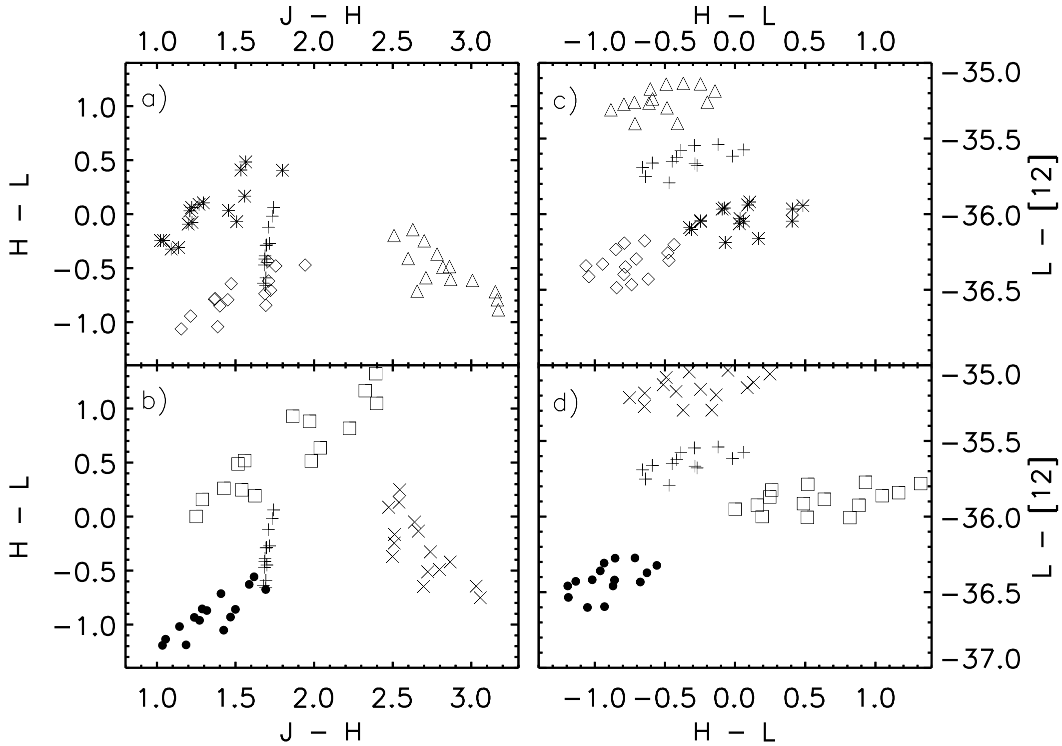

Figure 3.5: Synthetic colours: Upper panels: left: (J−H) vs. (H−L) for the instants of time at maximum and minimum luminosity of consistent models; crosses denote the *Rouleau* data, asterisks the *Jäger1000* data, diamonds the *Jäger400* data and triangles the *Zubko* data; right: (H−L) vs. (L−[12]) for the same models (same symbols). Lower panels: "inconsistent" colours, all based on the model calculated with the *Rouleau* data, in comparison to the consistent *Rouleau* colours (crosses): circles represent spectra calculated with the *Jäger400* data, squares denote the *Jäger1000* data and "x" the *Zubko* dust data.

The models calculated with the *Jäger1000* dust data have the reddest colours in (H−L). The *Jäger400* colours are the bluest, while *Rouleau* and *Zubko* lie in between. In (J−H) models with the *Zubko* data are reddest and the others do not differ much. The reason for the different slopes of *Rouleau* and *Zubko* compared to both of the *Jäger* data sets is that in these cases the maxima of the SEDs are changing between the J and the H filter depending on the phase. The maxima of the SEDs resulting from the *Jäger1000* model structures are always at longer wavelengths and the ones of the *Jäger400* structures lie mainly in one filter. From Fig. 3.5b, which shows the "inconsistent" colours based on a model where the structure was calculated with the *Rouleau* data and the spectra with other dust data in addition to the consistent *Rouleau* colours, it is clear that the influence of the different dust data used in the radiative transfer calculation is much stronger than the effect of the underlying hydrodynamic model structure.

Figure 3.5 shows a sequence of successive maximum and minimum phases of a simulation run. Other pulsational phases would fill in the gaps between successive extremes. The colours are strongly related to the formation of a new dust shell which takes place every 5 to 6 pulsation cycles. After this time-scale the colours match very closely the ones of the preceeding dust formation cycle as shown in Fig. 3.6. When connecting successive maxima, minima, maxima, etc., it can be seen that they form a spiral. The minima (circles) are always redder than the following maxima (asterisks).

To investigate additionally the mid-IR properties of the models, we calculated the 12 μm colour. A (L$-$[12]) vs. (H$-$L) diagram (Fig. 3.5c) shows, that again the consistent colours fall into distinct regions. The sequence in (L$-$[12]) (*Zubko - Rouleau - Jäger1000 - Jäger400*) is a sequence of decreasing optical depths. In Fig. 3.5d the inconsistent colours based on the model structure calculated with the *Rouleau* data are shown for comparison.

From Fig. 3.5 we can infer that the influence of the different amorphous carbon dust data used in the radiative transfer calculation is much stronger than their effect on the model structures. The colours resulting from the same dust data fall approximately into the same region of a two-colour-diagram, whether they are calculated on top of the corresponding model structure (upper panel) or a fixed model sequence (lower panel). This applies to all data sets.

In addition, we computed synthetic colours for the *Maron* and the *Preibisch* data, to avoid overlaps in the plot they are not shown in Fig. 3.5. The *Preibisch* colours fall into the same region as the *Zubko* colours as one expects from the very similar $Q_{\rm ext}/a$ values. The same applies to the *Maron* and the *Rouleau* data. Only the J flux differs between *Maron* and *Rouleau*, the reason being that the *Maron* data do not extend below 1 μm and therefore the corresponding contribution to the J filter is missing.

3.2.6 Conclusions

We have investigated the direct influence of different dust optical properties on the properties of the dynamical models. On top of various dynamic model structures we have performed detailed radiative transfer calculations to obtain the

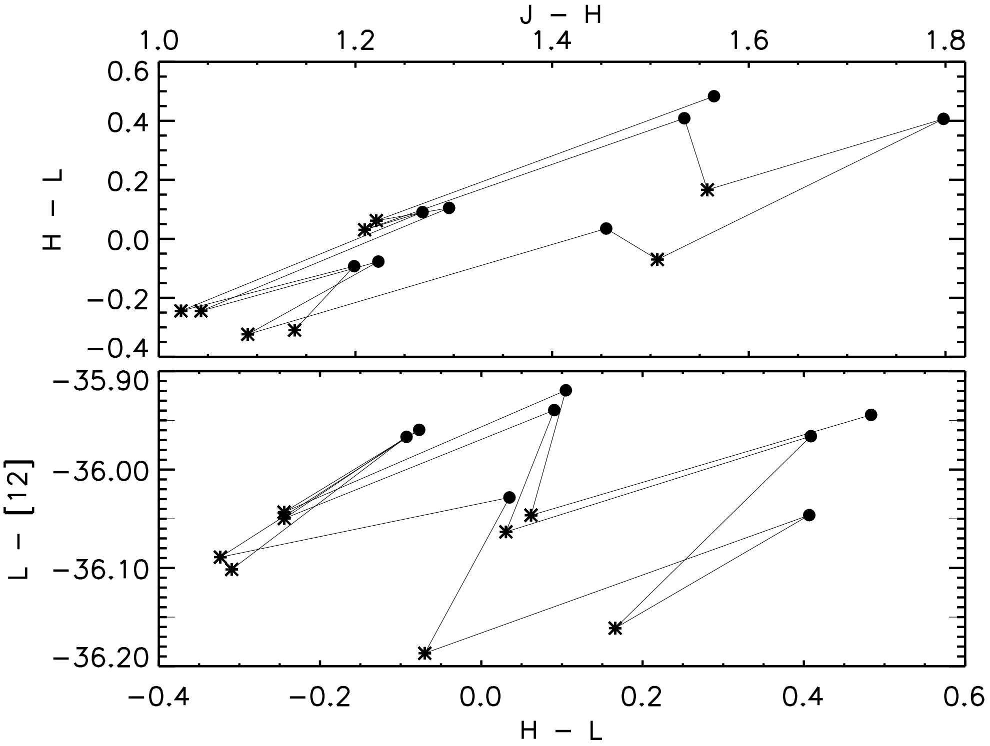

Figure 3.6: Upper panel: (J−H) vs. (H−L) for maxima (asterisks) and minima (circles) of a model computed with the *Jäger1000* data. When connecting the points following each other one finds the result to be a spiral; the minima are always redder than the following maxima. Lower panel: Same as above, only (H−L) vs. (L−[12]) is shown.

spectral energy distribution of the circumstellar dust shells; molecules have been neglected in our computations. Regarding infrared colours, the influence of the different dust data used in the radiative transfer calculation is much stronger than the effect of the underlying hydrodynamic model structure. However, one should not try to fit observations by arbitrarily choosing the optical properties of the dust grains for a given model structure. In a consistent model the dynamical properties (e.g. outflow velocities, mass loss rate) and the appearance of the circumstellar envelope are related in a complex way.

3.3 Effects of dynamics on the model structures and the spectra

The influences of different parameters on the hydrostatic initial models of the dynamical calculation are the same as in the classical hydrostatic MARCS models which were described in detail in Sect. 2.4. Therefore, we will focus on the dynamical computations here. Currently, only four proto-type models exist for which the structure has been calculated with a fully frequency-dependent radiative transfer, both for gas and dust (see Table 3.1). As a consequence, a systematic investigation where one specific parameter is varied is not yet possible for all parameters. However, we can study the effects of the most important parameters, namely of $T_{\rm eff}$, of the C/O ratio, and of the piston velocity $\Delta u_{\rm p}$. A complete investigation for the set of dynamical models calculated with Planck mean opacities has been published for the atmospheric structures in Höfner et al. (1998) and for the synthetic spectra in Loidl et al. (1999a). As far as the structure is concerned, we do not expect that the qualitative influence of the parameters is very different in the non-grey case as compared to the grey case. However, it should be mentioned here that the synthetic spectra in Loidl et al. (1999a) were calculated with a plane parallel radiative transfer and that although the depletion of carbon due to dust formation was taken into account, the dust opacities were not included in the radiative transfer computation. Now we can calculate the spectra consistently with the atmospheric structure in spherical geometry and the dust opacities are included. In the spherical case, strong absorption features can be filled up with emission and as a consequence the variation of spectral features over a pulsation cycle can considerably differ from their behaviour in the plane parallel case. Figure 3.7 shows a maximum (upper panel) and a minimum (lower panel) phase spectrum of model L7C14U6RO calculated with spherical (black curve) and plane parallel (red curve) radiative transfer.

In the following, we will focus on the four proto-type models which have been calculated with frequency-dependent radiative transfer. For the computation of the atmospheric structure as well as for the synthetic spectra the *Rouleau* dust data have been used for the following reasons: The *Rouleau* data cover the largest wavelength range of all available data, and longwards of 1 μm the *Rouleau* data are very similar to the *Maron* data which we used in the computation of the older model series. The atmospheric structure is phase dependent; in the following, 8 different phases are selected of each model and used for the discussion. The phases were chosen such that they are almost equally spaced over a complete cycle. When talking about "model structures" in the following we mean the temperature-pressure stratifications of the models.

3.3.1 Model L52C11U2RO

Model L52C11U2RO was designed to represent a moderately variable star of irregular or semiregular type. Its variation of the bolometric magnitude amounts to 0.22 mag. In Figure 3.8, gas pressure versus temperature is plotted for the hydrostatic initial model and the eight selected phases. A maximum light model will

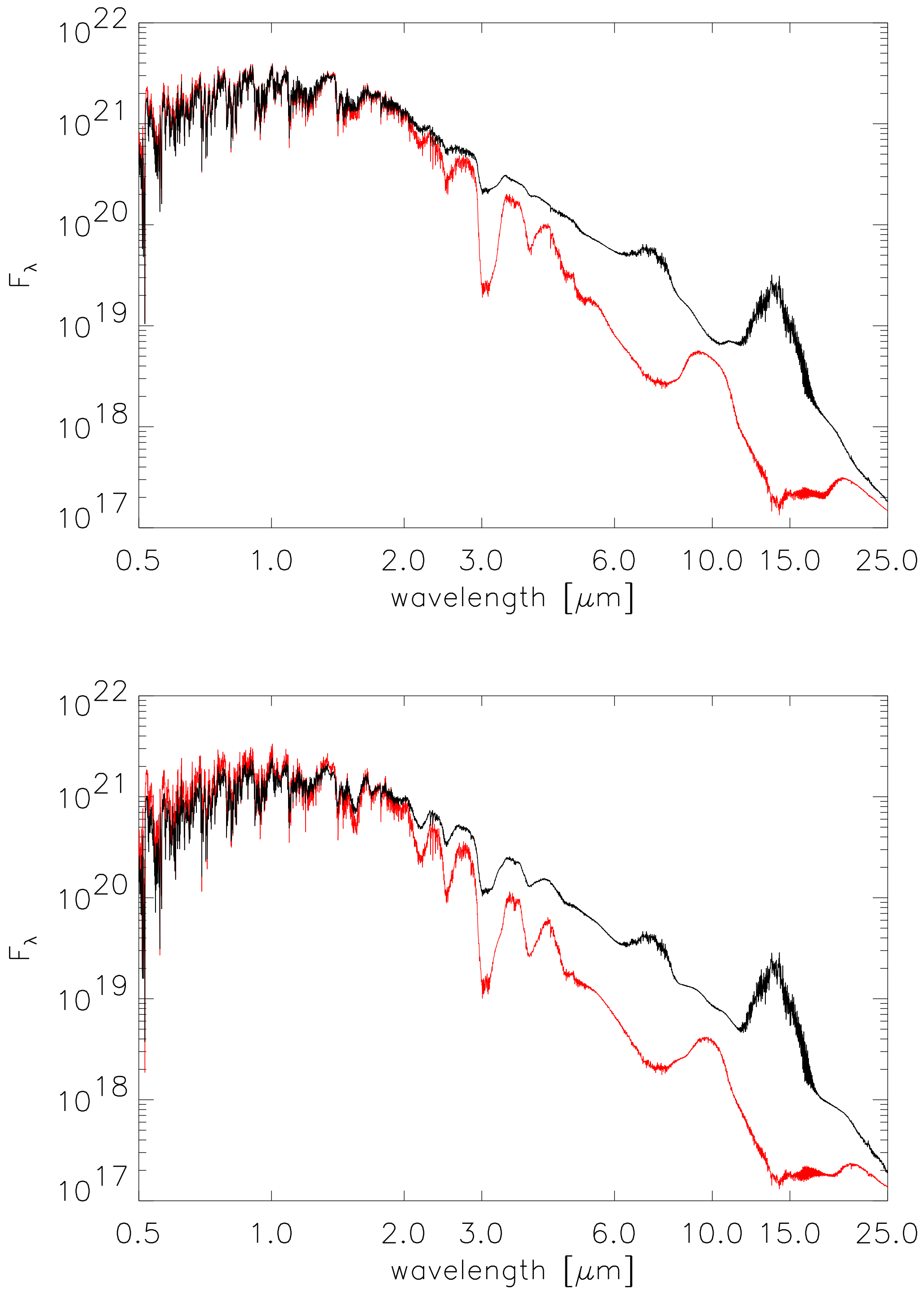

Figure 3.7: Maximum (upper panel) and minimum (lower panel) phase spectrum of model L7C14U6RO calculated with spherical (black curve) and plane parallel (red curve) radiative transfer. In the spherical case, strong absorption features can be filled up with emission.

be designated as phase 0.0 in the following and a minimum light model as phase 0.5. The thick black line shows the structure of the hydrostatic initial model. The coloured thin lines denote various phases.

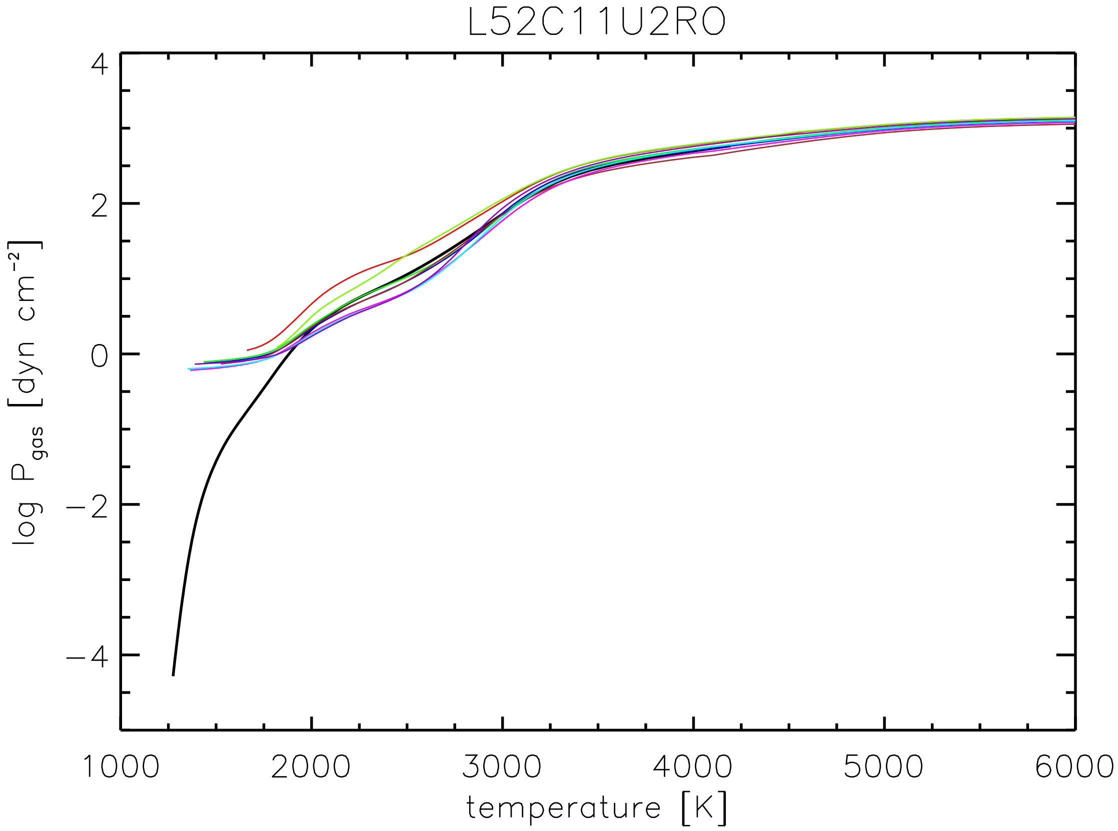

Figure 3.8: Gas pressure versus temperature for the hydrostatic initial model and eight selected phases of model L52C11U2RO. The red curve denotes a minimum light model, the turquoise one a maximum light model.

For temperatures above ≈ 3250 K all pressure-temperature stratifications look essentially the same. Between temperatures of 3250 and about 2000 K the pressure-temperature stratifications of the dynamical models differ slightly from the one of the hydrostatic initial model; the hydrostatic case represents a mean of all the dynamical models. Below 2000 K the stratification of the dynamic models deviates significantly from the one of the hydrostatic initial model. Dynamics causes a levitation of the atmosphere, i.e. a density enhancement in these outer layers. The amount of the levitation depends on the piston velocity Δu_{p}. In model L52C11U2RO the levitation is small. No dust forms and no stellar wind develops in this model, therefore the dynamic model structures are compact, they terminate at temperatures between 1300 and 1700 K depending on the phase. Phases around maximum light are more compact (i.e. have a smaller radius and terminate at higher temperatures) than those around minimum light. The second influence of dynamics on the structures (which is barely visible in this case) is that shock waves are propagating through the atmosphere. The shock waves are caused by the pulsation, i.e. by the variable inner boundary in our case.

In Figure 3.9 the partial pressures of the most important molecules are shown for the selected phases. The thick black line shows the hydrostatic initial model, the coloured thin lines denote various instants of time of the dynamical calculation (the colours correspond to the ones in Fig. 3.8). The partial pressures of CO (upper left panel) illustrate nicely the effect of the levitation of the atmosphere for temperatures below 2000 K in the dynamical case. At temperatures between 2000 and 3000 K, the partial pressures of CO enclose the one in the hydrostatic model; phases close to the maximum phase (red and light green curves) have higher partial pressures, phases closer to minimum phase have lower partial pressures. All other molecules show the same behaviour at temperatures between 2000 and 3000 K. The partial pressures of CN (upper right panel) are higher than the hydrostatic one by about an order of 1 magnitude in the outermost layers in the dynamical calculations around minimum phase. Around maximum light, the model is very compact, the temperature-pressure stratifications terminate at rather high temperatures where the partial pressure of CN is still high. Therefore, no deviation from the hydrostatic behaviour is visible in these cases. This applies also for C_2 (left middle panel) and C_3 (left lower panel). The partial pressures of the remaining two important molecules, HCN (middle right panel) and C_2H_2(lower right panel), however, deserve a separate discussion. For phases close to maximum light (red and light green curves). the partial pressures of HCN and C_2H_2 are significantly enhanced at temperatures below 3000 K compared to the hydrostatic case. For all other phases, the enhancement becomes pronounced at temperatures below 2000 K. In both cases, the dynamical model structures stop *before* the partial pressures of HCN and C_2H_2 start to significantly decrease again. This means, that at some phases (around minimum in the case of C_2H_2), the maximum of the partial pressure is reached at the outer boundary. Due to the termination of the model structures at temperatures at which the partial pressures of HCN and C_2H_2 did not start to decrease again, the resulting spectra are not at all reliable. The enhancement of the partial pressures compared to the hydrostatic case is much stronger for C_2H_2 and HCN than for CN, C_2 and C_3. It should be mentioned further that the partial pressures of CO follow exactely the behaviour of the gas pressure with temperature. This applies to all models.

In Fig. 3.10, the synthetic spectra of the same phases as in Fig. 3.9 are plotted. The spectra were forced to have equal flux at 3.5 μm (indicated by the black arrow in the middle panel) in order to better illustrate the variations. In the wavelength region between 0.5 and 2.9 μm, the intensities of the spectral features vary

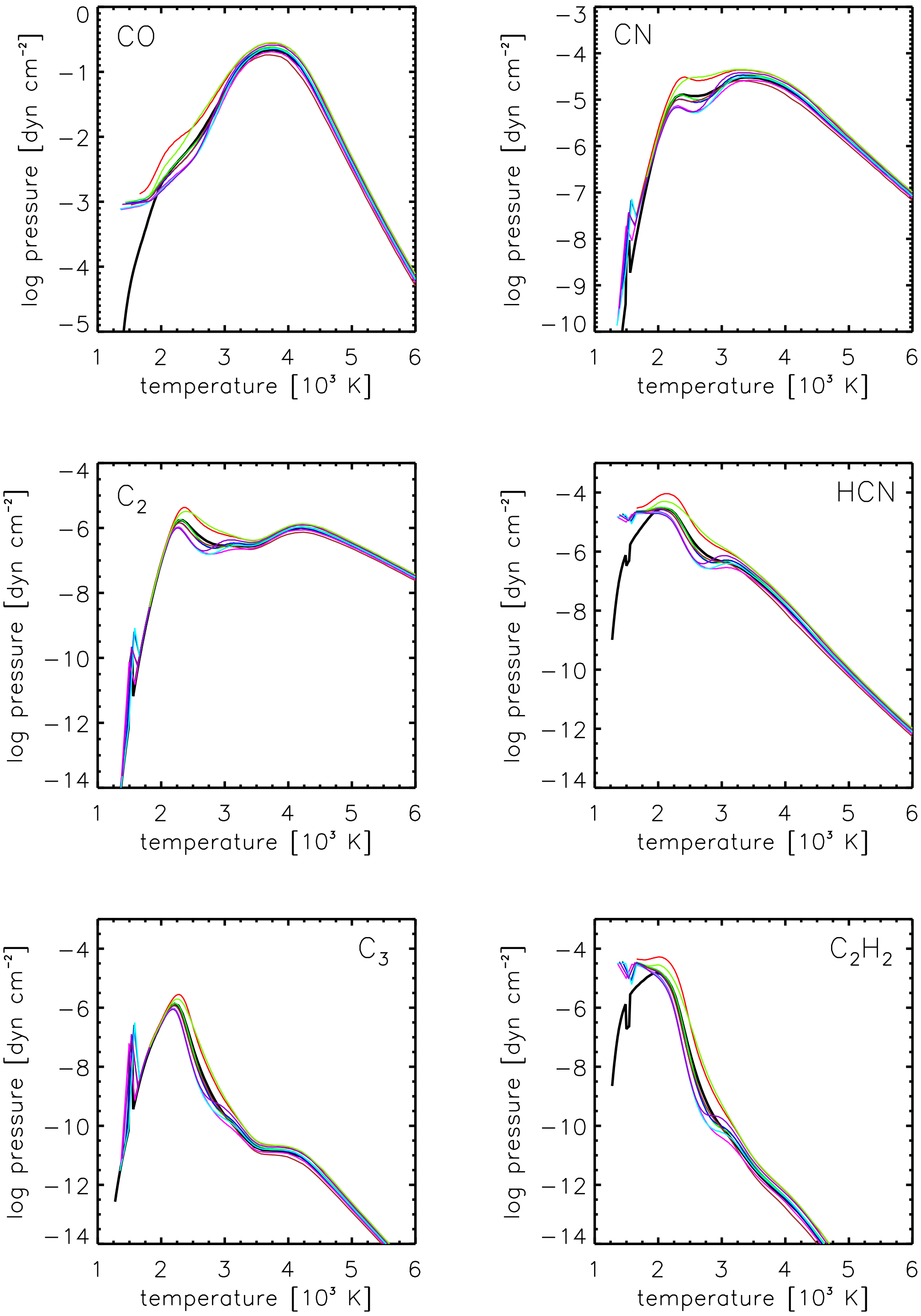

Figure 3.9: Partial pressures of the most important molecules for selected phases of model L52C11U2RO.

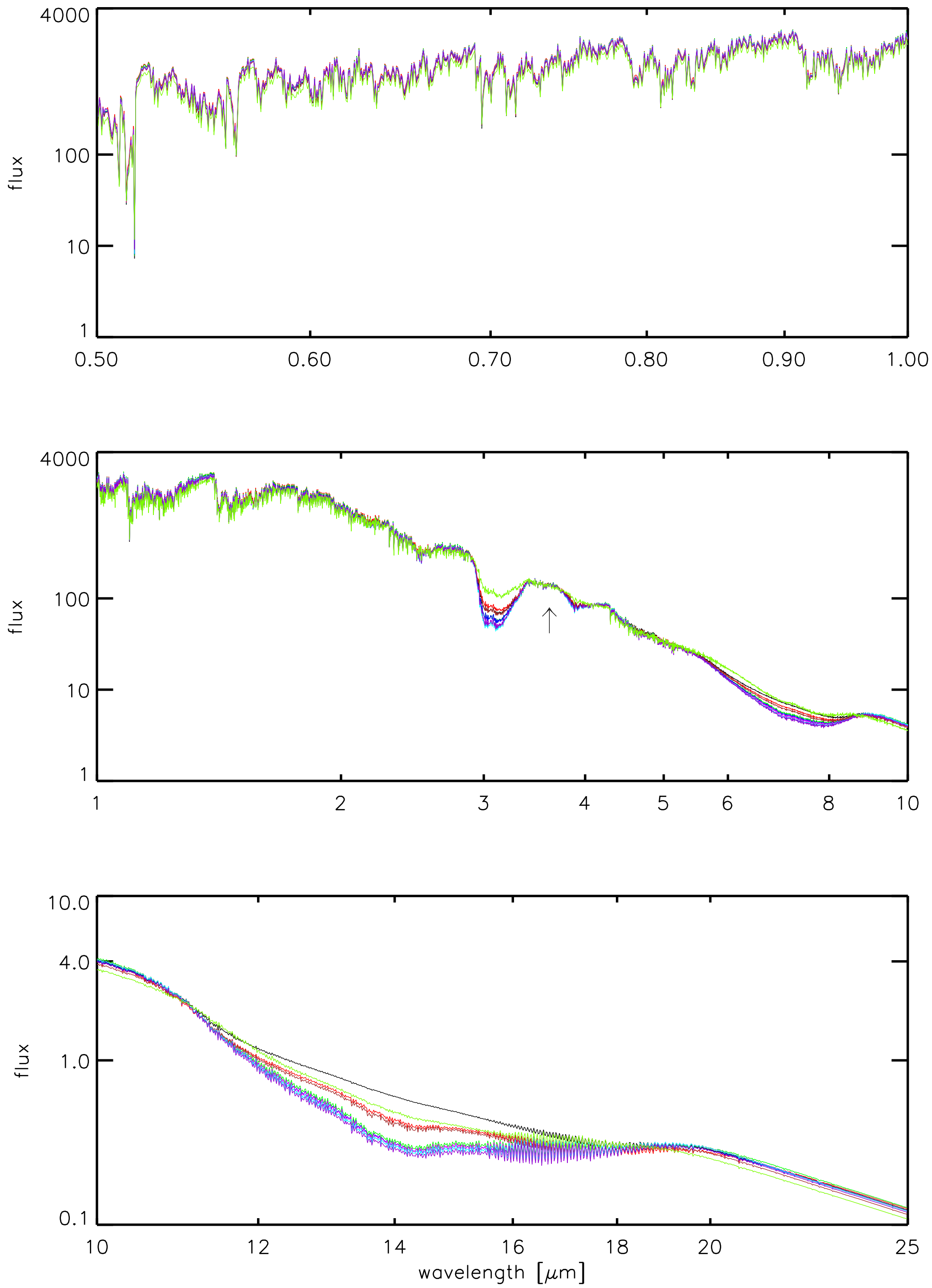

Figure 3.10: Synthetic spectra of the hydrostatic initial model and of eight selected phases of model L52C11U2RO. The arrow indicates the wavelength at which the spectra were forced to have equal flux.

marginally around those of the hydrostatic initial model. Basically, only those features show pronounced variations, which are due to HCN and/or C_2H_2. This is exactely what has to be expected from the partial pressure versus temperature plot: features, which are mainly formed in the temperature regime where the partial pressure of the dynamical calculations encloses the one of the hydrostatic case, should vary accordingly. For the 3 μm HCN/C_2H_2 feature this still applies, but the variations are already strong because the feature is mainly formed at temperatures around and slightly below 2000 K. The remaining two HCN/C_2H_2 features in the wavelength region 0.5 to 25 μm (around 7 and 14 μm) are formed at even lower temperatures where the enhancement of the partial pressures is significant compared to the hydrostatic case at all phases. As a consequence, these features are stronger at all phases than in the hydrostatic case. However, we stress again that we lack some HCN/C_2H_2 opacity due to the termination of the model structures at temperatures at which the partial pressures of HCN and C_2H_2 did not start to decrease again. Such a situation will not exist in a real star.

3.3.2 Model L7C14U6RO

Model L7C14U6RO was designed to represent a Mira variable. The variation of its bolometric magnitude amounts to 0.66 mag. In Fig. 3.11, gas pressure is plotted versus temperature for the eight selected phases together with the hydrostatic initial model. The thick black line shows the structure of the hydrostatic initial model. The coloured thin lines denote various phases. For temperatures above $\approx$4000 K all model structures look essentially the same. For a fixed gas pressure the dynamical model structures are in the mean hotter than the hydrostatic initial model in the temperature range between 4000 and 1500 K. At temperatures below 1500 K the dynamic structures deviate significantly from the hydrostatic structure. The enhancement of the gas pressure is strong, this is due to the large piston velocity $\Delta u_{\rm p}$ of the model. A stellar wind with a mass loss rate of about $3 \cdot 10^{-6}\,{\rm M}_{\odot}$/yr develops, the degree of condensation at the outer boundary amounts to 0.28. In this case the second influence of dynamics on the structures is nicely visible: one can easily trace the shock waves which are caused by the pulsation propagating through the atmosphere.

In Figure 3.12, the partial pressures of the most important molecules are shown for the eight selected phases together with the ones of the hydrostatic initial model. The thick black line shows the hydrostatic initial model, the coloured thin lines denote various phases of the dynamical calculation (the colours correspond to the ones in Fig. 3.11). The partial pressures of all molecules of the dynamical calculations enclose the ones of the hydrostatic model down to temperatures of about 4200 K. Between 4200 K and $\approx$ 1300 K, the partial pressure of CO (upper left panel) of the hydrostatic initial model is mostly higher than at all phases in

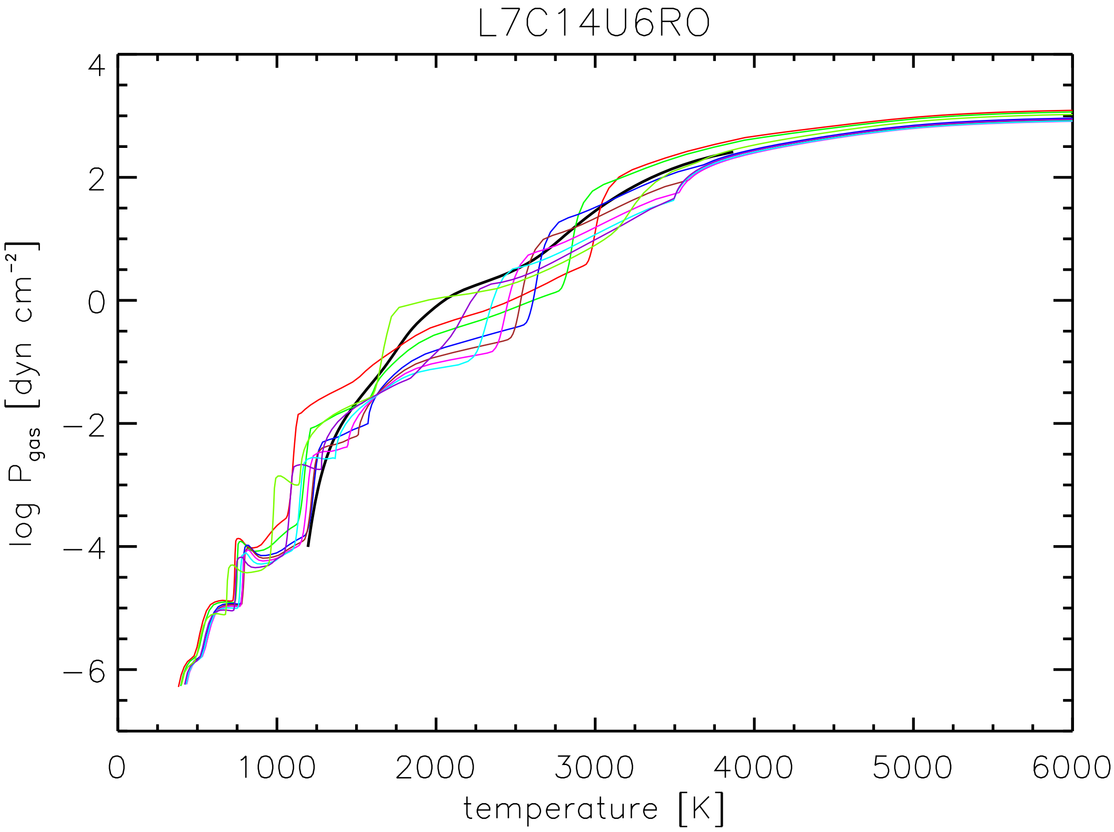

Figure 3.11: Gas pressure versus temperature for the eight selected phases of model L7C14U6RO and the hydrostatic initial model. The red curve denotes a minimum light model, the turquoise one a maximum light model.

the dynamical computation. This is probably due to the fact that in the dynamical model a considerable amount of the mass has moved to other layers or is lost already at the time we picked out various phases. At even lower temperatures, the partial pressure of CO is always significantly enhanced compared to the hydrostatic case. The partial pressures of the molecules CN (upper right panel), C_2 (middle left panel) and C_3 (lower left panel) behave similar: Down to 2000 K they behave like CO; below this temperature, the partial pressures of CN, C_2 and C_3 are equal to the one of the hydrostatic initial model with the exception if a shock wave is propagating through this low temperature region of the star. In this case, the partial pressure increases by 1 to 2 orders of magnitude, but only very locally. The partial pressures of the remaining two important molecules, HCN (middle right panel) and C_2H_2(lower right panel) show the same behaviour as the one of CO.

In Fig. 3.13, the synthetic spectra of the same phases as in Fig. 3.12 are plot-

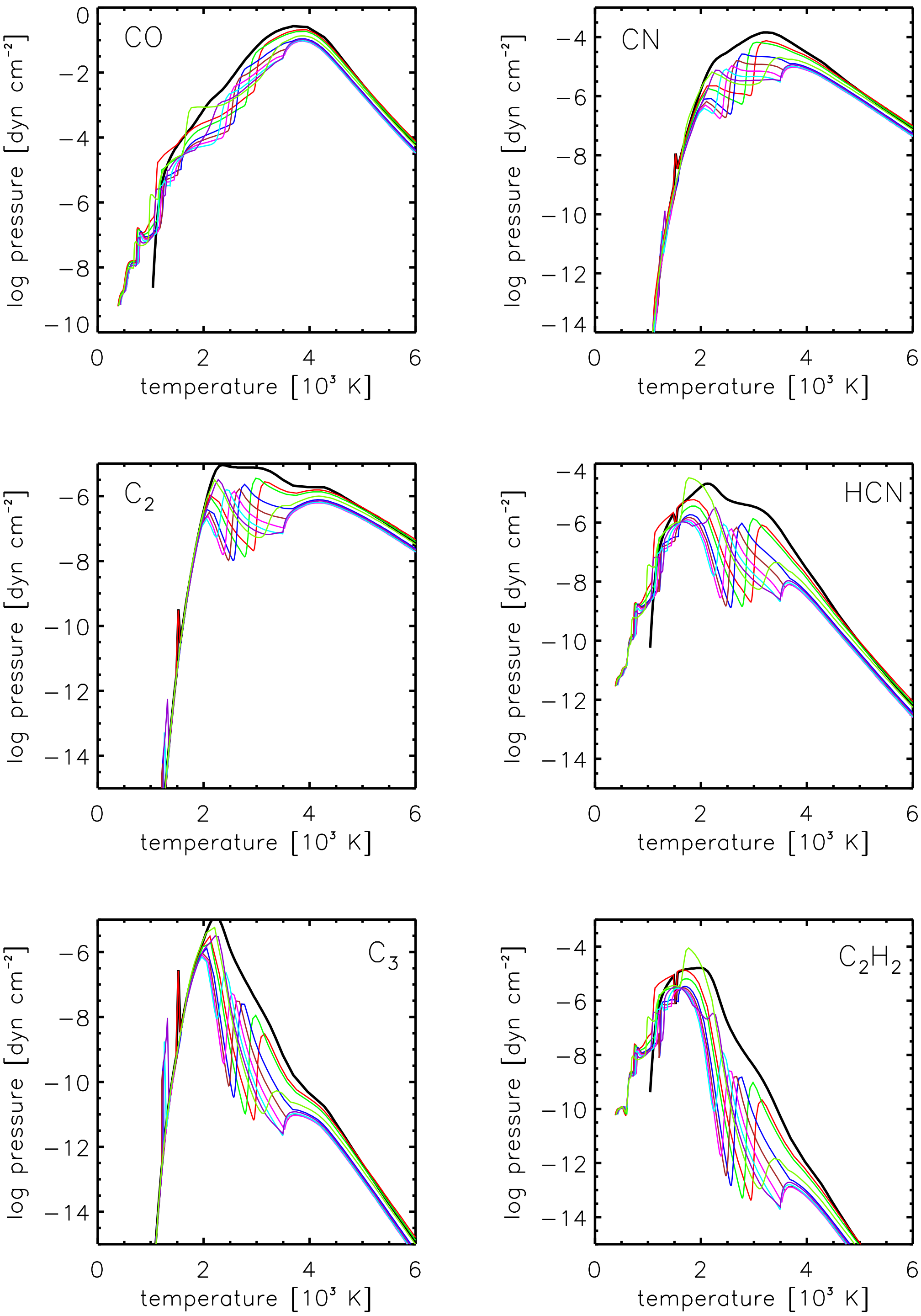

Figure 3.12: Partial pressures of the most important molecules for the chosen phases of model L7C14U6RO.

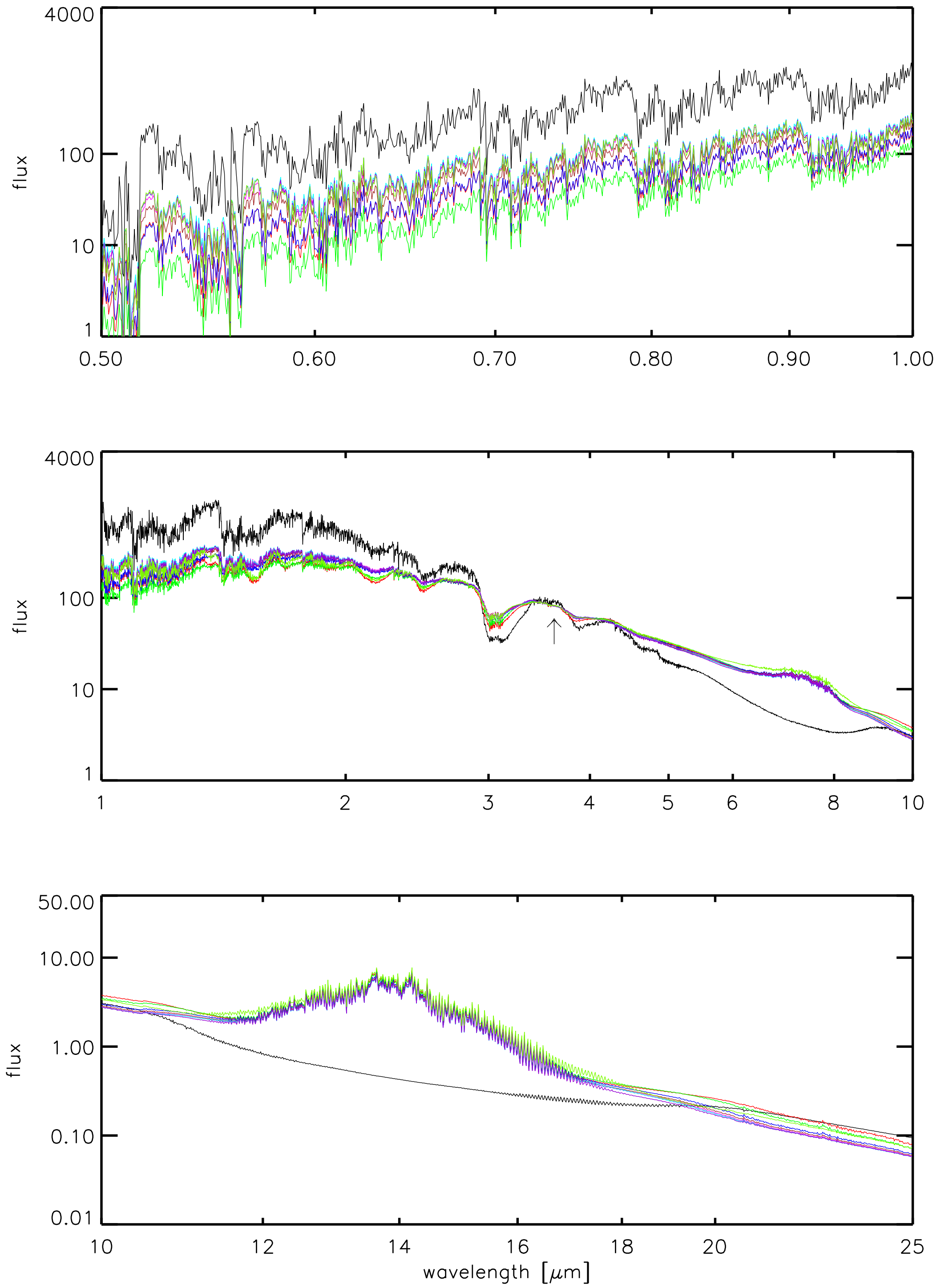

Figure 3.13: Synthetic spectra of the chosen phases of model L7C14U6RO. The arrow indicates the wavelength at which the spectra were forced to have equal flux.

ted. The spectra were forced to have equal flux at 3.5 μm (indicated by the black arrow in the middle panel) in order to better illustrate the variations. In this case the intensities of the spectral features differ remarkably from the ones of the hydrostatic initial model all over the investigated wavelength range. First of all, the shapes of the dynamical spectra are different. This is due to the constribution of the dust. In agreement with the behaviour of the partial pressures, the CN, C_2, and C_3 features are weaker in the dynamical calculations than in the hydrostatic case.

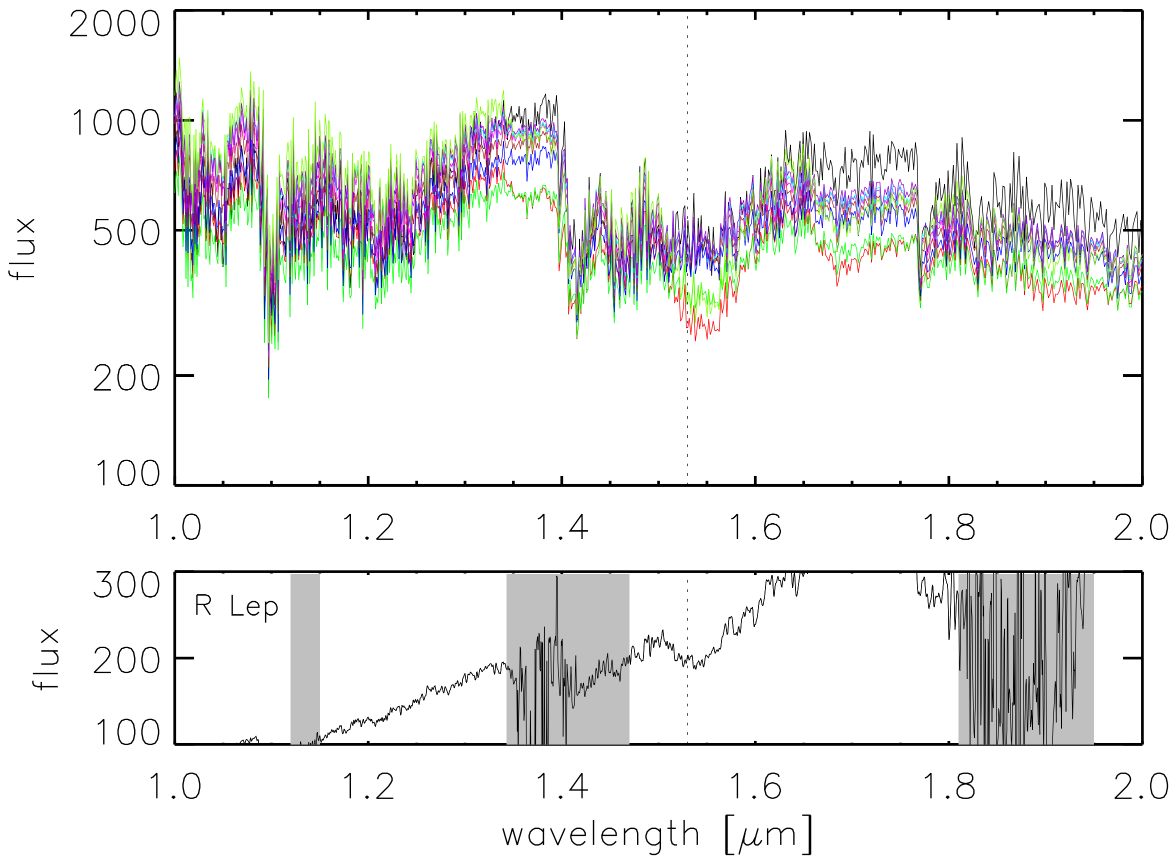

Figure 3.14: Synthetic spectra at the eight selected phases of model L7C14U6RO in the wavelength region between 1 and 2 μm (upper panel). The dotted line marks the short-wavelength edge of the 1.53 μm feature which is observed in cool carbon-rich Miras (lower panel). At phases close to minimum light, model L7C14U6RO predicts such a feature which favours the interpretation of this band to be due to a C_2H_2 and HCN combination band.

Very remarkable is the appearance of a strong band in the dynamical spectra (red and light green curve) at 1.53 μm at phases close to minimum light. Figure 3.14 shows a zoom-in at the appropriate region. Such a feature has been observed in spectra of a few cool carbon-rich Miras (lower panel of Fig. 3.14), e.g. in R Lep (Lançon & Wood 2000). The feature was tentatively attributed to C_2H by Lançon & Wood (2000) in accordance with the C_2H absorption cross sections presented in Goebel et al. (1983). Goebel et al. (1981), and later Joyce (1998), discussed the possibility of the 1.53 μm feature to be due to a HCN and/or C_2H_2 combination band. This later identification is in agreement with the results of our dynamical computations which attribute the 1.53 μm band to the (020−000) transition of HCN and the (10100−00000) transition of C_2H_2. These transitions are weak and only at very low temperatures they give rise to enough absorption in order that we can recognise the C_2H_2/HCN feature on top of the C_2 feature at the same position. However, C_2H might also contribute to the 1.53 μm feature. Due to the lack of appropriate laboratory data we are not able to include C_2H in our calculations currently.

Allover the investigated spectral region the C_2H_2 and HCN features respond differently to the influence of dynamics, depending on the temperature where they are *mainly* formed. The 3 and 3.8 μm features are formed at temperatures where the partial pressures of HCN and C_2H_2 in the dynamical structures are *lower* than the ones in the hydrostatic case, therefore these features are *weaker* compared to the hydrostatic initial model. The contributions of C_2H_2 and/or HCN to the 1.53 and 2.5 μm features originate from temperatures where the partial pressures of HCN and C_2H_2 are *slightly higher* than the ones in the hydrostatic case. Therefore, these features are *stronger* at all phases. In the remaining two C_2H_2 and HCN features around 7 and 14 μm we see a different phenomenon: our dynamical calculations predict strong *emission* where the hydrostatic model shows strong absorption. This emission is caused firstly by the contribution of the dust at these wavelengths, and secondly, by the outermost layers of the models where the partial pressures of C_2H_2 and HCN are severly increased compared to the hydrostatic case. We observe emission of single lines in the 14 μm region in stellar spectra (Aoki et al. 1999), but not such strong emission features as predicted in our models. We will discuss this problem in more detail in Sect. 3.3.5. Finally, it should be mentioned that the C_3 feature at 5.1 μm is also filled up with emission in the dynamical spectra.

3.3.3 Model L7TC14U5RO

Model L7TC14U5RO was also designed to represent a Mira variable. The variation of its bolometric magnitude amounts to 0.55 mag. Compared to model L7C14U6RO, the hydrostatic initial model has a slightly lower effective temperature (2800 instead of 2880 K), and the dynamical computations have a lower piston velocity $\Delta u_{\rm p}$ (5 instead of 6 km/s). Model L7TC14U5RO is very similar to model L7C14U6RO, therefore we will not discuss it in detail. The enhancement of the gas pressure is strong, this is due to the large piston velocity Δu_{p} of the model. A stellar wind with a mass loss rate of about $3.5 \cdot 10^{-6}\,\mathrm{M}_{\odot}/\mathrm{yr}$ develops, the degree of condensation at the outer boundary amounts to 0.34.

3.3.4 Model L7C18U4RO

Model L7C18U4RO was also designed to represent a Mira variable. The variation of its bolometric magnitude amounts to 0.44 mag. Compared to model L7C14U6RO, the hydrostatic initial model has a higher C/O ratio (1.8 instead of 1.4). A stellar wind with a mass loss rate of about $2.8 \cdot 10^{-7}\,\mathrm{M}_{\odot}/\mathrm{yr}$ develops, the degree of condensation at the outer boundary amounts to 0.25. Model L7C18U4RO is similar to model L7C14U6RO, therefore we will only discuss the differences in the following.

For a fixed gas pressure the dynamical model structures are in the mean cooler than the hydrostatic initial model in the temperature range between 4000 and 2200 K. At temperatures below 2200 K the dynamic structures deviate significantly from the hydrostatic structure. Between 4000 K and $\approx$ 2200 K, the partial pressure of CO of the hydrostatic initial model is mostly higher than at all pulsational phases. At even lower temperatures, the partial pressures of CO are always significantly enhanced compared to the hydrostatic case. The partial pressures of the molecules CN, C_2, and C_3 behave similar: Down to 2200 K they behave like CO; below this temperature the partial pressures of CN, C_2, and C_3 are equal to the one of the hydrostatic initial model with the exception if a shock wave is propagating through this low temperature region of the star. The maxima of the partial pressures of HCN and C_2H_2 are shifted to lower temperatures compared to the hydrostatic case. As model L7C14U6RO, this model shows a strong 1.53 μm band, but in this case the band is present during most of the cycle and not only around minimum light. Due to the very high C/O ratio of this model (1.8) the C_2, C_3 and C_2H_2 features are very strong. The C_2H_2 and HCN features shortwards of 7 μm are stronger than in the hydrostatic initial model at all phases of the dynamical model. This is consistent with the corresponding partial pressures being higher in the relevant range. The CO feature around 4.6 μm varies considerably during the cycle, indicating that layers with cool temperatures (where the partial pressure of CO is increased compared to the hydrostatic case) are still contributing to this feature. The 5.1 μm C_3 feature is partly filled up with emission in the dynamical calculations, but the feature is still a prominent absorption feature. In the remaining two C_2H_2 and HCN features around 7 and 14 μm we again see emission, but less pronounced than in the case of model L7C14U6RO. This is probably due to two facts: firstly the piston velocity of the model and hence the amount of the levitation of the atmosphere (and, as a consequence, the increase of the partial pressures, the mass loss rate, and the degree of condensation) is smaller, and secondly due to the higher C/O ratio of the model more emission is needed to fill up the absorption feature.

3.3.5 Origin of the emission in the dynamical spectra

As already mentioned in Sect. 3.3.2, observations in the 14 μm region of carbon stars show single lines in emission (Aoki et al. 1999). The emission features are, however, not as strong as our dynamical models predict. To find the origin of this strong emission we therefore tried two things: first we calculated the synthetic spectra neglecting the dust opacity, and the depletion of carbon due to dust formation when calculating the partial pressures. In a second attempt, we simply cut off layers of the atmospheric structure which had temperatures below a fixed threshold, namely below 800 and 1000 K. Figure 3.15 shows the results for a minimum light model of L7C14U6RO. The spectra were forced to have equal flux at 3.5 μm (indicated by the black arrow). On first sight the spectra seem to differ most at short wavelengths. This is caused by the contribution of the dust in this wavelength region, which absorbs and scatters the radiation and thus causes a shift of the maximum of the energy distribution. The intensity of the spectral features shortwards of $\approx 2.5\,\mu$m *does not differ*. Only the C_2H_2/HCN, CO and C_3 features are affected and out of these, only the 7 and 14 μm feature in a way that it is worth mentioning. The omission of dust in the computation of the spectra (red line) has only a small influence on the 7 μm feature but a stronger well noticable effect on the 14 μm feature; the spectrum shows still clear and much too strong emission around 7 and 14 μm. This means that the dust can be excluded as the dominant source of the emission in our dynamical model spectra. Cutting the model structures at arbitrary temperatures (800 and 1000 K in this case) prevents layers below these temperatures to contribute to the features. The synthetic spectrum based on the model structure cut below 800 K (green line) shows less emission in the 7 and 14 μm feature than the spectrum calculated without dust contribution. But there is still some emission left in this case. When cutting the structure below 1000 K (blue line) the emission is completely gone in both wavelength regions. Therefore, we conclude that in the case of model L7C14U6RO the layers with temperatures below 1000 K are the main source of the emission in the spectra.

For model L7C18U4RO it turned out that the layers with temperatures below 800 K are the main sources of emission. The lower temperature value in the second case is probably due to the higher C/O ratio (a higher C/O ratio causes stronger molecular absorption of C_2H_2 and HCN and as a consequence more C_2H_2 and HCN from cool layers is needed to fill up the absorption feature), and due to the lower piston velocity $\Delta u_{\rm p}$ (and hence the slightly smaller increase of the partial pressures of C_2H_2 and HCN due to the dynamic effects in this model).

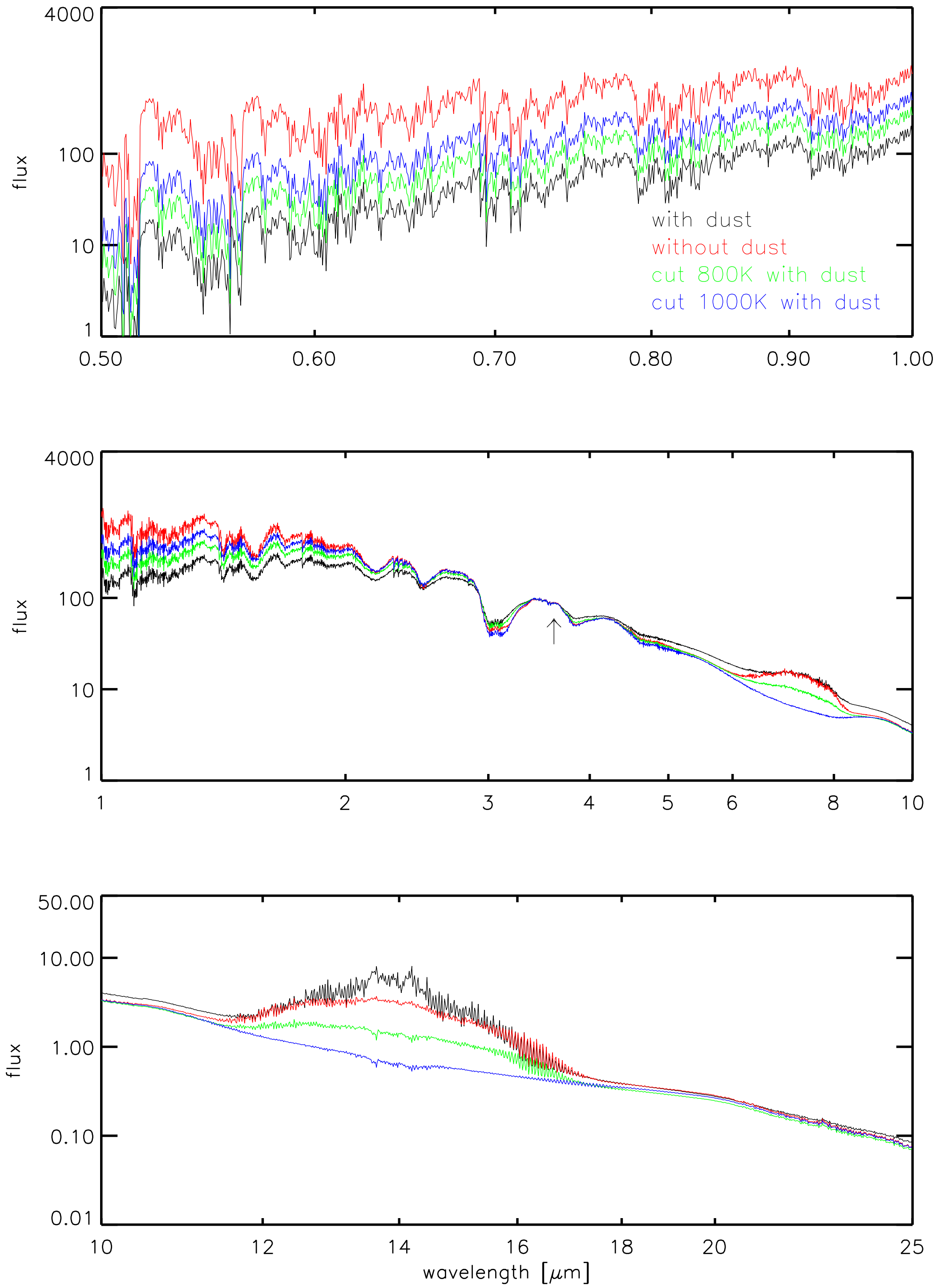

Figure 3.15: Synthetic spectra of a minimum-light model of L7C14U6RO for a full structure (black line), a full structure but with dust opacity being neglected in the computation of the synthetic spectra (red line), for a structure which stopped at 800 K (green line), and for a structure which extends only to 1000 K (blue line). The arrow indicates the wavelength at which the spectra were forced to have equal flux.

A detailed comparison of the 14 μm region with observations will be presented in Sect. 4.7.

Currently, three different reasons for the unrealistic strong emission can be proposed: (1) the equilibrium chemistry which we use for our calculations may be unrealistic and give wrong results at such low temperatures (due to the effects of pulsation and the stellar wind at low densities), (2) layers with even lower temperatures (and hence dust around the star) prevent that the observer can see the layers where the strong emission originates, or (3) the chosen piston velocities in our models are too high (the levitation of the atmosphere too strong). Reducing the piston velocities would, however, not produce realistic stellar winds for the chosen stellar parameters, which on the other hand are used to explain other important spectral features. Unfortunately at present none of these possibilities can be rejected.

3.4 Conclusions

A detailed comparison of the model structures, partial pressures, and synthetic spectra of our dynamical models L52C11U2RO, L7C14U6RO, L7TC14U5RO, and L7C18U4RO gives the following results:

1. A higher C/O ratio resulted in stronger C_2, C_3 and C_2H_2 features.
2. The higher the piston velocity in a model was, the stronger was the levitation of the atmosphere, and hence the stronger was the filling-up of absorption features with emission produced in high atmospheric layers.
3. The intensity of the CO feature around 4.6 μm, the intensity of the C_3 feature around 5.1 μm, and the intensity of the C_2H_2 feature at 3 μm decreased in the models that developed a stellar wind and where dust formed. This is either due to the dust emission superposing the features, or due to the depletion of carbon due to dust formation.
4. Two strong emission features around 7 and 14 μm occured in our synthetic spectra if the model showed a pronounced mass loss and dust formed. The emission originated in layers cooler than ≈ 1000 K.
5. Dynamical models are able to reproduce a spectral feature around 1.53 μm which is observed in cool carbon stars. The origin of this band is still debated; in our models it could be attributed to a contribution of C_2H_2 and HCN at the same wavelengths where a band of C_2 is present. Thus, our models favour the interpretation of the 1.53 μm band in cool carbon stars to be caused by a C_2H_2/HCN combination band.

Chapter 4

Comparison of models with observations

The following different sets of observational data are arranged with increasing wavelength. We start with indices measured in the optical range and end with spectra covering the near infrared region till about 45 μm. The last two sections of this chapter are reserved for a detailed discussion of a few stars and to a summary.

4.1 Baumert measurements in the Wing filter system

4.1.1 The Photometric System

The Photometric System used in Baumert's study (Baumert 1972) is a system of interference filters specifically designed for the study of late-type stars. This system is described in Wing (1971). It evolved from Wing's 27−colour system used in an earlier study of late-type stars with a scanner (Wing 1967). Table 4.1, adapted from Baumert (1972), lists the characteristics of the remaining eight filters, numbered in direction of increasing wavelength. Column 2 gives the measured effective wavelengths of the various filters. Column 3 lists the widths of the filters, defined as the full width at half transmission. Table 4.1 differs considerably from the one in Baumert (1972) concerning the main spectral features and the contaminants in the filters. Where Baumert lists "continuum", in at least two cases (10395 and 10544) non negligible contributions of C_2 are found. Figure 4.1 illustrates this, where a synthetic spectrum including all molecules and synthetic spectra of CN and C_2 alone are plotted.

Table 4.1: Characteristics of the eight filters

Filter	Effective Wavelength	Filter Width	Main Features	Contaminants
1	7117 Å	60 Å	CN Δv = +3	C_2
2	7544 Å	50 Å	weak CN	C_2
3	7809 Å	40 Å	local continuum	weak C_2
4	8122 Å	50 Å	CN Δv = +2	C_2
5	10395 Å	50 Å	C_2	weak CN
6	10544 Å	60 Å	C_2	weak CN
7	10804 Å	60 Å	local continuum	C_2, CN
8	10975 Å	70 Å	CN (0,0)	C_2

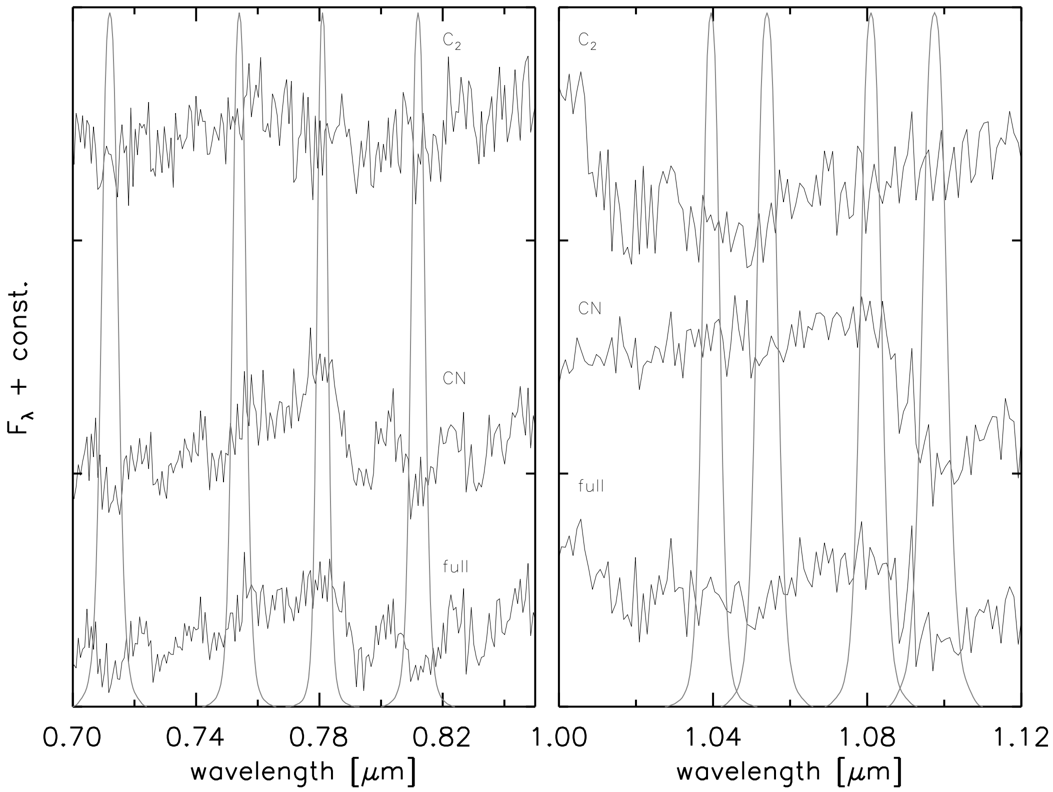

Figure 4.1: Synthetic spectrum including all molecules and synthetic spectra of CN and C_2 alone overplotted by the Wing filter curves to illustrate the contributions of the different molecules to the colours.

4.1.2 Observations

The observations discussed in the following were obtained at three different observatories with seven telescopes and three photometers (Baumert 1972). The telescopes were the 32″ Schottland reflector at Perkins Observatory in Delaware, Ohio; the 72″ Perkins reflector at Lowell Observatory in Flagstaff, Arizona; the 21″, 24″ and 42″ reflectors of Lowell Observatory; and the No. 4 (16″) and No. 2 (36″) reflectors of Kitt Peak National Observatory.

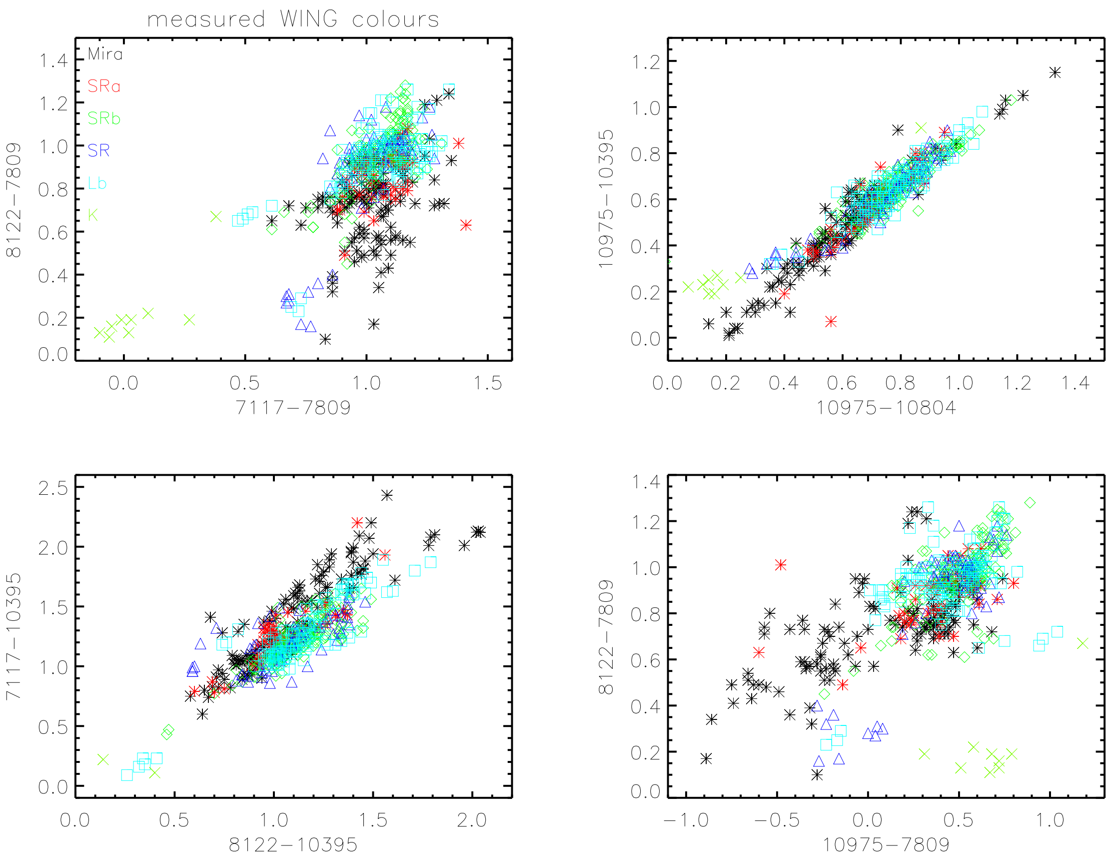

Figure 4.2: Two-colour diagrams of the observations of Baumert (1972). Different types of stars are labeled by the following symbols and colours: Black asterisks: Miras; red asterisks: SRa's; green diamonds: SRb's; blue triangles: SR's; turquois squares: Lb's; light green crosses: K giants.

Figure 4.2 shows two-colour diagrams of the observations, where the different types of variables are denoted by different symbols and colours as labeled in the plot. The different types of stars do not lie in clear distinct regions in all colours. In the 8122−7809 colour index, which measures the strength of the CN $\Delta v = +2$ band, the Miras tend to have smaller values. Also the 10975−10804 and 10975−10395 colours of Miras, which measure the CN (0,0) band strength, are bluer. The differences in the 10975−7809 colour index reflect the different effective temperatures of the stars, the Miras are on average cooler than semiregular and irregular variables.

Baumert (1972) derived colour temperatures from a blackbody fit to the 7809 and the 10804 Å filters for all sample stars. Figure 4.3 shows the colour indices plotted versus the colour temperature. Symbols and colours correspond to the ones in Fig. 4.2. For all types of AGB variables the following correlations are found:

- 7117−7809: This index measures the intensity of the CN $\Delta v = +3$ band. Stars with lower colour temperatures tend to have slightly higher 7117−7809 indices. This means that the CN $\Delta v = +3$ band is slightly stronger in cooler stars.
- 8122−10395: This index measures the intensities of the CN $\Delta v = +2$ and a C_2 band. Cooler stars have larger indices.
- 7117−10395: This index measures the intensities of the CN $\Delta v = +3$ and a C_2 band. Cooler stars have larger indices.
- 10975−7809: This index measures the intensities of the CN (0,0) band. Cooler Miras and semiregular variables of type "a" have smaller indices. For the other types of AGB stars there is no clear correlation visible.

It is interesting that the 8122−7809 index, which measures the intensity of the CN $\Delta v = +2$ band, the 10975−10804 index, which measures the CN (0,0) band, and the 10975−10395 index, which measures the CN (0,0) and a C_2 band, show no correlation with the colour temperature.

In all colour indices the Miras and semiregular variables of type "a" seem to be split up in two sequences parallel to each other, one from colour temperatures between 1800 and 2500 K, the other at colour temperatures higher than 2500 K. We were not able to find any correlation between this behaviour and parameters like the period or the amount of variation in the V filter in a first investigation. The clear separation at a certain temperature, however, hints at an artificial effect. Probably one or both of the chosen filters for the calculation of the colour temperature are not very suitable for stars with low temperatures. More detailed investigations are necessary to clarify the situation.

4.1.3 Models

The observations are compared with our set of hydrostatic plane parallel and spherical models calculated with the MARCS code, as well as with dynamical models. All indices are defined as $-2.5 \log(\text{flux})$.

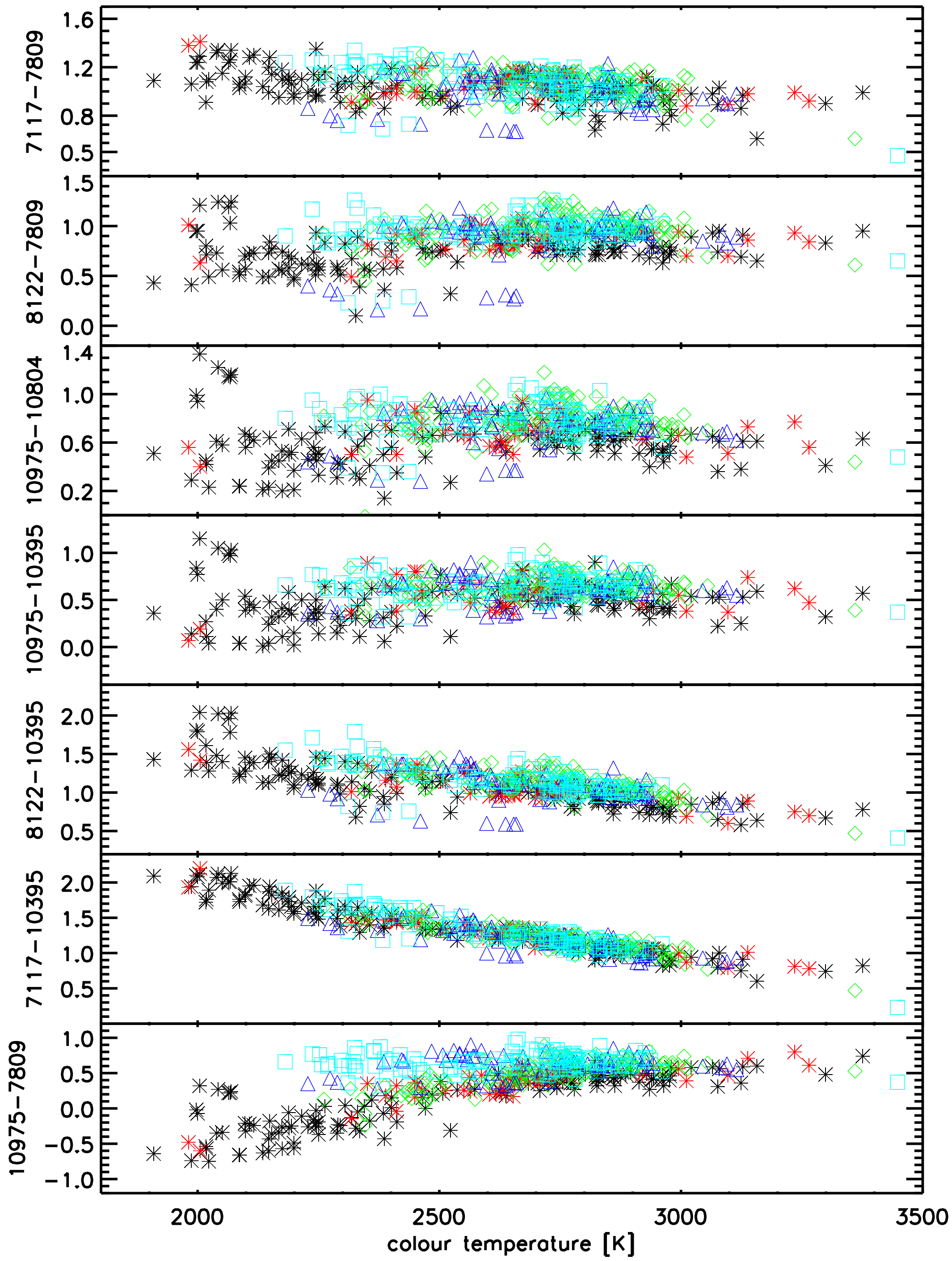

Figure 4.3: Colour indices versus colour temperature. The denotations of the symbols and colours are the same as in Fig. 4.2.

Zero point

Baumert (1972) measured a few K giants, unfortunately he did not measure α Tau which we use as standard star. For α Tau, which is a K5 giant, a model with $T_{\rm eff} = 3870$ K, $\log(g) = 0.0$, $\mathrm{M} = 1\,\mathrm{M}_\odot$ and C/O = 0.43 is adopted. The star matching α Tau closest observed by Baumert is HD178717, which is a carbon-rich K3.5 giant. Taylor (1999) lists an effective temperature of 3870 K and a V$-$K colour of 3.784 for HD178717. This is close to the temperature of α Tau (3850 K) with its V-K colour of 3.88. But in contrast to α Tau, HD178717 is carbon-rich. We calculated the colours for the α Tau model and added corrections in order to reproduce the observed HD178717 colours. Table 4.2 gives the calculated α Tau colours, the measured HD178717 colours and the applied corrections.

Table 4.2: Corrections

Colour	α Tau model	HD178717 measured	Correction
7117$-$7809	0.52	0.27	-0.25
7117$-$10395	1.09	0.22	-0.87
8122$-$7809	0.19	0.19	0.00
8122$-$10395	0.76	0.14	-0.62
10975$-$7809	-0.14	0.31	0.45
10975$-$10395	0.43	0.26	-0.17
10975$-$10804	0.47	0.25	-0.22

Theoretical results

Figure 4.4 shows the Wing colour indices versus effective temperature for all hydrostatic models with C/O = 1.10. Black diamonds denote plane parallel models with $\log(Z/\mathrm{Z}_\odot) = 0.0$, black squares plane parallel models with $\log(Z/\mathrm{Z}_\odot) = -0.3$, red diamonds spherical models with $\log(Z/\mathrm{Z}_\odot) = 0.0$, and red squares spherical models with $\log(Z/\mathrm{Z}_\odot) = -0.3$. Plane parallel and spherical models show the same trends. Depending on the colour index, the indices of the models with lower metallicity (squares) deviate strongly or only moderately from the ones calculated with solar metallicity. In the plane parallel spectra the effect is much more pronounced than in the spherical ones. The effect of $\log(g)$ on the indices is very small, the same applies to the effect of the C/O ratio (not shown here). As in the case of the observations, correlations between the 7117$-$7809, 8122$-$10395, 7117$-$10395, 10975$-$7809 colour indices and the effective temperature do exist. The 8122$-$7809, 10975$-$10804, and 10975$-$10395 indices do not show a clear correlation; this is consistent with the observations.

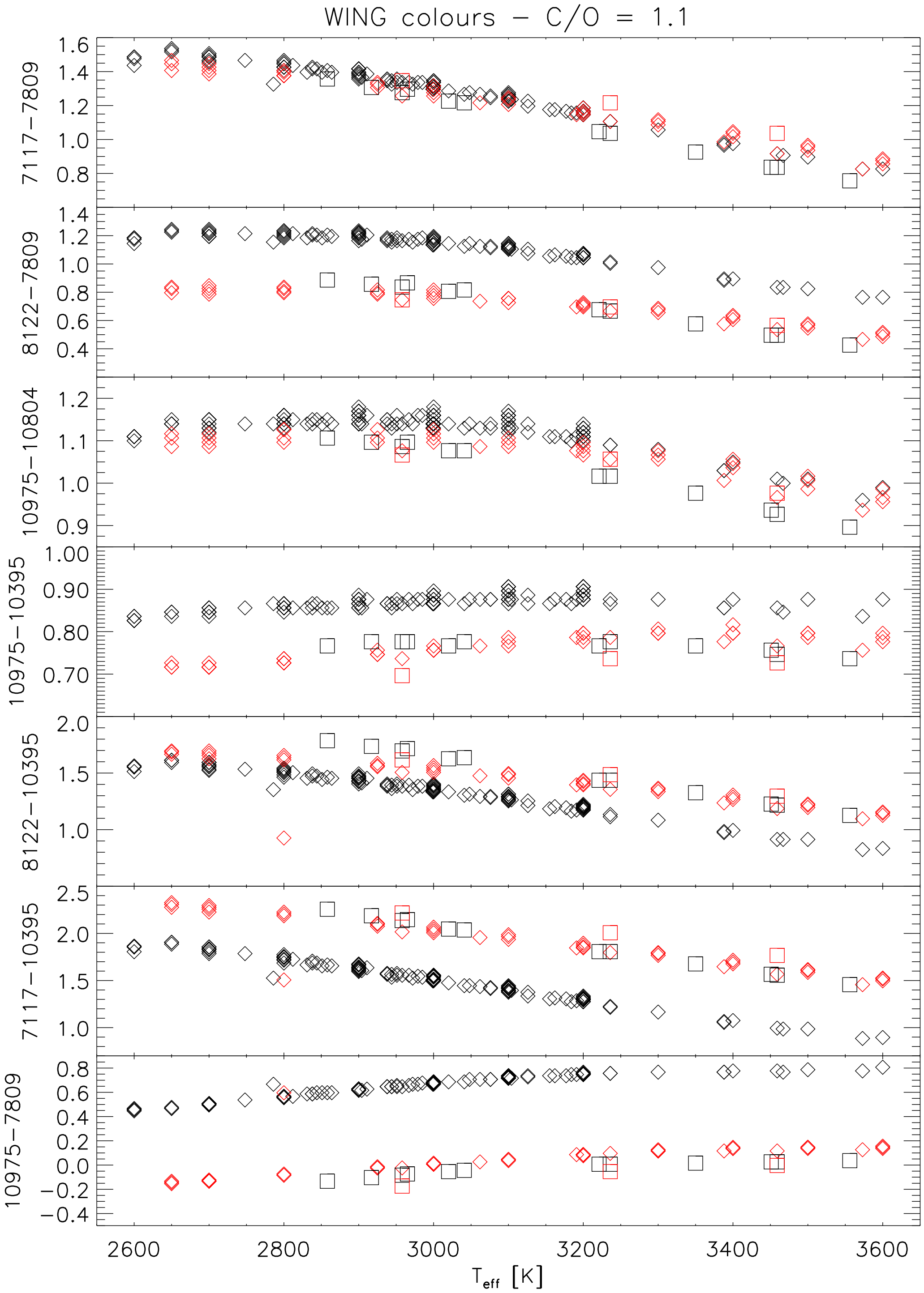

Figure 4.4: Wing indices versus effective temperature for the models with C/O = 1.10. Black diamonds denote plane parallel models with $\log(Z/Z_{\odot}) = 0.0$, black squares plane parallel models with $\log(Z/Z_{\odot}) = -0.3$, red diamonds spherical models with $\log(Z/Z_{\odot}) = 0.0$, and red squares spherical models with $\log(Z/Z_{\odot}) = -0.3$.

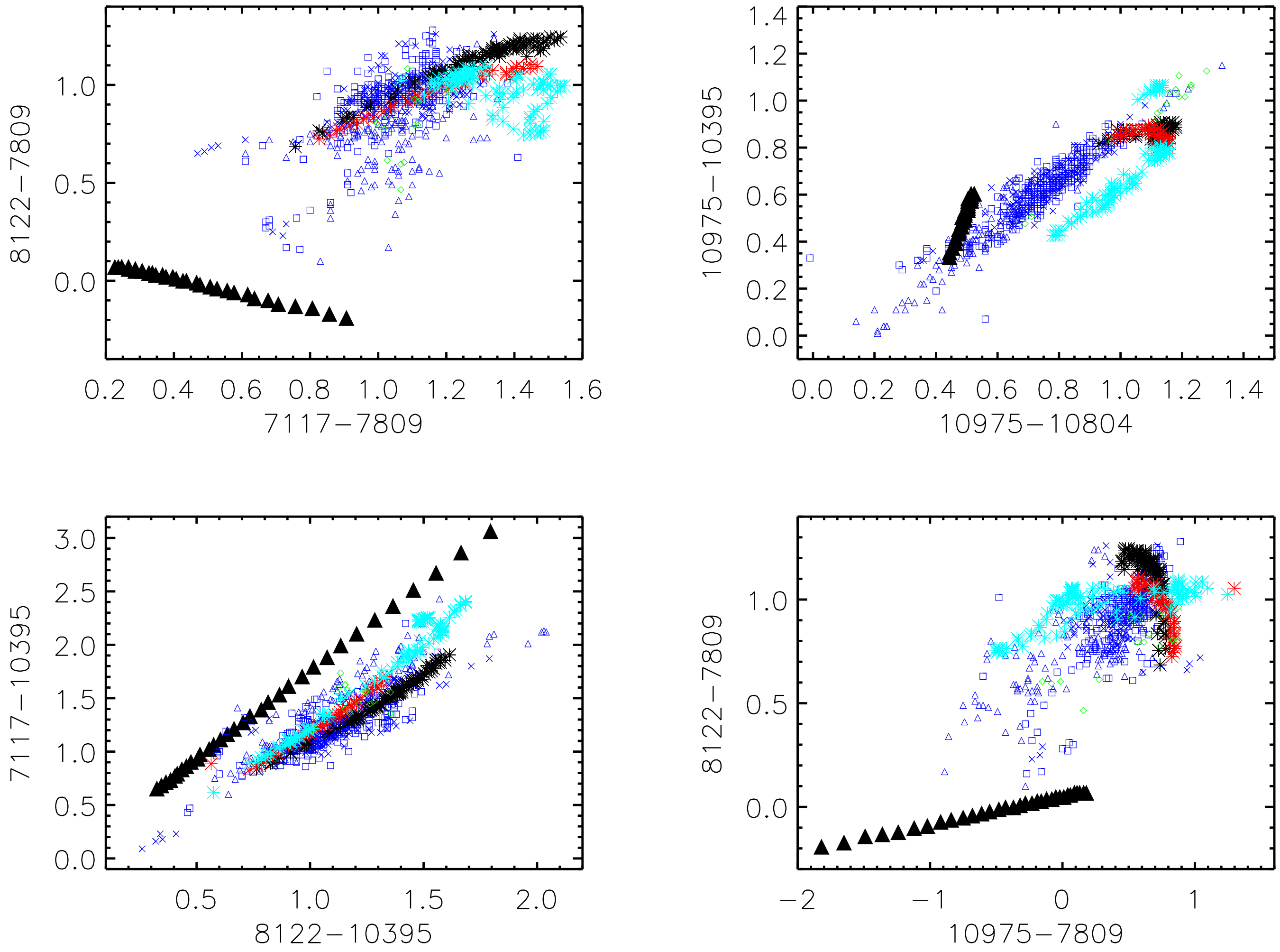

Figure 4.5: Comparison of observed and theoretical colour indices. The black asterisks denote plane parallel models; red asterisks spherical models; black triangles blackbodies with temperatures between 5000 and 1800 K; turquoise asterisks dynamical models; blue squares, triangles and crosses the Baumert observations; and green diamonds the indices which were calculated from the spectra of Lançon & Wood (2000).

4.1.4 Comparison of theoretical with observational results

The hydrostatic models should be able to explain irregular variables which show no significant pulsation and do not posess a thick dust shell. The dynamical models should eventually be able to cover the range in the two-colour diagrams occupied by Miras. In Fig. 4.5, observations and theoretical results are compared. The black full triangles mark the colours of blackbodies with temperatures between 5000 and 1800 K. The black asterisks denote plane parallel hydrostatic models, red asterisks spherical hydrostatic models, turquoise asterisks dynamical models. Blue squares (SR's), triangles (Miras) and crosses (Lb's) stand for the Baumert observations, green diamonds for the indices which were calculated from the spectra of Lançon & Wood (2000). In all cases all models lie in the region of parts of the observations. They can explain the observed variations in the colours to different extents, depending on the indices. The models cover almost the full range of the observations in the 7117−7809, 8122−10395, and 7117−10395 colours. In all indices in which the 10975 filter is involved, the models cover only a small part of the observed range. Additionally, in these cases the chosen zero point seems problematic. This is probably due to the fact that this filter measures the (strong) CN (0,0) band which should be present in HD178717, but not in our synthetic α Tau spectrum. All other filters are affected less than the 10975 filter by this problem because the bands in the other filters are weaker. The dynamical models cover larger ranges in almost all colours than the hydrostatic models. In 7117−7809 and in 10975−10804 the dynamical models mostly lie in different regions than the observations. Generally, the scatter in the observations is much larger than what our models predict, this is probably due to different metallicities and mass loss rates of the observed stars. The locations of the very cool Miras in the two-colour diagrams are not reproduced correctly.

4.1.5 Conclusions

Hydrostatic and dynamic model spectra are able to reproduce the correct trends of colour indices in the wavelength range between 0.7 and 1.1 μm. The model colour indices lie in the correct regions. Depending on the index, the range of the observed colour indices can be reproduced to different extents. The locations of Miras in the two-colour diagrams cannot be reproduced currently.

4.2 Lançon spectra

4.2.1 Observations

The near-IR spectra were obtained by Ariane Lançon and Peter Wood on the Australian National University 2.3 m Telescope at Siding Spring Observatory, using the cross-dispersed grism mode of the Cryogenic Array Spectrometer and Imager CASPIR. For each of the IJ, JH and HK grisms, five orders are imaged onto the CASPIR array. The spectra were acquired through the 1″x15″ slit providing a resolving power of approximately 1100. Low resolution optical spectra were acquired using the so-called Reynolds Spectrograph at the 1.88 m Telescope on Mount Stromlo. Details about the data reduction can be found in Lançon & Wood (2000). Here, we only briefly recall the properties of the resulting spectra.

The pixel-to-pixel noise in the spectra is due to photon and read-out noise, to residual telluric absorption features, and in the optical to changing seeing-determined spectral resolution and calibration. The signal-to-noise ratio per resolved element typically has values around 50 in clear atmospheric windows (1 σ noise). It drops strongly in regions of strong telluric CO_2 or H_2O absorption.

The uncertainties on the energy distribution and colours result from the combined effects of instrumental changes, of the focusing and positioning of the stellar image on the slit, of the choice of a model for the intrinsic spectrum of the spectrophotometric reference stars, and of telluric absorption that reaches into the overlap region between the optical and near-IR data. An uncertainty of 0.15 mag affects colours that combine optical and near-IR fluxes. The uncertainty on purely near-IR colours increases with the separation between the central wavelengths of the combined filters; in most cases, it remains below 0.1 mag for a separation of 1 μm.

Table 4.3 lists the observed carbon stars used in the following. All spectra are plotted in Lançon & Wood (2000). Here, we will not discuss the extremely cool large amplitude carbon rich Mira R Lep, for which circumstellar dust is likely to already play a significant role.

4.2.2 Comparison of observed spectra with model spectra

Since the variations in the spectra are small, we have selected one particular spectrum of each star (the january 1996 data) for a detailed comparison with synthetic spectra based on plane-parallel hydrostatic atmospheres. The effects of the various model parameters are not independent of each other. For instance, as long as the $^{12}C/^{13}C$ ratio remains a free parameter (because its determination is difficult at low spectral resolution) the derived effective temperatures and C/O ratios are affected by uncertainties. We calculated opacity sampling data for all included

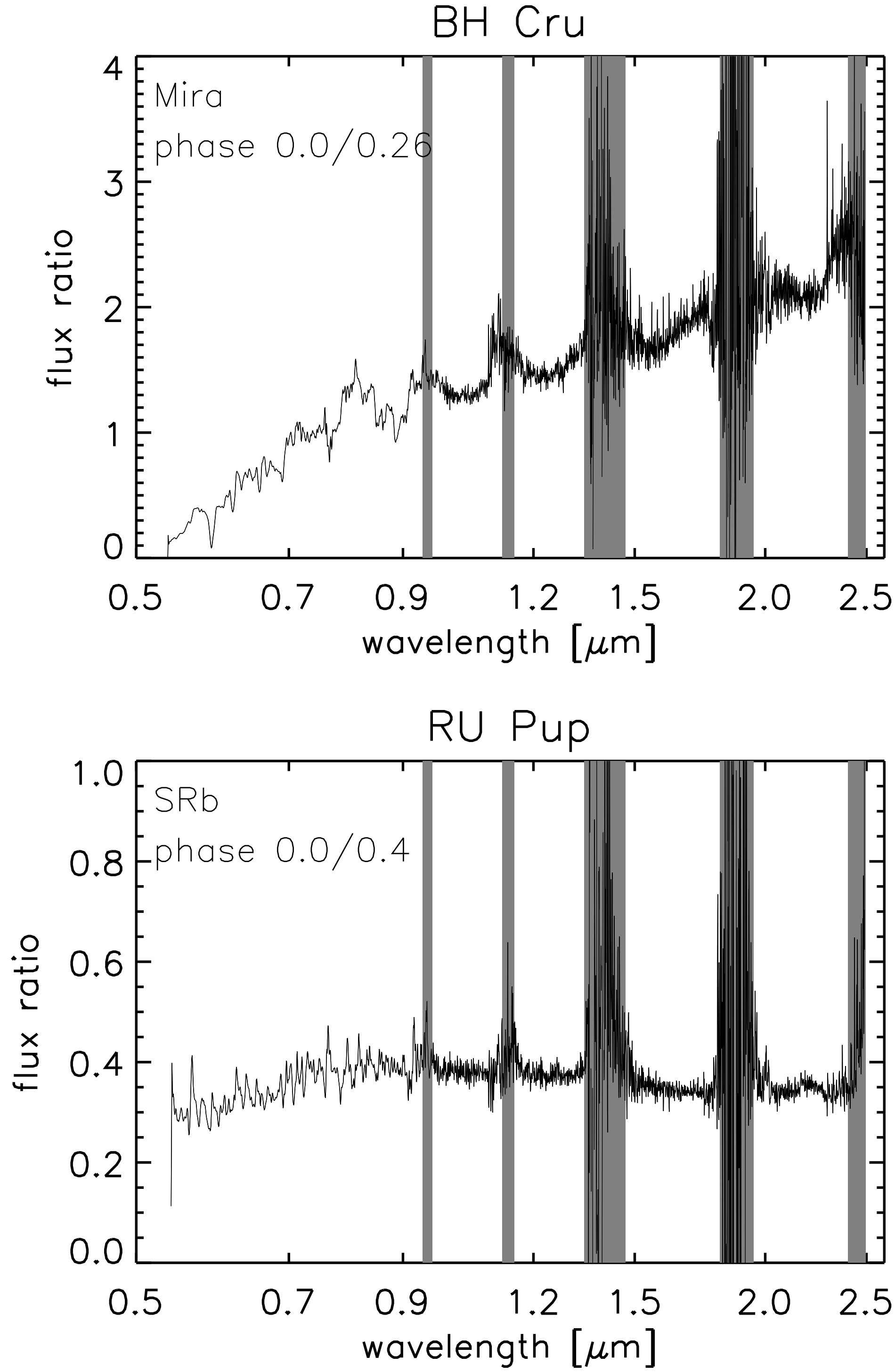

Figure 4.6: Flux ratio of two different phases of the Mira star BH Cru (top) and the semi-regular variable RU Pup (bottom; note that most of the noise in the optical range is due to spectral resolution/calibration mismatch.)

Table 4.3: Main properties of observed carbon stars

Name	variability type	δV	Period [1] (days)	Spectral type
Y Hya	SRb	3.7 [2]	302.8	C5,4 (N3P)
BH Cru	M	2.8	421.0	SC4,5/8e
S Cen	SR	1.5	65	C
T Cae	SR	1.8	156	C6,4 (N4)
RU Pup	SRb	1.9	425	C5,4 (N3)

[1] periods as given in the GCVS of Kholopov et al. (1988).
[2] significantly overestimated according to AAVSO/AFOEV data.

molecules with $^{12}C/^{13}C$ ratios of 89 (the solar value), 3.5 (the CNO cycle equilibrium, which is the theoretical minimum value) and 40 (an intermediate value). Varying the $^{12}C/^{13}C$ ratio between 3.5 and 89 typically results in a best fit obtained with a difference in effective temperature of 100 K and a difference in the C/O ratio of about 0.05. Therefore we want to stress that best fits as those presented in the following sections, are never necessarily unique fits.

As main temperature indicators the overall energy distributions were used and especially the intensities of the CN features at 0.69, 0.78, 1.08 and around 1.46 μm. Once the temperature range was determined we tried to fix the C/O ratio. As main C/O ratio indicators the CO band at 2.29 and the C_2 bands at 0.77, 0.88, 1.02, 1.20 (all belonging to the Phillips system) and 1.77 μm (Ballik-Ramsay fundamental band) were used. Unfortunately the absorption coefficient of C_2 beyond 1.1 μm is quite uncertain (see Sect. 2.2). Therefore, the unblended 1.77 μm C_2 band is less suitable for the determination of the C/O ratio than expected. In the detailed fits presented in the following often different C_2 bands fit or do not fit, depending on which of the C_2 bands we tried to fit (depending on the C/O ratio and the effective temperature of the star). This reflects nothing else than the uncertainties in the C_2 opacities. Fig. 4.7 shows the result of an attempt to put our stars in a sequence of decreasing effective temperature (upper panel) and in a sequence of increasing C/O ratio (lower panel).

For the stars in our sample not a lot of other observational data and analyses in the literature exist. As shown by Jørgensen et al. (2000) the 3 μm C_2H_2/HCN and the 5.1 μm C_3 features are powerful tools to determine effective temperatures and C/O ratios for relatively hot carbon stars surrounded only by small amounts of dust. Unfortunately, no spectra covering these two regions simultaneously exist for our sample stars. Therefore, the parameters derived for the stars are based only on our spectra covering the wavelength region between 0.5 and 2.5 μm.

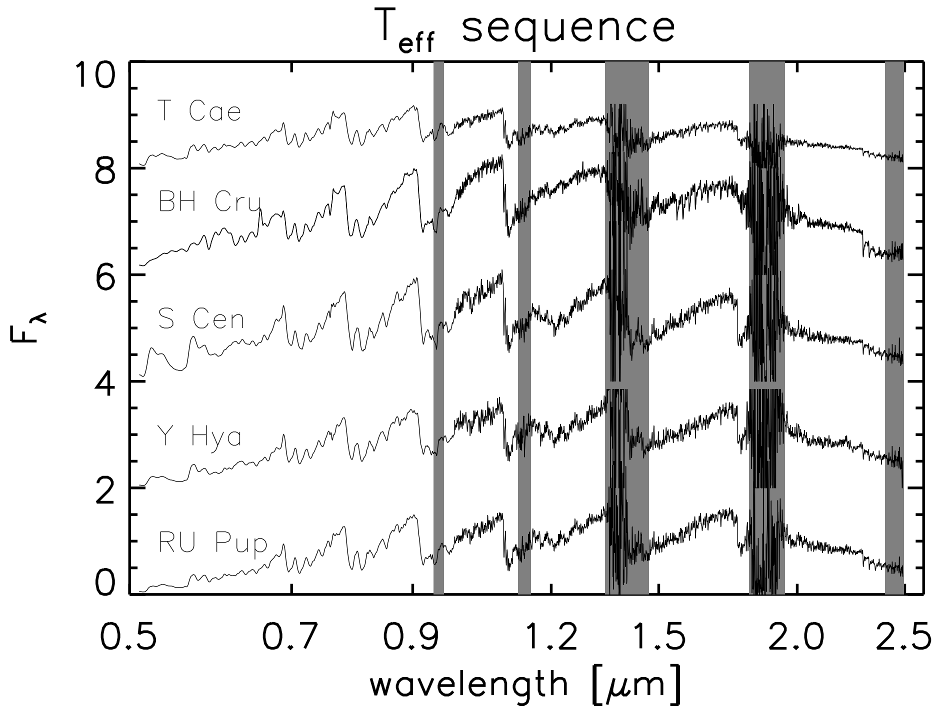

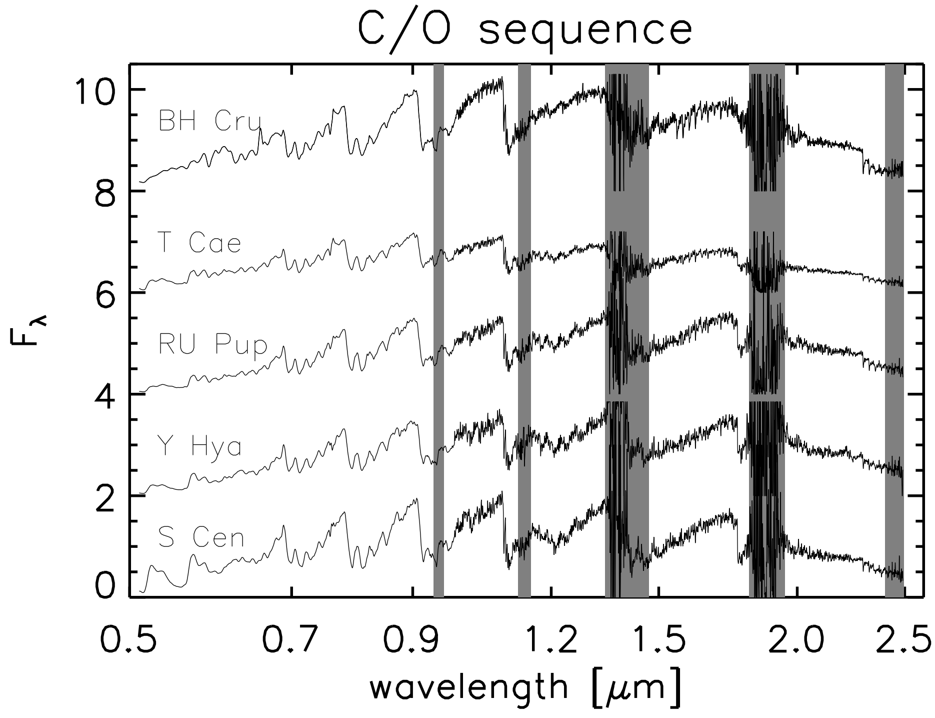

Figure 4.7: Sequence of decreasing effective temperatures of our sample stars (from top to bottom in upper panel) and sequence of increasing C/O ratio (increasing from top to bottom in lower panel). The grey shaded areas mark regions of the spectra which are contaminated by the Earth's atmosphere.

4.2.3 Discussion of the individual stars

BH Cru

BH Cru had been classified as an SC star with strong ZrO and no C_2 bands in 1965 to 1973 by Catchpole & Feast (1971) and by Keenan & Boeshaar (1980). In 1980, Lloyd Evans (1985) found moderately strong C_2 and probably no ZrO bands, in 1984 C_2 was strong and ZrO absent. Since then he had followed the star around its pulsation cycle and finds it to be a stable CS star with no ZrO bands (Lloyd Evans, private communication). Bedding et al. (2000) show that during the same time the period of the star has increased from 421 to about 535 days presently, around the time of our observations the period was about 520 days. The IRAS-LRS spectrum of BH Cru is essentially continuous with a hint of circumstellar emission (Lambert et al. 1990). Therefore, the star is not surrounded by a lot of dust. Kipper & Wallerstein (1990) analysed the wavelength region 6685 to 6721 Å of SC stars. They determined Li abundances and abundances of a few other elements. For this determination they adopted a model atmosphere with $T_{\rm eff} = 3500\,$K, $\log(g) = 0.0$, C/O = 1.00 and $M = 2\,M_\odot$ for BH Cru. Abia & Isern (1997) derived a $^{12}C/^{13}C$ ratio of 8, assuming an effective temperature of 3500 K for the star. Abia & Wallerstein (1998) analysed spectra taken in the wavelength region between 4850 an 9300 Å with a resolution of 20 000. Their spectrum showed the H_α line in emission, the observation was made close to the visual maximum light. They determined abundances of heavy elements. For their analysis they used a model with an effective temperature of 3500 K, a $\log(g)$ of 1.0, a mass of $2\,M_\odot$ and a C/O ratio of 1.00 which they assume as representative values for SC stars.

The previous observations of BH Cru imply that the C/O ratio of BH Cru has to be close to 1.00. The effective temperatures and $\log(g)$ values used in previous studies were only representative values for SC stars (Abia & Wallerstein 1998), and we therefore put lower weight to them as measures for a specific star. Our spectrum of BH Cru, taken in January 1996, was obtained close to the visual maximum (phase 0.03 according to AAVSO data). It shows the H_α line at 6565 Å in emission.

We were able to obtain a good fit (see Fig. 4.8) with $T_{\rm eff} = 3200$ K, $\log(g) = 0.0$, C/O = 1.01 and $v_{\rm mic} = 3\,$km/s when adopting $^{12}C/^{13}C = 3.5$ (which is the value closest to the ratio of 8 determined by Abia & Isern (1997) for which we have computed opacity sampling data). In the uppermost panel of Fig. 4.8 the observed spectrum of BH Cru (black line) and the model spectrum (grey line) are plotted together. In the panel below, the flux ratio of observed spectrum and the model spectrum is shown. The grey shaded areas always mark regions of the spectra which are contaminated by the Earth's atmosphere. The spectra have been forced to have equal flux at a wavelength of 1.29 μm. Below these two pan-

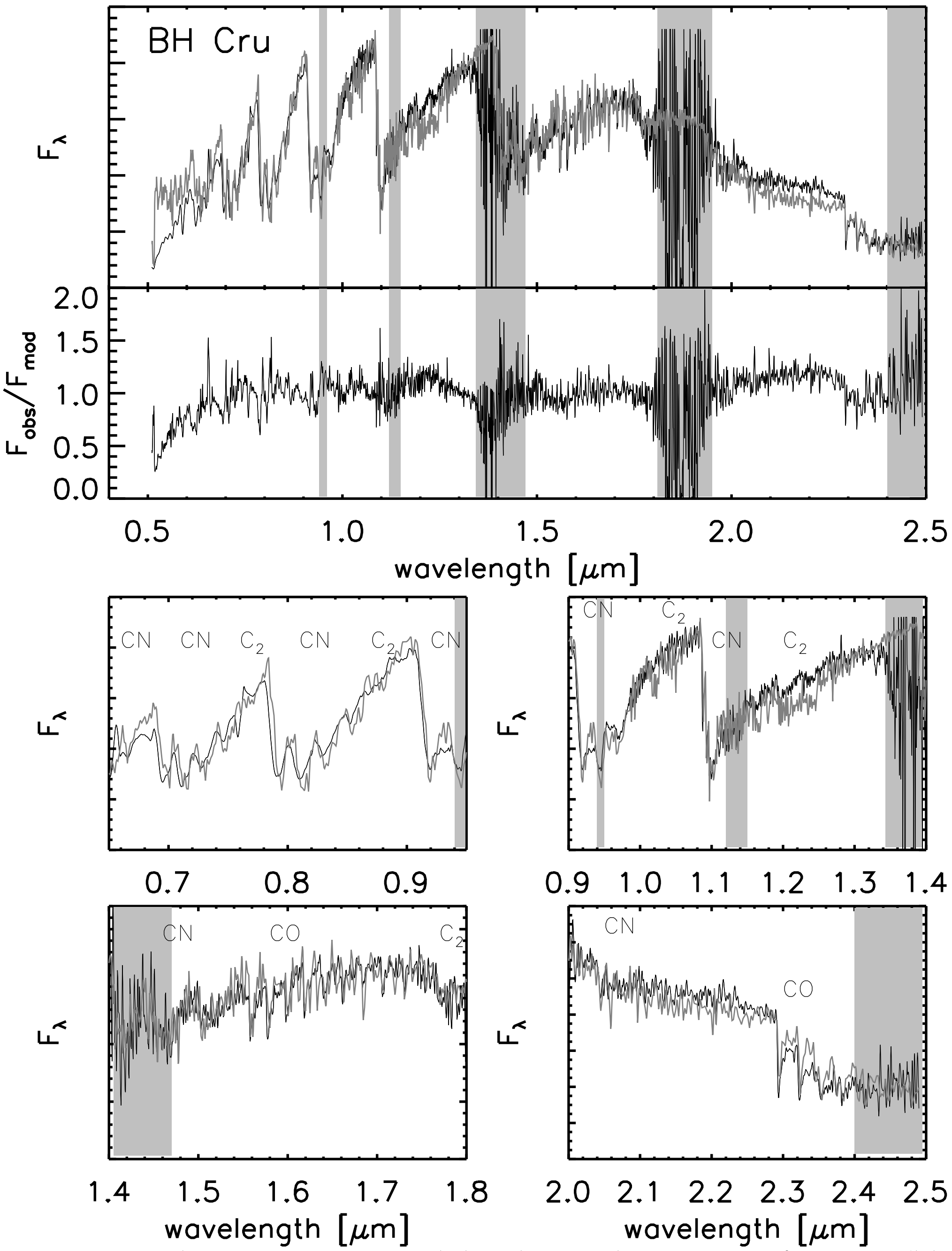

Figure 4.8: In the uppermost panel the observed spectrum of BH Cru (black line) and the model spectrum (grey line) are plotted, below that the flux ratio of observed and model flux. The spectra have been forced to have equal flux at a wavelength of 1.29 μm. Below four zooms of the uppermost plot are shown and the identifications of the molecular bands are given. The parameters of the model are: $T_{\rm eff} = 3200$ K, $\log(g) = 0.0$, C/O = 1.01, $\rm v_{mic} = 3$ km/s and ^{12}C/^{13}C = 3.5. In the last zoom we have forced the fluxes of observed and model spectra to be equal at the CO band head at 2.29 μm.

els, four selected zoom-ins into the uppermost panel are plotted, showing the main bands which have been used for the determination of effective temperature and C/O ratio. In addition, the identifications of the molecular bands are given. In the last of these four small plots, the one showing the CO 2.29 μm band, we have forced the fluxes of observed and model spectra to be equal at the CO band head at 2.29 μm, in order to make the determination of the C/O ratio easier.

The discrepancy between observation and model from 0.5 to approximately 0.7 μm (which exists in all stars we looked at) will be discussed in detail in Sect. 4.2.4. The overall energy distribution and the intensities of the CN, CO and the C_2 bands at 0.77, 0.88, 1.02 and 1.77 μm fit very well, while the computed C_2 band at 1.20 μm is too strong. There is also some discrepancy obvious at 1.79 μm, which is a common feature of all stars and will therefore be discussed in Sect. 4.2.4.

BH Cru is the only star in our sample showing strong variability. The spectrum closest to minimum light which we have (July 1996; phase 0.34) can be fitted with a spectrum based on a hydrostatic model with an effective temperature of 2800 K if all the other parameters used for the fit of the January 1996 spectrum are kept constant.

T Cae

T Cae is classified as a C6,4 (N4) star in the GCVS of Kholopov et al. (1988). In his revised classification for C stars, Keenan (1993) assigned the C_2 index 4.5 to T Cae. The star was observed twice by Baumert (1972) in the Wing filter system. From these measurements between 7117 and 10975 Å he derived colour temperatures of 2926 and 3115 K at the date of his observations. The IRAS-LRS spectrum shows evidence of weak SiC emission at 11.3 μm.

Figure 4.9 shows our best fit obtained with $T_{\rm eff} = 3400$ K, $\log(g) = 0.0$, C/O = 1.05 and $v_{\rm mic} = 3$ km/s when adopting $^{12}C/^{13}C = 3.5$. For T Cae no determination of the $^{12}C/^{13}C$ ratio exists, we chose 3.5 because the overall model spectrum matched the observation best in this case. It has not been determined by a detailed line analysis. A difference between our effective temperature and the colour temperatures of a few hundred degrees is as expected. Also in the case of the irregular variable carbon star TX Psc, the colour temperature of Baumert was 200 to 300 K below the effective temperature determined with detailed hydrostatic model atmospheres (Jørgensen et al. 2000).

The overall energy distribution, the CN, CO, and the C_2 bands at 0.77, 0.88, 1.02, and 1.20 μm fit the observations very well while the synthetic C_2 band at 1.77 μm is too weak. In addition to the minor general discrepancies between observation and model spectra in common for all the stars (which will be discussed in Sect. 4.2.4), we remark that the observed spectrum shows a flux excess com-

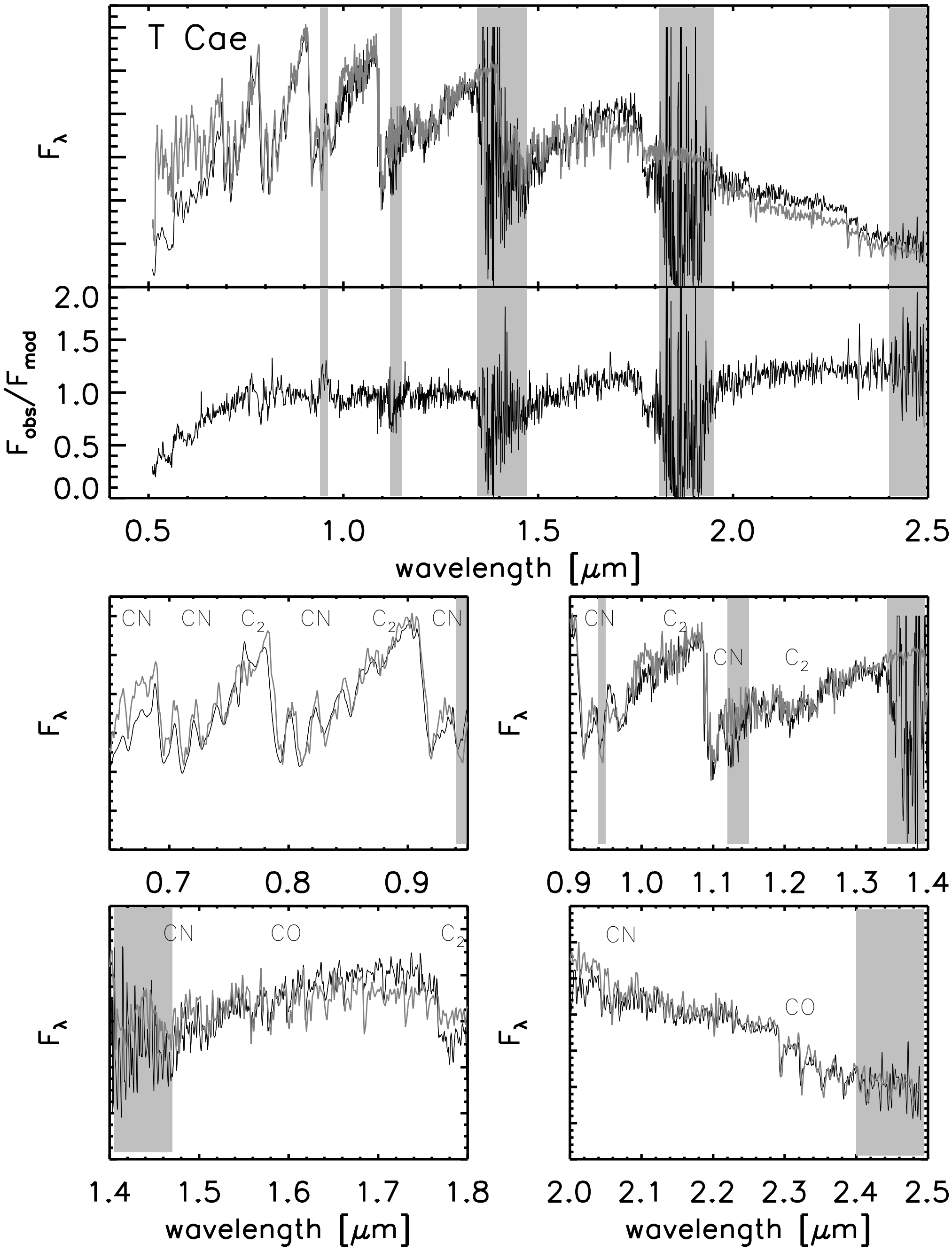

Figure 4.9: Best fit to the spectrum of T Cae. The plot layout is the same as in Fig. 4.8. The parameters of the model are: $T_{\rm eff} = 3400\,$K, $\log(g) = 0.0$, C/O = 1.05, $v_{\rm mic} = 3\,$km/s and $^{12}C/^{13}C = 3.5$.

pared to the model beyond about 1.7 μm. This could be caused either by a contribution of warm dust around the star or by dynamic effects which we are not accounting for in our hydrostatic models. The star has only a very weak 11.3 μm SiC feature, hinting that the amount of dust around the star should be small.

S Cen

S Cen is classified as a C star in the GCVS of Kholopov et al. (1988). Chan (1994) calls S Cen a "stellar blackbody source" based on its IRAS-LRS data. There is no sign of a SiC emission feature, only an excess in the 60 and 100 μm flux, hence there is no sign of warm dust around this star. The star was observed twice by Baumert (1972) in the Wing filter system. From these measurements he derived colour temperatures of 2928 and 2909 K at the date of his observations.

Figure 4.10 shows our best fit obtained with $T_{\rm eff} = 3100$ K, $\log(g) = 0.0$, C/O = 1.4 and $v_{\rm mic} = 3$ km/s when adopting $^{12}C/^{13}C = 40$. For S Cen, where no determination of the $^{12}C/^{13}C$ ratio exists, we chose a ratio of 40 because the model spectrum matched the observation best in this case. The $^{12}C/^{13}C$ ratio has not been determined by a detailed line analysis.

The overall energy distribution and the intensities of the CN bands, the CO bands and the C_2 bands at 0.77 and 1.77 μm fit very well, while the computed C_2 bands at 0.88 and 1.02 μm are stronger than observed.

RU Pup

RU Pup is classified as a C5,4 star in the GCVS of Kholopov et al. (1988). In his revised classification for C stars Keenan (1993) assigned to RU Pup the C_2 index 7. Claussen et al. (1987) looked at a sample of Galactic carbon stars taken from the $Two\ Micron\ Sky\ Survey$ to provide estimates of their space distribution and mass-loss rates. For RU Pup they derived a distance of 1.03 kpc, a mass-loss rate of $10^{-6.8}$ $M_\odot$/yr and a luminosity of 7300 $L_\odot$. The IRAS-LRS spectrum shows weak SiC emission at 11.3 μm. The star was observed four times by Baumert (1972) in the Wing filter system. From these measurements he derived colour temperatures between 2760 and 2785 K at the epochs of his observations.

S. Bagnulo (private communication) provided us with unpublished photometry from B to L from March 1997 at SAAO which is about one cycle later than our own observation of January 1996. A blackbody fit to the photometry resulted in a blackbody temperature of 2260 K and a dust temperature of 400 K (see Kerschbaum & Hron 1996 for details of the fitting). We obtain the best fit of our spectrum with an effective temperature of 2900 K. This is in good agreement with the finding of Kerschbaum & Hron (1996) that the effective temperature of semi-regular variables is usually about 500 K higher than the blackbody temperature.

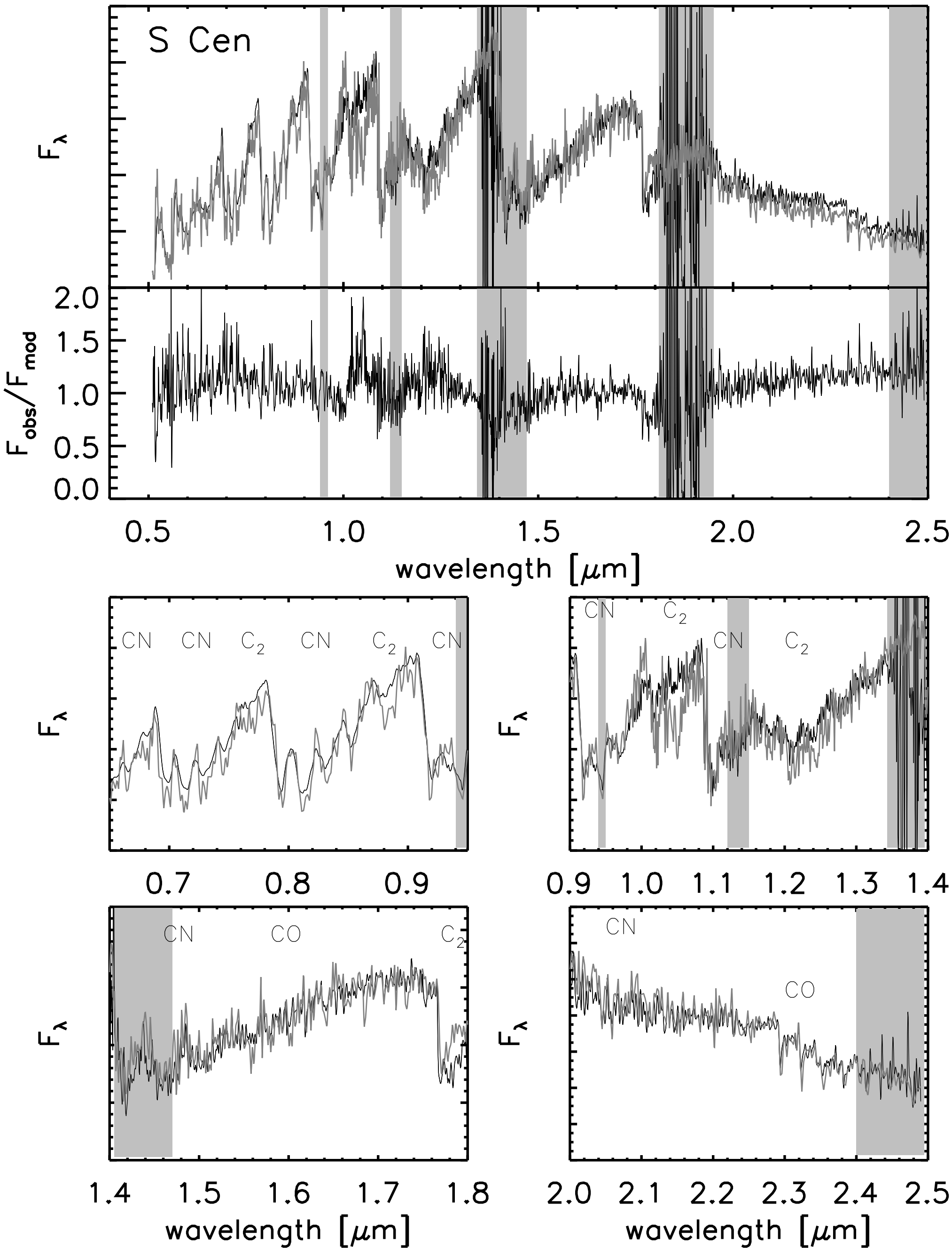

Figure 4.10: Best fit to the spectrum of S Cen. The plot layout is the same as in Fig. 4.8. The parameters of the model are: $T_{\rm eff} = 3100\,$K, $\log(g) = 0.0$, C/O = 1.40, $v_{\rm mic} = 3\,$km/s and ^{12}C/^{13}C = 40.

Tanaka et al. (1996) measured infrared indices of RU Pup two times. One of their observations was done close to ours, also in January 1996. Their colour index, which they suggest to be a good measure of the effective temperature, supports an effective temperature of the star of 2900 K at that time.

Figure 4.11 shows our best fit obtained with $T_{\mathrm{eff}} = 2900$ K, $\log(g) = -0.61$, C/O = 1.1 and $v_{\mathrm{mic}} = 3$ km/s when adopting $^{12}C/^{13}C = 89$. For RU Pup no determination of the $^{12}C/^{13}C$ ratio exists, we chose 89 because the model spectrum matched the observation best in this case. It has not been determined by a detailed line analysis. The $\log(g)$ value of -0.61 was chosen in order to match the derived luminosity of Claussen et al. (1987) when assuming $M = 1\,M_{\odot}$.

The overall energy distribution and the intensities of the CN bands and the C_2 band at 1.77 μm fit well, while the CO bands and the C_2 bands at 0.77, 0.88, 1.02 and 1.20 μm are too strong. This suggests that the adopted C/O ratio of RU Pup is slightly too high or that the metallicity (solar value adopted) is too high. As for T Cae, we remark that the observed spectrum shows a flux excess compared to the model beyond about 1.7 μm, which could be caused either by a contribution of warm dust around the star or by dynamic effects which we are not accounting for in our hydrostatic models. The presence of the SiC feature indeed suggests the existence of circumstellar dust. However, if its blackbody temperature is 400 K as indicated by the photometry, the contribution of the dust to the 2 μm flux should be small.

Y Hya

Y Hya is classified as a C5,4 (N3F) star in the GCVS of Kholopov et al. (1988). Claussen et al. (1987) derived a distance of 0.54 kpc and a luminosity of 5500 $L_{\odot}$ for Y Hya. Lambert et al. (1986) determined a C/O ratio of 1.52 and a $^{12}C/^{13}C$ ratio of 82 for this star, when an effective temperature of 2770 K was adopted. In contrast to that, Ohnaka and Tsuji (1996) have determined a $^{12}C/^{13}C$ ratio of 25 for Y Hya, based on an effective temperature determined with the infrared flux method of 3050 K. Eglitis & Eglite (1995) derive a C/O ratio of 1.46. S. Bagnulo (private communication) provided us with unpublished photometry from March 1997 at SAAO, but the data were not sufficient to determine a very reliable blackbody temperature. However, we can see that Y Hya must have a higher effective temperature than RU Pup, so the photometric data do not support the low effective temperature value adopted by Lambert et al. (1986). Tanaka et al. (1996) measured infrared indices of Y Hya three times. Their observations were done 8, 4 and 3 years, respectively, before our own observation in January 1996. Their colour index, which they suggest as a good measure of the effective temperature, lends support to effective temperatures of the star of 3100, 2600, and 2800 K at the time of their respective observations. This might indicate that Y Hya can vary

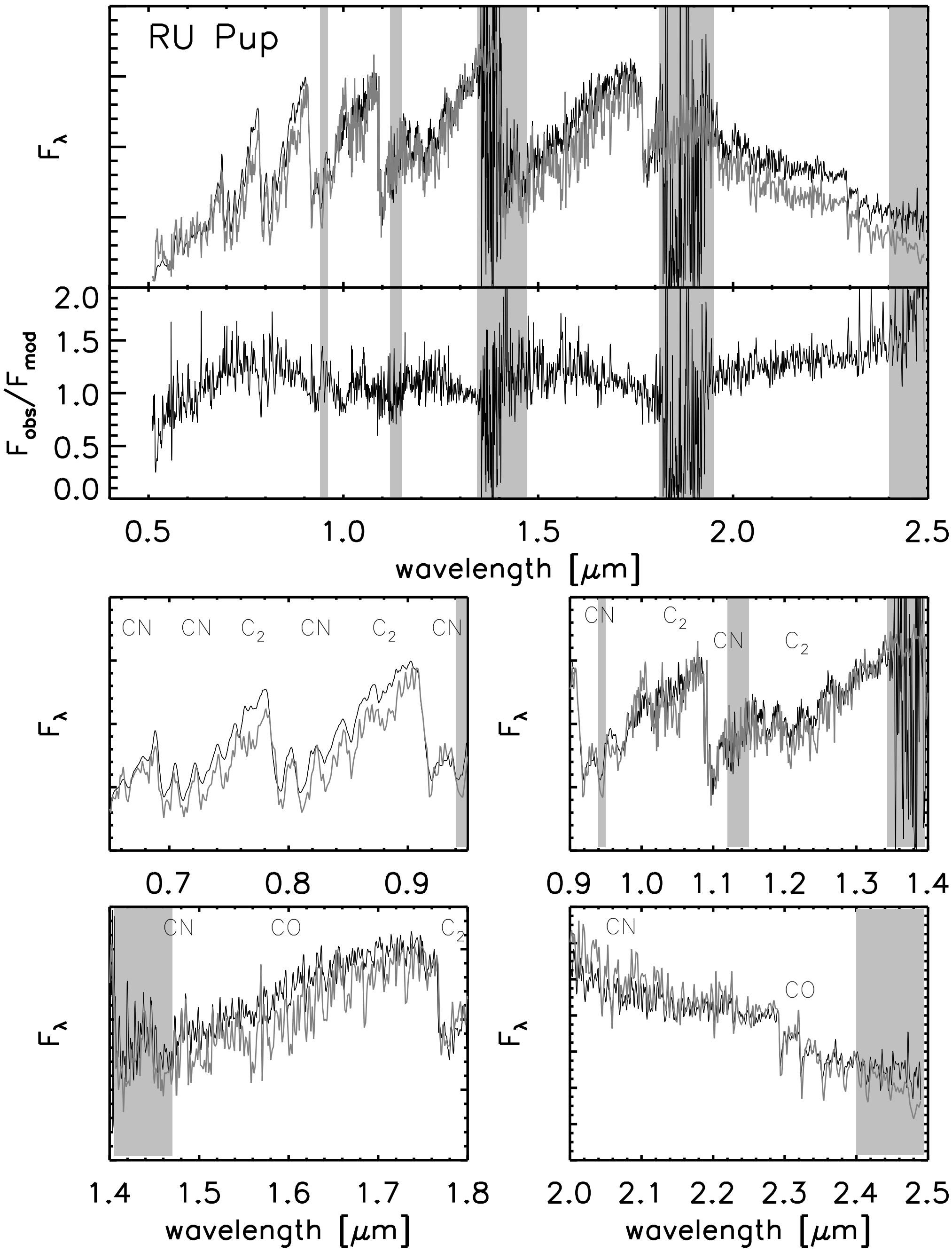

Figure 4.11: Best fit to the spectrum of RU Pup. The plot layout is the same as in Fig. 4.8. The parameters of the model are: $T_{\rm eff} = 2900\,$K, $\log(g) = -0.61$, C/O = 1.10, $v_{\rm mic} = 3\,$km/s and ^{12}C/^{13}C = 89.

remarkably, but it did not so during the time we observed it.

Figure 4.12 shows our best fit obtained with $T_{\rm eff} = 3100$ K, $\log(g) = -0.40$, C/O = 1.4 and $v_{\rm mic} = 3$ km/s when adopting ^{12}C/^{13}C = 89. For Y Hya two determinations of the ^{12}C/^{13}C ratio exist and they give remarkably different results. Lambert et. al (1986) derived a value of 82 from the CN Δv = -2 sequence around 2 μm, while Ohnaka & Tsuji (1996) determined a value of 25 using lines of the CN red system around 8000 Å, based on the iso-intensity method and line-blanketed model atmospheres. We therefore tried to find best fits for ^{12}C/^{13}C ratios of 40 and 89. We obtained a better fit with a ^{12}C/^{13}C ratio of 89. The $\log(g)$ value of -0.40 was chosen in order to match the derived luminosity of Claussen et al. (1987) when assuming $M = 1\,{\rm M}_{\odot}$.

The overall energy distribution and the intensities of the CN bands and the C_2 bands at 0.77, 0.88 and 1.77 μm fit well, while the computed C_2 bands at 1.02 and 1.20 μm are stronger than observed. As for T Cae and RU Pup, the observed spectrum shows a flux excess compared to the model beyond about 1.7 μm, with the same potential reasons.

4.2.4 Discussion

From our fits of the spectra we obtained a sequence of effective temperatures and C/O ratios of our sample stars (see Fig. 4.7). We derived an increasing C/O sequence from BH Cru, T Cae, RU Pup, Y Hya to S Cen. From its classification and the reports in the literature about the ongoing transition from a SC to a C star it was clear that BH Cru will be the star with the lowest C/O ratio in our sample. Support for the lower C/O ratio of T Cae compared to RU Pup comes from the revised classification for C stars of Keenan (1993) who assigned T Cae a smaller C_2 index (4.5) than RU Pup (7). Y Hya was already mentioned in the literature to be a star with high C/O ratio. For the effective temperatures, we found a decreasing sequence from T Cae, BH Cru/S Cen, Y Hya to RU Pup for the epoch of our observations in January 1996. However, especially BH Cru (which is a Mira) varies its effective temperature during the pulsation cycle, and although we estimate the effective temperature to have been 3200 K in January 1996, the other two spectra obtained at about phase 0.26 and 0.34 can be nicely fitted with effective temperatures of about 2800 K, ranking BH Cru cooler than RU Pup, the coolest star in our January 1996 sample. The other stars in our sample did not change much during the period we observed them. But in the case of Y Hya, there is evidence from other measurements (see Sect. 4.2.3) for changes in effective temperature which probably do not occur in a regular way. While our own determination of the effective temperature closely resembles the one of Ohnaka & Tsuji (1996), the measurement of Tanaka et al. (1996) taken in 1988, photometry provided by S. Bagnulo from 1997, and two other measurements of Tanaka et al. (1996) taken in

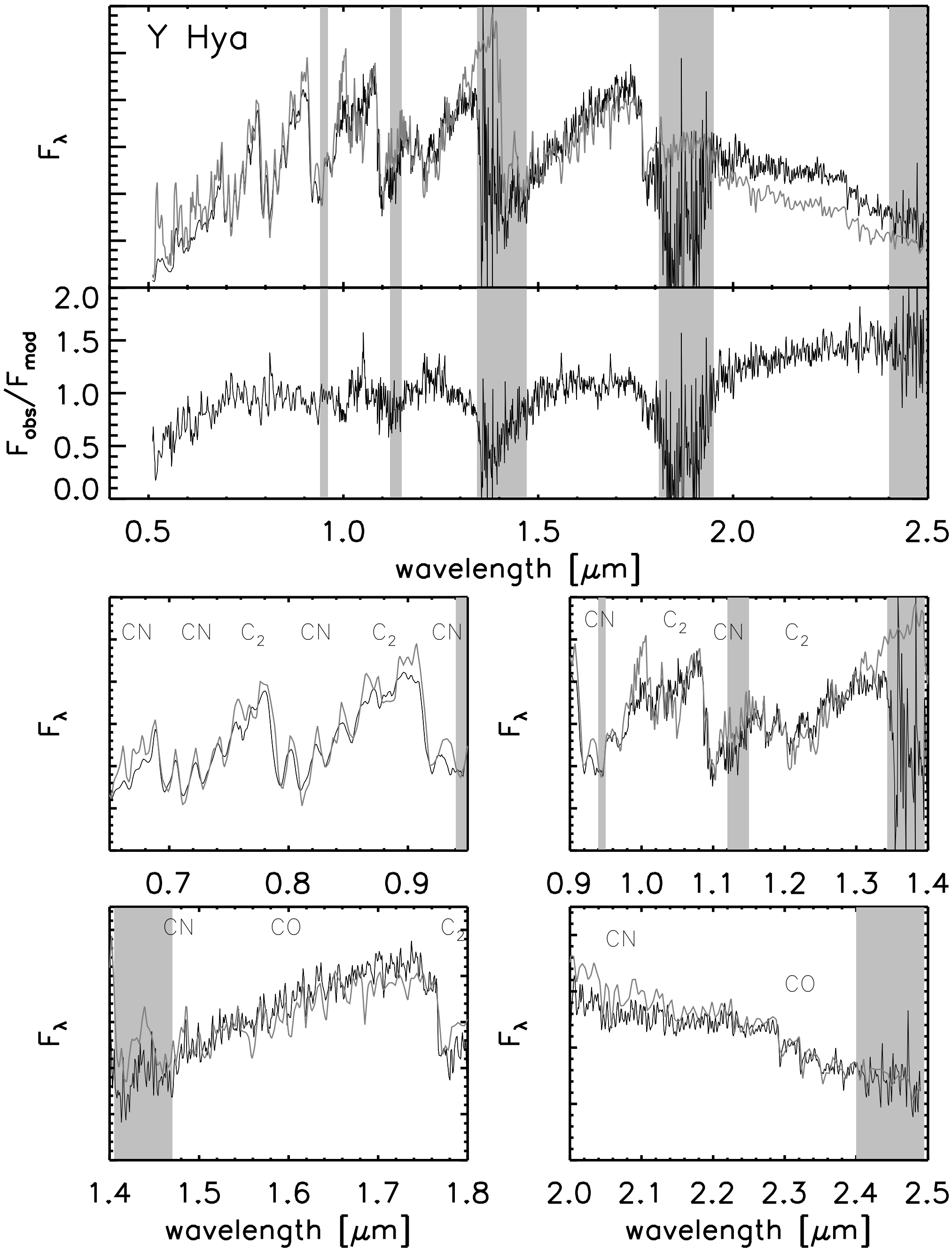

Figure 4.12: Best fit to the spectrum of Y Hya. The plot layout is the same as in Fig. 4.8. The parameters of the model are: $T_{\rm eff} = 3100\,$K, $\log(g) = -0.40$, C/O = 1.40, $v_{\rm mic} = 3\,$km/s and ^{12}C/^{13}C = 89.

1992 and 1993 support the determination of Lambert et al. (1986).

In the fit of the spectra some systematic discrepancies were encountered. The most obvious discrepancy is that the models have much more flux than the observed spectra in the wavelength range between 0.5 and approximately 0.7 μm. The discrepancy is larger the hotter the model and the lower the C/O ratio. While the fit of S Cen is quite good in the whole range (high C/O ratio, "modest" $T_{\rm eff}$), the one of T Cae is bad shortwards of 0.7 μm (low C/O ratio, "high" $T_{\rm eff}$). This hints at the fact that these discrepancies are mainly due to the lack of the inclusion of the atomic lines in our calculations.

The second discrepancy is the "flux excess" of the observations longwards of approximately 1.7 μm compared to the models which is very pronounced in RU Pup and especially in Y Hya, and which is small, but still present, in BH Cru, T Cae, and S Cen. The discrepancy seems to become worse, the cooler the star and the higher the C/O and $^{12}C/^{13}C$ ratio is. We think that the reason for this disagreement is either due to the contribution of dust surrounding the star or to dynamic effects which we can not account for in hydrostatic models.

The third discrepancy occuring in all spectra is at 1.78 to 1.79 μm. In our synthetic spectra this wavelength region is dominated by the fundamental C_2 Ballik-Ramsay band. The bandhead at 1.77 μm can be fitted, but not the region beyond. In all observed spectra, the feature at 1.78 μm is stronger than the C_2 bandhead. We are lacking some opacity at this wavelength.

There is also some discrepancy visible longwards of about 2.40 μm in all spectra, but this is due to noise (and therefore this region was superposed by a shaded area too).

In general we have problems with fitting all C_2 bands with one C/O ratio. This problem should be solved in the near future if better opacity data are available.

4.2.5 Conclusions

For the first time we were able to fit spectra of carbon stars in the huge wavelength region, all the way from 0.5 to 2.5 μm, based on spectra taken simultaneously and therefore at the same pulsational phase. On the observational side this became possible due to the unique possibility of taking spectra of the stars simultaneousily in several spectral regions. On the theoretical side, this is mainly due to the drastic improvement of available molecular opacitites. The stars chosen for the comparison with spectra based on hydrostatic model atmospheres are (with one exception – BH Cru, which is a Mira star) so called semi-regular variables which vary only moderately during their pulsational cycle. We restricted ourselves to analyse in detail only the spectra taken in January 1996, because it is not possible to model the variations in the spectra self-consistently with hydrostatic models.

Table 4.4 summarizes the results of our fits to the spectra of January 1996, giving the effective temperature, $\log(g)$, C/O ratio, $^{12}C/^{13}C$ ratio and in addition the changes in effective temperature $\Delta T_{\rm eff}$ that were needed to get also good fits for the spectra of the stars taken at other phases (if all parameters other than $T_{\rm eff}$ are kept constant).

Table 4.4: Results of our fits

name	$T_{\rm eff}$ [K]	$\log(g)$	C/O	$^{12}C/^{13}C$	$\Delta T_{\rm eff}$ [K]
BH Cru	3200	0.00	1.01	3.5	≈ 400
T Cae	3400	0.00	1.05	3.5	≈ 200
S Cen	3100	0.00	1.40	40	≈ 100
RU Pup	2900	-0.61	1.10	89	≈ 100
Y Hya	3100	-0.40	1.40	89	≈ 200

The determinations of the fundamental parameters are in good agreement with results from other methods published in the literature. In the case of Y Hya, there is evidence from some other measurements for changes in effective temperature which probably do not occur regularly.

A major advantage of the analysis of low resolution spectra over a wide spectral range, as presented here, is that all the fundamental parameters can be determined simultaneously. In studies of high resolution spectra, it will often be necessary to adopt photometric determinations of $T_{\rm eff}$ that are not necessarily determined at the same pulsation phase as the spectrum. No general high-resolution method is known for determining $\log(g)$ in cool giant stars. The value of the $^{12}C/^{13}C$ ratio can be determined with better accuracy from high-resolution spectra, while we believe that the accuracy in the C/O determination has the same reliability in the two methods. An additional advantage of the low-resolution method is that it can be applied to stars in remote galaxies too.

Our analysis has shown that the state-of-the-art of carbon star observations and modelling now, for the first time, has reached a level where a complete and self-consistent agreement between observational and computed low-resolution spectra is possible across basically the whole photospheric spectral region. Combined with our previous analysis of ISO spectra (Jørgensen et al. 2000) of similar carbon stars, using the same models as presented here, we conclude that the agreement between synthetic and observed spectra is good for the full wavelength region from at least 5000 Å to 10 μm, and that all major spectral features can be accounted for.

4.3 Bessell colours

For a detailed discussion of broad-band colours of our models we chose the filter system that was defined by Bessell & Brett (1988) for the following reasons: Their filter system, which we will call "Bessell filters" for brevity, includes filters from V to M, and in their paper (Bessell & Brett 1988) they provide the necessary correlations for a transformation from one system into the other. Figure 4.13 shows a synthetic spectrum on top of which the Bessell filter curves are plotted. Synthetic colours have also been calculated for the ESO and the SAAO system. However, the dependence and trend of the colours as a function of the effective temperature of the models are the same for all these filter systems; only the absolute values of the colours differ. Therefore, we will not discuss ESO and SAAO colours separately. We use data obtained in the SAAO filter system by Whitelock et al. (1997) and by Catchpole et al. (1979) for a comparison with our synthetic SAAO colours. Figure 4.14 shows $J_{\mathrm{Bessell}}-J_{\mathrm{SAAO}}$, $H_{\mathrm{Bessell}}-H_{\mathrm{SAAO}}$, $K_{\mathrm{Bessell}}-K_{\mathrm{SAAO}}$, and $L_{\mathrm{Bessell}}-L_{\mathrm{SAAO}}$ to illustrate the differences of the various filters with temperature from one filter system to another.

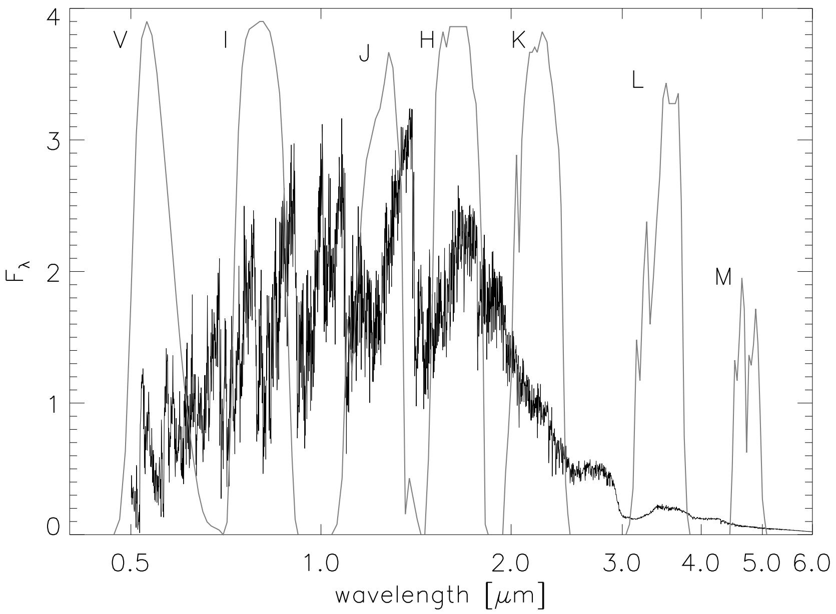

Figure 4.13: Synthetic spectrum on top of the Bessell filter curves.

4.3.1 Theoretical results

Figure 4.15 shows the Bessell colours versus effective temperature for all hydrostatic models with C/O = 1.10. Black diamonds denote plane parallel models with

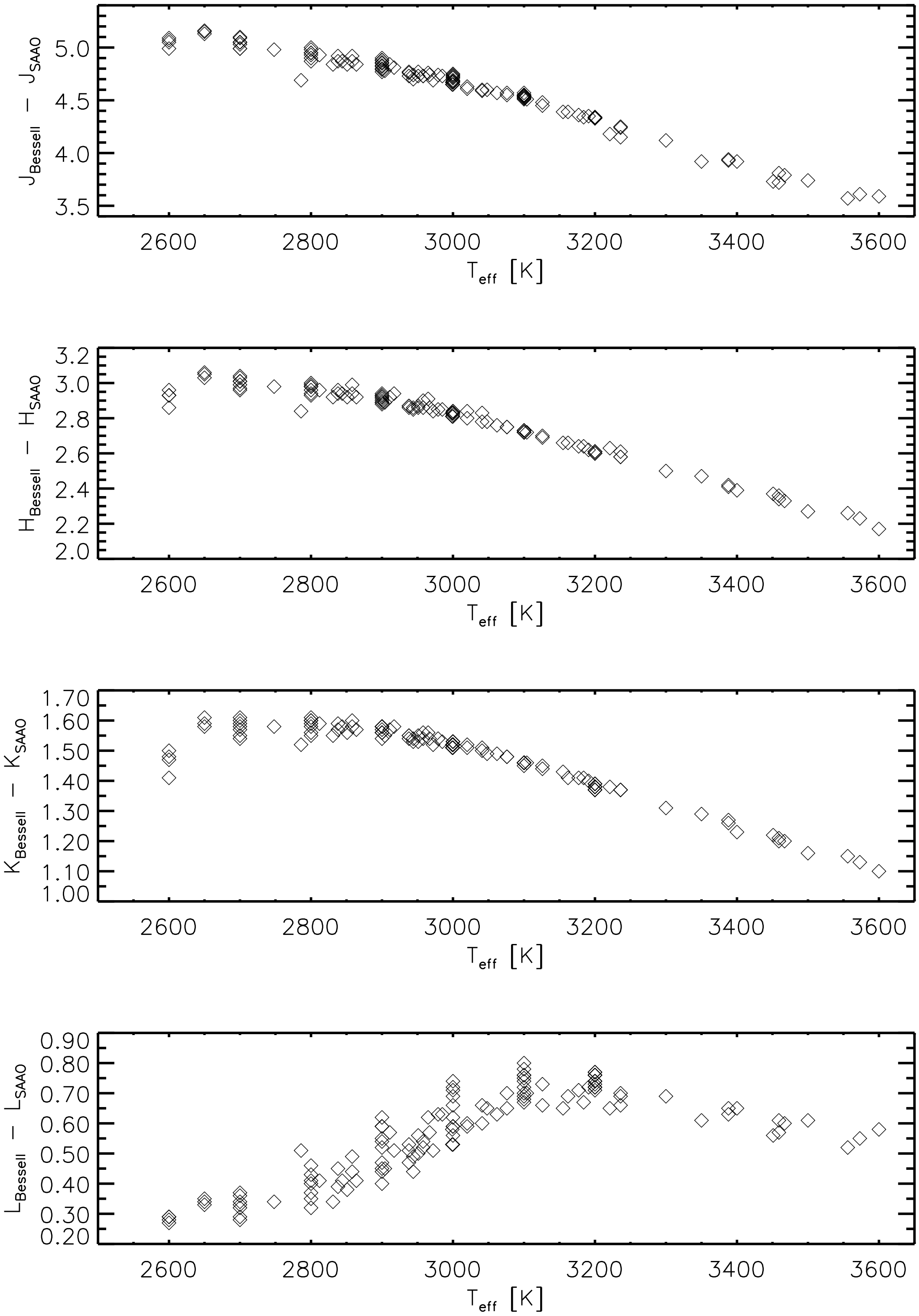

Figure 4.14: $J_{\mathrm{Bessell}}-J_{\mathrm{SAAO}}$, $H_{\mathrm{Bessell}}-H_{\mathrm{SAAO}}$, $K_{\mathrm{Bessell}}-K_{\mathrm{SAAO}}$, and $L_{\mathrm{Bessell}}-L_{\mathrm{SAAO}}$ plotted versus effective temperature of plane parallel hydrostatic models.

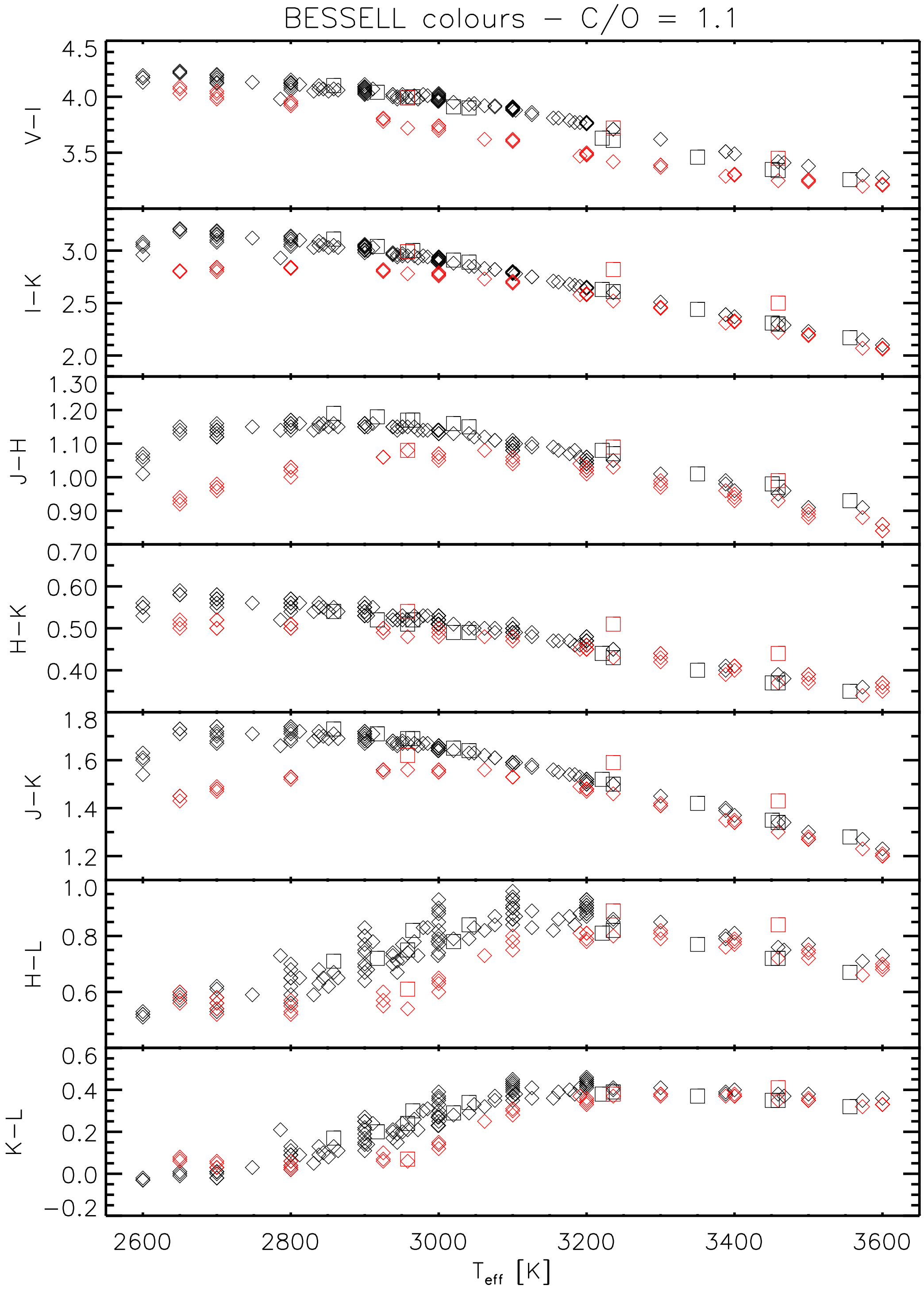

Figure 4.15: Colour indices versus effective temperature for the models with C/O = 1.10. Black diamonds denote plane parallel models with $\log(Z/Z_\odot) = 0.0$, black squares plane parallel models with $\log(Z/Z_\odot) = -0.3$, red diamonds spherical models with $\log(Z/Z_\odot) = 0.0$, and red squares spherical models with $\log(Z/Z_\odot) = -0.3$.

$\log(Z/Z_{\odot}) = 0.0$, black squares plane parallel models with $\log(Z/Z_{\odot}) = -0.3$, red diamonds spherical models with $\log(Z/Z_{\odot}) = 0.0$, and red squares spherical models with $\log(Z/Z_{\odot}) = -0.3$. Plane parallel and spherical models show the same trends. Depending on the colour index, the indices of the models with lower metallicity (squares) deviate moderately from those calculated with solar metallicity. In the spherical spectra, the effect is more pronounced than in the plane parallel ones. The V−I index proves to be a very useful measure of the effective temperature across the whole range of investigated temperatures: Lower effective temperatures cause higher V−I colours. Almost equally suited for the determination of the effective temperature are the I−K and H−K colours. However, V−I will be very much influenced by possible dust extinction in a real star. The rest of the investigated colours, namely J−H, J−K, H−L, and K−L do not show such a unique dependence on the effective temperature. The maximum of the energy distribution moves to longer wavelengths with cooler effective temperatures. For stars with high effective temperatures the maximum of the energy distribution lies shortwards of the J filter; J, H and K measure the flux at the Rayleigh-Jeans tail of the energy distribution. Below a certain effective temperature the maximum lies longwards of the J filter; then J measures the flux shortwards of the maximum, H and K the flux longwards of the maximum. At this point the trend inverses.

The effect of $\log(g)$ on the colour indices is very small; the same applies to the effects of the mass and the C/O ratio. Figure 4.16 illustrates the influence of different masses and metallicity (upper four panels), and of the C/O ratio (lower four panels). In the upper four panels, four two-colour plots are shown. Black diamonds denote models with $1\,M_{\odot}$ and $\log(Z/Z_{\odot}) = 0.0$, red diamonds are models with $5\,M_{\odot}$ and $\log(Z/Z_{\odot}) = 0.0$, green diamonds models with $2.25\,M_{\odot}$ and $\log(Z/Z_{\odot}) = 0.0$, blue diamonds models with $1.5\,M_{\odot}$ and $\log(Z/Z_{\odot}) = 0.0$, green squares models with $2.25\,M_{\odot}$ and $\log(Z/Z_{\odot}) = -0.3$, and black squares models with $1\,M_{\odot}$ and $\log(Z/Z_{\odot}) = -0.3$. No systematic dependence on the mass is obvious. For models with different C/O ratios, a model with a higher C/O ratio has in the mean a slightly smaller J−H, V−I, and a higher H−K, H−L, J−K, and K−L colour. We want to stress again that the same applies for the ESO and SAAO colours; in these cases only the absolute values are different, the dependencies are similar.

In Fig. 4.17, similar four two-colour plots are shown for our dynamical models. A comparison with the results of the hydrostatic spectra yields the following results:

- The colours of model L52C11U2RO occupy basically the same regions in the two-colour diagrams as the hydrostatic models. This is as expected because no dust formation takes place and no stellar outflow develops in this model. Therefore, in this dynamical model we see the pure photosphere and this

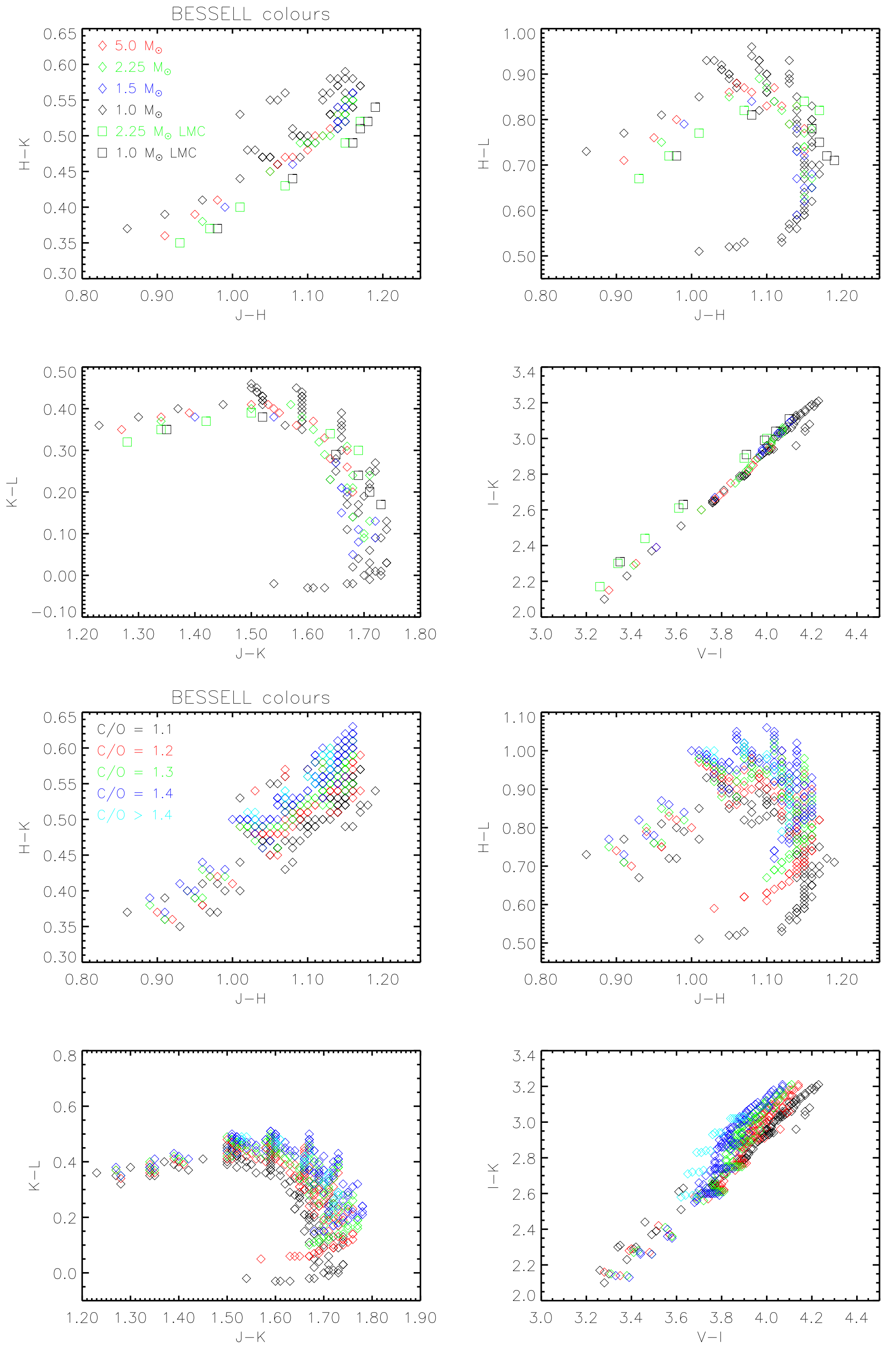

Figure 4.16: Two-colour plots for plane parallel models with different masses and metallicities (upper four panels), and with different C/O ratios (lower four panels).

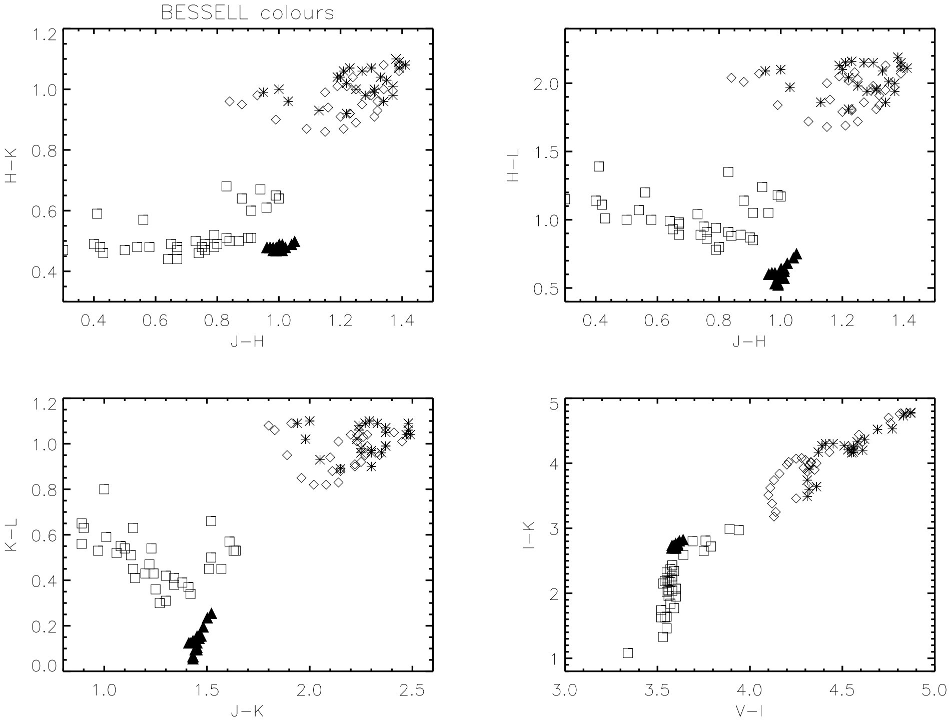

Figure 4.17: Two-colour plots for the dynamical models. Filled triangles denote phases of model L52C11U2RO, asterisks phases of model L7TC14U5RO, diamonds phases of model L7C14U6RO, and squares phases of model L7C18U4RO.

should be equivalent to a classical hydrostatic model.

- The three dynamical models with larger piston velocities span a much larger range in all investigated colours than the hydrostatic models.

- The J−H and I−K indices of models L7TC14U5RO, L7C14U6RO, and L7C18U4RO are either smaller or larger than the ones of the hydrostatic models. This is due to the low "effective" temperatures of the dynamical models and due to the contribution of the dust to the spectra; the higher the amount of dust around the star is, the further is the maximum of the energy distribution shifted to longer wavelengths. The same applies for the J−K colours.

- The V−I, H−K, H−L, and K−L colours of models L7TC14U5RO, L7C14U6RO, and L7C18U4RO are redder than the ones of the hydrostatic models. This is consistent with dust contributing to the flux in the K and L filter and hence reddening the colours.

4.3.2 Comparison of theoretical with observational results

For a comparison with the theoretical results we chose observations of carbon-rich Miras and SRa's from Whitelock et al. (1997) and of SRb's and Lb's from Catchpole et al (1979) in the SAAO filter system. We selected 7 stars from the sample of Whitelock et al. (1997), which were R Scl, GM CMa (which both seem to have detached shells; see Whitelock et al. 1997), TT Cen, V Cru (both have very thin dust shells), R For, R Lep, and R Vol (stars with moderately thick dust shells). In Fig. 4.18 H−K is plotted versus J−H for the observations and the models; grey circles denote observations of R Scl, grey "+" stand for R For, grey asterisks for R Lep, grey diamonds for TT Cen, grey triangles for R Vol, grey squares for V Cru, and grey crosses for GM CMa. The small grey diamonds show the locations of the carbon-rich stars from the samle of Catchpole et al. (1979). Coloured diamonds denotate hydrostatic models, coloured squares dynamic models. A closer inspection shows that an overlap region exists between the loci of the observations and the models. Moderately variable stars surrounded by small amounts of dust can be explained by our set of hydrostatic and dynamical models. However, there exists barely an overlap between the regions occupied by the Miras and SRa's and the loci predicted by our models. Our models can only reproduce a small region of the absolute J−H and H−K values of dust enshrouded stars. However, the dynamical models presented here were designed to be representative for R Scl, hence none of our models posesses a mass loss rate (and as a consequence enough dust) which is high enough to explain stars like R Lep.

Figure 4.19 shows a comparison of the J (circles), H (diamonds), K (triangles), and L (squares) light curves of R Scl observed by Whitelock et al. (1997) versus phase (upper left panel) as well as the J, H, K, and L light curves versus phase of models L7C14U6RO (upper right panel), L7TC14U5RO (lower left panel), and of model L7C18U4RO (lower right panel). Phase 0.0 in the observations was chosen at visual maximum light. We can see that models L7C14U6RO and L7TC14U5RO describe the *absolute* values of J, H, K, and L quite well (in the models J, H, K, and L have all been shifted by the same constant value in order to match approximately the observed J values at phase 0.0), while model L7C18U4RO fails. The amount of dust which forms in model L7C18U4RO is too low. A closer inspection shows that model L7TC14U5RO describes the amount of variation in the various colours better than model L7C14U6RO. However, one can also see that our models predict the minima in the colours at other phases than what is observed. The observed minimum in J in R Scl occurs around phase 0.35, while in our models it is predicted around phase 0.55. The observations of R Scl seem to indicate that the minima in the colours shift to earlier phases from J to at least K, for L it is practically impossible to give a minimum phase. In our models the minima of the colours also shift to earlier phases from J to K. The mismatch of the minima

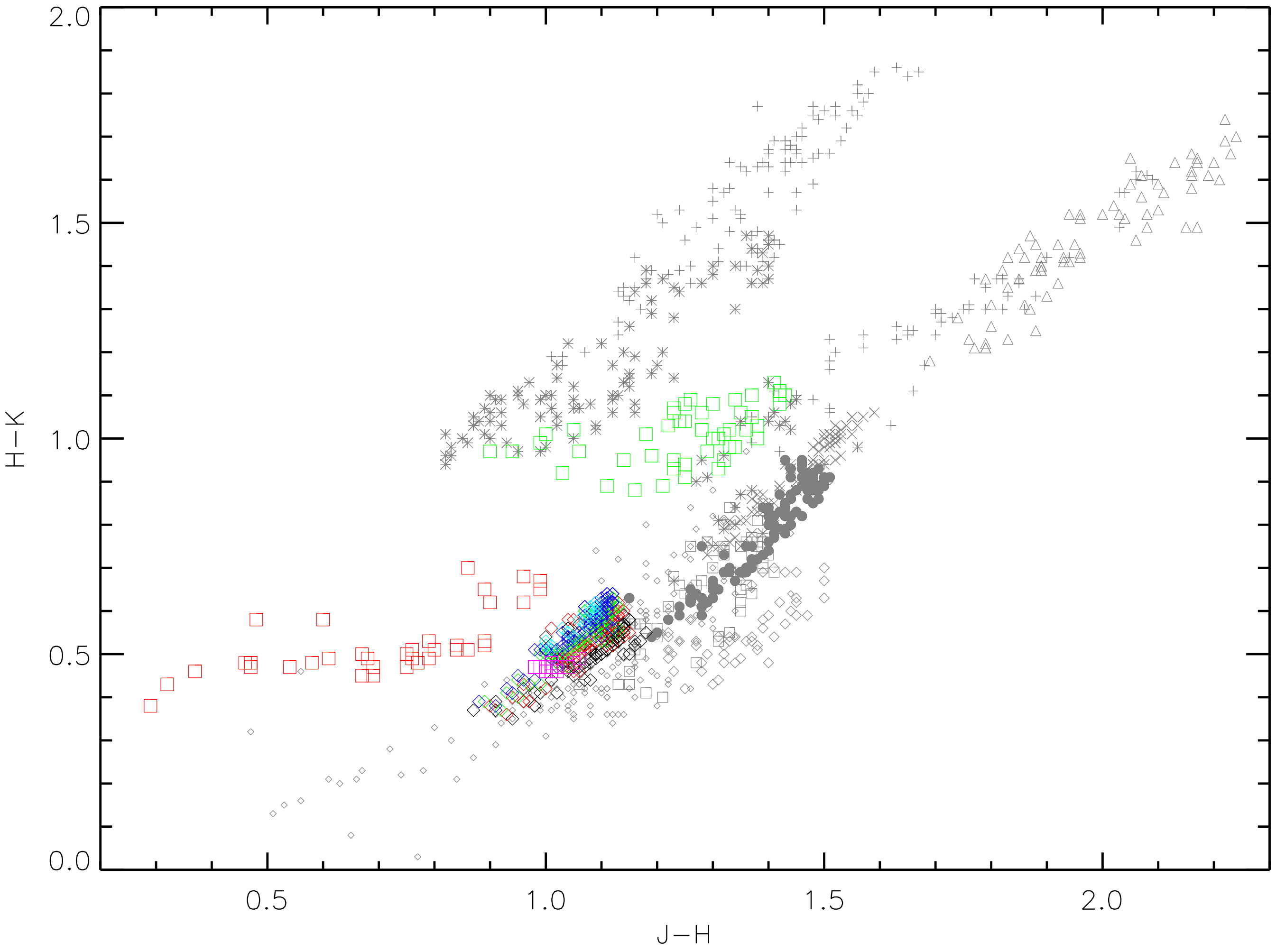

Figure 4.18: H−K versus J−H for the observations and the models; grey circles denote observations of R Scl, grey "+" stand for R For, grey asterisks for R Lep, grey diamonds for TT Cen, grey triangles for R Vol, grey squares for V Cru, and grey crosses for GM CMa. The small grey diamonds show the locations of the carbon-rich stars from the samle of Catchpole et al. (1979). Coloured diamonds denotate hydrostatic models and coloured squares dynamic models.

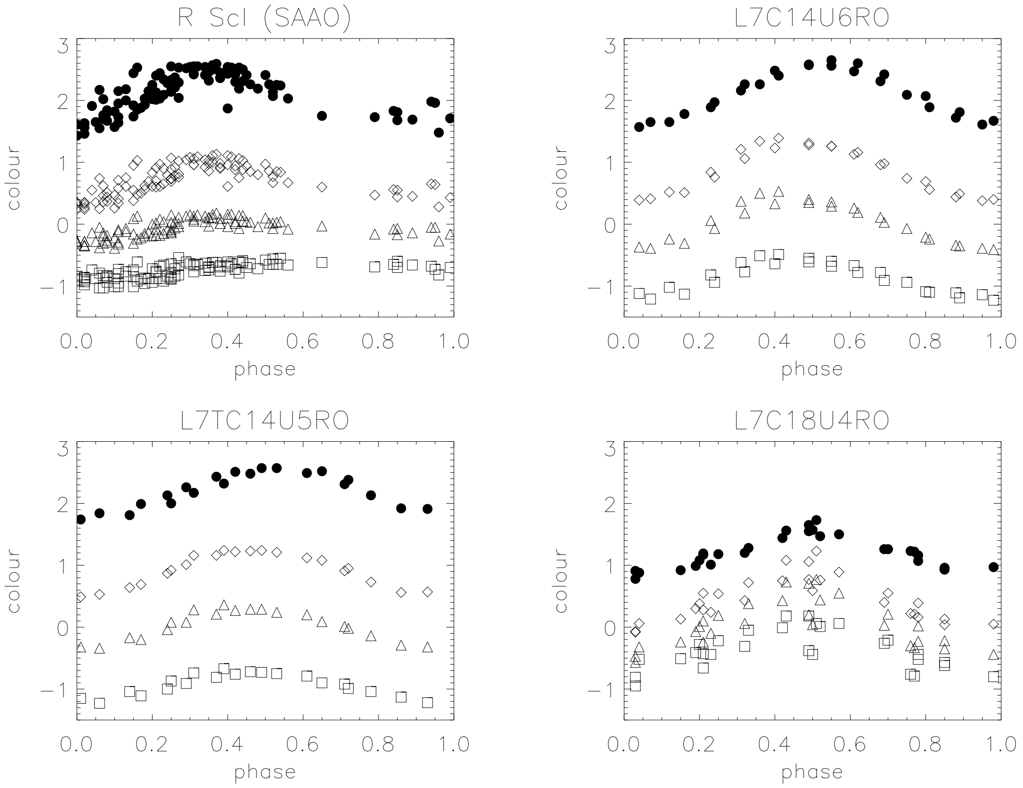

Figure 4.19: J (circles), H (diamonds), K (triangles), and L (squares) light curves of R Scl versus phase (upper left panel) as well as the J, H, K, and L light curves versus phase of models L7C14U6RO (upper right panel), L7TC14U5RO (lower left panel), and of model L7C18U4RO (lower right panel). In the models J, H, K, and L have all been shifted by the same constant value in order to match approximately the observed J values at phase 0.0.

phases between observations and models is probably due to the fact that our dynamical models are not constructed based on consistent pulsational models, thus we currently assume that phase 0.0 occurs at maximum luminosity. As long as we have this "arbitrary" inner boundary condition the resulting phases have to be regarded with caution.

4.3.3 Conclusions

We discussed the dependence of various broad-band colours in the optical and infrared range on the effective temperature. The V−I, I−K, and H−K indices proved to be useful measures of the effective temperature across the whole investigated range ($2600 \leq T_{\rm eff} \leq 3600\,$K). Other colours are less useful for a determination of the effective temperature. The loci of moderately variable stars surrounded by small amounts of dust can be explained by our set of hydrostatic and dynamical models. Due to the lack of dynamical models with high mass loss rates at present, our dynamical models are not able to reproduce the whole observed values of J−H and H−K colours of dust enshrouded Miras and SRa variables. Models designed for R Scl are able to describe the J, H, K, and L light curves as well as the corresponding colours very well.

4.4 DENIS measurements

4.4.1 Observations

The **De**ep **Ne**ar **I**nfrared **S**urvey of the Southern Sky (DENIS) was the first attempt to carry out a complete survey of the southern sky in three near-infrared photometric bands (I, J and K_S). The spatial resolution is 3″ in J and K_S, and 1.5″ in I. Table 4.5 summarises the most important characteristics of the DENIS photometry channels. The survey is undertaken with a dedicated IR camera, installed at the ESO 1 m telescope on La Silla in Chile. The survey started in December 1995 and is close to completion. The limiting magnitude for point sources in I, J and K_S are 18^m, 16^m and 13.5^m, respectively. Specific calibration nights are dedicated for the determination of the global extinction coefficient, the zero points, and the colour terms. More detailed descriptions of the DENIS survey can be found in e.g. Fouqué et al. (2000).

Table 4.5: Characteristics of the DENIS channels

Channel	I	J	K_S
Central wavelength (μm)	0.80	1.25	2.15
Number of pixels	1024x1024	256x256	256x256
Pixel size (arcsec)	1	3	1
Limiting magnitude ($5\,\sigma$)	18.0	16.0	13.5

DENIS is very sensitive to low-temperature stellar photospheres and to objects surrounded by warm dust envelopes. Therefore, DENIS is particulary suited for studying stars with strong mass loss on the AGB, low-mass stars, brown dwarfs, young stellar objects, and active galactic nuclei.

For the comparison with our models, we used DENIS data of carbon-rich stars in the Large Magellanic Cloud that have been kindly provided by M. Schultheis (private communication).

4.4.2 Models

The observations are compared with our set of hydrostatic plane parallel and spherical models, calculated with the MARCS code, as well as with dynamical models. We used α Tau as zero point.

Theoretical results

Figure 4.20 shows I$-$J (upper panel) and J$-$K indices (lower panel) versus effective temperature for the hydrostatic models with C/O = 1.10. Black diamonds

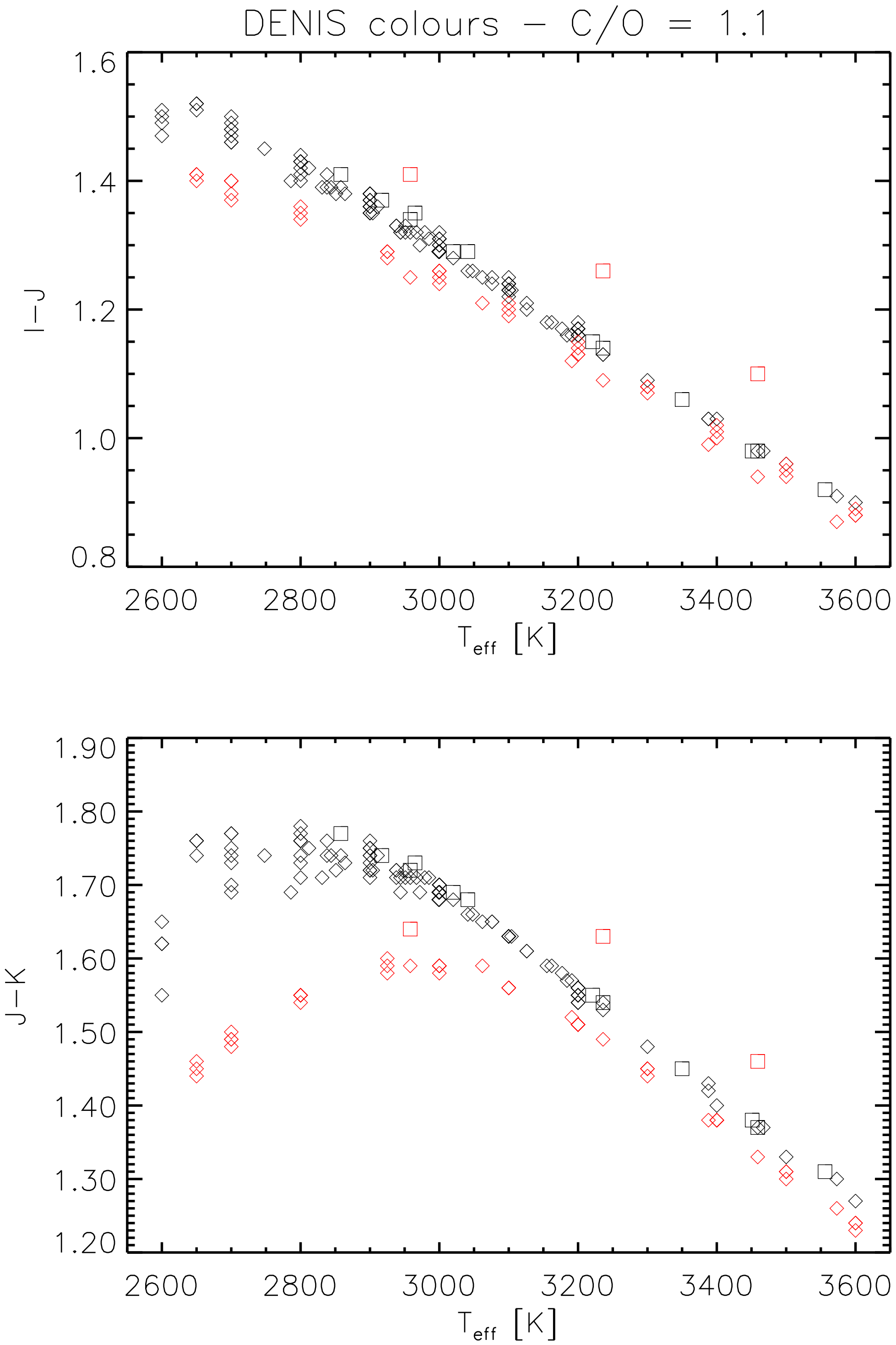

Figure 4.20: I–J (upper panel) and J–K colour indices (lower panel) versus effective temperature for the hydrostatic models with C/O = 1.10. Black diamonds denote plane parallel models with $\log(Z/Z_\odot) = 0.0$, black squares plane parallel models with $\log(Z/Z_\odot) = -0.3$, red diamonds spherical models with $\log(Z/Z_\odot) = 0.0$, and red squares spherical models with $\log(Z/Z_\odot) = -0.3$.

denote plane parallel models with $\log(Z/\mathrm{Z}_\odot) = 0.0$, black squares plane parallel models with $\log(Z/\mathrm{Z}_\odot) = -0.3$, red diamonds spherical models with $\log(Z/\mathrm{Z}_\odot) = 0.0$, and red squares spherical models with $\log(Z/\mathrm{Z}_\odot) = -0.3$. The I$-$J index is an excellent measure of effective temperature across the whole range of our investigation, a lower effective temperature induces a higher I$-$J colour. The influences of $\log(g)$, mass, and C/O ratio on this index are very small. Models with lower metallicity show redder I$-$J colours than corresponding models calculated with solar metallicity; the effect is much more pronounced in spherical models than in hydrostatic ones. The J$-$K colour is less useful to measure the effective temperature than the I$-$K index. Down to temperatures of about 2900 (in the plane parallel case) or 3000 K (in the spherical case), a lower effective temperature leads to higher J$-$K colours. For even lower temperatures the trend reverses. The maximum of the energy distribution moves to longer wavelengths with cooler effective temperatures. For stars with high effective temperatures the maximum of the energy distribution lies shortwards of the J filter; J, H and K measure the flux at the Rayleigh-Jeans tail of the energy distribution. Below a certain effective temperature the maximum lies longwards of the J filter; then J measures the flux shortwards of the maximum, H and K the flux longwards of the maximum. As for the I$-$K colour, the influences of $\log(g)$, mass, and C/O ratio on the J$-$K colour are small.

4.4.3 Comparison of theoretical with observational results

In Fig. 4.21, we show a comparison of observed and theoretical colours. The grey circles show the carbon-rich stars in the LMC. Black, red, green, blue, and turquoise diamonds denote hydrostatic models with C/O ratios of 1.1, 1.2, 1.3, 1.4 and > 1.4, respectively. Magenta (C/O = 1.1), red (C/O = 1.8) and green (C/O = 1.4) squares mark the colours of the dynamical models L52C11U2RO, L7C18U4RO, L7C14U6RO and L7TC14U5RO. We see that our hydrostatic and dynamic model colours lie in the correct regions of the two-colour diagrams. The dynamical models are able to reproduce almost the complete range in which the observations are situated in I$-$J, J$-$K and I$-$K. The larger spread of the relations between the colours in the observations is probably due to different mass loss rates and hence amounts of dust present around the stars.

4.4.4 Conclusions

Hydrostatic and dynamic models are able to globally reproduce the observed I$-$J, J$-$K, and I$-$K colours of carbon-rich stars in the LMC. The complete ranges in I$-$J, J$-$K and I$-$K in which the observations are situated can be covered by a combination of hydrostatic and dynamic models.

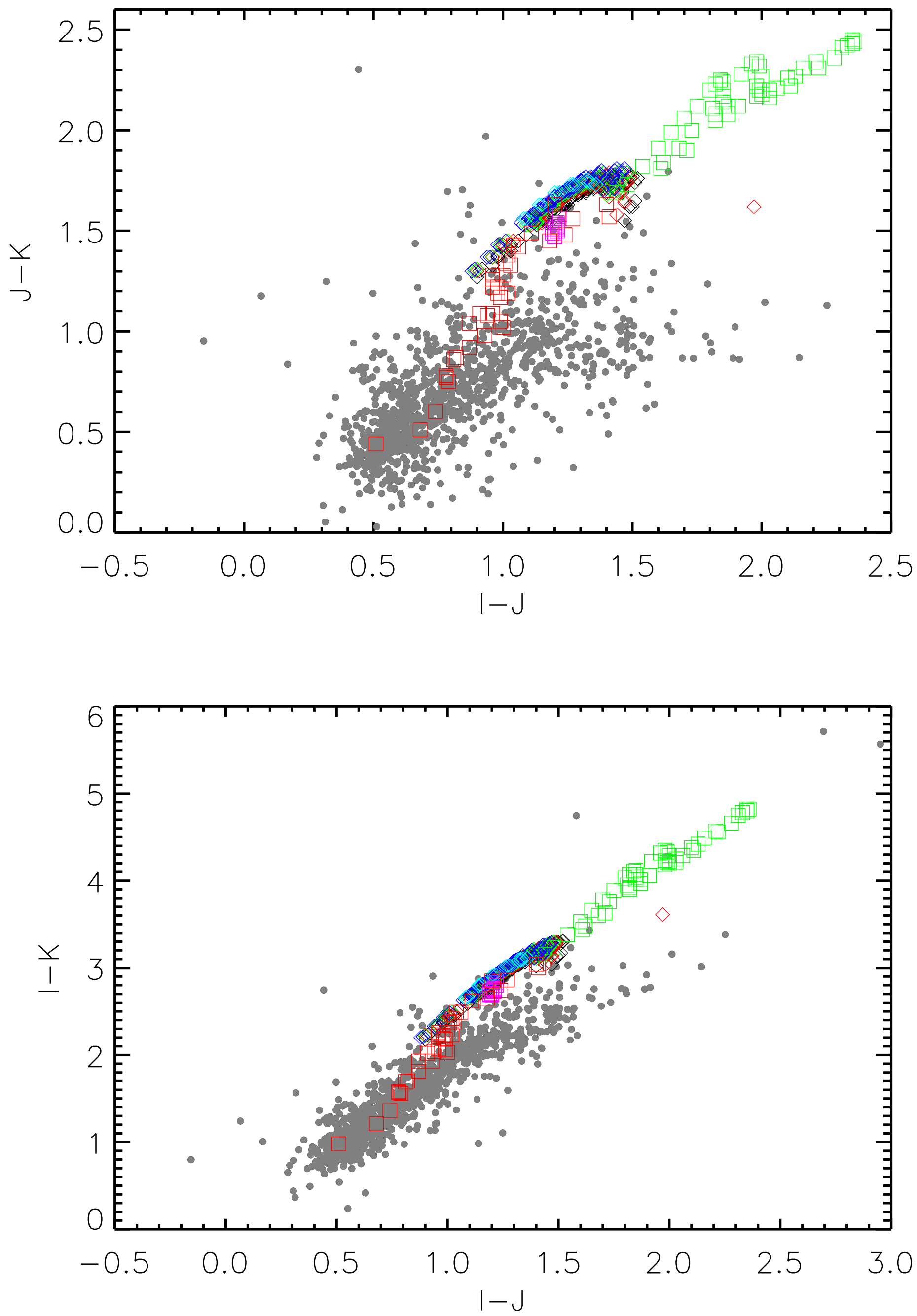

Figure 4.21: Comparison of observed and theoretical colours. The grey circles show the carbon-rich stars in the LMC. Black, red, green, blue and turquoise diamonds denote hydrostatic models with C/O ratios of 1.1, 1.2, 1.3, 1.4 and >1.4, respectively. Magenta (C/O = 1.1), red (C/O = 1.8) and green (C/O = 1.4) squares mark the colours of the dynamical models L52C11U2RO, L7C18U4RO, L7C14U6RO and L7TC14U5RO.

4.5 Lázaro indices

4.5.1 Observations

Lázaro et al. (1994) observed 15 bright carbon stars during two campaigns in 1983 and 1985. Both times, the Imperial College cooled grating spectrometer (CGS1), mounted at the Cassegrain focus of the 1.5 m Carlos Sanchez Telescope (TCS) of the Observatorio del Teide in Tenerife was used. The observations were made by driving the grating at a constant speed across the various wavelengths of interest (1.0−1.40 μm, 1.50−1.90 μm, 1.90−2.45 μm and/or 2.9−4.20 μm). The spectra have a resolution of about 500, the authors estimated the uncertainty in the fluxes to be lower than 7 %. Some of the sample stars were observed twice, nevertheless the sample is small. Lázaro et al. (1994) defined the following four indices:

- $[1.36] = -\log(F_{1.360}/F_{1.338})$ for Lázaro observations
  $[1.36] = -\log(F_{1.407}/F_{1.383})$ for models and other observational data
  This index measures the (0−1) band of the red system of CN and the (1−0) band of the Ballik-Ramsay system of C_2. The different definitions are necessary because the wavelength calibration in Lázaro et al. (1994) for this region seemingly did not work properly. We tried therefore to define an index comparable to theirs. Figure 4.22 illustrates the problem.

- $[1.78] = -\log(F_{1.777}/F_{1.725})$
  This index measures the Ballik-Ramsay (0−0) band head of C_2.

- $[2.29] = -\log(F_{2.294}/F_{2.283})$
  This index measures the vibration-rotation (2−0) band of CO.

- $[3.1] = -\log(F_{3.07}/F_{\mathrm{cont},3.07})$
  This index measures HCN and C_2H_2. The continuum flux is calculated from a linear fit to the wavelength interval between 2.9 and 3.4 μm.

4.5.2 Results

The original spectra were kindly provided by Carlos Lázaro. For this investigation, the indices given in the paper of Lázaro et al. (1994) were not used for the comparison with the models. Instead, the indices were calculated in exactely the same way as it is done for the model spectra. This is particularly important for the [3.1] index where the continuum flux is involved in the calculation of the index. Therefore, the indices which we calculated for the observed spectra can differ from the ones given in the paper (Lázaro et al. 1994). Additionally, we calculated the indices for spectra provided by Ariane Lançon (Lançon &

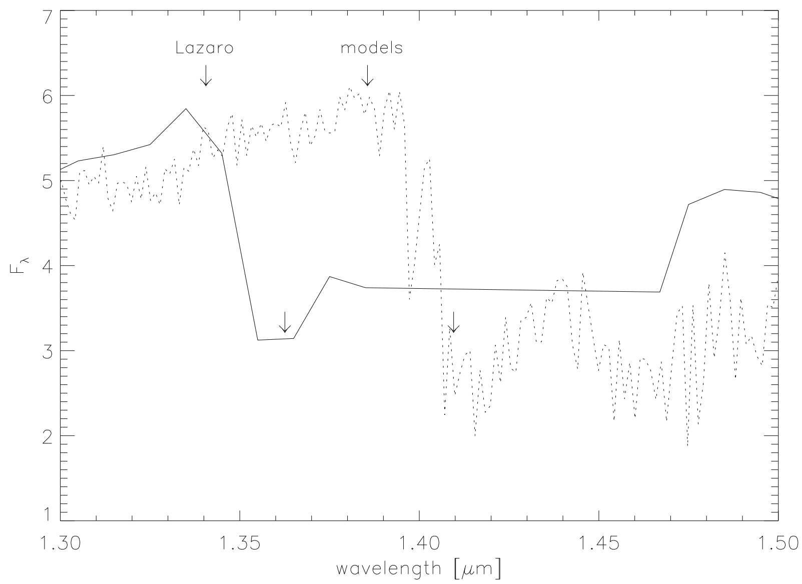

Figure 4.22: The wavelength calibration problem.

Wood 2000; $\lambda/\Delta\lambda \approx 1000$) and by Dick Joyce (Joyce 1998; $\lambda/\Delta\lambda \approx 200$). However, when combining data of different observational sets one has to keep in mind that the indices depend on the resolution of the spectra. Joyce (1998) mentioned already that especially the [2.29] index, which measures the strength of the (2−0) vibration-rotation band of CO, is very sensitive to the resolution of the spectra. Tests with the model spectra show that the resolution effects become negligible once the resolution exceeds 1000; below this limit the effects become more and more significant with lower resolution. Comparing spectra with resolution 1000 and 500 yielded the following: The [1.36], and [1.78] index decreased in the mean by about 10 %, the [2.29] index increased by up to 20 %, the [3.1] index was changed by about 5 %.

The paper of Lázaro et al. (1994) contains effective temperatures from Lambert et al. (1986) for the sample stars. For the January 1996 data of the Lançon observations, effective temperatures were derived from model fits to the spectra (see Sect. 4.2.1). Adding the spectra of Lançon & Wood (2000) in our investigation increased the sample of stars where [1.36] indices can be measured by a factor of two. Figure 4.23 shows the indices versus effective temperature for all observations. Diamonds denote the observations of Lázaro et al. (1994), asterisks the ones of Lançon & Wood (2000).

For all plane parallel and spherical hydrostatic models, as well as for all available dynamical models, the Lázaro indices were computed based on spectra with a resolution of 5000 for a comparison with the observations. Figures 4.24 and 4.25 show the different indices versus effective temperature for the spherical model

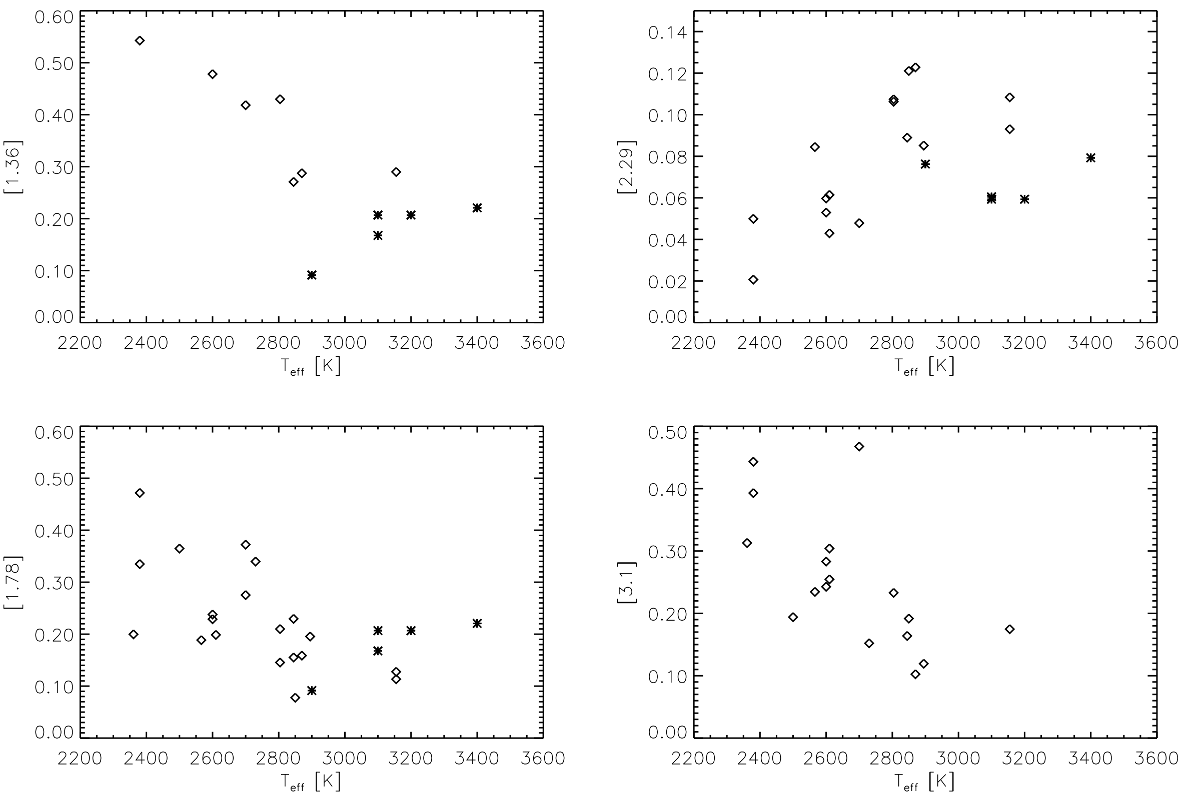

Figure 4.23: Observed Lázaro indices versus effective temperature; diamonds denote the Lázaro et al. (1994) data, asterisks the Lançon & Wood (2000) data of January 1996.

spectra with solar composition (diamonds) and with $\log(Z/Z_\odot) = -0.3$ for different C/O ratios. Black symbols denote models with C/O = 1.02, red symbols stand for models with C/O = 1.1, green ones for C/O = 1.2, blue ones for C/O = 1.3 and turquoise ones for C/O = 1.4.

Effects of temperature and C/O ratio

In Fig. 4.24 and 4.25 one can see the influence of temperature and C/O on the Lázaro indices:

1. The [1.36] index decreases with increasing temperature, lower C/O ratio, higher $\log(g)$, and higher metallicity. The mass of the star has a negligible influence on the index.

2. For models with effective temperatures above 2800 K, the [1.78] index decreases with increasing temperature, lower C/O ratio, lower $\log(g)$, higher

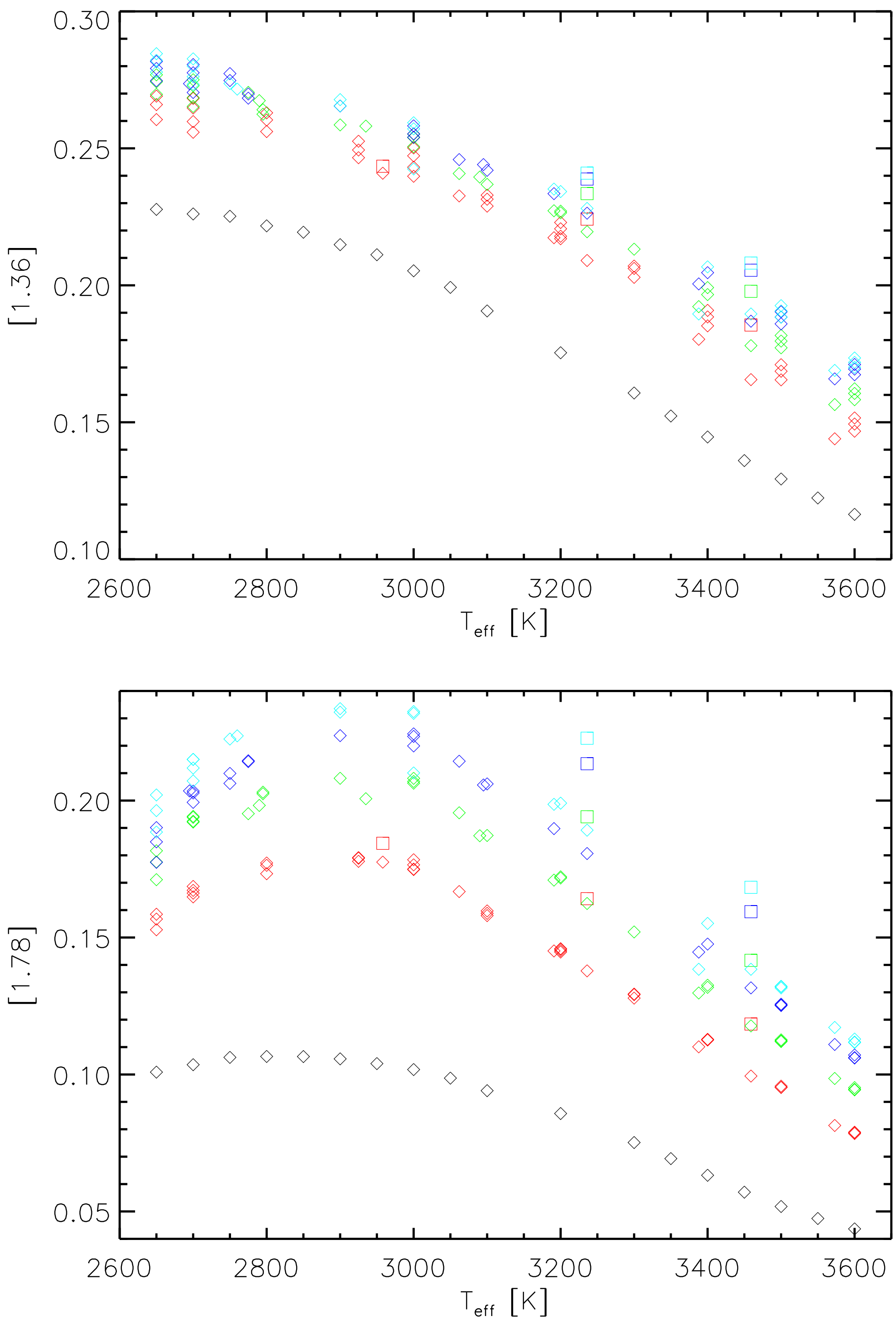

Figure 4.24: Lázaro indices versus effective temperature for spherical hydrostatic models. Black symbols denote models with C/O = 1.02, red symbols stand for models with C/O = 1.1, green ones for C/O = 1.2, blue ones for C/O = 1.3 and turquoise ones for C/O = 1.4.

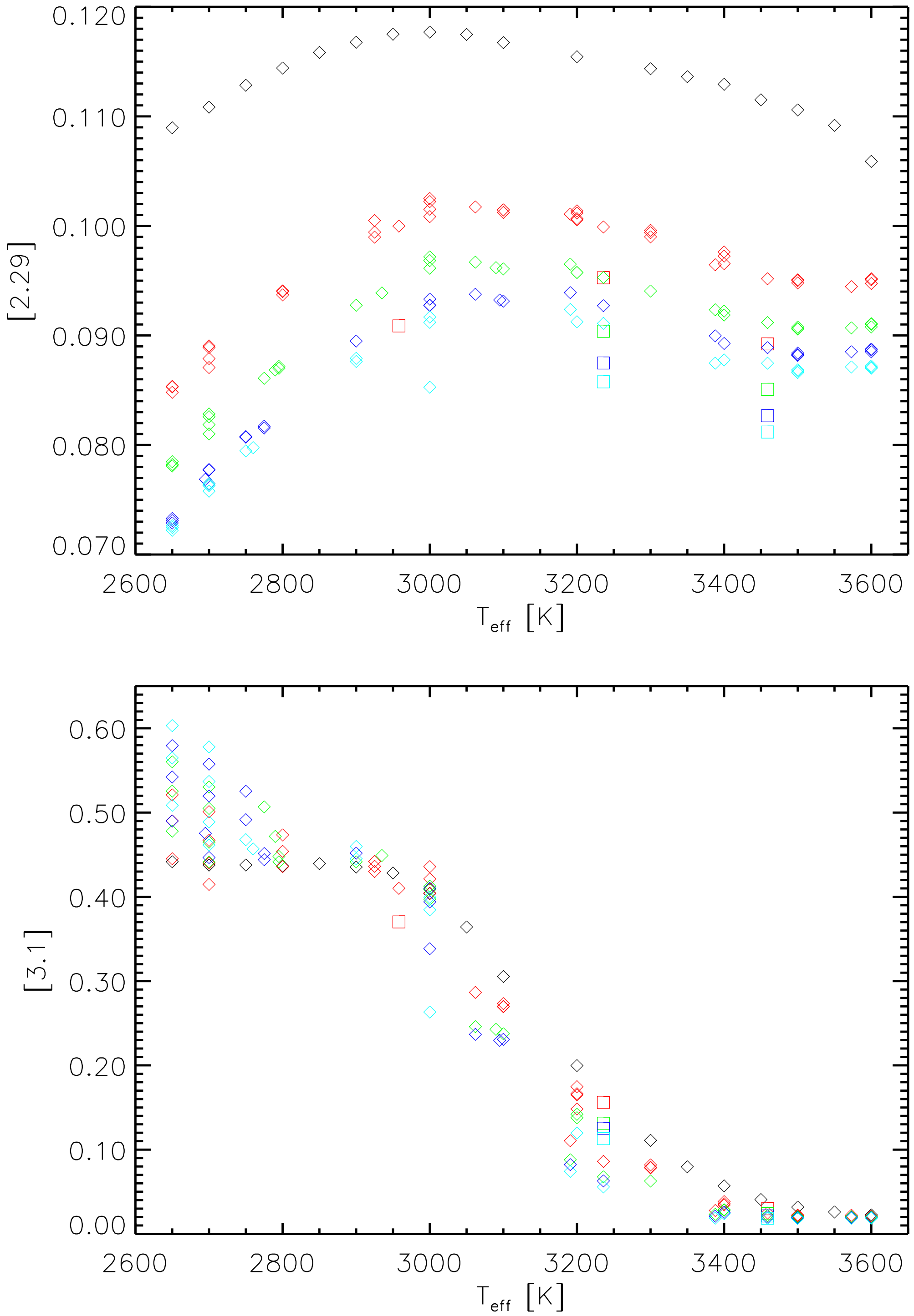

Figure 4.25: Lázaro indices versus effective temperature for spherical hydrostatic models. Black symbols denote models with C/O = 1.02, red symbols stand for models with C/O = 1.1, green ones for C/O = 1.2, blue ones for C/O = 1.3 and turquoise ones for C/O = 1.4.

mass and higher metallicity. Below effective temperatures of 2800 K the trend with temperature reverses.

3. The [2.29] index increases slightly with decreasing temperature down to a temperature of about 3000 K, then the trend reverses. A higher C/O ratio, a higher $\log(g)$, a lower mass, and lower metallicity result in a decreasing [2.29] index.

4. The [3.1] index increases with decreasing temperature until a value is reached where the feature becomes saturated. A smaller $\log(g)$ and smaller C/O ratio result in a higher [3.1] index down to effective temperatures of about 3000 K. The reason for this on first sight astonishing result is a change of the partial pressure balance: When the C/O ratio of the model is higher, more C_3 is formed, but less C_2H_2, C_2, and CO.

From plotting two-colour diagrams the following relations (upper panels of Figs. 4.26, 4.27, and 4.28) can be deduced:

1. A good correlation exists between the [1.36] and the [1.78] index for each C/O and $\log(g)$ sequence. A higher C/O ratio results in both a higher [1.78] and [1.36] index at a constant temperature. This diagram alone is not suitable to simultaneously determine the effective temperature and the C/O ratio of a star.

2. No useful correlation is visible between the [1.78] and the [2.29] index. There occurs a turning point in the [2.29] index around temperatures of 3000 K. A higher C/O ratio results in a higher [1.78] and a lower [2.29] index at a constant temperature.

3. A good correlation exists between the [1.78] and the [3.1] index for each C/O and $\log(g)$ sequence. A higher C/O ratio results in a higher [1.78] and a lower [3.1] index at constant temperature.

For comparison, the same two-colour diagrams for the dynamical models (middle panels) and for the Lázaro observations (diamonds), the Lançon observations (asterisks) and the Joyce observations (triangles) are shown in Figs. 4.26, 4.27, and 4.28.

4.5.3 Results of dynamical model spectra

We calculated the [1.36], [1.78], [2.29] and [3.1] indices for all phases of the four dynamical models. To check additionally the temperature sensitivity of the Lázaro indices in the dynamical models, the temperature was calculated arbitrarily at

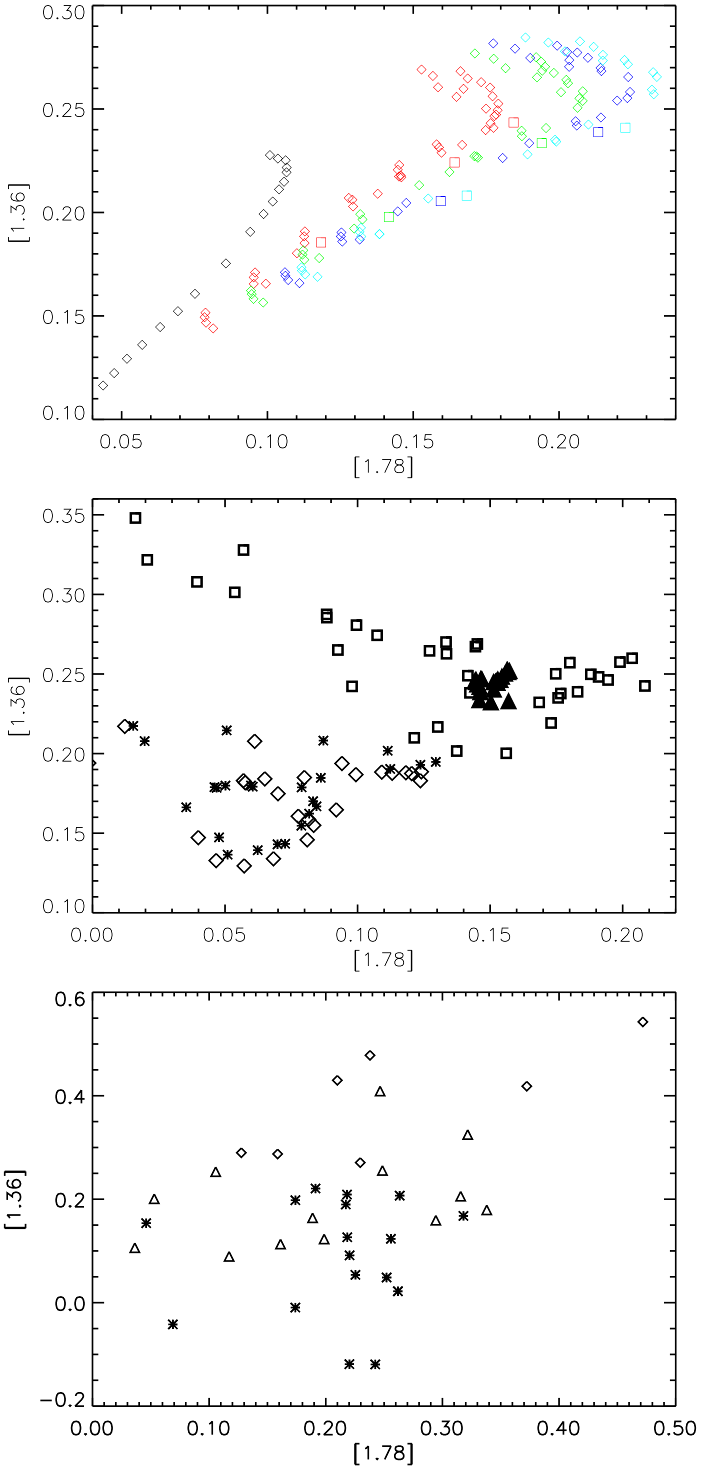

Figure 4.26: Lázaro two-colour diagrams: [1.36] versus [1.78] for spherical hydrostatic models (upper panel), for dynamical models (middle panel) and for the observations (lower panel). For details see the corresponding texts. Note the different scales!

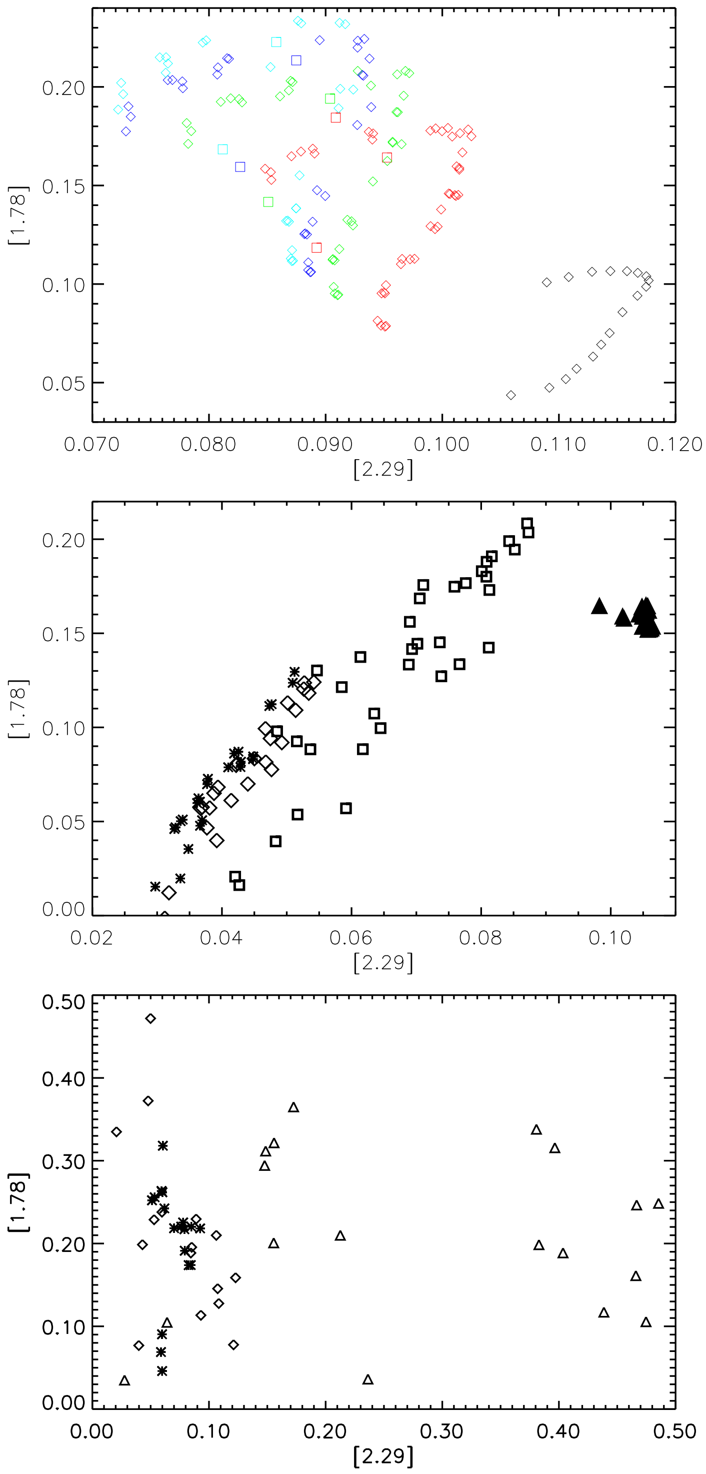

Figure 4.27: Lázaro two-colour diagram: [1.78] versus [2.29] for spherical hydrostatic models (upper panel), for dynamical models (middle panel) and for the observations (lower panel). For details see the corresponding texts. Note the different scales!

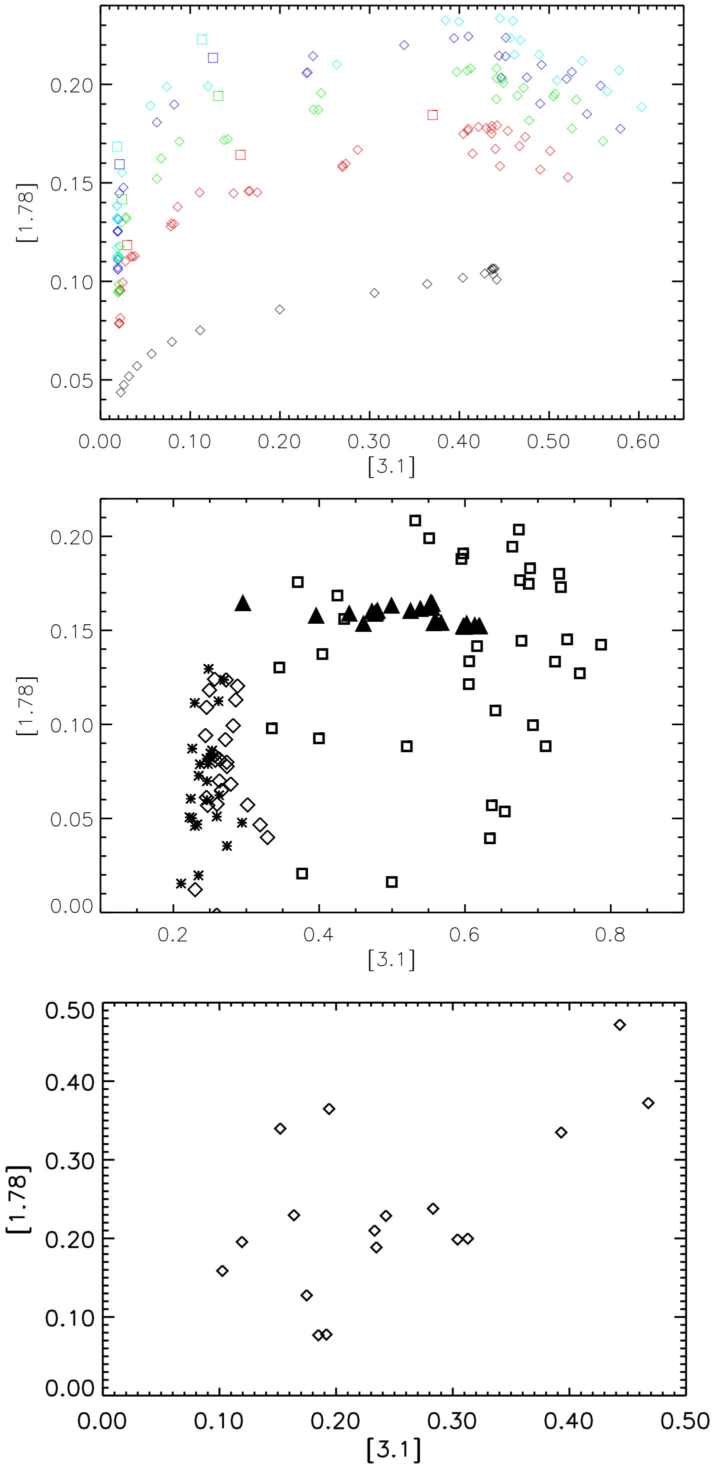

Figure 4.28: Lázaro two-colour diagram: [1.78] versus [3.1] for spherical hydrostatic models (upper panel), for dynamical models (middle panel) and for the observations (lower panel). For details see the corresponding texts. Note the different scales!

$\tau_{\text{Planck}} = 1$ for each model structure. Fig. 4.29 shows the [1.36] index versus phase and versus the temperature for models L52C11U2RO, L7TC14U5RO, L7C14U6RO and L7C18U4RO. In all cases except for L7C18U4RO the positions of minima and maxima are indicated. Model L7C18U4RO does not show periodicity on a short time scale, therefore the diagram is too crowded and the indication of the minima and maxima was omitted. Similar diagrams were made for the [1.78], [2.29] and [3.1] indices.

Comparing the four dynamical models with each other yields the following results:
[1.36] versus phase: Model L52C11U2RO shows a very periodic behaviour, the variations repeat regularily from one cycle to the next. The minimum value of the [1.36] index is reached around phase 0.4, its maximum value around phase 0.55. The change in the [1.36] index with phase amounts to ≈ 0.03. Model L7TC14U5RO is double periodic, i.e. the variations in the indices repeat after two cycles. Around phase 0.3 the [1.36] index approaches its maximum value, around phase 0.6 its minimum value. The change in the [1.36] index with phase amounts to ≈ 0.10. Model L7C14U6RO shows basically the same behaviour as model L7TC14U5RO; in this case, the variation in [1.36] is slightly higher, namely ≈ 0.11. Model L7C18U4RO is less periodic than the last two cases, it repeats only after 6 to 7 cycles. Due to the significantly lower mass loss rate and higher C/O ratio in this model compared to the others, the variation of the [1.36] index with phase is stronger than in the other models; it amounts to ≈ 0.16.
[1.36] versus temperature: In model L52C11U2RO the temperatures of the minimum phases (which we will call "minima" in the follwoing for brevity) are higher than those of the maximum phases ("maxima" in the following). The maxima have a slightly lower [1.36] index than the corresponding minima. In model L7TC14U5RO the minima are in the mean cooler than the maxima. The maxima have higher [1.36] indices than the corresponding minima. The same applies for model L7C14U6RO. The behaviour of model L7C18U4RO is too irregular to allow a general description.
[1.78] versus phase: Model L52C11U2RO shows barely any variation in the [1.78] index. The minimum value of the [1.78] index is reached around phase 0.2, the maximum value around phase 0.6, the variation amounts only to 0.02. In model L7TC14U5RO, the minimum value of the [1.78] index is reached around phase 0.4, the maximum value around phase 0.9. The variation in the [1.78] index is almost a factor of 10 higher than in model L52C11U2RO, namely ≈ 0.14. Model L7C14U6RO shows basically the same behaviour as model L7TC14U5RO. For model L7C18U4RO, the variation of the [1.78] index amounts to ≈ 0.22.
[1.78] versus temperature: For model L52C11U2RO the maxima have slightly lower [1.78] indices than the corresponding minima. Models L7TC14U5RO, L7C14U6RO

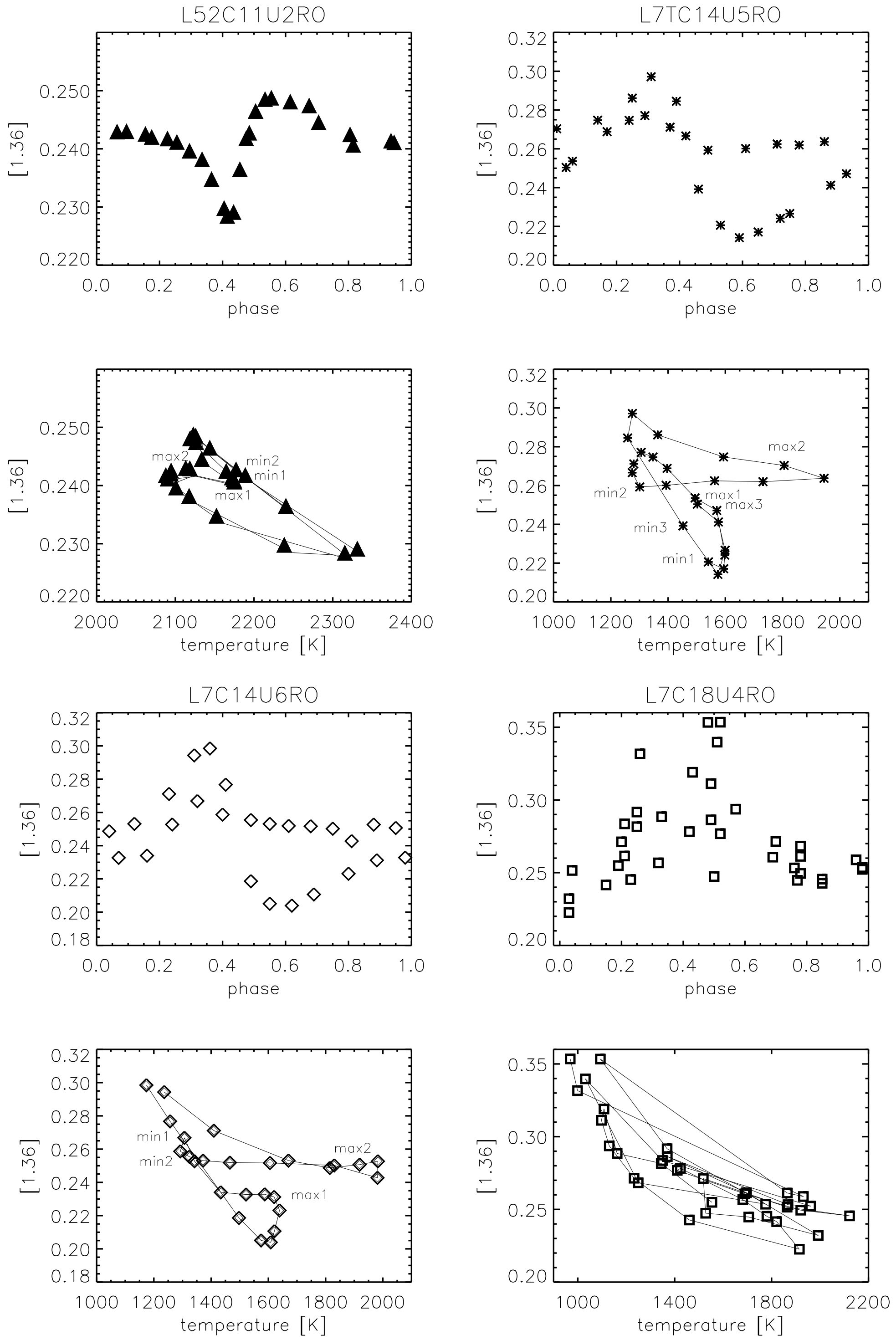

Figure 4.29: The [1.36] index versus phase and versus the temperature at $\tau_{\rm Planck} = 1$ for models L52C11U2RO, L7TC14U5RO, L7C14U6RO and L7C18U4RO. In all cases except for L7C18U4RO, the positions of the indices at minimum and maximum phase are indicated.

and L7C18U4RO show the opposite behaviour.
[2.29] versus phase: Model L52C11U2RO shows barely any variation in the [2.29] index. The minimum value of the [2.29] index is reached around phase 0.45, the maximum value around phase 0.35, but the variation amounts only to 0.01! In model L7TC14U5RO the minimum value of the [2.29] index is approached around phase 0.3, the maximum value around phase 0.9. The amount of variation of the [2.29] is small too, $\Delta[2.29] \approx 0.03$. The remaining two models, L7C14U6RO and L7C18U4RO behave similar.
[2.29] versus temperature: In all models the maxima have higher [2.29] indices than the corresponding minima.
[3.1] versus phase: Model L52C11U2RO shows a strong variaton in the [3.1] index. The minimum value of the [3.1] index is reached around phase 0.45, the maximum value around phase 0.25. The variation amounts to ≈ 0.4. For all other models no explicit phases can be given for the minimum and maximum of the [3.1] index. This is due to the fact, that the [3.1] index is strongly influenced by dust formation. Therefore, the models behave very differently and no general rules apply. The smaller variations of the [3.1] index in models L7TC14U5RO and L7C14U6RO (≈ 0.15) compared to model L52C11U2RO also illustrate the influence of the dust on this index.
[3.1] versus temperature: In all models the maxima show in the mean smaller [3.1] indices than the corresponding minima.

The [1.36] – [1.78], [1.78] – [2.29], and the [1.78] – [3.1] diagrams for all four dynamical models are shown in the middle panels of Figs. 4.26, 4.27, and 4.28. Diamonds denote the phases of model L7C14U6RO, asterisks the ones of model L7TC14U5RO, squares the ones of model L7C18U4RO, and filled triangles the instants of time of model L52C11U2RO.

4.5.4 Comparison of theoretical with observational results

1. $[1.36]$ index versus effective temperature: The [1.36] observational data are scarce, but they seem to show the same trend as the hydrostatic and our four dynamical models, namely that higher [1.36] indices are due to cooler temperatures. The indices of both types of models lie in the correct range, but neither of them is able to fully reproduce the observed ranges of the [1.36] index. We have to keep in mind that firstly we had to define the index differently than it was originally done by Lázaro et al. (1994) due to the wavelength calibration problem of their observations, and secondly that the different resolutions of the observed spectra might very well contribute to this larger range in the observations.

2. $[1.78]$ index versus effective temperature: The hydrostatic models are able

to reproduce the observed behaviour of the [1.78] C_2 index. However, all four dynamical models fail to reproduce the correct behaviour with temperature. In contrast to what is observed, the models give lower [1.78] indices for lower temperatures. The [1.78] indices of hydrostatic and dynamic models lie in the correct range, but again, they do not cover the full range of observations. Surprisingly, the dynamical models predict a weaker C_2 feature for lower temperatures. A closer inspection shows that this strange behaviour is caused by emission contributions in the model spectra; the lower the effective temperature is, the stronger is the amount of emission and hence the weaker is the feature. We do not observe such a behaviour, thus there seems to be a problem with our model structures, probably due to the high uncertainty in the C_2 opacities (see Sect. 2.2) in this wavelength region.

3. $[2.29]$ index versus effective temperature: The observed data are too scarce to test the predictions of the hydrostatic models. The hydrostatic models are not able to reproduce the large range in [2.29] which the observations are situated in. Three of the dynamical models lie in the correct range, cover the full range, and show the correct trend of the observations, namely that higher [2.29] indices are due to higher temperatures. Only model L52C11U2RO shows barely any variation at all. The decrease of the [2.29] CO index with lower effective temperature is due to a change in the pressure balance between various carbon-containing molecular species.

4. $[3.1]$ index versus effective temperature: The hydrostatic models reproduce the observed [3.1] indices and the full range of the observations. The dynamical models reproduce the trend of the [3.1] index with temperature correctly too, they lie in the appropriate region, but they cover a larger range than the observations.

5. $[1.36]$ index versus [1.78] index: Hydrostatic and dynamic models describe the trend of the observations correctly. The full ranges of the observations can not be reproduced.

6. $[1.78]$ index versus [2.29] index: The [2.29] index is strongly affected by the different resolutions of the observed spectra. The triangles at the right end of the diagram are spectra of Joyce with a resolution of 200, the few triangles in the left part of the diagram are spectra of Joyce with a resolution of 400. Nothing conclusive about a trend can be said as long as the sample of stars with the same resolution is that small. Hydrostatic models cannot cover the full range of the observations. Dynamical models behave similar as hydrostatic models with effective temperatures below 3000 K. The higher

the mass loss rate of a dynamical model is, the lower are the [2.29] and [1.78] indices.

7. [1.78] index versus [3.1] index: The observed relation seems to be reproduced correctly by the hydrostatic models, only - as already stated above - the observed range in [1.78] can not be reproduced. The dynamical models predict in the mean higher [1.78] indices for stars with higher [3.1] indices in accordance with what is observed.

4.5.5 Conclusions

Excluding the [2.29] index where nothing conclusive can be said presently, plane parallel and spherical hydrostatic models are able to reproduce the trends of the indices. All the calculated indices fall into the same range as the observations. But they are not able to cover the full observed range in most cases. Dynamical models reproduce all trends with temperature correctly except the one of the [1.78] C_2 index.

Neither hydrostatic nor dynamical models cover the full observed ranges of the [1.36], [1.78], and [2.29] indices. This is very likely partly due to the different resolutions of the three sets of observations referred to here. For the [2.29] index, this has already been mentioned by Joyce (1998). The higher the resolution of the spectra, the smaller is the range which is covered by the indices. Contrary to that, in our dynamical and hydrostatic models the [3.1] index reaches considerably higher values than in the observed spectra. This might either be caused by the fact that the chosen pseudo-continuum points (at 2.9 and 3.4 μm) are no continuum points in spectra with low resolution, or that stars with low temperatures are surrounded by larger amounts of dust than what our models predict and which leads to a weakening of the 3 μm feature.

4.6 Tanaka indices

4.6.1 Observations

Tanaka et al. (1990, 1992, 1996) observed carbon stars with a **F**ourier **T**ransform **S**pectrometer (FTS) mounted at the 1.88 m reflector of the Okayama Astrophysical Observatory. A total of 104 carbon stars were analyzed, 65 of them were observed twice, 30 three times or more. Spectral range and resolution were 4000-7000 cm^{-1} and 2 cm^{-1} in wavenumber, respectively. Reference spectra of α Boo were obtained for every observing night. The response curve of the spectrometer was corrected with the help of the reference star. The error in the indices is approximately 0.05, at most 0.1. Tanaka et al. (1990) defined the following three indices:

- $colour = -2.5 \cdot \log(F_{6000}/F_{4500})$
  The *colour* index is proportional to the logarithm of the flux ratio at wavenumbers 6000 cm^{-1} (1.6667 μm) and 4500 cm^{-1} (2.2222 μm). Both wavenumbers are regarded as continuum points. This *colour* index is supposed to be a good indicator of the effective temperature.

- $C_2 = -2.5 \cdot \log(F_{5656}/F_{cont,5656})$
  The C_2 index is proportional to the logarithm of the flux ratio of the bandhead and the continuum of the C_2 Ballik-Ramsay $(0-0)$ band. This index measures mostly the over-abundance of carbon to oxygen. The wavenumber 5656 cm^{-1} corresponds to 1.768 μm.

- $CO = -2.5 \cdot \log(F_{4360}/F_{cont,4360})$
  The CO index is proportional to the logarithm of the flux ratio of the bandhead and the continuum of the CO vibration-rotation $(2-0)$ band at 4360 cm^{-1} (2.2936 μm). The CO index is a measure of the oxygen abundance.

4.6.2 Results

Osamu Hashimoto and Wataru Tanaka kindly provided the original spectra. Instead of using directly the indices given in the paper series of Tanaka et al., we read in the spectra and calculated the indices in exactely the same way as we did it for the model spectra. This is particularly important for the CO and the C_2 index, where the continuum flux is involved in the calculation of the index. Therefore, the indices we calculated for the observed spectra can differ from the ones given in the paper series of Tanaka et al. For the calculation of the CO index, wavenumbers 4390 and 4327 cm^{-1} were assumed to be continuum points. For the

C_2 index, wavenumbers 5684 and 5588 cm^{-1} were chosen as continuum points. Figure 4.30 shows an FTS spectrum of TX Psc (upper panels) and a model spectrum (lower panels) where the corresponding wavenumbers are indicated. The choice of a continuum point was particulary difficult at the long wavelength side of the C_2 Ballik-Ramsay (0−0) band-head because the Earth's atmosphere does not allow reliable observations close to this region (see Fig. 4.30). Therefore, we had to chose a continuum point at a wavenumber where it was clear from model spectra that it is not very well suited for stars with low effective temperatures. As a consequence, we expect the uncertainties of the C_2 index to be higher than the ones of the CO index. The continuum flux $F_{\rm cont,5656}$ was computed by linear interpolation between the fluxes at 5684 and 5588 cm^{-1}, the continuum flux $F_{\rm cont,4360}$ as obtained by linear interpolation between the fluxes at 4390 and 4327 cm^{-1}. The *colour* index is defined as the ratio of the flux at two wavenumbers which lie far apart. This implies, that the index strongly depends on the correction of the response curve of the spectrometer referring to a reference star which was necessary to reconstruct the shape of the spectra. Wavenumbers 6000 and 4500 cm^{-1} were assumed to be continuum points by Tanaka et al. (1990, 1992, 1996). From Fig. 4.30 it is clear that there is a line in the model spectra at wavenumber 6000 cm^{-1}. At 4500 cm^{-1}, we have a (at least pseudo) continuum point down to effective temperatures of about 3000 K. The lower the effective temperature of the model, the stronger is the band around 6000 cm^{-1} and the further away it lies from the continuum. We conclude that wavenumber 4500 cm^{-1} is a much better continuum point than the 6000 cm^{-1} one. Finally, it should be noted that all three indices depend on the resolution of the spectra. A different resolution changes the absolute values of the indices but not their relative dependencies as long as the resolution is higher than about 1000; at lower resolution it can happen that also the dependencies change. For all plane parallel and spherical hydrostatic models as well as for all available dynamical models, the synthetic Tanaka indices were computed with a resolution of 5000 which corresponds approximately to the one of the observed spectra.

The recalculation of the indices of the observations as described above, altered some of the conclusions presented in Tanaka et al. (1990, 1992, 1996). Therefore, we briefly summarise their conclusions and update them where necessary:

1. The *colour* index is a good indicator for the effective temperature.

2. The CO index is a measure of the oxygen abundance.

3. The C_2 index measures the over-abundance of carbon to oxygen.

4. No correlation is visible between the *colour* index and the sub-class x in $C_{x,y}$ of the C-classification system.

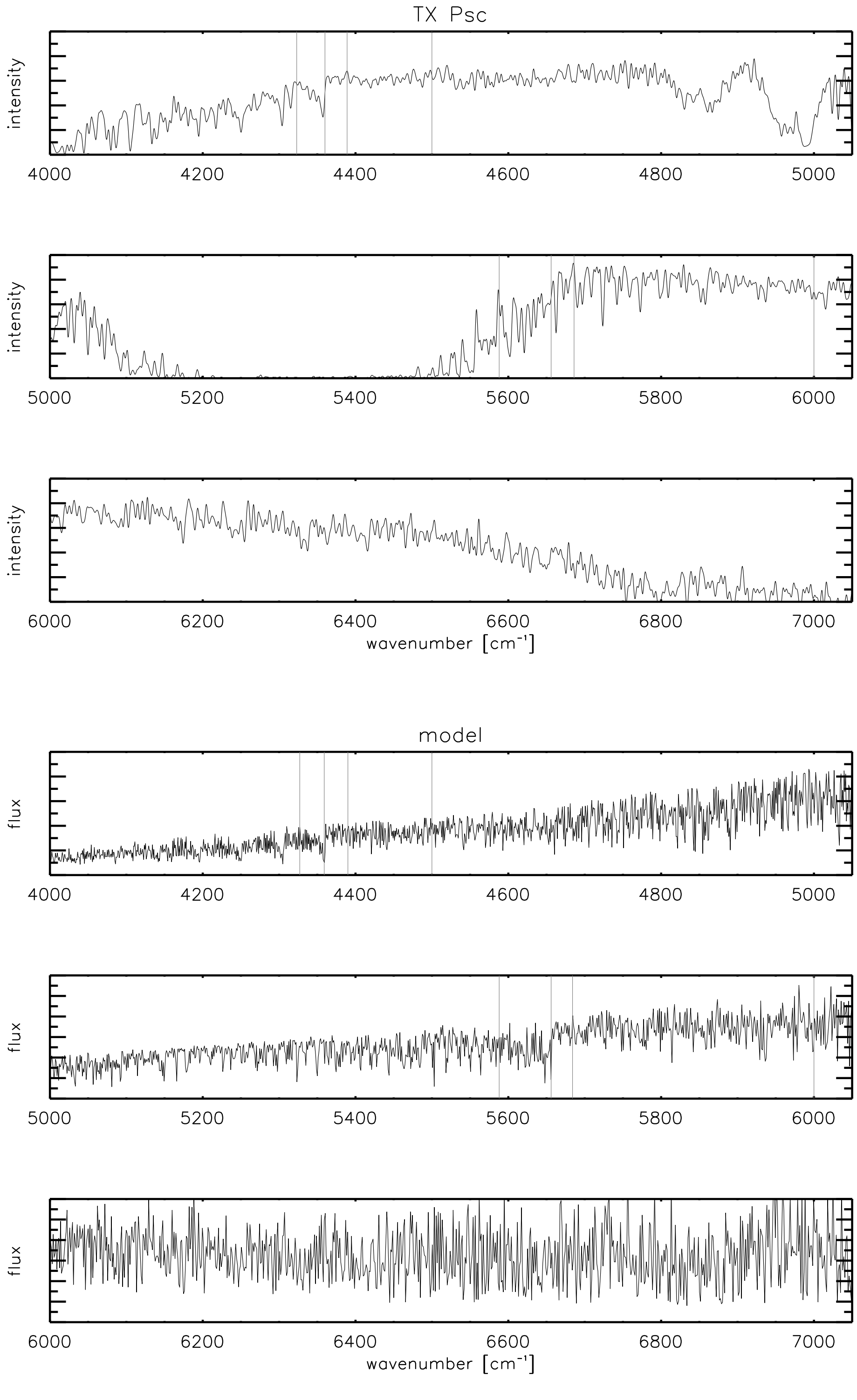

Figure 4.30: FTS spectrum of TX Psc (upper panels) and a model spectrum (lower panels) where the wavenumbers defining the three indices are indicated.

5. A good correlation exists between the C_2 index and the sub-class y in $C_{x,y}$ of the C-classification.

6. A weak correlation is visible between the C_2 index and the *colour* index for irregular variables.

7. An inverse correlation between the CO index and the C_2 index is observed for all variability types except for Miras.

8. The CO indices are probably reduced by emission originating in the dust shells in Mira variables.

In Fig. 4.31, the CO index is plotted versus the *colour* index (upper panel), the C_2 index versus the *colour* index (middle panel) and the CO index versus the C_2 index (lower panel). Different variability types are marked by different symbols and colours as labeled in the plot; "unid" stands for stars for which no variability type was given. The position of single stars in these diagrams can vary considerable: R Scl for example shows a $\Delta\,colour \approx 0.6$, $\Delta\,\mathrm{CO} \approx 0.25$, and $\Delta\,\mathrm{C}_2 \approx 0.4$.

Table 4.6.2 summarises the correlations which emerge after the recalculation of the indices for the different types of AGB stars:

variability type	CO vs. C_2	C_2 vs. *colour*	CO vs. *colour*
Lb	CO $\uparrow$ for $C_2 \downarrow$	C_2 $\uparrow$ for *colour* $\uparrow$	CO $\downarrow$ for *colour* $\uparrow$
SR	no correlation	no correlation	CO $\downarrow$ for *colour* $\uparrow$
SRb	CO $\uparrow$ for $C_2 \downarrow$	no correlation	no correlation
SRa	CO $\uparrow$ for $C_2 \downarrow$	no correlation	CO $\downarrow$ for *colour* $\uparrow$
M	no correlation	no correlation	no correlation

Effects of temperature and C/O ratio

Figures 4.32 and 4.33 show the different synthetic Tanaka indices versus effective temperature for the spherical model spectra with solar composition (diamonds) and with $\log(Z/\mathrm{Z}_\odot) = -0.3$ for different C/O ratios. Black symbols denote models with $\mathrm{C/O} = 1.02$, red symbols stand for models with $\mathrm{C/O} = 1.1$, green ones for $\mathrm{C/O} = 1.2$, blue ones for $\mathrm{C/O} = 1.3$, and turquoise ones for $\mathrm{C/O} = 1.4$. Figures 4.34 and 4.33 show the correlations between the synthetic indices.

1. The *colour* index does not show a unique dependence on the effective temperature. The relation has the form of a parabola. For models with effective

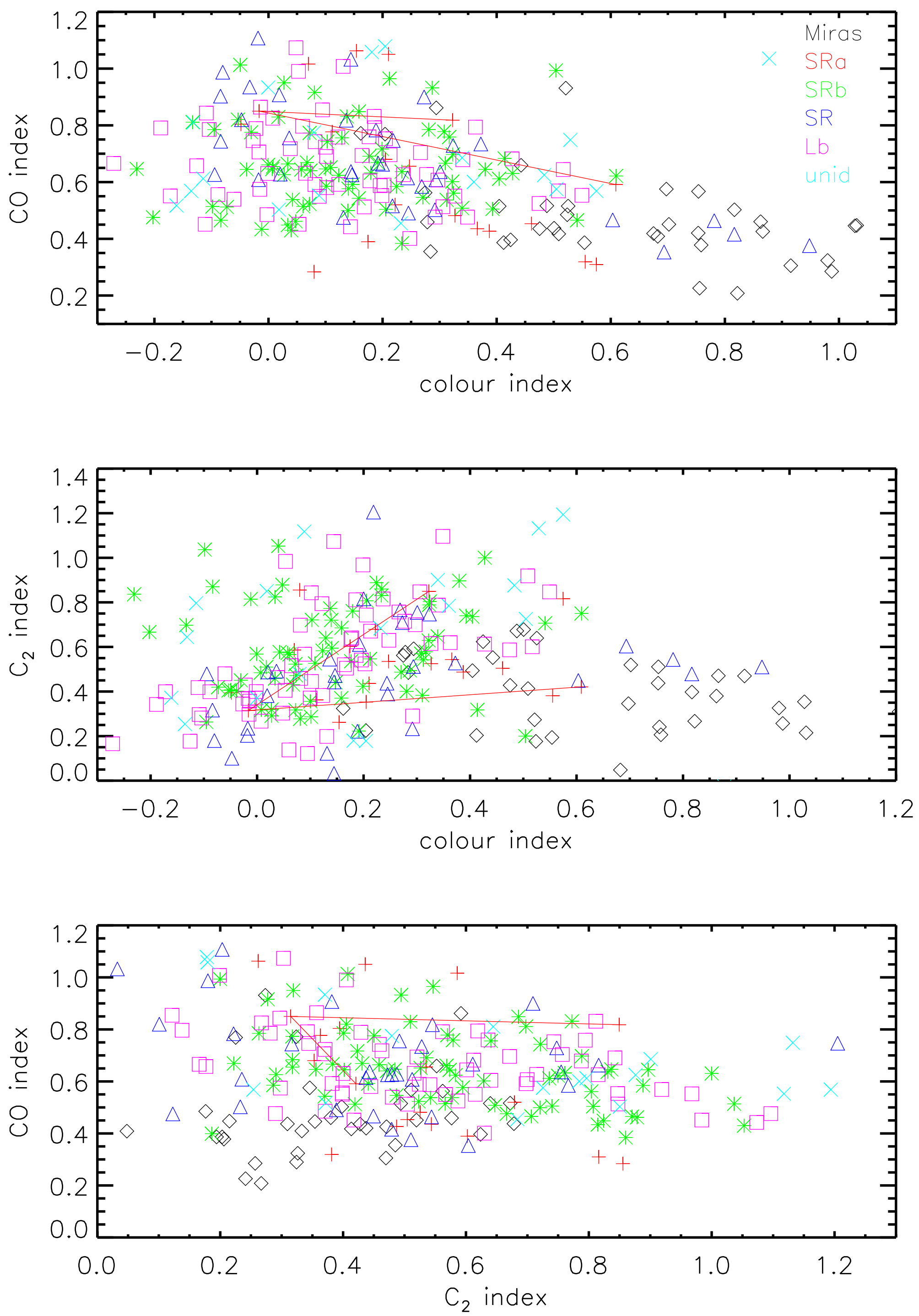

Figure 4.31: Recalculated Tanaka indices for the stars observed by Tanaka et al. (1990, 1992, 1996); the different types of AGB stars are indicated by different symbols and colours. Additionally, the variations of the indices are indicated by the full lines for the SRa variable R Scl.

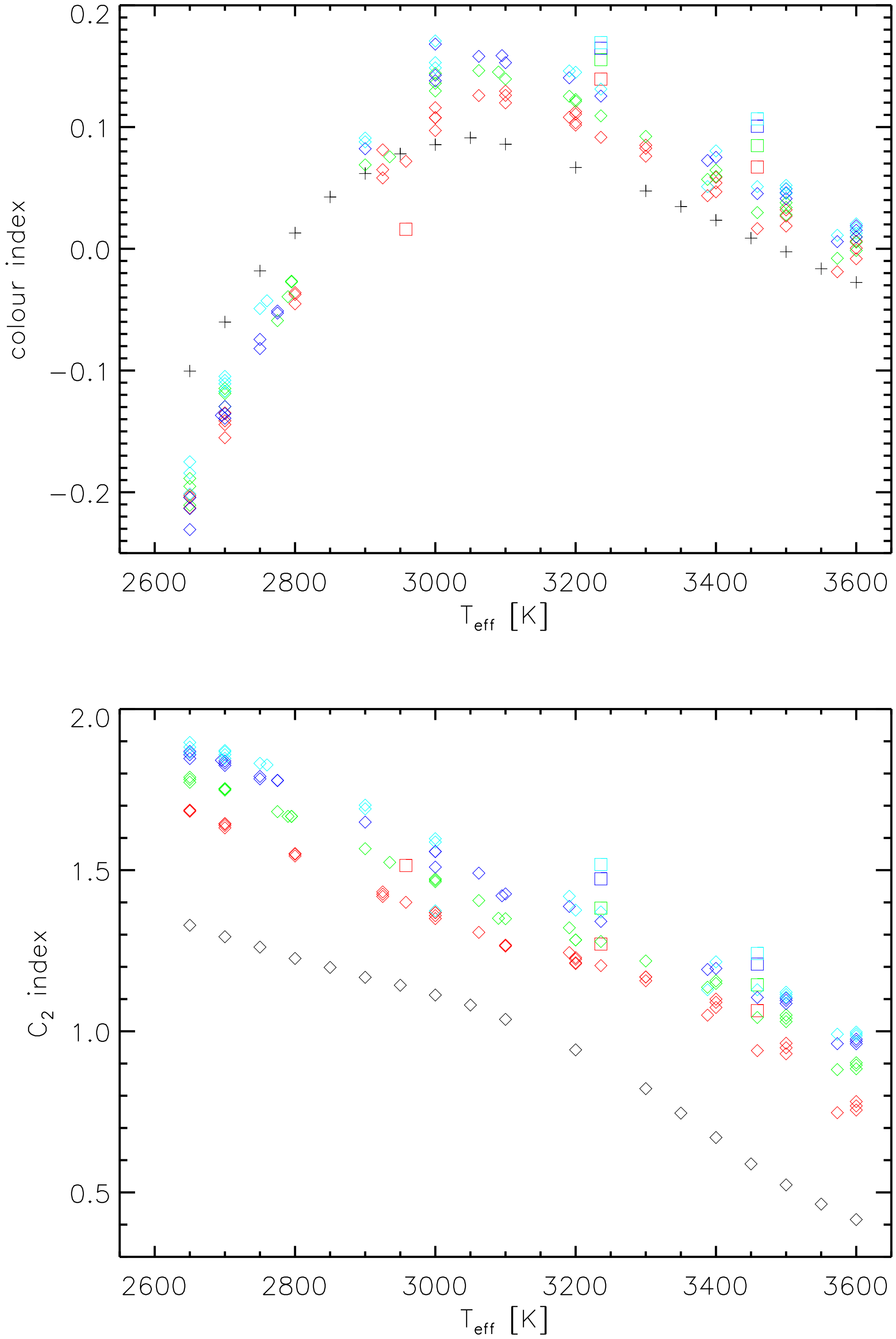

Figure 4.32: *Colour* index and C_2 index versus effective temperature for spherical hydrostatic models. Black symbols denote models with C/O = 1.02, red symbols stand for models with C/O = 1.1, green ones for C/O = 1.2, blue ones for C/O = 1.3, and turquoise ones for C/O = 1.4.

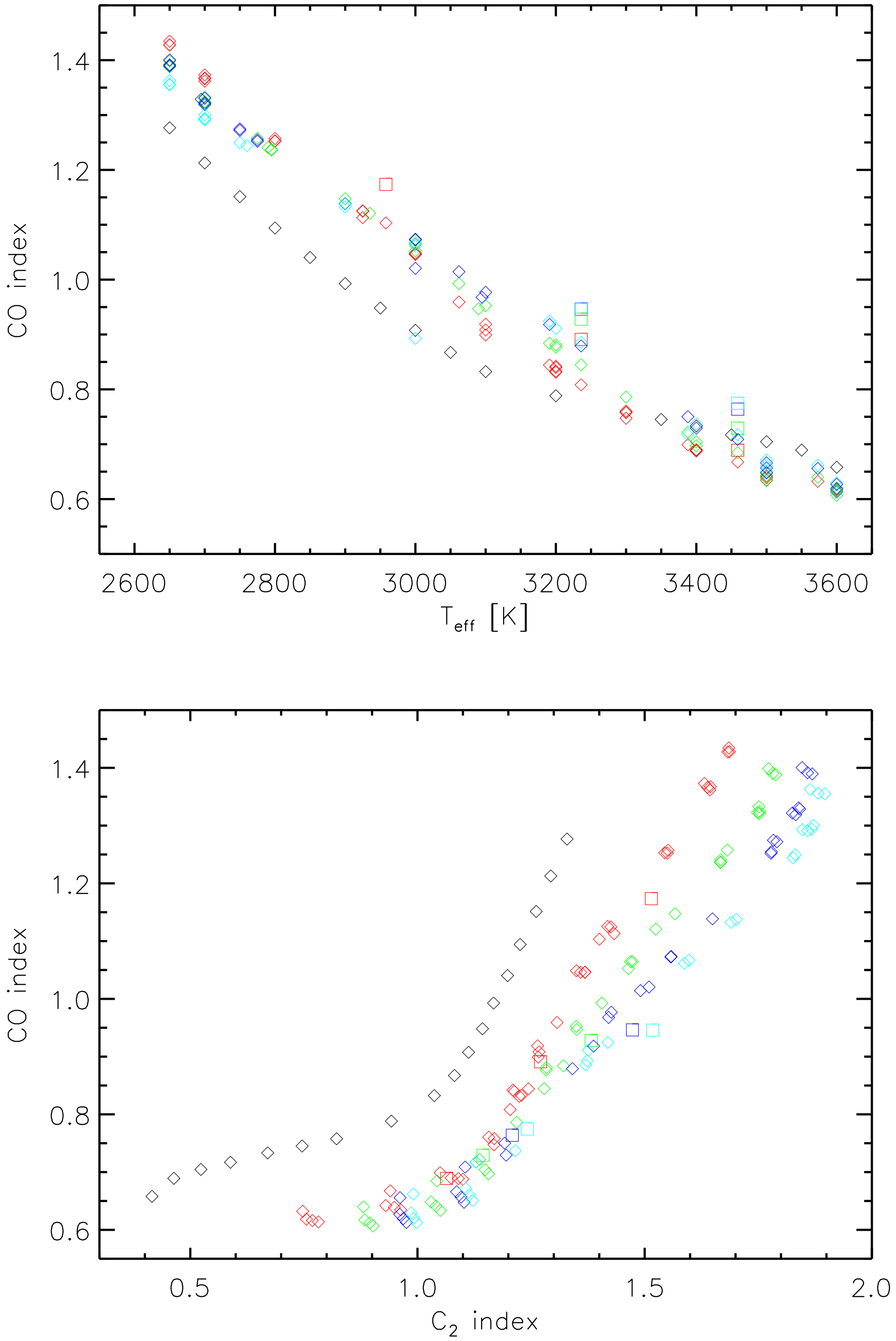

Figure 4.33: CO index versus effective temperature and CO index versus C_2 index for spherical hydrostatic models. Black symbols denote models with C/O = 1.02, red symbols stand for models with C/O = 1.1, green ones for C/O = 1.2, blue ones for C/O = 1.3, and turquoise ones for C/O = 1.4.

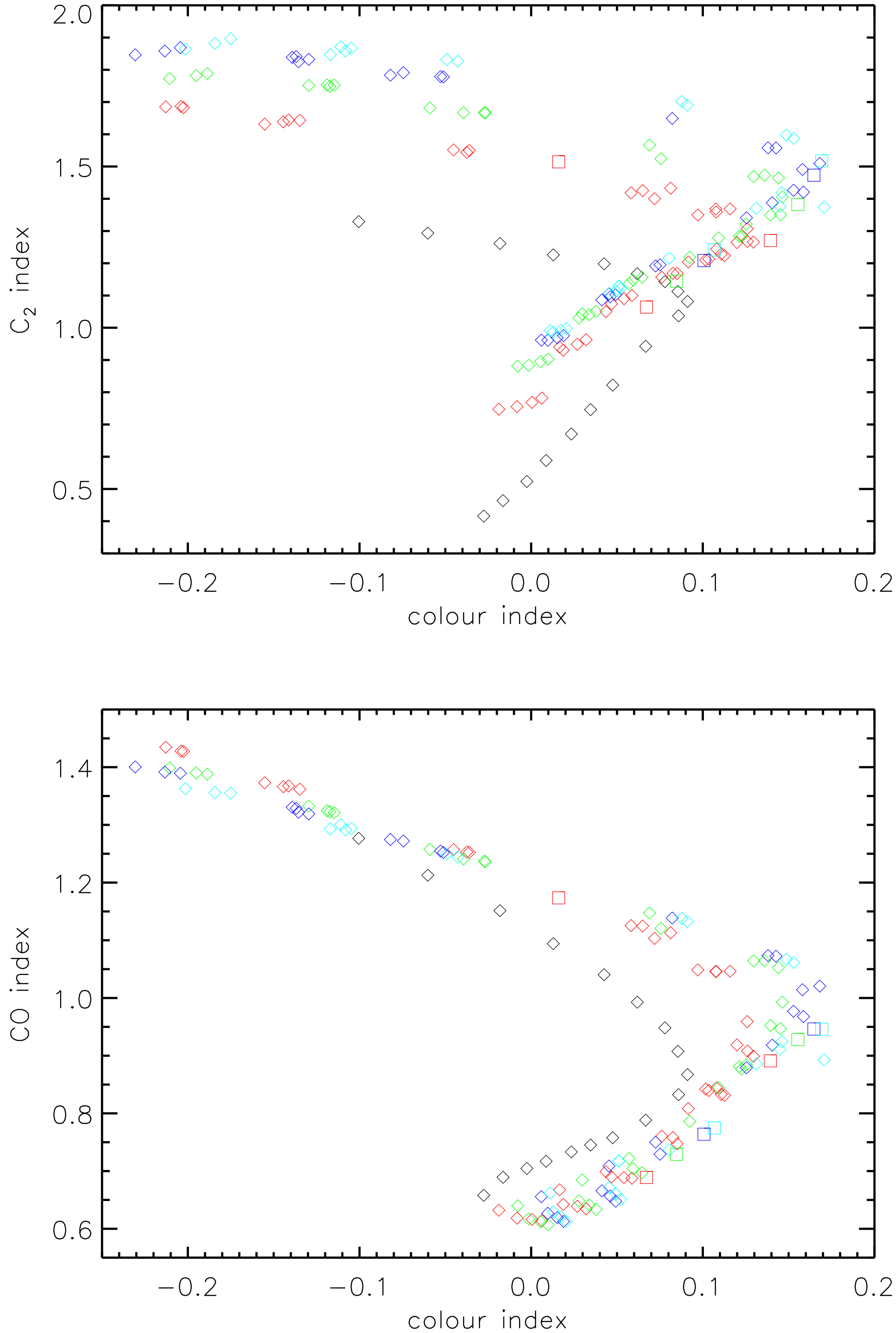

Figure 4.34: C_2 index (upper panel) and CO index (lower panel) versus *colour* index for spherical hydrostatic models. Black symbols denote models with C/O = 1.02, red symbols stand for models with C/O = 1.1, green ones for C/O = 1.2, blue ones for C/O = 1.3, and turquoise ones for C/O = 1.4.

temperatures above about 3200 K, the *colour* index increases (becomes positive), between effective temperatures of 3000 and 3200 K it stays more or less constant and for effective temperatures below 3000 K the *colour* index decreases again. A higher C/O ratio results in a slightly higher *colour* index for models with effective temperatures higher than 3000 K. The dependence of the *colour* index on $\log(g)$ is stronger at lower effective temperatures. A lower $\log(g)$ (i.e. higher luminosity) results in a higher *colour* index. The plane parallel models show a similar behaviour. The decrease in *colour* index with lower effective temperature is less steep than in the spherical case, and the effects of different luminosities become much smaller.

2. The C_2 index increases with decreasing effective temperature and with increasing C/O ratio. Model parameters such as $\log(g)$ or mass have almost no influence on the C_2 index. The plane parallel models have lower C_2 indices than the spherical models.

3. The CO index increases with decreasing effective temperature. The dependence of the CO index on the luminosity is very small. No clear correlation is visible between the CO index and the C/O ratio. Plane parallel models behave in the same way, the increase of the CO index with lower effective temperature is slightly steeper.

4. C_2 versus *colour* index: A well defined sequence is visible for each C/O ratio. Due to the behaviour of the *colour* index a turning point occurs in the relation between these two indices.

5. CO versus *colour* index: A well defined sequence is visible for each C/O ratio. Due to the behaviour of the *colour* index a turning point occurs in the relation between these two indices.

6. CO versus C_2 index: The CO index increases with increasing C_2 index.

4.6.3 Results of dynamical model spectra

We calculated the *colour*, CO, and C_2 indices for all pulsational phases of the four dynamical models. To check additionally the temperature sensitivity of the Tanaka indices in the dynamical models, the temperature was calculated arbitrarily at $\tau_{\rm Planck} = 1$ for each model structure. Fig. 4.35 shows the CO index versus phase and versus the temperature for models L52C11U2RO, L7TC14U5RO, L7C14U6RO, and L7C18U4RO. In all cases except for L7C18U4RO, the positions of the minimum and maximum phases (denoted as "minima" and "maxima" in the following) are indicated. Model L7C18U4RO does not show periodicity on a short time scale, therefore the diagram is too crowded and the minima and maxima labels were omitted. Similar diagrams were made for the *colour* and C_2 indices.

Comparing the four dynamical models with each other yields the following results:
Colour index versus phase: Model L52C11U2RO shows a very periodic behaviour, the variations repeat regularly from one cycle to the next. The minimum value of the *colour* index is reached around phase 0.2 and its maximum value around phase 0.45. The amplitude in the *colour* index with phase amounts to ≈ 0.15. Model L7TC14U5RO is double periodic, i.e. the variations in the indices repeat after two cycles. Around phase 0.8 the *colour* index approaches its maximum value and around phase 0.35 its minimum value. The variation in the *colour* index with phase amounts to ≈ 0.25. Model L7C14U6RO shows basically the same behaviour as model L7TC14U5RO; the variation in the *colour* index is slightly higher, namely ≈ 0.3. Model L7C18U4RO is less periodic than the other cases, it repeats only after 6 to 7 cycles. Due to the significantly lower mass loss rate and higher C/O ratio in this model compared to the others, the variation of the *colour* index with phase is stronger than in the other models; it amounts to ≈ 0.6.
Colour index versus temperature: In model L52C11U2RO the temperatures at the minimum phases of the luminosity (which we will call "minima" in the follwoing for brevity) are lower than those of the maximum phases ("maxima" in the following). The maxima can either have a higher or a lower *colour* index than the corresponding minima. In model L7TC14U5RO, in the mean the minima are cooler than the maxima. The maxima have larger *colour* indices than the corresponding minima. The same applies to model L7C14U6RO. The behaviour of model L7C18U4RO is too irregular to allow for a general description.
CO index versus phase: Model L52C11U2RO shows only small variations in the CO index. The minimum value of the CO index is reached around phase 0.45 and the maximum value around phase 0.55, the variation amounts to 0.2. In model L7TC14U5RO, the minimum value of the CO index is reached around phase 0.6 and the maximum value around phase 0.35. The variation in the CO index amounts to ≈ 0.30. Model L7C14U6RO shows the same behaviour as model L7TC14U5RO, the variation of the CO index is slightly larger, namely 0.4. For model L7C18U4RO, the variation of the CO index amounts to ≈ 1.0.
CO index versus temperature: For model L52C11U2RO, the maxima have slightly lower CO indices than the corresponding minima. Models L7TC14U5RO, L7C14U6RO, and L7C18U4RO show the opposite behaviour.
C_2 index versus phase: The minimum value of the C_2 index in model L52C11U2RO is reached around phase 0.45 and it peaks around phase 0.55; the variation amounts to 0.1. In model L7TC14U5RO, the minimum value of the C_2 index is reached around phase 0.6 and the maximum value around phase 0.35. The

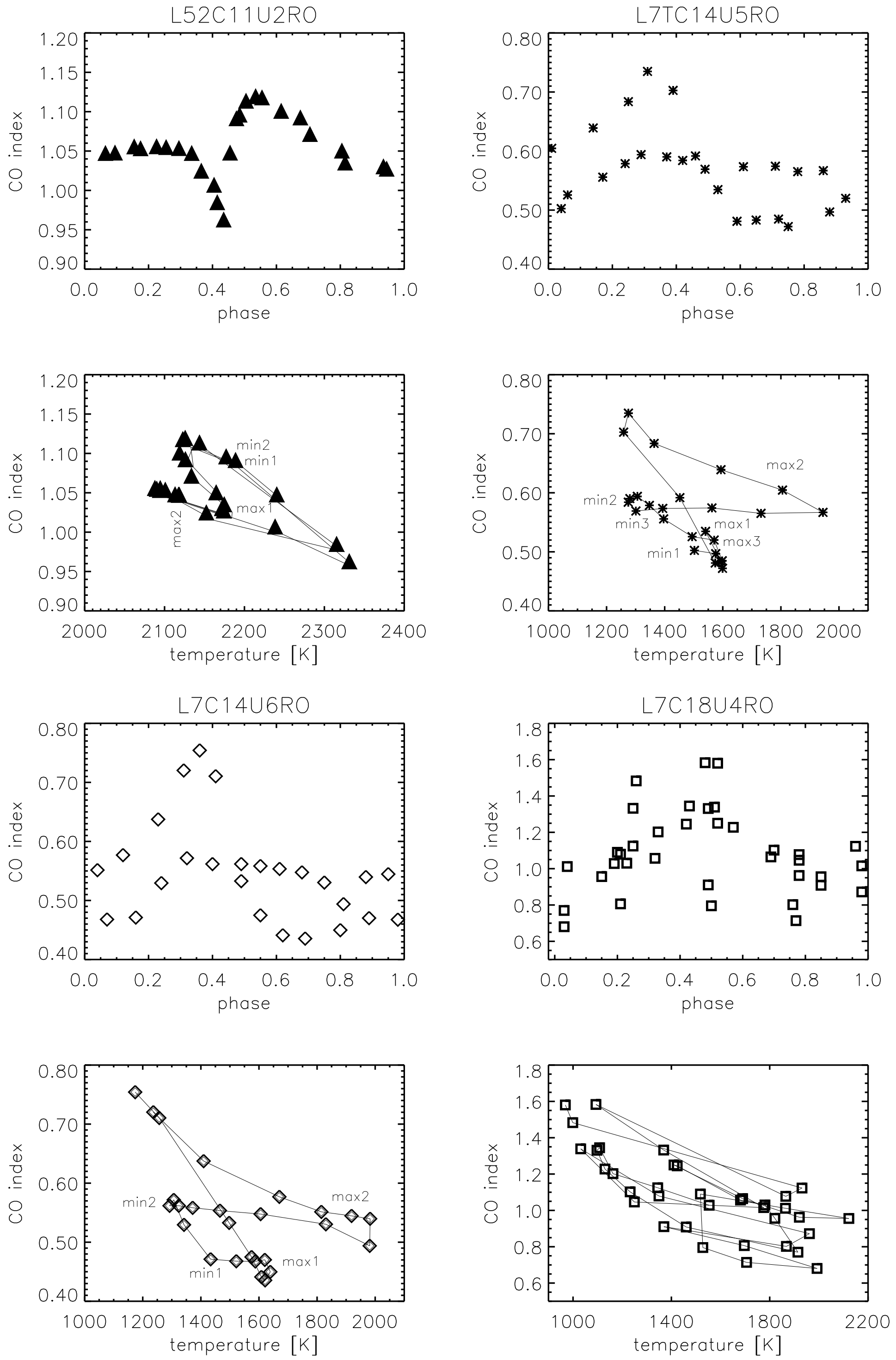

Figure 4.35: The CO index versus phase and versus temperature at $\tau_{\rm Planck} = 1$ for models L52C11U2RO, L7TC14U5RO, L7C14U6RO, and L7C18U4RO. In all cases except for L7C18U4RO, the positions of the indices at minimum and maximum phase are labeled appropriately.

variation in the C_2 index amounts to ≈ 0.4. Model L7C14U6RO shows the same behaviour as model L7TC14U5RO. For model L7C18U4RO, the variation of the C_2 index amounts to ≈ 0.9.
C_2 index versus temperature: In all models except in model L52C11U2RO the maxima have higher C_2 indices than the corresponding minima.

Fig. 4.36 shows the CO index versus the *colour* index (upper left panel), the C_2 index versus the *colour* index (lower left panel), and the CO index versus the C_2 index (upper right panel) for all four dynamical models. Diamonds denote the phases of model L7C14U6RO, asterisks the ones of model L7TC14U5RO, squares the ones of model L7C18U4RO, filled triangles the phases of model L52C11U2RO, and grey small diamonds show the locations of the spherical hydrostatic models for comparison.

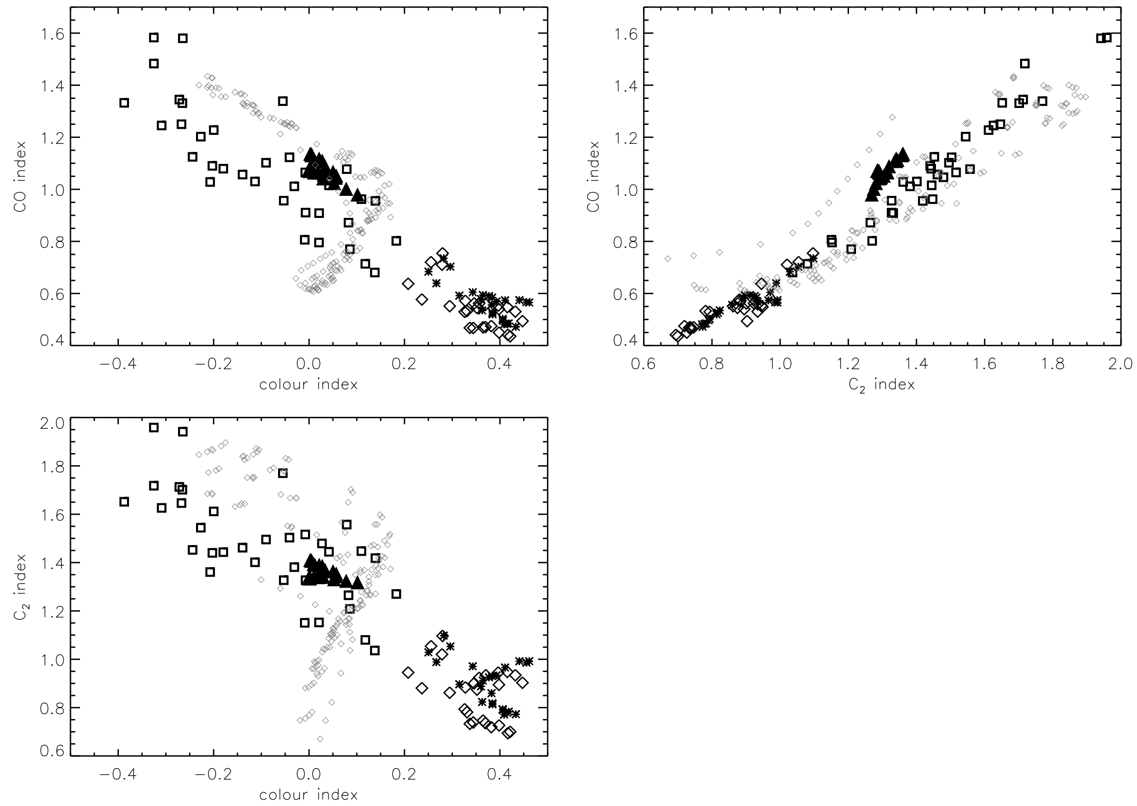

Figure 4.36: CO index versus the *colour* index (upper left panel), the C_2 index versus the *colour* index (lower left panel), and the CO index versus the C_2 index (upper right panel) for all four dynamical models. Diamonds denote the phases of model L7C14U6RO, asterisks the ones of model L7TC14U5RO, squares the ones of model L7C18U4RO, filled triangles the phases of model L52C11U2RO, and grey small diamonds show the locations of the spherical hydrostatic models for comparison.

4.6.4 Comparison of theoretical with observational results

To check the dependencies of the Tanaka indices on the effective temperature we took stars from the sample of Tanaka et al. (1990, 1992, 1996) for which Ohnaka & Tsuji (1996) listed effective temperatures. This selection restricts our discussion of the temperature dependence to AGB stars of irregular and semi-regular type. However, assigning to observations of Miras and SRa's effective temperatures, which had been measured at other pulsational phases and epochs, would not help for an investigation of the temperature dependencies due to their strong variability. We even have to note that the scatter due to assigning the effective temperatures derived in Ohnaka & Tsuji (1996) to our data of irregular and semi-regular variables at all epochs is considerable. Figure 4.37 shows *colour* index, CO index and C_2 index versus effective temperature and two-colour diagrams for these "Ohnaka" stars.

1. *Colour index versus effective temperature*: The hydrostatic models do not show a unique dependence of the *colour* index on the effective temperature. Contrary to the behaviour of the hydrostatic models, all our dynamical models show larger *colour* indices for higher temperatures. The reason for this - on first sight - discrepancy is that all our dynamical models have effective temperatures below ≈ 3000 K, i.e. below the value where the turning point in the relation between the *colour* index and the effective temperature occurs for the hydrostatic models (see Fig 4.32). At effective temperatures below ≈ 3000 K, the hydrostatic models predict the same behaviour of the *colour* index with temperature as the dynamical models. In the upper left panel of Fig. 4.37, the observed *colour* index is plotted versus the effective temperature for the Ohnaka stars. The observations suggest that a relation giving a lower *colour* index at higher effective temperatures prevails at least in the temperature range between 2900 and 3300 K. The scatter in the observational data is high which must be attributed to our way of assigning effective temperatures to the observations and to the variability of the stars. If we compute mean values of the *colour* index for the observations with effective temperatures as low as 3000 K, the resulting mean values match very closely the ones of our hydrostatic models.

2. *CO index versus effective temperature:* The hydrostatic models and the dynamical models L52C11U2RO and L7C18U4RO show larger CO indices for lower effective temperatures. The other two dynamical models show in the mean the same behaviour. In model L52C11U2RO (as well as in all hydrostatic models where it is impossible to account for dynamic phenomena), no stellar wind formed and hence the CO index cannot be reduced by emission contributions from a shell. The same applies for model L7C18U4RO

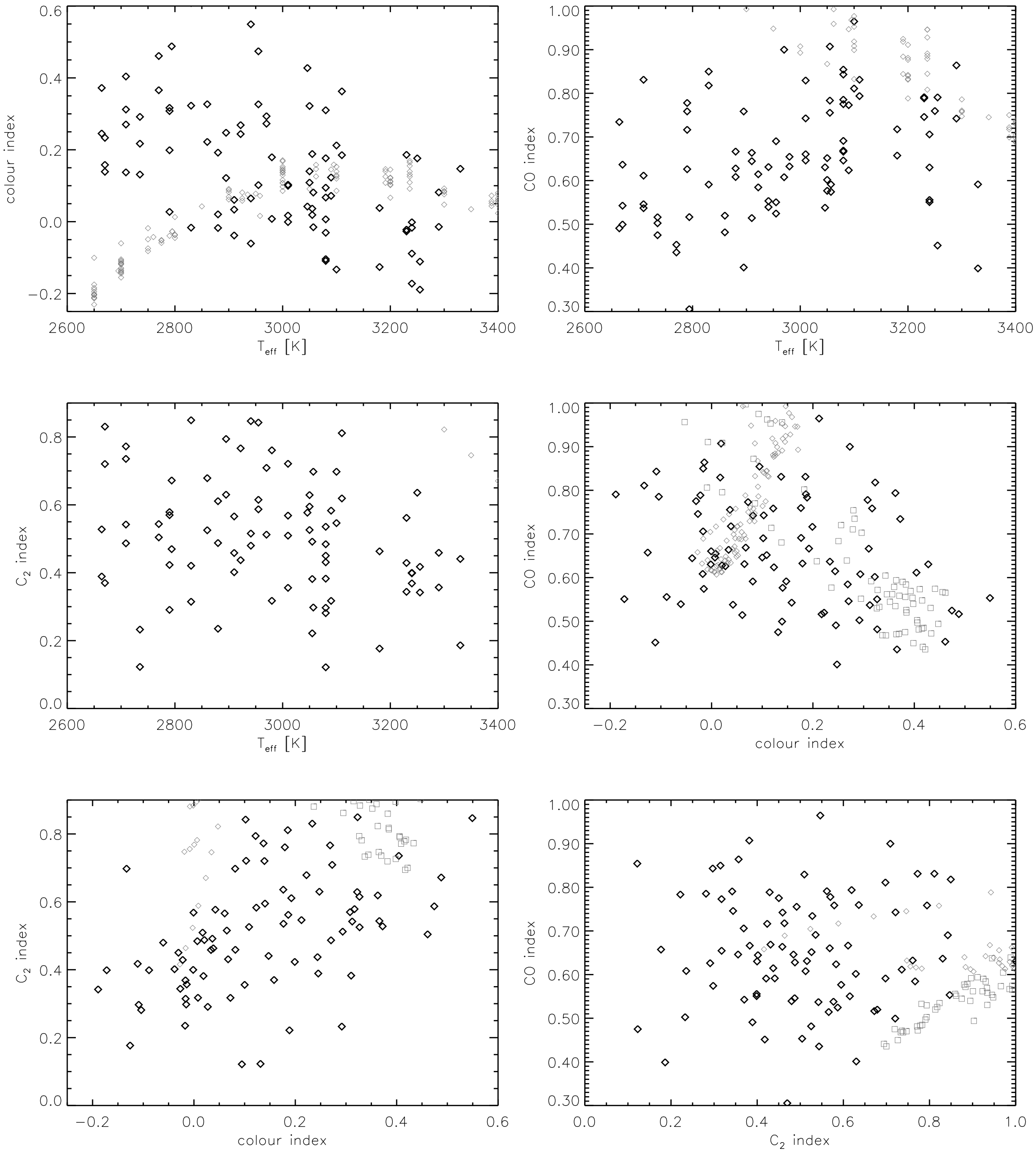

Figure 4.37: *Colour* index, CO index, and C_2 index versus effective temperature, and two-colour diagrams for the Ohnaka stars. The grey small diamonds denote hydrostatic models, grey small squares dynamical models.

where the resulting wind is too weak that emission contributions occur. The Ohnaka stars do not show a clear correlation between the CO index and the effective temperature. The values of the model CO indices lie above the observed ones.

3. *C_2 index versus effective temperature:* The hydrostatic models and all dynamic models show higher C_2 indices at lower temperatures. The observations indicate a similar behaviour, but the values of the model C_2 indices lie quite above the ranges of the observed ones.

4. *CO index versus C_2 index:* The hydrostatic (see Fig. 4.33) and the dynamic models (see Fig. 4.36) predict higher C_2 indices for higher CO indices. The Ohnaka stars (lower right panel of Fig. 4.37) and all the observations of Tanaka et al. (see Fig. 4.31) do not show a clear correlation between these two indices. However, the inverse relation of what is predicted by our models is seen when plotting semi-regular variables only. The observed values of the CO and the C_2 index cannot be well reproduced by our models.

5. *CO index versus colour index:* The observations show barely any trend of the CO index with the *colour* index. The dynamical models and the hydrostatic models with effective temperatures below 3000 K give the following trend: higher CO indices are found at higher *colour* indices. The observed high *colour* indices (> 0.2) can only be reproduced by dynamical models with a pronounced stellar outflow.

6. *C_2 index versus colour index:* The Ohnaka stars show higher C_2 indices for higher *colour* indices. Contrary to that, when plotting all observations of the sample of Tanaka et al., no clear correlation is visible anymore between these two indices. Hydrostatic models with effective temperatures down to 3000 K roughly reproduce the observed behaviour of the Ohnaka stars. Dynamical models predict the inverse trend of what is observed; this can be attributed to their low effective temperatures (< 3000 K). Hydrostatic models with effective temperatures below 3000 K fail to describe the observed trend. The observed absolute values of the C_2 index cannot be well reproduced by any of our models.

4.6.5 Conclusions

Plane parallel and spherical hydrostatic models are able to reproduce the trends of the *colour*, CO, and C_2 indices (at least partly) correctly. The behaviour of the *colour* index with effective temperature can be understood as follows: for stars with high effective temperatures the flux at 6000 cm^{-1} is higher than the one at

$4500\,\mathrm{cm}^{-1}$ (hence the *colour* index is a negative number), at certain effective temperatures the flux at $6000\,\mathrm{cm}^{-1}$ equals the one at $4500\,\mathrm{cm}^{-1}$ (*colour* index gets 0), at even lower effective temperatures the flux at $6000\,\mathrm{cm}^{-1}$ is lower than the one at $4500\,\mathrm{cm}^{-1}$ (hence the *colour* index is a positive number). The reason why our models fail to reproduce the observed behaviour is that wavenumber $6000\,\mathrm{cm}^{-1}$ is not a continuum point in models with effective temperatures lower than 3000 K, thus the trend reverses (see Fig. 4.32). The observational data (Ohnaka stars) are too scarce at low effective temperatures to test the model predictions. If the model predictions prove to be correct in the future, then the *colour* index proposed by Tanaka et al. (1990, 1992, 1996) is a less suitable measure of the effective temperature of a star than previously thought. If further observational data prove that the model predictions are wrong, then the failure of the models is probably due to a problem with the opacities, in particular with the C_2 opacities.

Dynamical models fail to reproduce the trend of the *colour* index with temperature correctly (in accordance with the failure of hydrostatic models with such low effective temperatures). The full range of the observed *colour* indices is covered by our dynamical models. Dynamical models with a pronounced stellar outflow reproduce the observed high *colour* indices; actually the effect of dust surrounding the star on the *colour* index is much larger than the effect of changing the effective temperature in a hydrostatic model on the *colour* index. Our observations contain dustless stars as well as stars with dust; one of the reasons for the large spread of the data points in Fig. 4.37 might well be due to the fact that both "types" of stars are plotted together, another reason is the variability of the stars.

A remarkable feature concerning the dynamical model indices is their multiperiodicity. This illustrates that although the main contributions to the features measured by the indices come from regions close to the photosphere, layers from further outside also contribute to the features.

Hydrostatic as well as dynamic models predict larger C_2 and CO indices than what is observed. One of the pseudo continuum points used to calculate the C_2 index is problematic in the observations due to its location close to a region where the Earth's atmosphere prevents reliable observations. Additionally, this pseudo continuum point is not a good continuum point for stars with low effective temperatures. However, due to the fact that we are also not able to reproduce the observed CO index values another more severe problem must exist. As far as possible we tried to calculate the indices in the same way for the observations and the models. The observations are FTS spectra where no absolute fluxes can be recovered, instead we have intensities between 0 and 1. However, ideally this should not make a difference if the shape of the FTS spectra is recovered correctly. This is a tricky attempt and although Tanaka et al. (1990, 1992, 1996) observed reference star spectra each night this might be the main problem for the comparison of their observations with our model spectra. As our models are able to fit the spectra of at least a few AGB stars which are also included in the large sample of Tanaka et al. (see e.g. Sect. 4.2.3, Sect. 4.7.3 or Sect. 4.8) in the same wavelength range where the indices are measured, we are confident that the disagreement originates mainly in problems with the recovering of the correct shape of the spectra.

4.7 ISO Spectra

4.7.1 The Satellite

The Infrared Space Observatory (ISO) had various capabilities to make photometric, polarimetric, imaging, and spectroscopic observations between 2.4 and 240 μm. The satellite was essentially a large cryostat containing more than 2000 litres of superfluid helium at launch to maintain the telescope at temperatures between 2 and 8 K. It was launched on November 17, 1995 and operated until April 8, 1998. The ISO telescope was a 60 cm diameter Richey-Chrétien system. Four instruments were operated on board: a Short-Wavelength-Spectrometer (SWS), a Long-Wavelength-Spectrometer (LWS), a Photo-Polarimeter (PHOT) and a Camera (CAM).

All the observations used here were obtained with the SWS (de Graauw et al. 1996). Therefore, only the properties of this instrument will be discussed briefly. The SWS provided medium and high spectral resolution in the infrared. Its grating spectrometers cover the wavelength region 2.36$-$45.2 μm, with an overall spectral resolution of about 1000. Table 4.6 gives the wavelength coverage and the resolution of the SWS "Astronomical Observation Templates" (AOT) bands for the modes we used. The SWS has 48 detectors in total, 12 for each band. All our spectra were taken either with AOT01, i.e. they are full grating scans (2.36 μm to 45.2 μm) or with AOT06 where mostly only wavelength ranges of special interest were monitored (see Table 4.7). The scanning speeds of AOT01 were either 1 or 2 which results in a typical resolution of 400 (Leech et al. 1998). Detailed information about the instrument can be found in the SWS Observer's Manual (http://www.iso.vilspa.esa.es/manuals/HANDBOOK/VI/swshb).

The spectra to be discussed in the following sections are part of different observational programs. Table 4.7 summarises the properties of the spectra. For the SWS01 spectra we introduce a quality flag "Q" which is either 1or 2 depending on the correction factors which were necessary to join AOT bands 1A to 3D to obtain a single spectrum covering the whole wavelength range. If none of the applied factors exceeded 1.3 or was lower than 0.7, the quality flag equals one. If single applied factors were higher or lower than these values, we assigned the quality flag 2 to the spectrum. For SWS06 spectra, a quality flag is only given if the full wavelength range was observed. All spectra discussed in this work are available at the ISO data archive at http://www.iso.vilspa.esa.es/ida/index.html.

4.7.2 Data reduction

The pipeline processed data (OLP versions 8.7 and 9.5) were further reduced with the ISO Spectroscopic Analysis Package (ISAP; http://www.ipac.caltech.edu/iso/

Table 4.6: Properties of the AOT bands

band	wavelength[1] [μm]	$R = \lambda/\Delta\lambda$ speed 1[2]	$R = \lambda/\Delta\lambda$ speed 2[2]
1A	2.38 – 2.61	540 – 606	465 – 522
1B	2.59 – 3.02	416 – 478	358 – 412
1D	3.00 – 3.55	515 – 665	444 – 573
1E	3.50 – 4.09	330 – 440	285 – 379
2A	4.06 – 5.35	439 – 663	378 – 571
2B	5.27 – 7.07	296 – 374	256 – 322
2C	6.94 – 12.2	373 – 603	322 – 520
3A	11.9 – 16.46	426 – 528	369 – 460
3C	16.3 – 19.5	670	580
3D	19.4 – 29.1	400 – 427	347 – 370
4	27.6 – 45.2	562 – 618	490 – 538

[1] wavelength ranges used for the reduction
[2] values according to Rosario (1998)

isap/isap.html). Most reduction steps are similar for AOT01 and AOT06 spectra. For AOT01 as well as for AOT06 data “cook books” for the reduction exist (http://www.ipac.caltech.edu/iso/sws/sws.html). We will only recall briefly the most important reduction steps here and those things which cannot be found in the “cook books”. First of all we use the available function “Remove bad data” to eliminate all data points which have been marked as “bad” by the pipeline. Remaining bad data points which have not been identified by the pipeline are removed manually. Then we look at each of the 12 AOT bands separately. First we cut the bands shortwards and longwards of those wavelengths where the data are not reliable anymore. Usually short regions of overlap between the 12 AOT bands remain. As a next step we check whether one or more of the 12 detectors produces weird spectra. This happens quite often, with increasing frequency the longer the wavelength of the spectrum. Several detectors systematically behave strangely (e.g. 21, 26, 29, 36). Elimination of the data points of such detectors increases dramatically the quality of the resulting spectra! The next thing to check is whether a significant offset exists between the data points recorded in scan direction 1 (decreasing wavelength) and the ones recorded in scan direction -1 (increasing wavelength) due to memory effects. For most spectra, a significant offset between the two scan directions was found in band 2C (7 μm to 12 μm). In such cases we rejected the down-scan direction (-1) in SWS01 data. In some of the SWS06 spectra, we also find a difference between up and down scan. Because the

Table 4.7: ISO spectra

name	mode of observation	wavelength [μm]	date	exposure time [s]	archive number	proposal	spectrum	Q(2)
BS 8411	SWS01	2.36 – 45.20	08.05.1997	1440	53904837	sprice	K3 III	1
HD 149447	SWS01	2.36 – 45.20	11.03.1998	6538	84700107	ldecin	K6 III	1
α Tuc	SWS01	2.36 – 45.20	30.03.1998	6539	86602401	ldecin	K3 III	2
HR 6705	SWS01	2.36 – 45.20	26.03.1997	1140	49603004	SWS_CAL	K5 III	1
HR 6688	SWS01	2.36 – 45.20	24.01.1996	1144	06800697	SWS_CAL	K2 III	1
R Scl	SWS01	2.36 – 45.2	21.07.1996	1912	24701012	jhron	C6,4	1
R Scl	SWS01	2.36 – 45.2	03.01.1997	1912	41401514	jhron	C6,4	1
S Cep	SWS01	2.36 – 45.2	05.12.1997	1140	75100424	fkerschb	C7,3	1
S Sct	SWS01	2.36 – 45.2	29.04.‘996	1834	16401849	tdejong	C6,4	2
TT Cyg	SWS01	2.36 – 45.2	03.05.1997	1140	56100935	ttsuji	C5,4	1
TT Cyg	SWS01	2.36 – 45.2	20.11.1997	1140	73600518	fkerschb	C5,4	1
TX Psc	SWS01	2.36 – 45.2	24.05.1997	1140	55501379	sprice	C7,2	1
TX Psc	SWS01	2.36 – 45.2	11.12.1997	1912	75700419	fkerschb	C7,2	1
V460 Cyg	SWS01	2.36 – 45.2	11.01.1997	1140	42201734	ttsuji	C6,4	1
V460 Cyg	SWS01	2.36 – 45.2	29.11.1997	2208	74500512	fkerschb	C6,4	1
VX And	SWS01	2.36 – 45.2	17.01.1997	2912	42801502	ttanabe	C4,5	1
W Ori	SWS01	2.36 – 45.2	22.03.1998	3454	85801604	ablanco	C5,4	1
R Scl	SWS06	3,19 – 4.51	25.05.1997	780	55701822	keriksso	C6,4	–
		4.83 – 5.30						–
RV Aqr	SWS06	2.60 – 5.30(1)	17.04.1997	1550	51801745	keriksso	C6,3	–
		12.96 – 27.30(1)						–
S Cep	SWS06	2.60 – 5.30(1)	28.04.1997	1140	52902049	keriksso	C7,3	–
		12.96 – 27.30(1)						–
S Cep	SWS06	2.83 – 5.30	05.12.1997	3058	75100425	fkerschb	C7,3	–
		12.96 – 15.06						–
SS Vir	SWS06	2.44 – 3.02	14.06.1996	1028	21100139	ttsuji	C5,3	–
		12.96 – 15.06						–
T Lyr	SWS06	2.36 – 45.2	12.11.1996	8752	36100832	ttsuji	C6,5	1
TT Cyg	SWS06	2.44 – 3.02	30.05.1997	1140	56100936	ttsuji	C5,4	–
		12.96 – 15.07						–
TT Cyg	SWS06	2.83 – 5.30	20.11.1997	2208	73600526	fkerschb	C5,4	–
TX Psc	SWS06	2.36 – 45.2	26.11.1996	7888	37501937	ttsuji	C7,2	1
V Aql	SWS06	2.94 – 3.04	19.09.1996	722	30800814	keriksso	C5,4	–
		4.27 – 4.61						–
		13.56 – 14.35						–
V Aql	SWS06	3.19 – 3.67	22.04.1997	778	52301925	keriksso	C5,4	–
		4.83 – 5.33						–
V CrB	SWS06	2.36 – 45.2	29.07.1996	8752	25502252	ttsuji	C6,2	1
V Cyg	SWS06	2.99 – 3.44	28.10.1996	2498	34601972	tdejong	C5,3	–
		3.52 – 3.71						–
		4.42 – 5.21						–
		7.18 – 10.21						–
V460 Cyg	SWS06	2.83 – 5.30	29.11.1997	2208	74500527	fkerschb	C6,4	–
VX And	SWS06	2.99 – 3.51	17.01.1997	2938	42801501	ttanabe	C4,5	–
		4.99 – 10.02						–
WZ Cas	SWS06	2.36 – 45.2	22.07.1996	8752	24801029	ttsuji	C9,2	1
Y CVn	SWS06	2.94 – 3.04	30.11.1996	724	34600408	keriksso	C5,5	–
		4.28 – 4.61						–
		13.56 – 14.35						–
Y CVn	SWS06	3.19 – 3.67	05.07.1997	778	59700524	keriksso	C5,5	–
		4.83 – 5.33						–
IRC+10216	SWS06	2.36 – 45.2	02.06.1996	7962	19900204	jcernich	C	1

(1) not the whole range covered, (small) gaps in between
(2) "Q" is a quality flag, it is either 1 or 2, depending on the correction factors necessary to join the bands

down scan has not been monitored immediately after the up-scan (as it is done in the SWS01) and therefore it is not clear which of the two scan directions is "more correct", the average of the two scan directions has been used. At this stage of the reduction we are left with spectra of each of the 12 (or less if detectors have been removed) detectors and we now have to find an average of the 12 spectra. Two possibilities exist for this averaging process and since we put a lot of effort into how to do this best, we will discuss this process in more detail below.

We process each of the 12 AOT bands in the same way as described above. We then have 12 pieces of spectra which we have to join together somehow in order to obtain one spectrum covering the full wavelength range between 2.4 and 45 μm. For the joining of the bands we use band 1A as a flux reference. Between all 12 bands short regions of overlap exist. We calculate the mean flux values of the neighbouring bands in the overlap region. We apply multiplicative (see discussion below) constants to join the bands together. As a final step we smooth the spectra and rebin them to the desired resolution.

The averaging of the detectors and the way of joining the 12 bands together is crucial for the final appearance of the ISO spectra and hence for the interpretation of the data. Following the instructions of the ISO calibration team, the individual detectors in a band were corrected to a mean value by additive constants if the flux was below 200 Jy and by multiplicative corrections otherwise. The multiplicative corrections at high flux levels are necessary due to the fact that gain effects dominate the spectrum. On the other hand, the dark current dominates at low flux levels, so that the additive corrections have been suggested for the flux range below 200 Jy. For the joining of the bands, originally the same procedure (additive constants if the flux is below 200 Jy; multiplicative constants otherwise) was suggested by the ISO calibration team. However, this change of the way of correction at a certain flux level influences the overall shape of the spectrum dramatically for most of our sample stars as they have low fluxes. We tested different reduction methods by comparing five K giants and three moderately variable AGB stars surrounded by almost no dust with the IRAS fluxes and continua of model spectra. Based on these results we concluded in accordance with members of the ISO calibration team (Kieron Leech, private communication):

1. If the flux in a band exceeds $\approx$ 200 Jy then correct the individual detectors to a mean value multiplicative, if the flux is below $\approx$ 200 Jy use additive corrections.

2. To join the bands, we use multiplicative corrections allover the spectrum, no matter what the actual flux level is. The errors due to incorrect dark subtraction in the pipeline should have been corrected already by shifting the individual detectors. Therefore, the multiplicative correction is an appropriate method for the whole spectrum when joining the different bands.

3. At fluxes lower than ≈ 40 Jy, the results are sometimes very sensitive to the treatment of bands 2A and 2C.

4. At flux levels below ≈ 10 Jy neither spectral features nor the slope of the spectrum can be trusted.

5. The IRAS fluxes are always higher than the corresponding ISO fluxes.

6. Use the IRAS 12 and 25 μm fluxes to cross-check the reduction as well as model continua in the case of stars with small amounts of dust. The dust, if present, should not vary much; therefore, the IRAS fluxes are probably the best references.

K giants

To develop a reliable reduction method and to get reliable estimates of the uncertainties, spectra of 5 K giants with different flux levels were extracted from the ISO archive. They are listed at the beginning of Table 4.7. Despite the presence of CO and SiO bands, the spectra of the K giants should be continuum like. The spectra were once reduced following the original instructions of the ISO calibration team (multiplicative corrections if $F > 200$ Jy, additive corrections otherwise for detectors and joining of the bands); in a second attempt, only multiplicative corrections were applied to join the bands throughout the whole spectral range. Additionally, the IRAS fluxes at 12 and 25 μm and model continua were used for comparison. We will call the first method "additive" in the following and the second one "multiplicative". Figure 4.38 shows the results for three of the K giants, the K2 III star HD149447, the K6 III star HR6688, and the K3 III star BS8411. The spectrum of HD149447, reduced with the "additive" method becomes unreasonably flat and the corrections needed were high for joining the individual pieces of the spectra together. In comparison to the IRAS 25 μm flux and the model continuum, the spectrum reduced with the "multiplicative" method had a better overall shape. The same applies in an even more severe fashion to the remaining two K giants: HR6688 (middle panel of Fig. 4.38) and BS8411 (lower panel of Fig. 4.38). The same problems arise in the case of the moderately varying carbon stars V460 Cyg and TT Cyg.

4.7.3 Spectra of moderately variable stars

Jørgensen et al. (2000) presented a detailed discussion of SWS01 spectra of the three moderately variable carbon stars TX Psc, V460 Cyg, and TT Cyg. They compared the observed spectra with spectra based on *plane parallel* model atmospheres. We show "fits" of SWS01 and SWS06 spectra of TX Psc, V460 Cyg, TT Cyg,

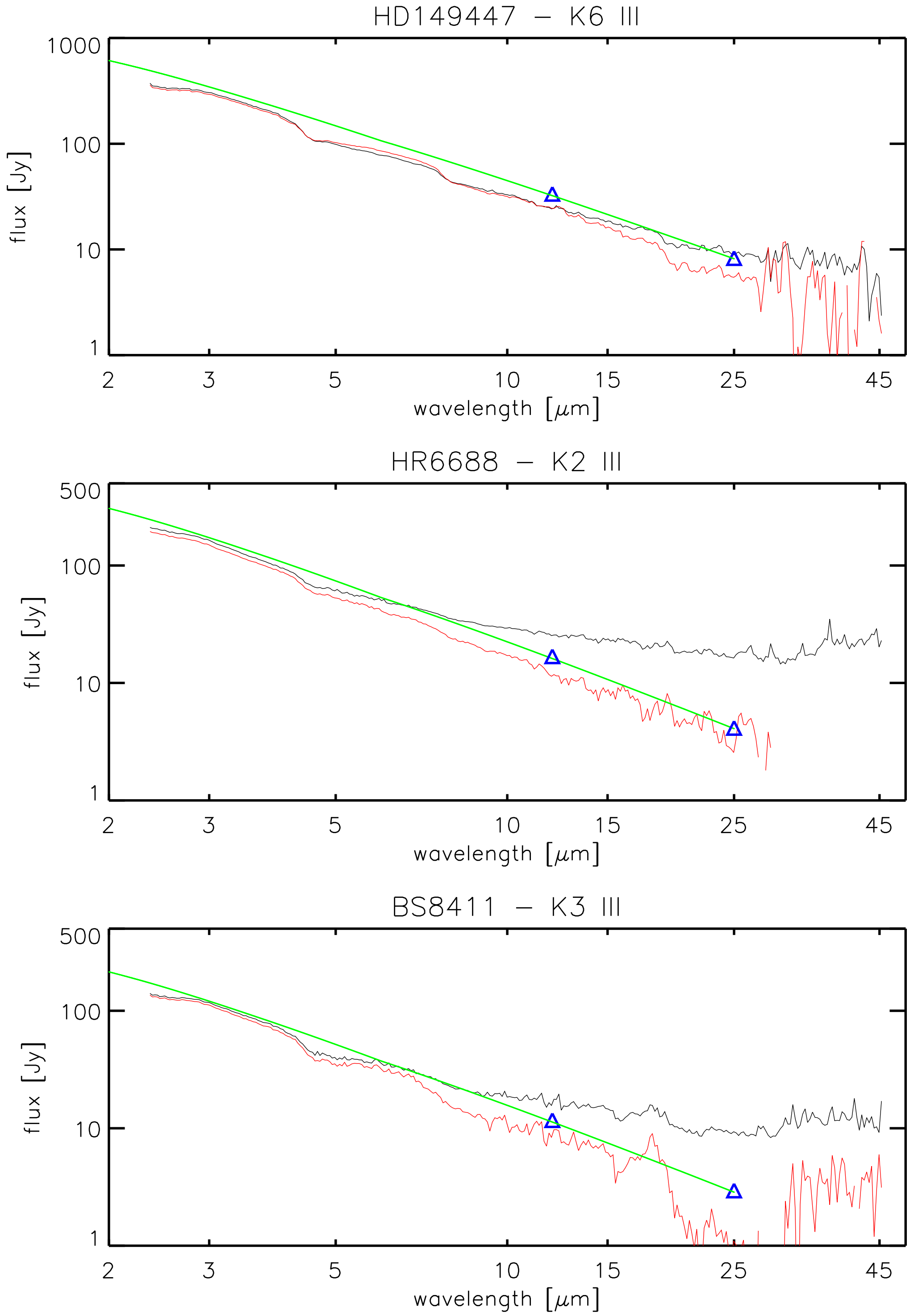

Figure 4.38: ISO spectra of the K giants HD149447, HR6688 and BS8411 reduced with the "additive" (black line) and the "multiplicative" method (red line). The IRAS 12 and 25 μm fluxes (blue triangles) and a model continuum (green line) are shown for comparison.

S Sct, W Ori, and WZ Cas based on *spherical* model spectra. For the three stars in common we can directly compare the results. The $^{12}C/^{13}C$ ratio and the microturbulent velocity were not fitted; as in Jørgensen et al. (2000), we assumed for all investigated model spectra $^{12}C/^{13}C = 89$ and $v_{mic} = 3\,km/s$. Thus, in the case of fits with plane parallel model spectra the parameters T_{eff}, $\log(g)$, and C/O had to be determined. In the spherical case one additional parameter, the mass of the star, is needed.

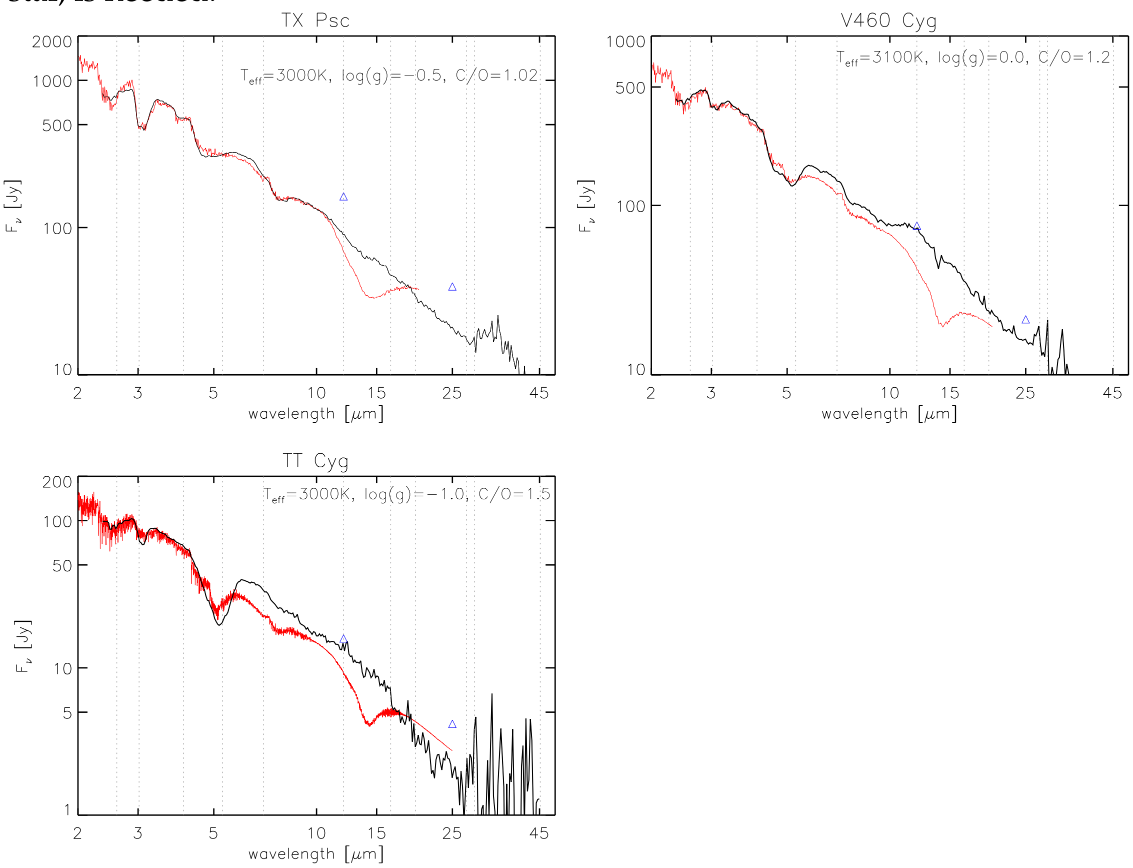

Figure 4.39: ISO SWS01 spectra of TX Psc (upper left panel), V460 Cyg (upper right panel), and of TT Cyg (lower left panel) plotted together with the best fitting synthetic spectra based on *plane parallel* model atmospheres. The model parameters are labeled in the plot. The blue triangles denote the IRAS fluxes. The grey lines show the various band borders of the ISO-SWS. Adopted from Jørgensen et al. (2000).

Figure 4.39 shows the ISO SWS01 spectra of TX Psc (upper left panel), V460 Cyg (upper right panel), and of TT Cyg (lower left panel) plotted together with the best fitting synthetic spectra based on *plane parallel* model atmospheres. The model parameters are labeled in the plot. The blue triangles denote the IRAS fluxes. We see that the observed spectrum of TX Psc can be fitted reasonably well over the whole wavelength region shorter than 10 μm. For the remaining two stars, V460 Cyg and TT Cyg, the fits are not as good as for TX Psc. The discrepancies between observed and model spectra start around 6 μm in those cases. The main cause for the better agreement of observed and model spectra for TX Psc is that the other two stars are surrounded by larger amounts of dust. The influence of the dust is particularly well visible around 11 μm; V460 Cyg shows a weak SiC emission feature. However, it should be noted that the small discrepancies between observed and model spectra (especially in the case of V460 Cyg) between 6 and 10 μm may well be due to the flux uncertainty of the ISO-SWS. The wavelength region longwards of 10 μm will be discussed separately in Sect. 4.7.5.

Figure 4.40 shows two ISO SWS01 spectra of TX Psc (upper left panel), two spectra of V460 Cyg (upper right panel), two spectra of TT Cyg (middle left panel), one spectrum of S Sct (middle right panel), one spectrum of W Ori (lower left panel), as well as a SWS06 spectrum of WZ Cas (lower right panel) plotted together with the "best fitting" synthetic spectra based on *spherical* model atmospheres (red and green curves). Blue triangles denote the IRAS fluxes. The grey lines show the various band borders of the ISO-SWS. In the cases where two observed spectra are plotted one of them has been shifted for illustration purposes. For a fit of the observed spectra with spherical model spectra different parameters were needed than in the plane parallel case. Table 4.8 summarises the results of our fits. We stress that our grid of spherical models was not large enough to really obtain "best fits". Therefore, the values given in Table 4.8 for the spherical "fits" should be taken with caution; they are listed to illustrate that investigations using *spherical* models instead of plane parallel ones lead to different results.

The ISO spectrum of TX Psc fitted with the red model spectrum is the same as the one fitted with a plane parallel model spectrum in Fig. 4.39; good fits in the plane parallel case were obtained with the parameter sets [$T_{\rm eff}$/log(g)/(C/O)] of [3000/$-$0.5/1.02] and [3000/0.0/1.1], for the spherical case we reached a best fit for the parameter set [$T_{\rm eff}$/log(g)/(C/O)/mass] of [3100/$-$0.1/1.1/2.25]. We have to stress however that our small grid of spherical models included only models with either 1 or 2.25 $M_\odot$ and three different luminosities for each effective temperature. We have to note as well that the fits presented in the following are never necessarily unique fits. The model parameters of the green line in the TX Psc plot are: $T_{\rm eff} = 3200$ K, $\log(g) = -0.4$, C/O = 1.1, $M = 2.25\,M_\odot$. Thus, we need a slightly higher effective temperature (100 K higher) and a considerably higher luminosity to describe the observed spectrum of TX Psc reasonably well. We see that the spherical spectra are also able to describe the wavelength range between 2.4 and 10 μm well. There remains however, some discrepancy between 5.5 and 7 μm which was not present in the fits with plane parallel spectra. This discrepancy is visible for all six stars investigated here, therefore it will be dis-

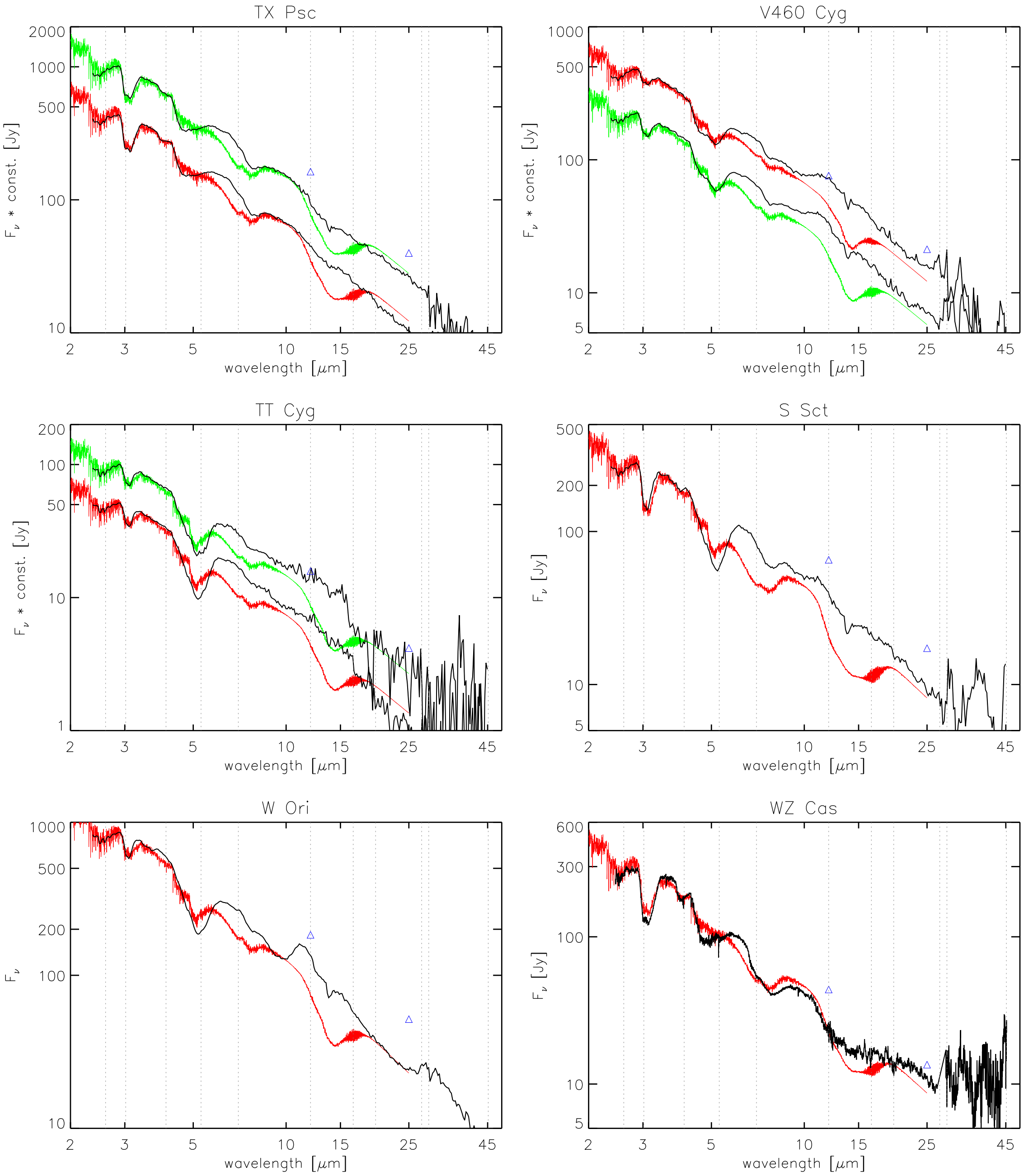

Figure 4.40: SWS01 spectra of TX Psc (upper left panel), V460 Cyg (upper right panel), TT Cyg (middle left panel), S Sct (middle right panel), and of W Ori (lower left panel), as well as a SWS06 spectrum of WZ Cas (lower right panel). The red and green curves show our best fit spherical model spectra, blue triangles denote IRAS fluxes. The grey lines show the various band borders of the ISO-SWS. Details are given in the text.

Table 4.8: Fit parameters

Star	Observing date	$T_{\rm eff}$ [K]	log(g)	C/O	mass [$M_\odot$]	pp/sph[1]
TX Psc	11.12.1997	3000	-0.5	1.02	–	pp
		3000	$+0.0$	1.10	–	pp
		3100	-0.1	1.10	2.25	sph
TX Psc	24.05.1997	3200	-0.4	1.10	2.25	sph
V460 Cyg	29.11.1997	3000	-0.5	1.20	–	pp
		2900	-1.5	1.10	–	pp
		3125	-0.1	1.40	2.25	sph
V460 Cyg	11.01.1997	3175	-0.1	1.40	2.25	sph
TT Cyg	20.11.1997	3000	$+0.0$	1.50	–	pp
		2900	-1.0	1.50	–	pp
		3125	-0.1	1.60	2.25	sph
TT Cyg	03.05.1997	3125	-0.1	1.60	2.25	sph
S Sct	29.04.1996	3000	-0.2	1.40	2.25	sph
W Ori	22.03.1998	3125	-0.1	1.40	2.25	sph
WZ Cas	22.07.1996	3100	-0.1	1.02	1.0	sph

[1] The fit parameters of the plane parallel spectra are adopted from Jørgensen et al. (2000)

cussed further below.

For V460 Cyg, a reasonable spherical fit needs a higher effective temperature (3125 instead of 3000 K) and a considerably higher C/O ratio (1.4 instead of 1.2) than a plane parallel fit to reproduce correctly the intensities of the 3 and the 5 μm features. The same applies to TT Cyg. For S Sct and W Ori we only attempted to describe the 3 and the 5 μm feature correctly. For a reasonable description of the 5 μm feature we needed much higher C/O ratios than what has been derived from optical spectra by Lambert et al. (1986), while our effective temperatures usually lie on the high temperature end of what has been published in the literature. For S Sct, Lambert et al. (1986) list a [$T_{\rm eff}$/(C/O)] of [2895/1.069]. We arrived at a set [3000/1.4]. For W Ori the discrepancy in $T_{\rm eff}$ is considerable, Lambert and coworkers list a [$T_{\rm eff}$/(C/O)] of [2680/1.16], we preferred [3125/1.4]. This illustrates the problems with obtaining "best fits", especially as long as all parameters are free parameters.

For a spectrum based on spherical model atmospheres the free parameters are: $T_{\rm eff}$, log(g), C/O, M, ^{12}C/^{13}C, and $v_{\rm mic}$. Usually, for giants one assumes a value of 3 km/s for $v_{\rm mic}$. The ^{12}C/^{13}C ratios published by various authors based on different wavelength regions where this ratio had been determined differ considerably in most cases (see the discussion in Sect. 4.2.3). Therefore, one is left with five parameters which can be varied within acceptable limits for AGB stars, which basically means that for a good fit of one star it is necessary to compute a grid of about 200 models. The reason that the amount of models to obtain a "best fit" is that large, is on one hand that the effects of $T_{\rm eff}$, log(g), and M work in opposite directions, and on the other hand that in the optical wavelength range (where up to now most of the information about stellar parameters was extracted) we have mainly CN and C_2 features which are less sensitive than the C_2H_2, HCN, and C_3 features to changes in $T_{\rm eff}$, log(g), and M.

A lower effective temperature causes a stronger 3 μm feature, a higher L, a higher M, and a higher C/O ratio weaken it. The dominating parameter is, however, $T_{\rm eff}$. For the 5 μm feature, the C/O ratio is the dominant parameter, a higher C/O ratio causes a stronger feature. On the other hand a higher $T_{\rm eff}$, lower M, and lower L weaken it. An additional problem in the computations are the considerable uncertainties in the C_2 and C_3 opacities, therefore it is not surprising that "fits" work usually well if the C/O ratio of the star is small (e.g. TX Psc and WZ Cas) and they become worse the higher the C/O ratio of a star becomes. In Sect 2.2 we mentioned that two (quite) different values for the $K_p(C_3)$ value exist; we arbitrarily adopted one of them. The choice of the $K_p(C_3)$ value strongly influences the intensity of the 5 μm feature and hence of the C/O ratio one derives from spectra in the ISO wavelength range.

The ISO SWS06 spectrum of WZ Cas (see Fig. 4.40) can be described well by our model spectrum. As in the case of TX Psc, the C/O ratio of WZ Cas is small. The low prevailing C/O ratio keeps uncertainties in the fits due to the small contributions of the C_2 and C_3 opacities low.

In all six stars we see a discrepancy between the observed and the *spherical* model spectra in the wavelength region 5.5 to 7μm. Our model spectra do not reproduce correctly the shape of the long-wavelength side of the C_3 feature, this is certainly due to the problems with the $K_p(C_3)$ value because we see this effect also in WZ Cas where the C/O ratio is well determined from optical spectra. We used the $K_p(C_3)$ value which gives a weaker C_3 feature at 5 μm for a fixed C/O ratio, this might explain why the C_3 features in our fits of TX Psc and WZ Cas are too weak. Close to 7 μm our spherical models predict too strong C_2H_2/HCN absorption. The fact that this problem does not show up in the *plane parallel* model spectra hints at an additional absorption originating from the outermost model layers (the spherical model structures have lower temperatures at a fixed pressure than plane parallel ones and hence the partial pressures of C_2H_2 and HCN are considerably higher in the spherical case). Hence, we must conclude that the uncertainties in the C_3, C_2H_2, and HCN opacities are the reason for the observed discrepancy in the wavelength region between 5.5 and 7 μm.

The fact that *plane parallel* model spectra seem to better "fit" the observations than *spherical* ones reflects nothing else than the spherical spectra being more sensitive to changes in fundamental parameters and to uncertainties in the opacities than the plane parallel ones. On the other hand, this tells us that further investigations should use *spherical* models exclusively.

4.7.4 Spectra of R Scl

Within our own ISO observing program, the spectral variations of a few representative AGB variables were monitored, among our carbon-rich targets the SRa variable R Scl is the star with the lowest amount of mass loss.

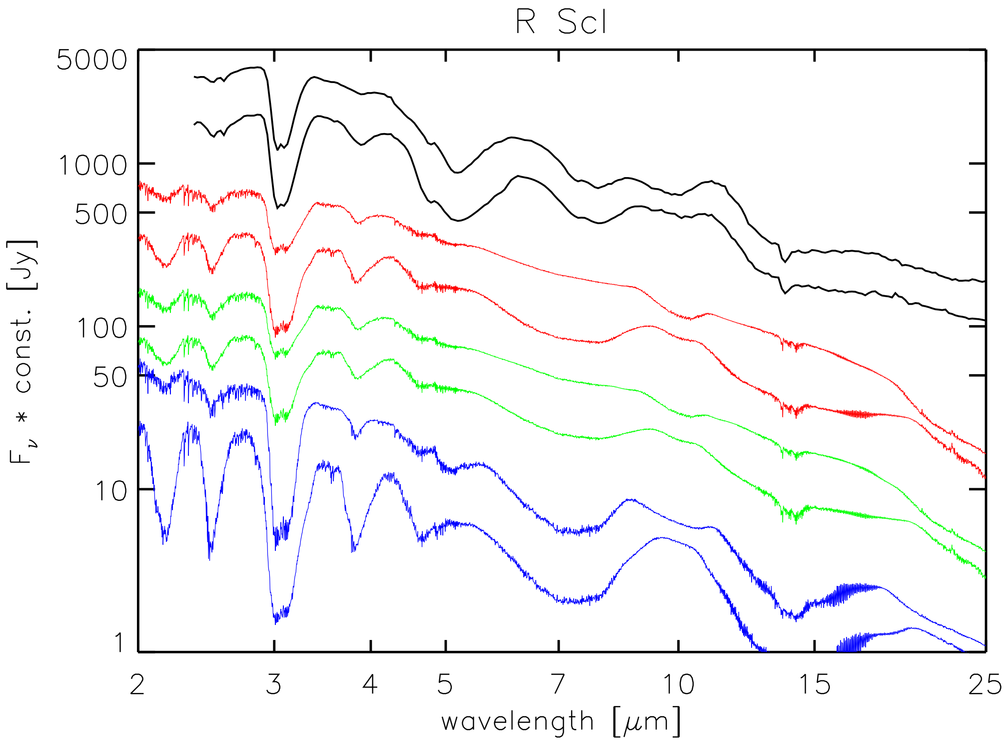

Figure 4.41: ISO SWS01 spectra of R Scl (black curves) observed closest to visual maximum (phase 0.9) and minimum light (phase 0.4). Red curves show spectra at maximum and minimum luminosity of model L7C14U6RO, green curves the ones of model L7TC14U5RO, and blue curves the one of model L7C18U4RO.

We selected the ISO spectra of R Scl observed closest to visual maximum (phase 0.9) and minimum light (phase 0.4) and compared them with synthetic maximum- and minimum-light spectra of our three dynamical models where the model structures were cut below 1000 K in order to eliminate the unrealistic strong emission around 7 and 14μm (see Sect. 3.3). In Fig. 4.41 the ISO SWS01 spectra of R Scl (black curves) observed closest to visual maximum (upper) and minimum light (lower) are plotted. Additionally we show spectra at maximum and minimum luminosity of model L7C14U6RO (red curves), spectra of model L7TC14U5RO (green curves), and spectra of model L7C18U4RO (blue curves). It is obvious on first sight that with none of these models we are able to present a quantitative fit of the observed spectra with dynamical model spectra. However, the dynamical models reproduce correctly the observed increase of the feature intensities at minimum light as compared to maximum light. The problems with the strong emission features are the key problem that must be solved before anything detailed can be said.

4.7.5 The 14 μm feature of carbon stars

In Sect. 4.7.3, we excluded the discussion of the wavelength region beyond 10 μm. Plane parallel as well as spherical hydrostatic models predict a deep absorption feature due to C_2H_2 and HCN around 14 μm. Compared to the computed spectra, the observed 14 μm band is quite weak in most stars, and it consists of, or includes a narrow, well defined absorption at 13.7 μm. If the 14 μm band indeed forms at photospheric depths and temperatures as it happens in self-consistent hydrostatic models, then it has to show up as very broad feature, because many hot-band transitions contribute to the observed band. The anharmonicity constants determining the widths of such an absorption feature in a hot gas are very well determined by laboratory experiments. Therefore, from the discrepancy between observations and models we can conclude that we do not see a pure photospheric spectrum in the long-wavelength region of the ISO spectra.

The idea of a so-called “warm molecular envelope” was introduced in the literature and discussed by several authors (e.g. Tsuji et al. 1997 and Yamamura et al. 1999) in order to explain the discrepancies between computed molecular bands and the observed cool stars-spectra. Basically, in the case of a “warm molecular envelope” one or more detached, relatively dense layers of molecular gas above the photosphere are introduced. Temperatures and densities are free parameters which can be adjusted to increase (i.e. absorption) or decrease (i.e. emission) the computed photospheric band intensities until they fit the observed intensities. The big disadvantage of such an approach to fit the 14 μm feature of carbon stars is that firstly one learns nothing about the real structure of the envelope due to the lack of self-consistency in this approach, and secondly that the 3 μm feature should respond similar to the changes in the temperature structure than the 14 μm feature. The intrinsic transition probabilities that give rise to the 3 and 14 μm bands are very similar, and the separation in the excitation energies of the vibrational levels that give rise to the hot-bands are almost identical in the two cases. This means that any temperature inversion in (or dense molecular layer above) the photosphere that weakens the 14 μm band would also weaken the

3 μm band.

Jørgensen et al. (2000) tried to simulate combined dust and gas spectra, firstly by adding a Planck function emission of low temperature to the photospheric spectrum and secondly by using the photospheric dust-free spectra as input to a program that computes dust envelopes. Based on these investigations, they propose that clumps of cool material with temperatures of about 500 K form in the upper part of the atmosphere and obscure about 10% of the surface area, and that the weak features seen around 13.7 μm originate in cooler layers above the region of such clumps.

The results of our dynamical models show that the contribution of the dust as well as emission due to the molecules C_2H_2 and HCN fill up the photospheric absorption feature with emission and the only part of the original feature which remains visible is the narrow feature around 13.7 (due to C_2H_2) and 14.0 μm (due to HCN). This is the case regardless of whether we cut the dynamical model structures below a certain arbitrary value (see Fig. 4.41) or not (see Fig. 3.17, 3.20, and 3.21).

In order to investigate the 14 μm feature of carbon stars in more detail, we extracted all stars from the ISO archive for which the 3 and 14 μm region was observed with the SWS06, i.e. with a resolution high enough to distinguish between emission and absorption lines. In Fig. 4.42 all these spectra are plotted with a resolution of 1000, in total there are only six stars where both wavelength ranges are covered. Aoki et al (1999) discussed already the 14 μm region of TX Psc, V CrB, and SS Vir. They identified HCN emission lines in TX Psc, and V CrB. A closer inspection of Fig. 4.42 suggests that other lines than the ones identified by Aoki and coworkers are in emission as well in the case of S Cep, WZ Cas, TX Psc, and TT Cyg. Therefore, we see that emission is present in the 14 μm region of carbon stars as predicted by our dynamical models, but the observed emission is weak.

T Lyr is the only star in our sample showing no SiC dust emission feature around 11 μm and a deep 14 μm feature. Additionally, it has strong 3, and 5 μm features as well as strong absorption in the 7 to 8 μm region. All of these features, except the 5 μm one, are due to a combination of C_2H_2 and HCN. The C_2H_2 contributions are stronger than the HCN ones in T Lyr. Contrary to all other stars in Fig. 4.42, with the exception of WZ Cas, it shows an additional feature around 12.3 μm. The shape of the spectrum of T Lyr as a whole suggests that we see a relatively pure photospheric spectrum of a cool carbon star. IRC+10216 on the contrary is a very dust enshrouded carbon star. It has basically no features shortwards of 10 μm (therefore it is excluded in the left panel of Fig. 4.42), but it shows the sharpest C_2H_2 feature at 13.7 μm of all stars in our sample. SS Vir shows also a narrow feature at 13.7 μm. S Cep and V CrB are cool enough for the contribution of C_2H_2 to dominate the 3 μm feature, both stars show broader absorption around 14 μm than the stars previously discussed. For TX Psc, WZ Cas, and TT Cyg the

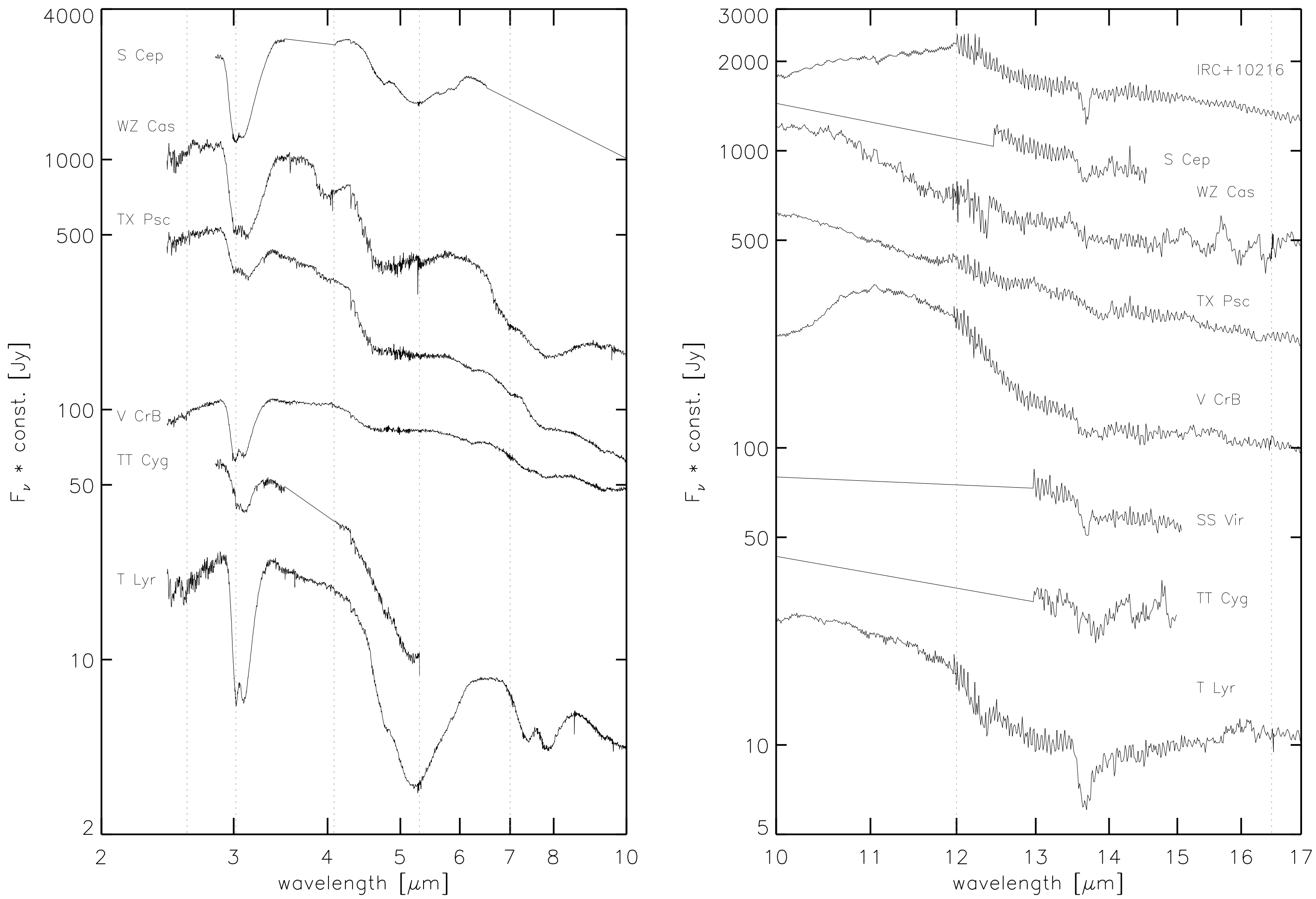

Figure 4.42: SWS06 spectra of carbon stars for which the 3 and the 14 μm region was observed simultaneously. The spectra have a resolution of 1000. Grey lines denote the band borders of the SWS.

contribution of HCN dominates the 3 μm feature, but for different reasons: TX Psc is too hot and the C/O ratio is too low in order that considerable amounts of C_2H_2 are formed; TT Cyg is a star with a high C/O ratio, but it is too hot to form huge amounts of C_2H_2; WZ Cas on the other hand is in principle cool enough, but there is not much carbon available to form C_2H_2. TT Cyg is the only star for which the contribution of HCN to the 14 μm feature is stronger than the one of C_2H_2. The 14 μm features of WZ Cas and TX Psc are barely visible.

4.7.6 Conclusions

Hydrostatic model atmospheres are able to explain reasonably well the observed spectra of relatively hot and moderately variable stars with low C/O ratios in the wavelength region between 2.4 and about 10 μm. The fact that *plane parallel* model spectra seem to better "fit" the observations than *spherical* ones reflects nothing else than the spherical spectra being more sensitive to uncertainties in the opacities. To obtain a fit of equal quality a much larger grid of model atmospheres and spectra is necessary in the spherical case than in the plane parallel one. This is due to an additional parameter (mass) and due to the fact that spherical model atmospheres are more sensitive to changes of fundamental parameters than plane parallel atmospheres. Therefore, further investigations should use *spherical* models.

Proper self-consistent modelling of the 14 μm region of carbon stars will be one of the challenging topics in the future. It will only be possible to describe it if the structure of the photosphere as well as of the envelope are modelled correctly. Our dynamical models show that the contribution of the dust as well as emission due to the molecules C_2H_2 and HCN can fill up the strong photospheric absorption feature predicted by hydrostatic models. The only part of the original feature which survives is the small feature around 13.7 (due to C_2H_2) and 14.0 μm (due to HCN).

4.8 Detailed fits of TX Psc, V460 Cyg and WZ Cas

For a small sample of stars, observational data exist over the whole wavelength range between 0.5 and 45 μm. We selected three stars, namely TX Psc, V460 Cyg, and WZ Cas and aimed to obtain detailed fits with spectra based on spherical model atmospheres. TX Psc and V460 Cyg are both irregular variables with small variations only. Therefore, we chose two models with different effective temperatures and luminosities and required these two models to be able to reproduce all the investigated observations well. WZ Cas is a SRb variable, to fit this star we also used only two models, but it is obvious that the fits with only two models are worse than in the other two cases.

4.8.1 TX Psc

TX Psc is the brightest carbon star and hence it is among the best studied ones. Numerous observational data exist. We picked out data of Baumert (1972), of Lázaro et al. (1994), one spectrum obtained by the **K**uiper **A**irborne **O**bservatory (KAO) spectrum provided by Martin Cohen, a spectrum by Joyce (1998), and three ISO SWS spectra. Figure 4.43 shows a comparison of all these observations and our two selected model spectra (for the parameters of the model spectra see Table 4.9).

Table 4.9: Model parameters for fits

Star	$T_{\rm eff}$ [K]	log(g)	C/O	mass [$M_\odot$]	$^{12}C/^{13}C$	$v_{\rm mic}$ [km/s]
TX Psc	3100	−0.1	1.10	1.0	89	3
	3200	−0.1	1.10	1.0	89	3
V460 Cyg	3125	−0.1	1.40	2.25	89	3
	3175	−0.1	1.40	2.25	89	3
WZ Cas	3100	−0.1	1.02	1.0	89	3
	3060	−0.1	1.02	1.0	89	3

Baumert (1972) measured TX Psc at ten epochs between november 1969 and june 1971. We adopted the maximum and minimum values of his colour measurements; the maximum values are denoted by diamonds in the upper left panel of Fig. 4.43, the minimum values by asterisks. Minimum observations and models were forced to have equal flux at 1.0395 μm. We see that the model spectra have too much flux in the wavelength region below at least 0.8 μm. The upper spectrum in the upper right panel shows a spectrum by KAO observed in june 1976; the one in the middle relies on data from Joyce (1998) which were obtained

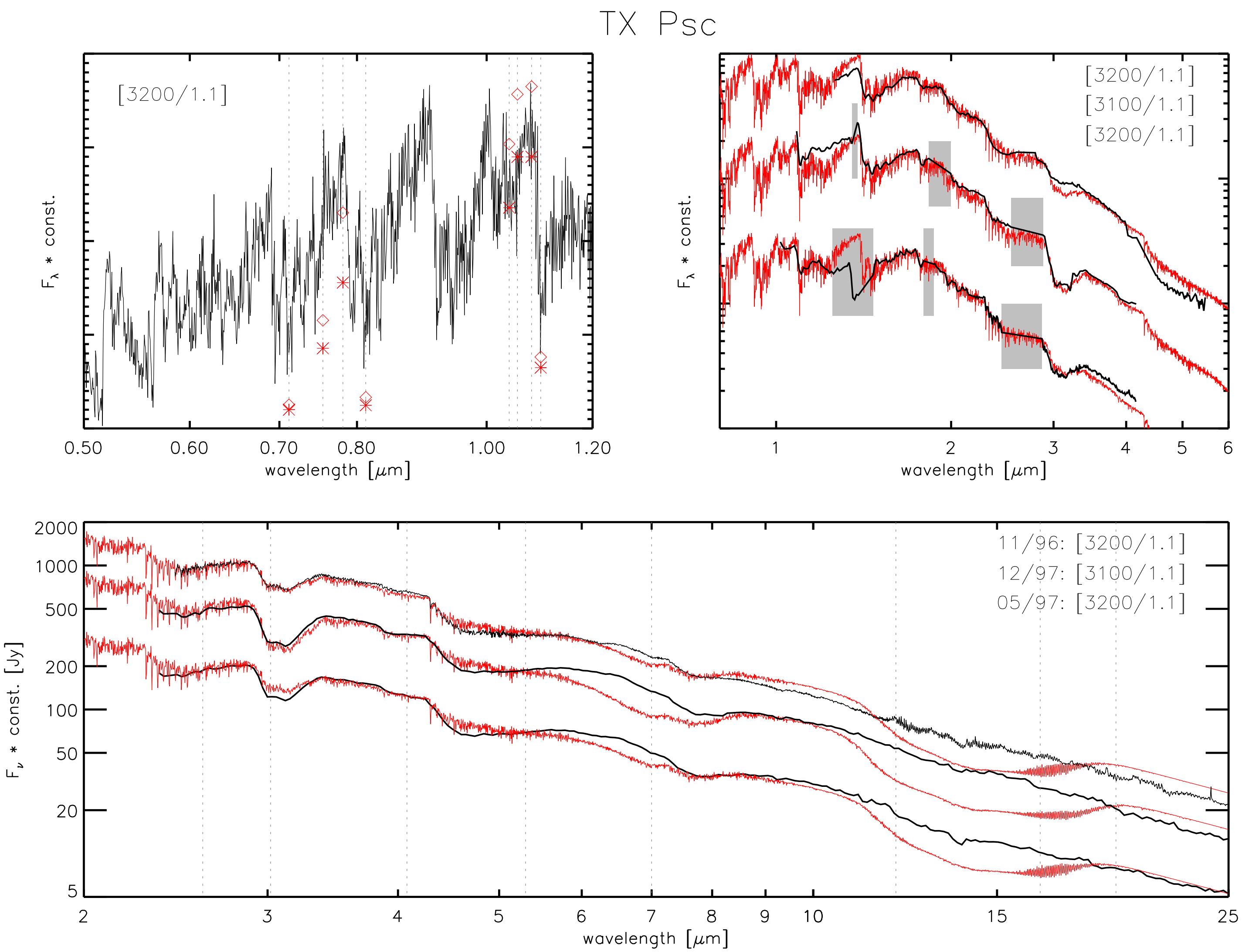

Figure 4.43: Various spectra of TX Psc. The red asterisks and diamonds in the upper left panel denote observed colours; grey shaded areas in the upper right panel show regions where Earth's atmosphere prevents reliable measurements. Black curves in the upper right and the lower panel show observations, red curves model spectra. Details are given in the text.

in september 1991. The lower spectrum is by Lázaro et al. (1994), it was observed in 1983. Grey shaded areas show regions where Earth's atmosphere prevents reliable measurements. Observed and model spectra were forced to have equal flux at 1.6 μm. The spectrum by Lázaro can be fitted very well with the model with an effective temperature of 3200 K, the one by Joyce with the 3100 K model. For a better fit of the 3 μm feature of the spectrum obtained with the KAO, a model with slightly higher effective temperature (3225 instead of 3200 K) than the one shown here is needed. In the lower panel of Fig. 4.43, two ISO SWS01 spectra and one ISO SWS06 spectrum are shown. The uppermost spectrum was observed in november 1996, the middle one in december 1997, and the lower one in may 1997. When looking at the 3 μm feature, we can see immediately that the star cooled constantly between the first and the last ISO observation. The SWS06 spectrum (uppermost) can be fitted very well with the model having an effective temperature of 3200 K, the middle one still reasonable with the 3100 K model. The lower spectrum needs a model slightly cooler than 3200 K for a good fit of the 3 μm feature. Observed and model spectra were forced to have equal flux at 2.8 μm. We see that the discrepancy in the 5.5 to 7 μm region (which was discussed in Sect. 4.7.3) between models and observations barely exists in the hottest spectrum of the star. However, it becomes progressively more pronounced towards lower effective temperatures. This might indicate that we see the C_2H_2 / HCN feature in emission while the CS contribution is still in absorption; unfortunately the resolution of the two cooler TX Psc ISO spectra is not high enough to confirm this conjecture. However, if this is indeed the case then it is clear that we are not able to model this wavelength region properly with hydrostatic model atmospheres because we then lack the contributions by the shell causing the emission.

We conclude that we can explain observed spectra of TX Psc quite well in the wavelength range between 0.8 and 10 μm with spherical model spectra with effective temperatures between 3100 and 3225 K.

4.8.2 V460 Cyg

For the irregular variable V460 Cyg, we posess observational data of Baumert (1972), of Lázaro et al. (1994), and two ISO SWS spectra. Figure 4.44 shows a comparison of all these observations and our two selected model spectra (for the parameters of the model spectra see Table 4.9).

Baumert (1972) measured V460 Cyg four times between november 1969 and november 1970. We took the maximum and minimum colour values of his measurements, the maximum values are denoted by diamonds in the upper left panel of Fig. 4.44, the minimum values by asterisks. Minimum observations and models were forced to have equal flux at 1.0395 μm. We see that the model spectra have slightly too much flux in the wavelength region below at least 0.8 μm. The

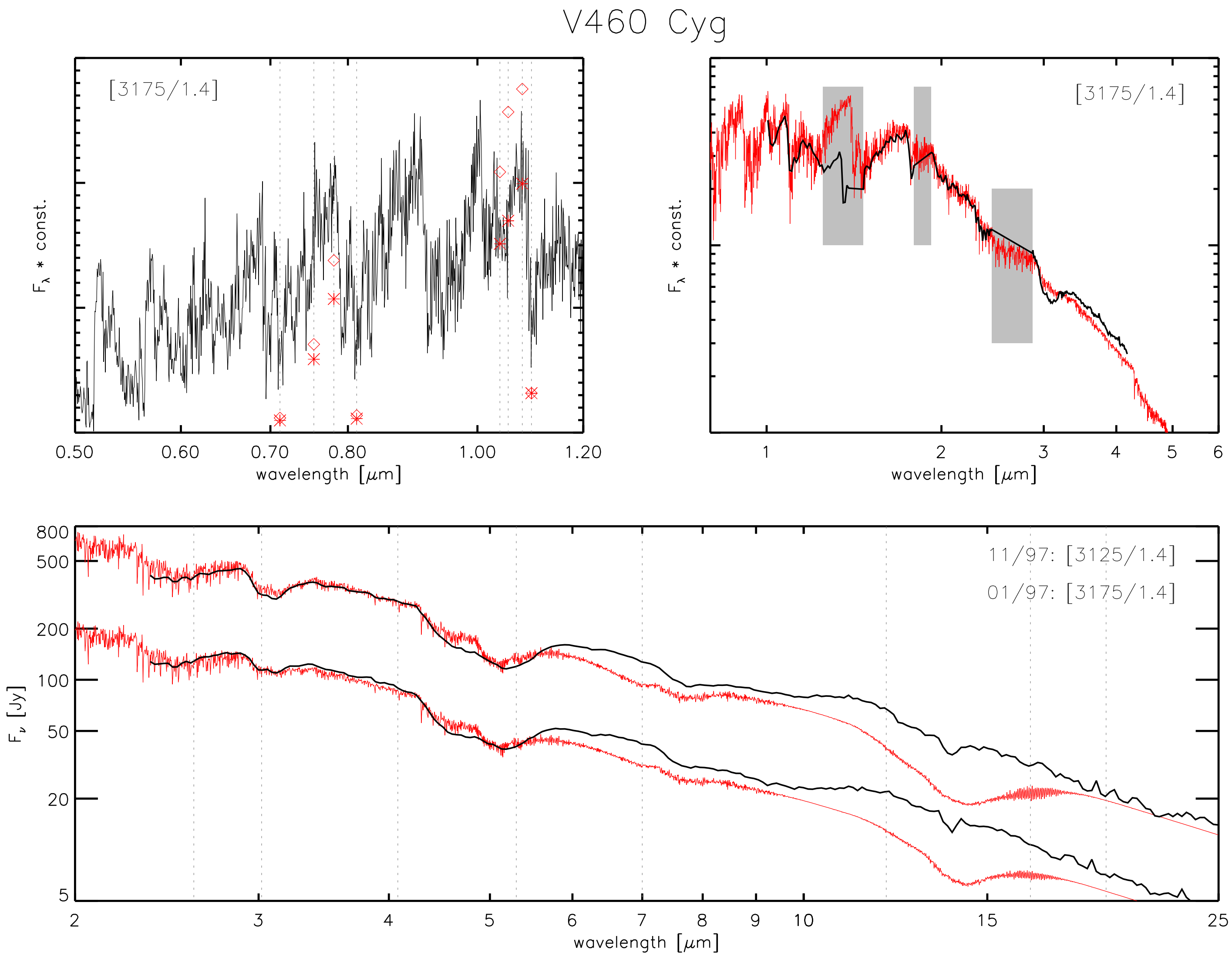

Figure 4.44: Various spectra of V460 Cyg. The red asterisks and diamonds in the upper left panel denote observed colours; grey shaded areas in the upper right panel show regions where Earth's atmosphere prevents reliable measurements. Black curves in the upper right and the lower panel show observations, red curves model spectra. Details are given in the text.

spectrum in the upper right panel shows a spectrum by Lázaro et al. (1994) observed in 1983. Grey shaded areas show regions where Earth's atmosphere prevents reliable measurements. The spectrum by Lázaro can be fitted well with the model with an effective temperature of 3175 K. In the lower panel of Fig. 4.44 two ISO SWS01 spectra are shown. The uppermost spectrum was observed in november 1997, the lower one in january 1997. When looking at the 3 μm feature, we can see that the star cooled between the first and the second ISO observation. The upper SWS01 spectrum can be fitted with a model with 3125 K, the lower one with the 3175 K model. The quality of the fit longwards of 6 μm is of poorer quality than the one of TX Psc.

We conclude that we can explain observed spectra of V460 Cyg well in the wavelength range between 0.8 and 6 μm with spherical model spectra with effective temperatures between 3125 and 3175 K.

4.8.3 WZ Cas

For the SRb variable WZ Cas, observational data of Baumert (1972), of Lázaro et al. (1994), of Joyce (1998), and one ISO SWS06 spectrum were available. Figure 4.45 shows a comparison of all these observations with our two selected model spectra (for the parameters of the model spectra see Table 4.9).

Baumert (1972) measured WZ Cas four times between november 1969 and november 1970. We took the maximum and minimum colour values of his measurements, the maximum values are denoted by diamonds in the upper left panel of Fig. 4.45, the minimum values by asterisks. Minimum observations and models were forced to have equal flux at 1.0395 μm. We see that the model spectra have too much flux in the wavelength region below at least 0.8 μm. The upper spectrum in the upper right panel shows data from Joyce (1998) which were obtained in september 1991; and the lower one is a spectrum by Lázaro et al. (1994) observed in 1983. Grey shaded areas show regions where Earth's atmosphere prevents reliable measurements. In this case we are not able to describe correctly the full shape of the 3 μm feature with any spherical model spectrum of our small grid. Additionally, the observations have more flux in the 2 μm region. This hints at too high an effective temperature which we adopted (3100 and 3060 K); the strengthening of the 3 μm feature with lower temperature must be compensated by a higher mass and higher luminosity. Despite not being able to present a good fit to WZ Cas, we chose to discuss it here because it has a lower effective temperature than TX Psc and V460 Cyg, and because a SWS06 spectrum exists of this star. In the lower panel of Fig. 4.45, this ISO SWS06 spectrum (obtained in july 1996) is shown. In Sect. 4.8.1 we stated that the discrepancy between models and observations in the 5.5 to 7 μm region may be due to emission in the observed spectra. Unfortunately, we can not unambigously identify emission contributions, but the

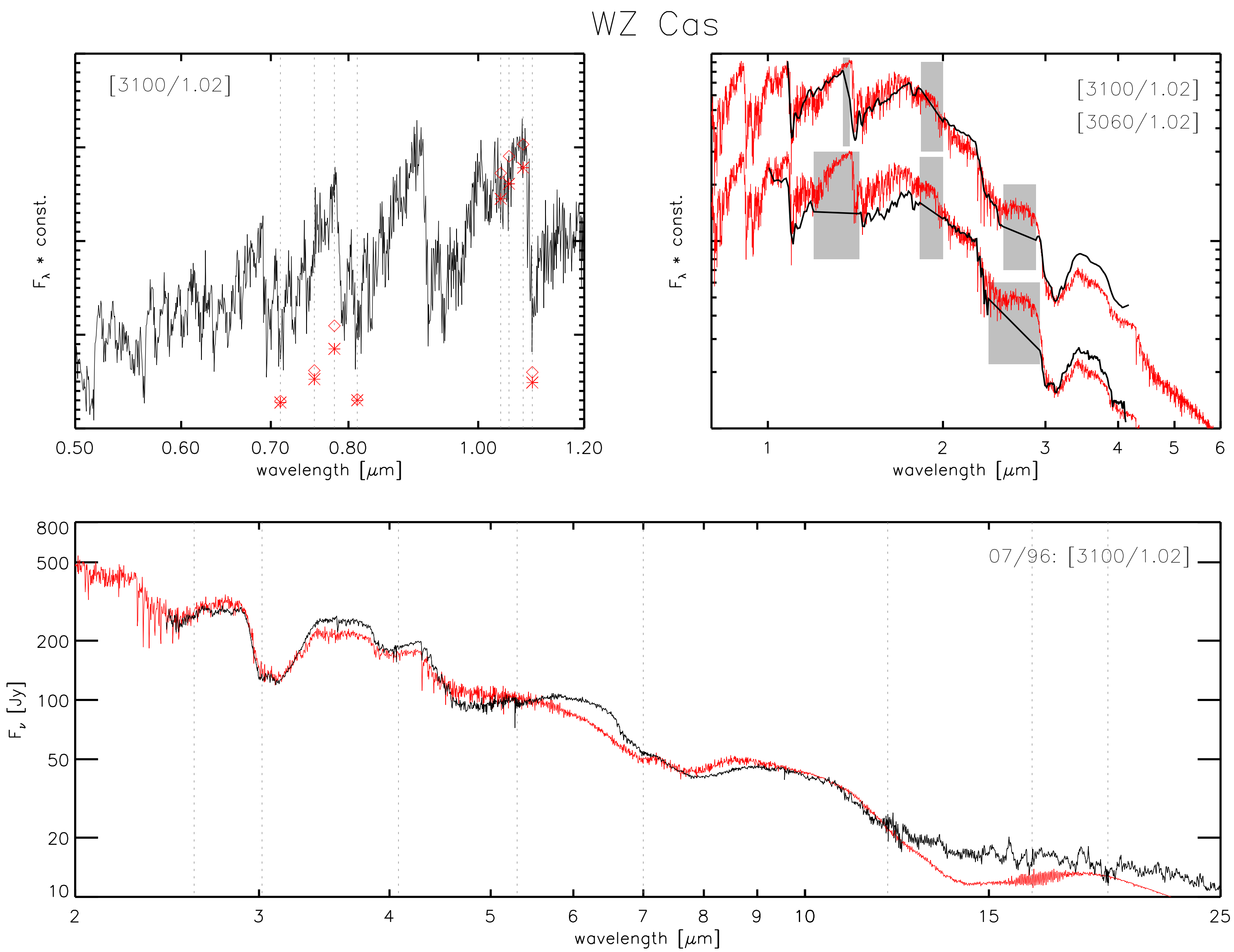

Figure 4.45: Various spectra of WZ Cas. The red asterisks and diamonds in the upper left panel denote observed colours; grey shaded areas in the upper right panel show regions where Earth's atmosphere prevents reliable measurements. Black curves in the upper right and the lower panel show observations, red curves model spectra. Details are given in the text.

slope of the observed spectrum compared to the model spectrum as well as the structures which are visible in the band at least suggest that likely we see emission in the observed spectra.

We conclude that it is likely that we see emission in the 5.5 to 7 μm region in spectra of cool carbon stars.

4.9 Conclusions

Our investigations show that we can describe low-resolution spectra, broad-, and narrow-band colours of relatively hot moderately variable stars with low C/O ratios surrounded only by small amounts of dust reasonably well with synthetic spectra based on hydrostatic model atmospheres. In such cases the agreement between observed and model spectra is good between 0.7 and 10 μm, at wavelengths shorter than 0.7 μm we lack the inclusion of atomic lines in our synthetic spectra, at wavelengths longer than 10 μm we do not see the pure photospheric spectrum of the star anymore. Our determinations of fundamental parameters are in good agreement with results from other methods published in the literature. The uncertainties of (mainly) the C_2 and C_3 opacity data are responsible for the limitation to stars with low C/O ratios.

For stars with high C/O ratios and stars surrounded by dust (which are by far the majority of the AGB stars) the situation is less satisfactory. Currently we are not able to fully reproduce spectra, broad-, and narrow-band colours of cool Miras due to the lack of appropriate dynamical models with high mass loss rates. However, our dynamical model spectra designed for the SRa variable R Scl describe narrow-band indices in the wavelength region between 0.7 and 1.1 μm correctly, as well as near-infrared broad-band colours including the I, J, H, K, and L filters. Longwards of about 4.5 μm our dynamical model spectra substantially disagree with the observed spectra. The model spectra predict strong emission where only single weak lines in emission are found in observed spectra.

Proper self-consistent modelling of the 14 μm region of carbon stars will be one of the challenging topics in the future. It will only be possible to describe it if the structure of the photosphere as well as of the envelope are modelled correctly. Our dynamical models show that the contribution of the dust as well as emission due to the molecules C_2H_2 and HCN fill up the strong photospheric absorption feature predicted by hydrostatic models. The only part of the original feature which survives is the small feature around 13.7 (due to C_2H_2) and 14.0 μm (due to HCN).

Additionally to the observations discussed above we also looked at colour indices specifically defined to measure the strength of C_2 and CO band-heads. Two sets of observational data are available for the comparison with our model spectra: low resolution spectra and medium-resolution FTS spectra. The indices are defined slightly different in the two sets of observations, nevertheless they both measure the same band-heads. While we are able to obtain reasonable agreement between the model and the observed indices in the case of the low-resolution spectra, no agreement is found between model and observed indices in the case of the medium-resolution FTS spectra. This hints at a severe problem in the way of comparing observed and model spectra, and/or at a problem of recovering the correct shapes of the FTS spectra.

A remarkable feature concerning the dynamical model CO and C_2 indices is their multi-periodicity. This illustrates that although the main contributions to the features measured by the indices come from regions close to the photosphere, layers from further outside also contribute to the features.

Generally speaking, for a comparison of models and observations of carbon-rich AGB stars spectra with a resolution between 1000 and 5000 covering a wavelength region as large as possible seem to be ideal. It is important that a large number of spectra is obtained with the same instrument in order to minimise artificial effects and problems due to the combination of different data sets, and that the data set is large enough to allow a systematic comparison with the models. Photometric data contain less information, they are less helpful if one is interested in improving the quality of the models or the molecular input data. The same applies for high-resolution spectra where usually only very narrow wavelength ranges can be monitored. FTS spectra seem to be problematic too due to the strong dependence of the shape of the resulting spectra on the calibrated spectral response curve of the spectrometer. A major advantage of the analysis of low resolution spectra covering a wide spectral range is that all fundamental parameters can be determined simultaneously. In studies of high resolution spectra, it will often be necessary to adopt photometric determinations of $T_{\rm eff}$ that are not necessarily determined at the same pulsation phase as the spectrum. No general high-resolution method is known for determining $\log(g)$ in cool giant stars. The value of the $^{12}C/^{13}C$ ratio can be determined with better accuracy from high-resolution spectra, while we believe that the accuracy in the C/O determination has the same reliability in the two methods. An additional advantage of the low-resolution method is that it can be applied to stars in remote galaxies too.

Chapter 5

Radii of AGB stars

5.1 Introduction

The pulsation variables populating the AGB belong to the most inflated stars known. Despite having only about one solar mass, they can extend over several hundred solar radii. This implies very tenuous envelopes whose huge superficial density/pressure scale heights render the determination of the linear dimensions of such stars problematic.

On the other hand, the huge diameters of LPVs make them prime candidates for optical and infrared stellar interferometry. The first direct measurements of angular diameters of stars were made possible by the development of stellar interferometry around 1920 (Michelson & Pease 1921). But mainly the last 30 years yielded most of the currently known stellar diameters; they were obtained from lunar occultation measurements (e.g. catalogue by White & Feierman 1987 which gives a summary; paper series by Ridgway et al. 1977, 1980, 1982), speckle methods (e.g. Hofmann et al. 2000), and intensity as well as amplitude interferometry (e.g. Tuthill et al. 1994; Haniff et al. 1995; Van Belle et al. 1996; Perrin et al. 1999). Depending on the method of radius determination, significantly discrepant results have been obtained. Accurate stellar diameter estimates are of particular interest for Mira and other long-period variables, for which the variation of the apparent diameter as a function of wavelength allows an investigation of their complex atmospheric structure (e.g. Labeyrie et al. 1977; Bessell et al. 1989). Angular diameter measurements are also valuable when studying the pulsational properties of these sources. If combined with reliable distance estimates, the pulsation mode can be determined. Since the first mode identification of old-disc Miras (Wood 1975), this issue has remained a contentious one. Depending on the method and the choice of the photometric passband the deduced radii can differ up to a factor of two (e.g. results of Tuthill et al. 1994 and Perrin et al. 1999 for R Leo). This leads to a qualitative divergence in the conclusion of the prevailing pulsation mode. Attempts to resolve the issue of the pulsation mode of Miras using stellar diameter measurements have been complicated mainly by two reasons: First, the complex atmospheric structure of Miras implies that the transformation of an observed "intensity" diameter to a stellar photospheric diameter is not straightforward. Secondly, most distance estimates to nearby Miras are far too inaccurate to allow for a reliable conversion of angular to linear measures of the stellar diameters. Recently, however, more accurate parallax measurements, those delivered by HIPPARCOS (e.g. Van Leeuven et al. 1997), are a first more solid step towards a direct conversion of angular diameters to linear sizes.

On the theoretical side, radii and wavelength-dependent limb-darkening for static and dynamic models have been discussed by Scholz & Takeda (1987), Bessell et al. (1989), Bessell et al. (1996), Hofmann & Scholz (1998a) and Hofmann et al. (1998b). Bessell et al. (1996) stated that "better agreement between theoretical and observed spectra, colors and radii of Mira variables can be expected to follow from improvements to the treatment of the molecular line opacity". As a further step along this avenue, we will base the investigations presented in this work on improved models and synthetic spectra calculated with detailed molecular opacities from the SCAN data base (Jørgensen 1997). The specific question to be addressed is: Which choice of stellar radius is the relevant one for pulsational inferences? We will refer to this radius as the *pulsation radius*. The radius seen by an observer and the one adopted by a theorist, even for the same kind of object need not be the same; this applies in particular to the tenuous stars along the AGB. Even if some agreement on the position of the radius can be found, we are still confronted with the additional complication of the temporal variability of the LPVs. Due to the large radius excursions during a pulsational cycle, single-phase radius estimates or even arithmetical means of multi-phase observations can be substantially off the pulsation radius.

5.2 Models

We used classical hydrostatic MARCS models as well as two dynamical models calculated with Planck mean opacities for our investigations, one of them is carbon-rich, the other one oxygen-rich. Tables 5.1 and 5.2 summarise the properties of the used models.

To understand the *dynamical* behaviour of AGB stars, the particular choice of chemistry in the models was found not to be crucial. This is due to the fact that for the variation of e.g. $T_{\rm eff}$ mainly the choice of the input quantities P and especially $\Delta u_{\rm p}$ is relevant. If $\Delta u_{\rm p}$ exceeds a critical value, the model develops regular variations at large amplitudes very much like Mira stars do; if $\Delta u_{\rm p}$ is

Table 5.1: Hydrostatic models

name	T_{eff} [K]	L [$L_\odot$]	C/O	M [$M_\odot$]
C2650	2650	7000	1.1	1.0
C3000	3000	5000	1.1	1.0
O2800	2800	2400	0.48	1.0
O3600	3600	4123	0.48	1.0

Table 5.2: Dynamical models

name	$T_{\text{eff}}^{(1)}$ [K]	L [$L_\odot$]	C/O	M [$M_\odot$]	Δu_{p} [km/s]	P [days]
"parent"	2940	7000	1.4	1.0	–	–
C000	2776	8300	1.4	1.0	4	390
C025	2544	7000	1.4	1.0	4	390
C050	2489	5600	1.4	1.0	4	390
C075	2879	7000	1.4	1.0	4	390
"parent"	3034	5000	0.48	1.0	–	–
O000	2975	5400	0.48	1.0	2	295
O025	2918	4900	0.48	1.0	2	295
O050	3048	4400	0.48	1.0	2	295
O075	3017	4900	0.48	1.0	2	295

(1) Values at $\tau_{\text{Ross}} = 1$, therefore they differ from the values given in Höfner et al. (1998).

small, then the models show only small and sometimes less regular temporal variations which are more representative of semi-regular and irregular variables.

For oxygen-rich stars, only one proto-type model was available. It showed only small variations and it is therefore more suited to describe semi-regular variables. For illustrative purposes, we present a Mira-like model for the carbon-rich case. This implies that when discussing aspects concerning the model structures in Sect. 5.4.2, we will use an oxygen-rich model when referring to carbon-rich irregular variables and a carbon-rich model when referring to an oxygen-rich Mira variable. That this apparent handicap might not be too serious is illustrated by the fact that Alvarez & Plez (1998) managed to explain qualitatively the temporal variations of TiO and VO features in Miras by calculating the spectra and corresponding colour indices with an oxygen-rich chemistry on top of a temperature-density structure of a carbon-rich dynamic model. Evidently, the argument that the particular chemistry that is used for the calculation of the model structure is not crucial does not apply to observables such as filter radii or spectra; they are dominated by the molecular features and therefore they are very much chemistry dependent.

5.3 The synthetic Spectra

We calculated synthetic opacity-sampling spectra for a few representative hydrostatic as well as dynamic model atmospheres. In the case of oxygen-rich chemistry the molecules CO, SiO, TiO and H_2O were included. In the carbon-rich case, CO, CH, CN, C_2, HCN, C_3 and C_2H_2 were accounted for. For carbon-rich stars we account for all molecules contributing in the wavelength region between 0.5 and 3 μm. In the oxygen-rich case we lack the contributions from VO which has features in the same wavelength range as TiO.

For carbon- and oxygen-rich LPVs, the molecules contributing to the spectra in the wavelength range between 0.5 and 3 μm form in distinct atmospheric regions. The features of CO, C_2 and CN are formed at temperatures between roughly 2200 and 5000 K. The weak temperature dependence works in the direction that the features grow stronger as the temperature drops. Since sphericity affects radiative transfer at model structures only below about 2200 K, these carbon-bearing molecules are not very sensitive to the geometric treatment. For a detailed discussion of spectral feature formation in carbon-rich stars see Sect. 1.4.1 or Loidl et al. (1999a).

In the oxygen-rich case, TiO and especially H_2O are temperature sensitive molecules. TiO forms approximately between 3000 and 1800 K; the formation of H_2O extends from about 2500 K out to the outer boundary of the model stars (Aringer 2000). Therefore, these latter two molecules are strongly affected by sphericity. It is not possible to fit the spectra in the visual and NIR range of oxygen-rich stars with spectral type later than M7 with hydrostatic model atmospheres (Alvarez & Plez 1998). This is due to two facts: the hydrostatic models do not extend to low enough temperatures and furthermore they lack the density enhancements in the outer layers which are produced by dynamical models and which favour the formation of TiO and H_2O (for a detailed comparison of hydrostatic and dynamic models see Höfner et al. 1998). The H_2O molecule is the reason why we will distinguish in the following between "hot" (no water bands) and "cool" (with water bands) oxygen-rich stars. In hydrostatic models, water bands occur in the spectra if the effective temperature drops below $\approx 3100\,\mathrm{K}$, in the dynamical models this limit is slightly shifted to lower temperatures (due to the higher densities at a given temperature).

5.4 Results

5.4.1 Structural and Pulsational Properties

Depending on the question asked, the "correct" radius lies in different atmospheric layers. As we are mainly interested in the prevailing pulsation mode of AGB variables, we must deal with the radius that is relevant for pulsational inferences: Accordingly, we will call it the *pulsation radius* of LPVs.

The pulsation-mode determination is canonically approached using only very basic stellar pulsation theory. The pulsation constant Q, which is defined by

$$Q = P(M/\mathrm{M}_\odot)^{1/2}(R/\mathrm{R}_\odot)^{-3/2} \tag{5.1}$$

is sufficient for this problem. The period P is measured in days; M and R stand for the stellar mass and radius, respectively. Linear (non)adiabatic pulsation theory easily predicts the magnitude of Q. For most types of pulsators, the Q value of the radial fundamental mode (Q_F) lies in the range $0.02 - 0.16$ and the first-overtone Q (Q_O1) is about 0.7 times smaller than the fundamental one. Extensive computations of Q for LPVs can be found in Fox & Wood (1982) and a recent recompilation in Gautschy (1999). In the relevant parameter domain for LPVs, $0.05 < Q_\mathrm{F} < 0.14$ and $0.03 < Q_\mathrm{O1} < 0.04$. Even if nonadiabatic eigenfrequencies are usually systematically shifted relative to adiabatic ones, the periods from adiabatic eigenanalyses are in most cases sufficiently accurate to be used for Q and the associated inferences. Comparing the observed period (together with an estimate of the variable star's mass) and its radius to the set of theoretical Q values, lets usually distinguish between fundamental and some overtone pulsation mode.

The application of eq. (5.1), using observational data, is unproblematic for sufficiently compact pulsating stars. For giants and supergiants with their very tenuous superficial layers and possibly large excursions during a pulsational cycle one has, however, to ensure that appropriately defined observables are used for comparison with theoretical quantities.

On the theoretical side, hardly anything can go wrong when computing Q for compact pulsators. Stellar modellers compute the eigenspectrum for a given stellar model with mass M and an equilibrium radius R which is defined by the stellar photosphere, placed usually somewhere between $\tau_{\rm Ross} = 2/3$ and unity. The precise choice of the photosphere is not crucial for geometrically thin atmospheres. Furthermore, the pressure scale-height close to the photosphere is large enough to efficiently reflect low-order acoustic waves so that the stellar surface can be imagined as a fully reflective outer wall of small geometrical thickness. The low superficial pressure scale-height in giant-like stars, however, reduces the reflectivity of the most superficial layers and leaky waves can possibly escape into the circumstellar environment. Therefore, the particular choice of the outer boundary condition is ambiguous for LPVs (cf. Fox & Wood 1982, Ostlie & Cox 1986). Nevertheless, the use of canonical stellar-evolution type models, stopping at the photosphere – defined by $\tau_{\rm Ross} = \mathcal{O}(1)$ – is still sufficiently accurate for the pulsation-mode assessment in LPVs (Loidl & Gautschy 2001). On the other hand, the question of mode excitation and damping needs a much more careful treatment of waves carrying energy out of the cavity; our results do not apply to this modeling complex.

After the theoretical ingredients going into Q are specified, correspondingly matching observables must be specified to observationally determine the pulsation constant. For the mass of LPVs, a canonical value of $1\,\mathrm{M}_\odot$ is frequently used. According to Gautschy's (1999) study, assuming fundamental-mode pulsators only in his sample, the mean mass spread is about $0.9\,\mathrm{M}_\odot$ so that a maximum error of about $40\,\%$ must be expected in the worst case. This factor alone is not capable, however, of changing an interpretation from a first-overtone pulsator to a fundamental-mode one, or vice versa. The other aspect contributing to the uncertainty of Q and requiring careful attention in LPV observations is the radius. First, it varies significantly throughout a cycle; secondly, the atmospheres have a non-negligible geometrical extension, and thirdly, the optical thickness changes during a cycle so that different mass shells with different geometrical locations become accessible during a pulsation cycle. Gautschy (1999) pointed out that a simple arithmetic averaging of radius and/or temperature observations over a cycle leads to results which are systematically off the equilibrium values. This work is devoted to this radius aspect; mainly addressing how to observe as closely as possible the "Rosseland" radius which is used in the theoretical computations.

5.4.2 Detailed Simulations

To study the location of the photosphere in different wavelengths we computed temperature (T_λ) and radius (R_λ) in the range from 0.5 to 3 μm where an optical depth (τ_λ) of unity is reached. Following the prescription of Scholz & Takeda (1987) we calculated filter radii

$$R_{\mathrm{f}} = \frac{\int R_\lambda I_\lambda f_\lambda d\,\lambda}{\int I_\lambda f_\lambda d\,\lambda}$$

and filter temperatures

$$T_{\mathrm{f}} = \frac{\int T_\lambda I_\lambda f_\lambda d\,\lambda}{\int I_\lambda f_\lambda d\,\lambda},$$

for a variety of filters which are referred to in the literature. The emitted intensity is denoted by I_λ and f_λ stands for the filter throughput function. Except for the V, I, J, H, and K filters, for which Bessell's filter definition was used (Bessell & Brett 1988), we chose rectangular filter shapes.

Table 5.3 lists the central filter wavelengths, the filter widths, the dominantly contaminating molecular features in the case of oxygen-rich and carbon-rich stars, and selected references for the filters accounted for in this study.

To visualize the particular molecular features which block the radiation in the various filters we calculated (1) synthetic spectra based on model O2800 (T_{eff} = 2800 K, log(g) = 0.0, M = 1 M$_\odot$, C/O = 0.48) for the molecules CO, SiO, TiO, and H_2O separately; (2) synthetic spectra based on model O3600 (T_{eff} = 3600 K, log(g) = 0.0, M = 1 M$_\odot$, C/O = 0.48) for the molecules CO, SiO, TiO, and H_2O alone, and (3) synthetic spectra based on model C2650 (T_{eff} = 2650 K, log(g) = –0.76, M = 1 M$_\odot$, C/O = 1.10) for the molecules CO, C_2, CN, and C_2H_2 (Fig. 5.1). Figure 5.2 displays the resulting spectra together with the V, I, J, H, and K filter passbands; the remaining filters are mainly contaminated by TiO in the oxygen-rich case and by C_2 and CN in carbon-rich stars.

Figure 5.3 shows temperatures and radii at optical depth unity for the hydrostatic carbon-rich model C3000 (with T_{eff} = 3000 K, L = 5000 L$_\odot$, M = 1M$_\odot$, C/O = 1.10, and a spectral resolution of 1000). This model was chosen since it fits well the observations of the irregular variable TX Psc in the wavelength range between 0.5 and 10 μm (Jørgensen et al. 2000). Figure 5.4 displays the same quantities as Fig. 5.3 but for the oxygen-rich model O2800 (T_{eff} = 2800 K, L = 2400 L$_\odot$, M = 1 M$_\odot$, C/O = 0.48). Figure 5.5 shows the same quantities for the "parent" model of the carbon-rich dynamical model and finally Fig. 5.6 contains the same data for the "parent" model of the dynamical oxygen-rich model. Various choices of opacity means were used to demonstrate their effect on the location of the corresponding photosphere. In all four figures, the red line indicates the photosphere when accounting for the continuum only and the green line delineates the

Table 5.3: Filter positions, widths and contaminating molecular features.

name	central wavelength [μm]	filter width [μm]	features O-rich stars[1]	features C-rich stars	references for radii
V	0.545	0.230	TiO	C_2, CN	
I	0.805	0.220	TiO	CN	
J	1.220	0.300	continuum in hot stars TiO, VO, H_2O in cool stars	CN, C_2	
H	1.630	0.380	CO in hot stars CO, H_2O in cool stars	CO, C_2, CN	
K	2.190	0.540	CO in hot stars CO, SiO, H_2O in cool stars	CO, C_2, CN	e.g. Perrin et al. (1999)
623	0.623	0.009	strong TiO	CN, C_2	e.g. Quirrenbach et al. (1993,1994)
672	0.672	0.006	strong TiO	CN, C_2	Q9394
701	0.701	0.006	continuum in hot stars TiO in cool stars	CN, C_2	
712	0.712	0.012	strong TiO	CN, C_2	
754	0.754	0.005	continuum in hot stars TiO in cool stars	CN, C_2	
800	0.800	0.022	TiO	CN, C_2	
700	0.700	0.010	continuum in hot stars TiO in cool stars	CN, C_2	e.g. Tuthill et al. (1994), Haniff et al. (1995)
710	0.710	0.010	strong TiO	CN, C_2	T94H95
833	0.833	0.041	weak TiO in hot stars Tio in cool stars	CN, C_2	
902	0.902	0.050	weak TiO in hot stars TiO in cool stars	CN, C_2	
830	0.830	0.050	weak TiO in hot stars TiO in cool stars	CN, C_2	Burns et al. (1998) B98
880	0.880	0.050	continuum in hot stars TiO in cool stars	CN, C_2	
905	0.905	0.050	continuum in hot stars TiO in cool stars	CN, C_2	
940	0.940	0.050	continuum in hot stars TiO in cool stars	CN, C_2	

(1) "Hot" oxygen-rich stars refer to stars showing no molecular bands of water; this corresponds to models with effective temperatures exceeding about 3100 K. Correspondingly, we will designate oxygen-rich stars with effective temperatures below about 3100 K as "cool" oxygen-rich stars.

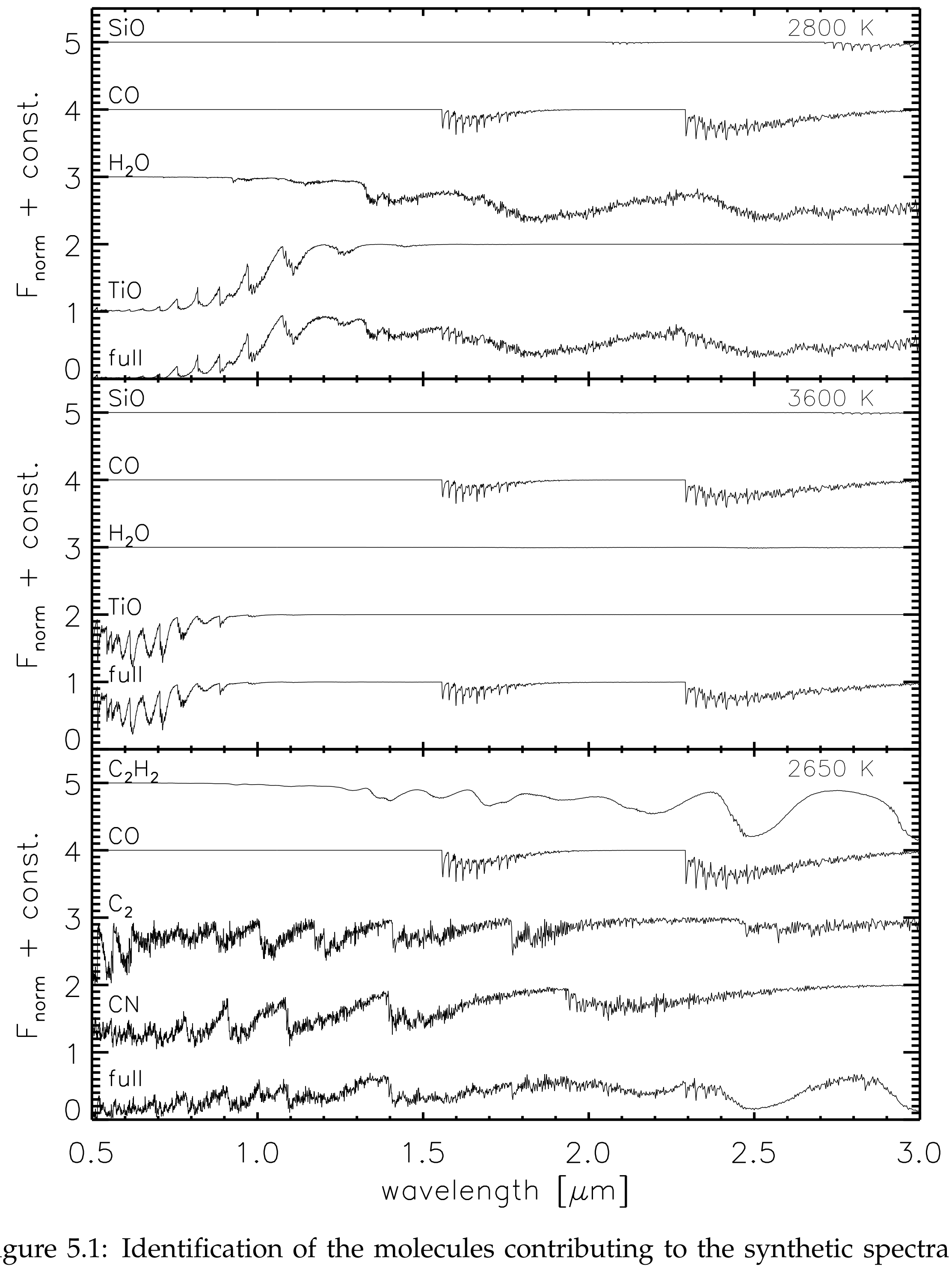

Figure 5.1: Identification of the molecules contributing to the synthetic spectra of a “cool” oxygen-rich star (upper panel; $T_{\rm eff} = 2800\,\rm K$), a “hot” oxygen-rich star (middle panel; $T_{\rm eff} = 3600\,\rm K$), and for a carbon-rich star (lower panel; $T_{\rm eff} = 2650\,\rm K$).

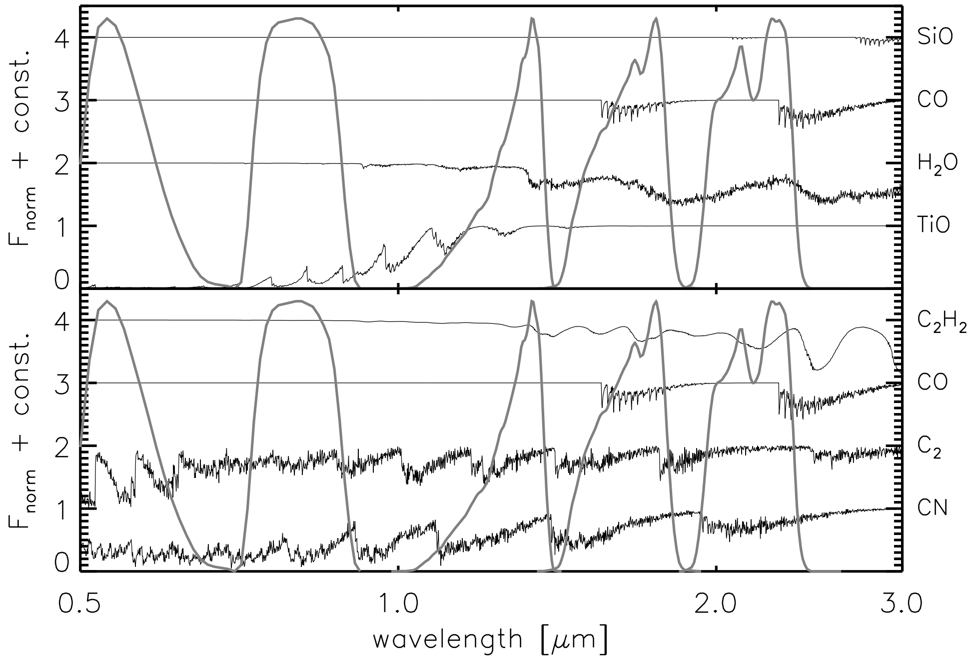

Figure 5.2: Contributions of single molecules to the synthetic spectra of a "cool" oxygen-rich star (upper panel) and for a carbon-rich star (lower panel), plotted together with filter passbands.

position of the photosphere when using the Rosseland mean opacity. The lower panels of Figures 5.3 to 5.6 show the position and the throughputs of various filters with appropriate zoom-ins into the relevant spectral regions. The abbreviations in the figure panels refer to the references described in Table 5.3.

As an observer probably can not see radiation coming from layers where $\tau_{\rm Ross}$ equals unity, we calculated the same quantities for an optical depth of 2/3. However, the radii and temperatures do not differ much, the radii are only about 1 % or less larger.

Figures 5.3 to 5.6 show clearly that the wavelengths below 1 μm are not well suited to determine effective temperature, pulsational radius, and hence the pulsation mode of an AGB star. This is due to molecular absorption by TiO in oxygen-rich stars and due to absorption by CN and C_2 in the carbon-rich stars as well as due to dust surrounding most of the AGB stars; this applies especially to Miras, where radiation is efficiently absorbed and scattered at short wavelengths. On the other hand, the infrared is contaminated by the re-emission spectrum of dust.

Many AGB stars have their flux maxima and therefore their maximum intensity between 1 and 2 μm. In addition, H^-, which is the dominating continuum source in cool stars, reaches its absorption minimum at 1.6 μm. Therefore, we see

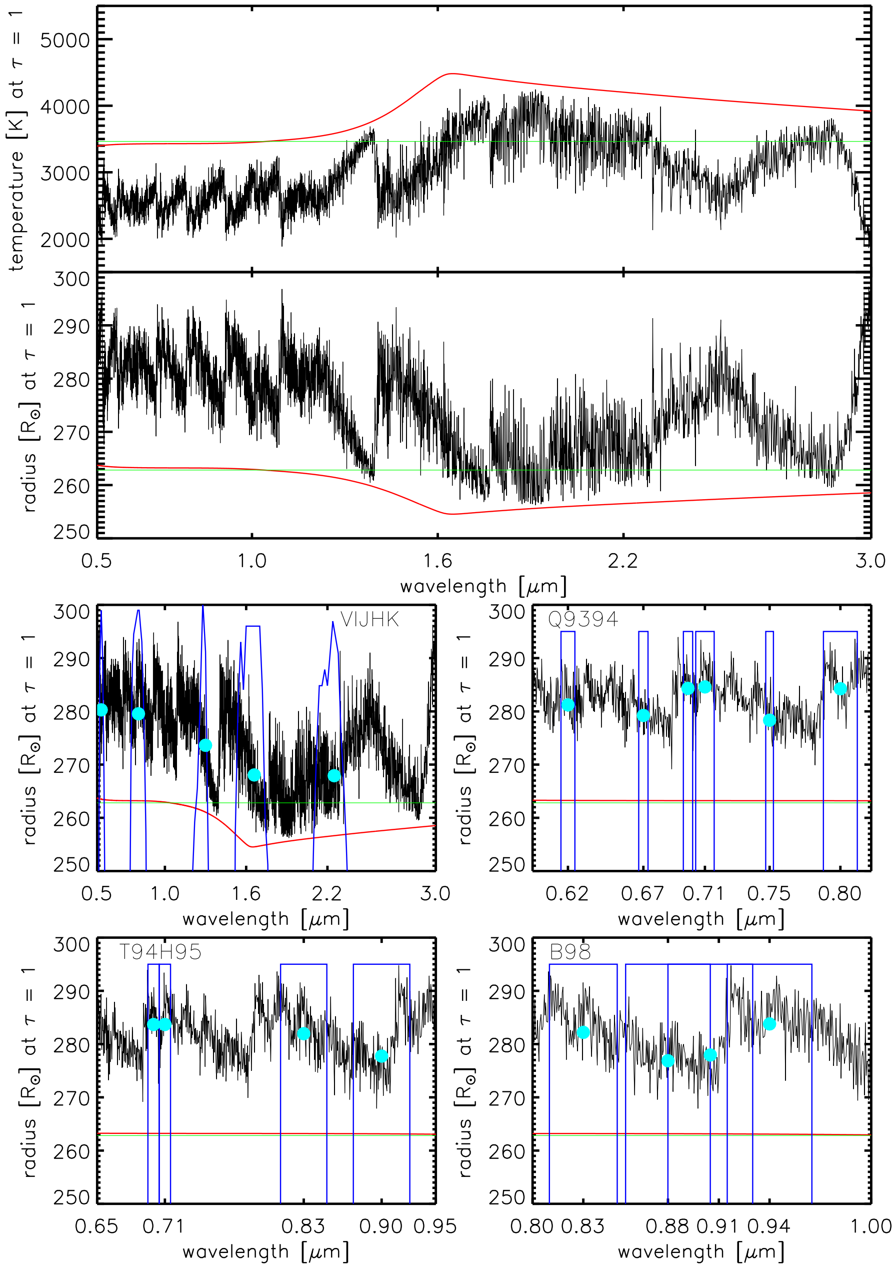

Figure 5.3: Temperatures and radii at $\tau_\lambda = 1$ in the wavelength range from 0.5 to $3\,\mu$m for a hydrostatic carbon-rich model with $T_{\rm eff} = 3000$ K, $L = 5000\,{\rm L}_\odot$, $M = 1\,{\rm M}_\odot$, C/O = 1.10 with a spectral resolution of 1000. The green line traces the magnitude of radius and temperature for $\tau_{\rm Ross} = 1$. The red line indicates radius and temperature at τ unity for continuum opacity only. The lower four small plots show the filters used by different research groups (the abbreviations correspond to those used in Table 5.3) and the resulting filter radii (turquoise dots).

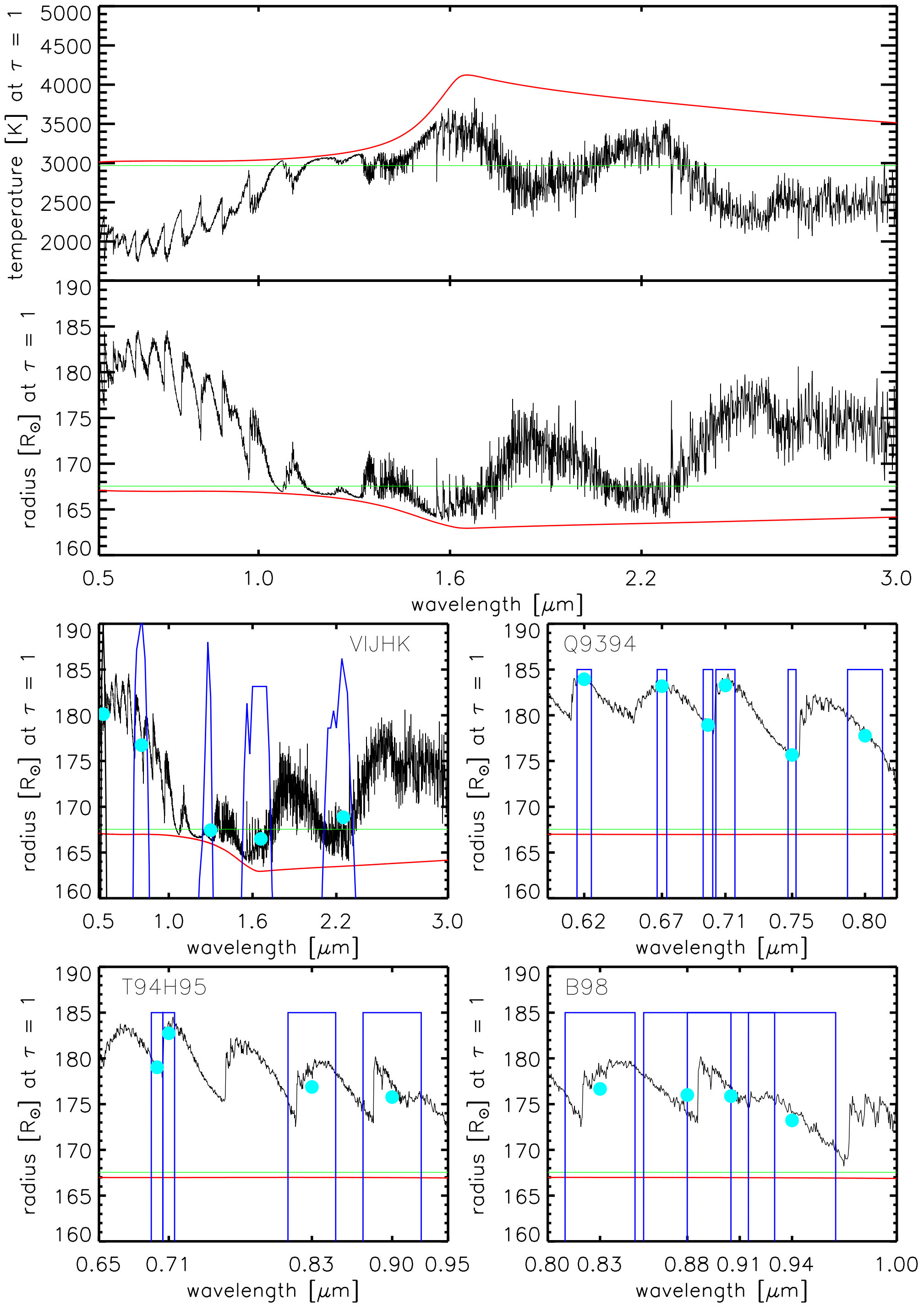

Figure 5.4: Same as Fig.5.3 but for a hydrostatic oxygen-rich model with $T_{\mathrm{eff}} = 2800\,\mathrm{K}$, $L = 2400\,\mathrm{L}_{\odot}$, $M = 1\,\mathrm{M}_{\odot}$, $\mathrm{C/O} = 0.48$.

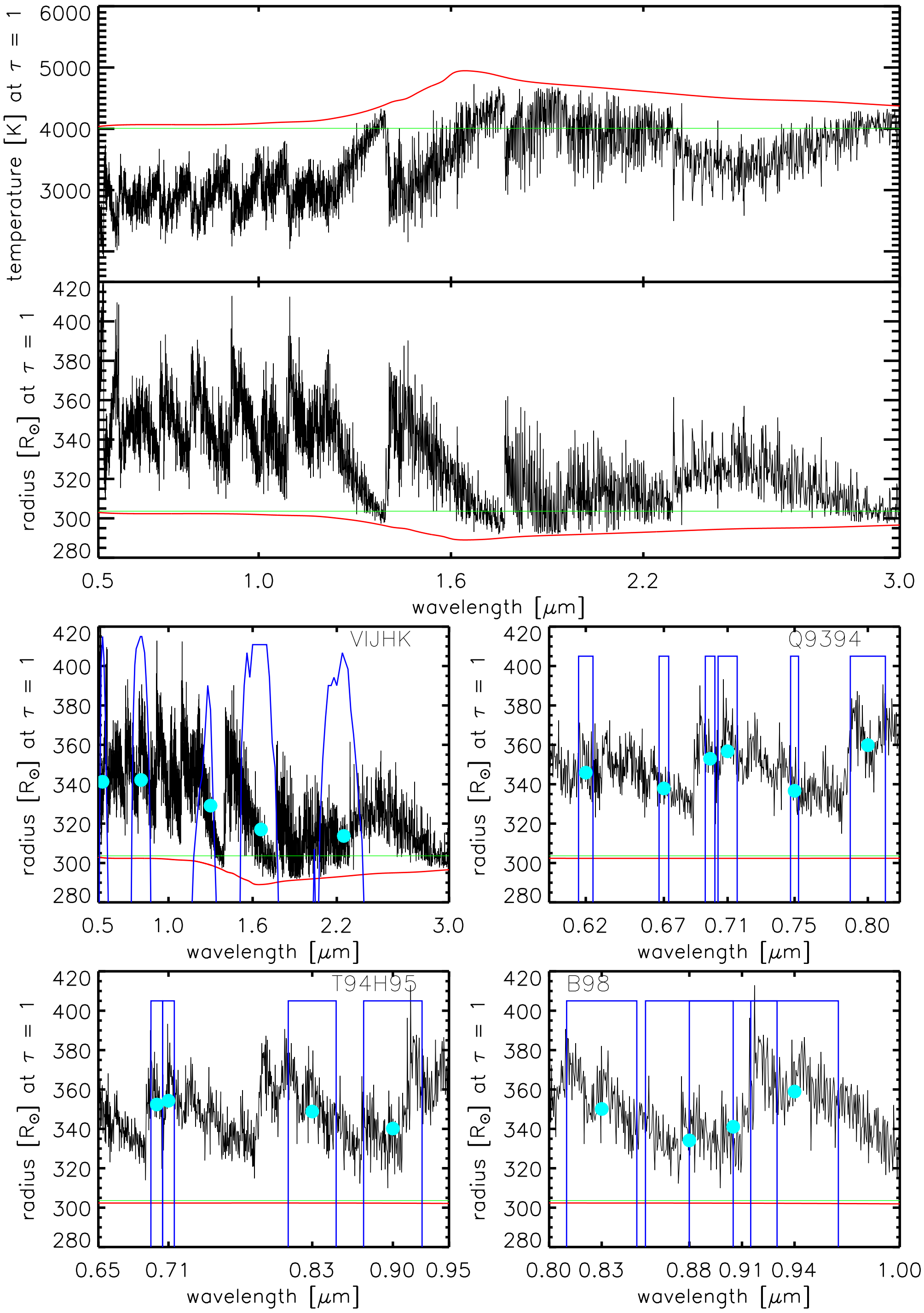

Figure 5.5: Same as Fig.5.3 but for the "parent" of the carbon-rich dynamical model ($T_{\rm eff} = 2940$ K, $L = 7000\,{\rm L}_{\odot}$, $M = 1\,{\rm M}_{\odot}$, C/O = 1.10).

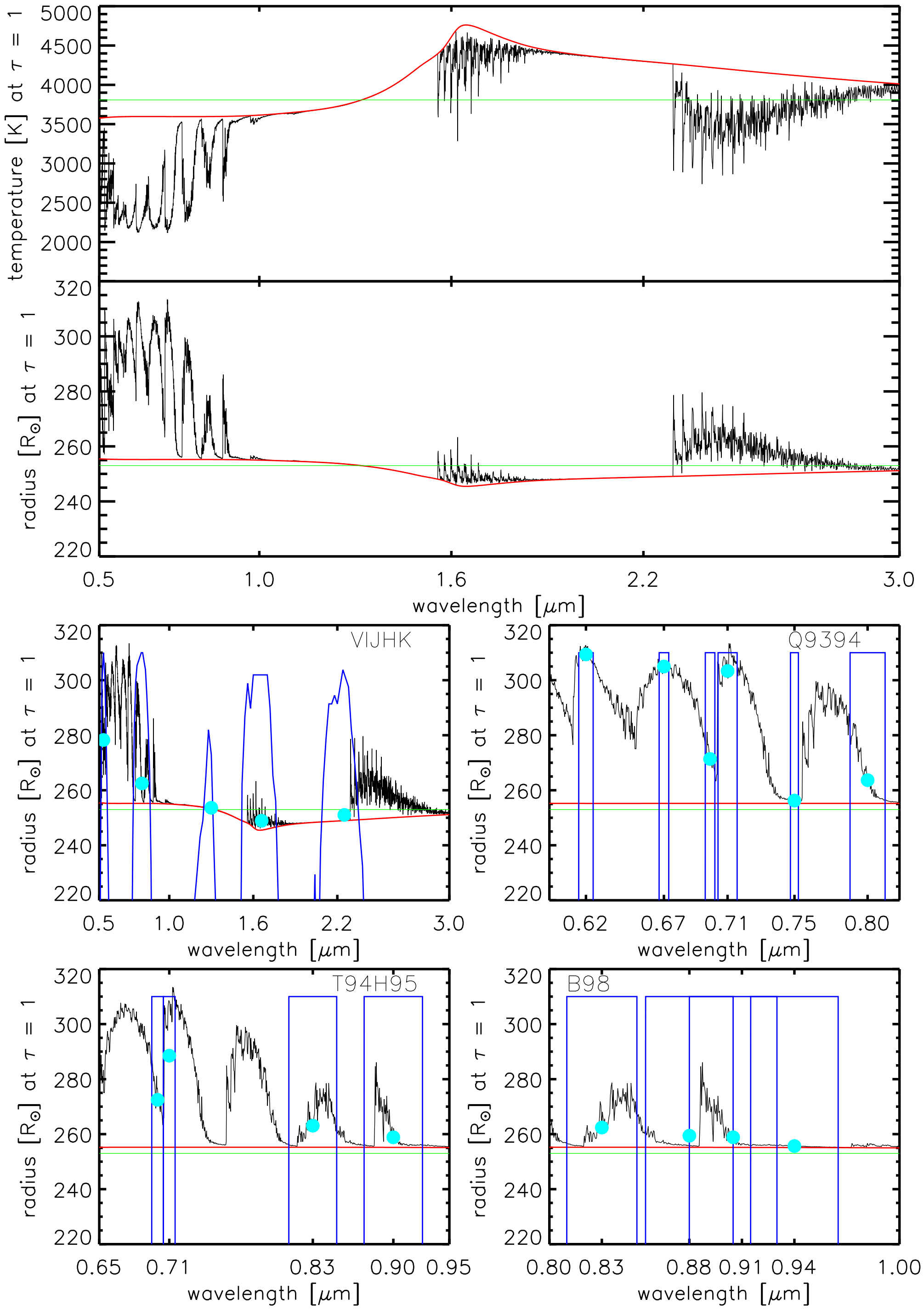

Figure 5.6: Same as Fig.5.3 but for the "parent" of the oxygen-rich dynamical model ($T_{\rm eff} = 3034\,$K, $L = 5000\,L_\odot$, $M = 1\,M_\odot$, C/O = 0.48).

in Fig. 5.4 that it is the region around $1.6\,\mu$m, where the H filter is located, where we see deepest into the star and hence closest to the radius which is relevant for the pulsation. From the spectra of Fluks et al. (1994) we can see that only in very late-type M stars (M9, M10) with effective temperatures below about 2600 K it is the K filter that is better suited. For carbon-rich stars (see Fig. 5.3) the K filter is slightly better than the H filter. All in all, the H filter appears to be the best choice for oxygen-rich stars and the K filter is best for carbon-rich stars to determine the effective temperatures, radii and hence the pulsation mode.

To estimate the influence of the dust on the filter radii we calculated the synthetic spectra and resulting filter radii with as well as without dust. We constrain the discussion to a carbon-rich model as we could simulate dust formation only on C-rich chemistry. The mean degree of condensation at the outer boundary of the model was 0.7 and it does not show a pronounced mass loss by a stellar wind. Figure 5.7 shows the ratios of selected filter radii computed with dust to the ones without dust as a function of pulsation phase. Crosses denote the K filter, asterisks the V filter, triangles the 902 filter, diamonds the 800 filter, and squares the 880 filter. The radii measured in the J, H, and K filters are almost unaffected by the presence of dust; measured in the V filter, however, the radius is about 50 % larger if dust is included. In all other filters, the radii differ between 10 and 20 %. Although no oxygen-rich dynamical models including dust formation do currently exist, we expect that the influence of the dust on the measured radii is of the same order in an oxygen-rich star with a similar mass loss rate. We have to note, however, that our approach only takes into account the absorption of the dust. Dust also causes emission and this might influence the K filter much more than the V filter. To clarify this one would have to calculate the intensity profiles.

Numerous attempts to determine effective-temperature and pulsation-mode for LPVs do exist in the literature. For our study here, we selected results for R Leo and TX Psc and compared them with our detailed model atmospheres and synthetic spectra computations to better understand the sources of discrepancy between different authors. All authors cited in Sect. 5.4.2 corrected their measured raw diameters with models of Bessell et al. (1989) or Bessell et al. (1996) which were designed for Mira itself. Dust is not accounted for in these models.

R Leo

R Leo is an oxygen-rich Mira star, varying by about 7 mag with a period of 312 days. For this star, numerous angular diameter measurements exist (see e.g. Haniff et al. 1995, Perrin et al. 1999). Tuthill et al. (1994) used for their observations filters at 833 nm and at 902 nm (see Table 5.3). They obtained a smaller uniform-disc parameter at 902 nm than at 833 nm ($\Theta_{902}/\Theta_{833} = 0.96$). This result can be quantitatively ($0.94 \leq \mathrm{R}_{902}/\mathrm{R}_{833} \leq 0.99$) reproduced by synthetic spectrum mod-

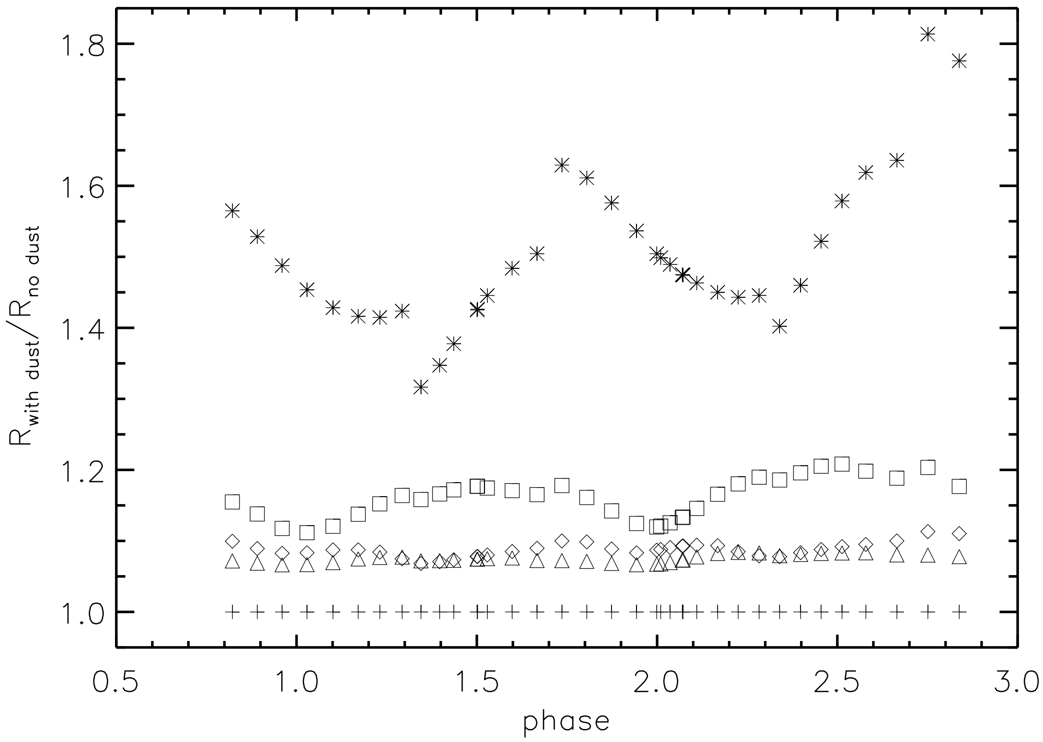

Figure 5.7: Ratio of filter radii computed with dust to those without dust as a function of phase. Crosses denote the results for the K filter, asterisks for the V filter, triangles for the 902 filter, diamonds for the 800 filter, and squares for the 880 filter.

els for a range of "low" effective temperatures ($T_{\rm eff} < 3500$ K). As can be seen in Fig. 5.4, the 902 nm filter is somewhat less contaminated by TiO than the 833 filter, and this applies at all pulsational phases (Table 5.4). Tuthill et al. (1994) compared their result with an older lunar occultation measurement by Di Giacomo et al. (1991) who used the Br γ line of atomic hydrogen at 2.16 μm for the observations performed at a comparable visual phase. Di Giacomo et al. (1991) inferred a smaller radius than Tuthill et al. (1994). According to Fig. 5.4, this is also consistent with our synthetic model spectra. Di Giacomo et al. derived an effective temperature of 2450 ± 150 K. Tuthill et al. (1994) obtained the same effective temperature and deduced eventually a first overtone pulsation to prevail in R Leo. The data of Tuthill et al. (1994) were rediscussed in Haniff et al. (1995). The inclusion of additional photometry data lead to a rise of the derived effective temperature to 2610 ± 110 K.

The very low "effective temperature" deduced for R Leo in Tuthill et al (1994) could be traced back to their blackbody fit to the JHKL photometric data. This restricted approach tends to underestimate the bolometric flux and therefore the "effective temperature". In Mira stars with pronounced dust shells as in R Leo at

Table 5.4: Filter radii of the models summarised in Tab. 5.1 and 5.2.

filter	R_{C2650} $[R_\odot]$	R_{C3000} $[R_\odot]$	$R_{Cparent}$ $[R_\odot]$	R_{C000} $[R_\odot]$	R_{C025} $[R_\odot]$	R_{C050} $[R_\odot]$	R_{C075} $[R_\odot]$	R_{O2800} $[R_\odot]$	R_{O3600} $[R_\odot]$	$R_{Oparent}$ $[R_\odot]$	R_{O000} $[R_\odot]$	R_{O025} $[R_\odot]$	R_{O050} $[R_\odot]$	R_{O075} $[R_\odot]$
V	435	280	341	589	570	517	576	180	168	278	301	313	269	275
I	432	279	342	427	435	399	393	177	167	262	280	275	251	260
J	423	274	329	372	368	336	342	167	166	254	268	265	243	252
H	414	268	317	352	346	315	323	166	164	249	260	251	240	248
K	414	268	314	347	340	307	316	169	165	251	261	255	242	250
623	436	281	346	480	473	443	447	184	174	309	332	377	396	332
672	434	279	338	434	459	418	402	183	172	305	328	370	372	305
701	440	284	353	469	477	448	431	179	167	271	294	309	254	268
712	440	285	357	474	478	457	446	183	172	303	327	368	363	316
754	430	278	337	412	429	389	383	176	167	256	271	260	245	255
800	439	284	360	472	473	447	447	178	167	264	282	281	250	261
700	439	284	352	470	475	444	433	179	167	272	295	310	256	269
710	438	284	354	469	472	448	439	183	171	289	310	325	301	294
833	436	282	349	436	447	416	408	177	167	263	282	284	250	260
902	430	278	340	422	427	389	388	176	167	259	275	267	247	257
830	436	282	350	440	449	420	412	177	167	262	281	280	249	260
880	428	277	334	407	414	372	369	176	167	259	276	269	248	257
905	430	278	341	424	429	392	391	176	167	259	275	267	247	257
940	438	284	359	459	462	438	433	173	167	256	270	259	245	254

least the M flux will still be significant. Therefore, the JHKL "effective temperature" should be referred to more precisely as a "colour temperature". Secondly, the cross-check of the previously obtained "effective temperature" using

$$T_{\rm eff} = {\rm const.} \left(\frac{F_{\rm bol}}{\Theta^2}\right)^{1/4}, \tag{5.2}$$

where $F_{\rm bol}$ denotes the bolometric flux and Θ the measured diameter in mas, is not unproblematic either. For the calculation of the bolometric flux with the help of a blackbody fit to photometric data, a blackbody temperature $T_{\rm bb}$ must be derived. Plugging the bolometric flux into eq. 5.2, the resulting temperature should be equal to the blackbody temperature again as it was the case in R Leo. If this is not the case, then the adopted diamteter is not consistent. To sum it up, "effective temperatures" of AGB stars derived from fits to IR photometric data alone are only a weak approximation to the formal effective temperature entering model atmosphere simulations. Kerschbaum & Hron (1996) have shown that the effective temperatures of AGB stars are on the average about 500 K higher than the derived blackbody temperatures which were obtained from two blackbody fits (one for the photosphere, one for the dust). The comparison of observed and synthetic spectra of carbon stars in the wavelength range between 0.5 and 2.5 μm leads to the same result (Loidl et al. 2001). Furthermore, a higher effective temperature would be more consistent with the spectral-type determinations available for R Leo (M6 to M9.5) making use of the relation between effective temperature and spectral type in Fluks et al. (1994). The higher effective temperature deduced for R Leo in Haniff et al. (1995) illustrates the shortcomings of using JHKL data only and a single blackbody fit: They reanalyzed the data of Tuthill et al. (1994), but used 1.04 μm, JHKL, IRAS data, and two blackbodies for the computation of the bolometric flux.

The second quantity, besides the bolometric flux, which enters the calculation of the effective temperature in eq. 5.2 is the stellar angular diameter in mas. To arrive at reliable photospheric radii from observations in the visual wavelength range, it is necessary to use information from spectral models to account properly for the strong prevailing TiO absorption and the contribution of dust; otherwise the diameters can be seriously overestimated. The smaller diameters that were reported by Di Giacomo et al. (1991) in the K filter already hint at such an effect in Tuthill et al. (1994) who used a model designed for Mira itself to correct for the TiO absorption in R Leo. Underestimating the bolometric flux and overestimating the diameter both contribute to assigning too low effective temperatures.

In their study of R Leo, Haniff et al. (1995) used the same two filters as Tuthill et al. (1994), but in addition they placed two filters at 700 and 710 nm. For stars with effective temperatures below about 3500 K, however, all four filters are contaminated by molecular absorption of TiO. In the 710 filter, the contamination is strongest, while it is weakest in the 902 nm one. And indeed, the measured raw diameters decrease along the sequence 710, 700, 833 and 902 nm filters ($\Theta_{710}/\Theta_{700} = 1.06$, $\Theta_{710}/\Theta_{833} = 1.51$, and $\Theta_{710}/\Theta_{902} = 1.57$), just as shown in the synthetic spectra (Fig. 5.4). The models are able to reproduce the range of R_{710}/R_{700} quantitatively, the other radii ratios are reproduced only qualitatively by our oxygen-rich dynamical model.

Haniff et al. (1995) determined radii and effective temperatures for nine more oxygen-rich Mira variables in the same way as described by Tuthill et al. (1994). In all cases, they concluded that the stars pulsate in the first overtone mode. As discussed before, we believe that also in the additional nine cases the measured radii are too large as at the wavelengths of their observations they can not measure the Rosseland radius which is relevant when applying the pulsation-constant argument to determine the pulsation mode. Therefore they have to correct their radii with a model accounting for the molecular absorption and dust. To do this properly very good models are actually needed; they must be able to describe the spectrum of the star reasonably well and reproduce the observed mass loss rate of the star in order to account also for the dust. This is far beyond the scope of all state-of-the-art dynamical models. Due to the temperature-sensitivity of TiO and H_2O and hence the huge changes in feature strength (and, as a consequence, the radii we observe) with decreasing effective temperature it is currently practically impossible to determine correct Rosseland radii of cool oxygen-rich Miras at wavelengths below 1 μm.

Effects of variability

To illustrate the effect of temporally varying radii and their association with other observable quantities we discuss now the behaviour of two dynamical models which were computed as described in Höfner et al. (1998). We chose the phasing to be compatible with observations: Phase zero is assumed at maximum luminosity. The carbon-rich dynamical model (Fig. 5.8) has a bolometric light variation of 0.46 mag. The oxygen-rich model's (Fig. 5.9) bolometric luminosity varies, on the other hand, only by 0.22 mag, being therefore more typical for a semi-regular variable. Since the spectral variations in the infrared of the SRa variable R Scl (Hron et al. 1998) could be explained qualitatively with the carbon-rich dynamical model and since comparable spectral variability is seen in C- and O-rich Mira stars (spectral features become stronger towards minimum visual light in both cases), we are positive that the carbon-rich model with its radius and effective temperature variations is dynamically quite representative of Miras. The behaviour of the spectro-photometric quantities is of course chemistry dependent.

Burns et al. (1998) observed R Leo in the 830, 880, 905 and 940 filters mentioned in Table 5.3 seventeen times during two pulsation cycles. The majority of the observations, however, was made either in the 830 or the 940 filter. The authors found the maximum apparent size of R Leo to be at visual phase of about 0.5, but that the star appeared faintest in the observed filter bands close to visual phase 0.55. In both filters (830 and 940) the brightest phases of the star corresponded to the smallest angular size. Our oxygen-rich model reproduces such a behaviour only in the filters with strong TiO contamination (623 filter in Fig. 5.9), but not in the 830 filter where it was measured. However, the model is designed to represent semi-regular variables rather than a Mira star, its variations of the effective temperature are too small for a Mira. In a slightly cooler atmosphere the contamination of 830 and 940 with TiO absorption will become stronger and hence the variation with phase might resemble closer the behaviour of the 623 filter in such a case. A quantiative clarification must, however, be postponed until better suited oxygen-rich Mira models become available.

Finally, Perrin et al. (1999) observed R Leo twice in the K band. The K-band radius is clearly the smallest one measured. Combined with the data of Burns et al. (1998), Perrin et al. found the diameter of R Leo to increase after phase 0.2 in K as well as in the visual bandpasses. The Bessell et al. (1996) models predict, however, the Rosseland radius to decrease around phase 0.2. Therefore, Perrin et al. interpreted their results as a strong disagreement with model predictions. We refer to Figs. 5.8 and 5.9 which might throw some light on this problem: In the strong TiO bands, the star's radius may not repeat very regularly during the pulsation as the TiO bands trace the motion of the propagating shocks and phase shifts relative to other bandpasses must be expected. For weaker absorption bands, on the other hand, the variation should be more regular as one sees deeper into the atmosphere (Fig. 5.9). In our models, the Rosseland radius decreases indeed after phase 0.2. If R Leo would indeed have effective temperatures of about 2500 K as reported by Tuthill et al. (1994) and Di Giacomo et al. (1991), then – due to the strong molecular absorption – no filter choice whatsoever would measure the Rosseland radius of the star. An effective temperature comparable to what Perrin et al. (1999) obtained, grants access to the Rosseland radius in H and K (as in our oxygen-rich dynamic model; Fig. 5.9). As a consequence, there must also exist effective temperature ranges at which no H_2O absorption contaminates the spectrum around maximum light while it happens around minimum light. Monitoring such a star over a cycle would allow us to look into quite different layers at different phases, it would be possible to catch the Rosseland radius only for a fraction of a cycle. This would hence mimic a different temporal variation of the stars' radius. Therefore, a detailed grid of oxygen-rich dynamic models seems necessary to quantify such effects.

Compared to earlier studies of R Leo, Perrin et al. (1999) obtained smaller linear radii and higher effective temperatures. The authors attribute the inability to reproduce short-wavelength data with any Mira model to missing physics in the models. They found that whatever they included additionally (limb brightening, convective cells, spots, underestimation of molecular absorption) in the modelling, it further decreased the stellar diameter by as much as 25 percent. Perrin et al. concluded R Leo to be a fundamental-mode pulsator with a mean photospheric radius of about 250 $R_\odot$. Additionally, the derived effective temperatures were higher and more consistent with the spectral-type determinations that were performed at the same epochs. We interpret the results of this group as good evidence for fundamental-mode pulsation of R Leo from the observational side because the Perrin et al. band measurements of the diameter were done at a wavelength which is very well suited for this kind of analysis and because they inferred effective temperatures which are consistent with spectral-type determinations.

Whoever determined the pulsation mode of R Leo referred to the pulsation constant Q. R Leo's period is well determined and a mass of about one solar mass seems likely. Therefore, the only problematic quantity in the equation for the pulsation constant (eq. 5.1) is the star's radius. The conversion from the measured diameters to the linear dimensions is cumbersome. First, some sort of distance estimate is necessary, be it through association of the star with a stellar aggregate whose distance is known, through the applicability of a period-luminosity relation, or through a parallax measurement. Whatever is used, the uncertainties are considerable to date (see e.g. Sect. 5.6). Additionally, the radius in the equation of Q corresponds usually to the star's equilibrium Rosseland radius (see the discussion in Sect. 5.4.1). LPV's, in particular Miras, undergo large radius variations during a pulsation cycle and they pass through the equilibrium phase only twice. As it can be seen in nonlinear pulsation simulations (e.g. Ya'ari & Tuchman 1996, or Wood 1989) large-amplitude pulsators spend most of their time during a cycle in an inflated state. Simple nonlinear modeling (Gautschy 1987) demonstrated already the growing asymmetry between compression and inflation as a function of the velocity amplitude. Unfortunately, no general rule is known about how brightness observations alone can be used to predict the phase when LPVs pass through their equilibrium state. Therefore, measuring radii *randomly* over a pulsation cycle or even arithmetically averaging a series of radius measurements cause the mean radii to be systematically to large.

TX Psc

For carbon-rich Miras much less radius determinations do exist and most of the few have been measured only once (e.g. Van Belle et al. 1997). This is not enough for a detailed comparison as it has been done for R Leo. As a consequence we chose the irregular variable TX Psc as example for a carbon-rich star, although it is not possible to say something about the pulsation mode in this case. TX Psc is the brightest, and therefore best studied carbon-rich irregular variable star in

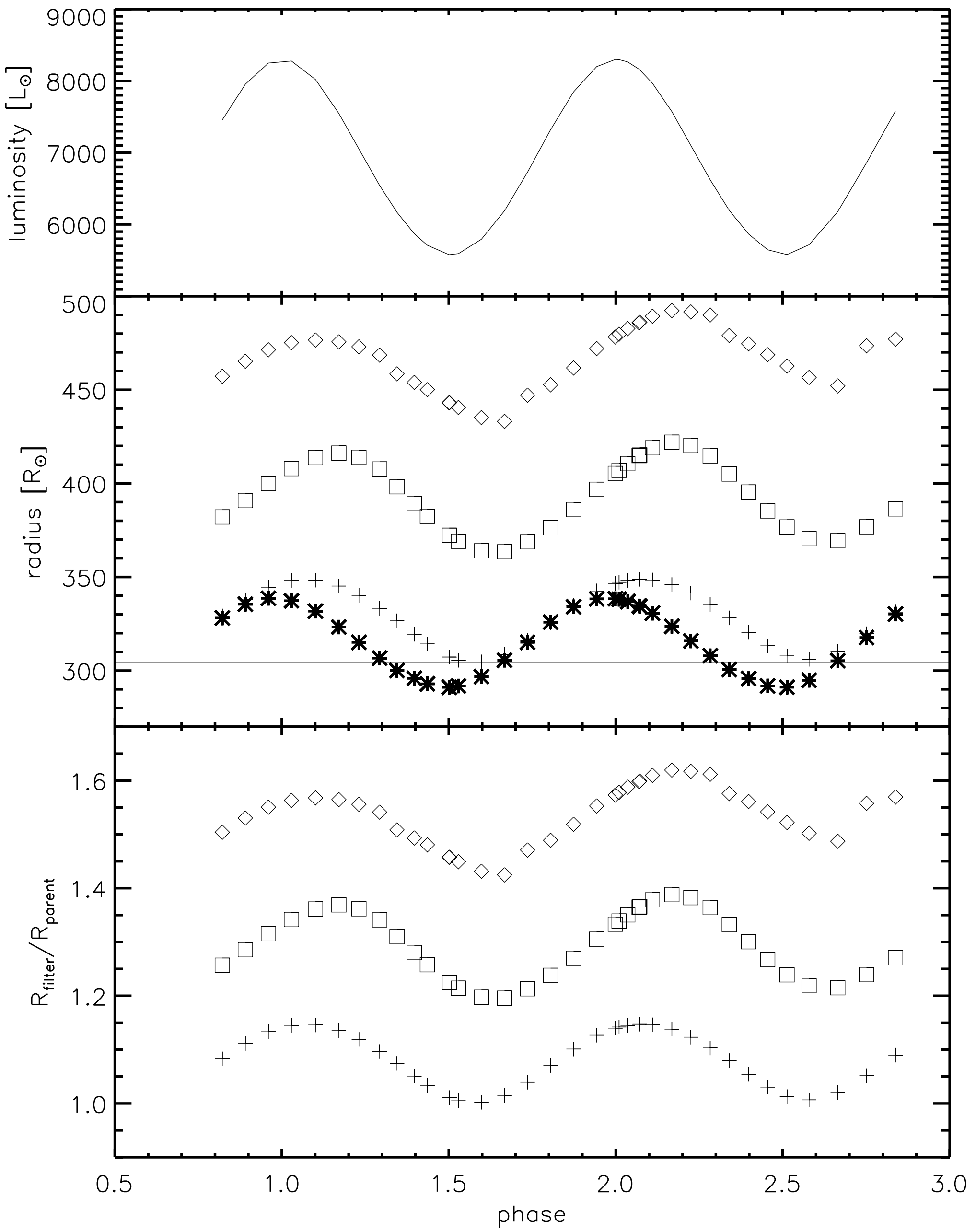

Figure 5.8: Temporal variation of selected physical quantities of a dynamical carbon-rich model: Luminosity versus phase (upper panel); radius at $\tau_{\text{Ross}} = 1$ (asterisks) and the filter radii for the K (crosses), 800 (diamonds) and 902 (squares) filters versus phase (middle panel); and the ratio of filter radii and radius of the parent (lower panel). The straight full line in the middle panel marks the value of the parent model; it corresponds to the equilibrium value entering the theoretical Q determinations.

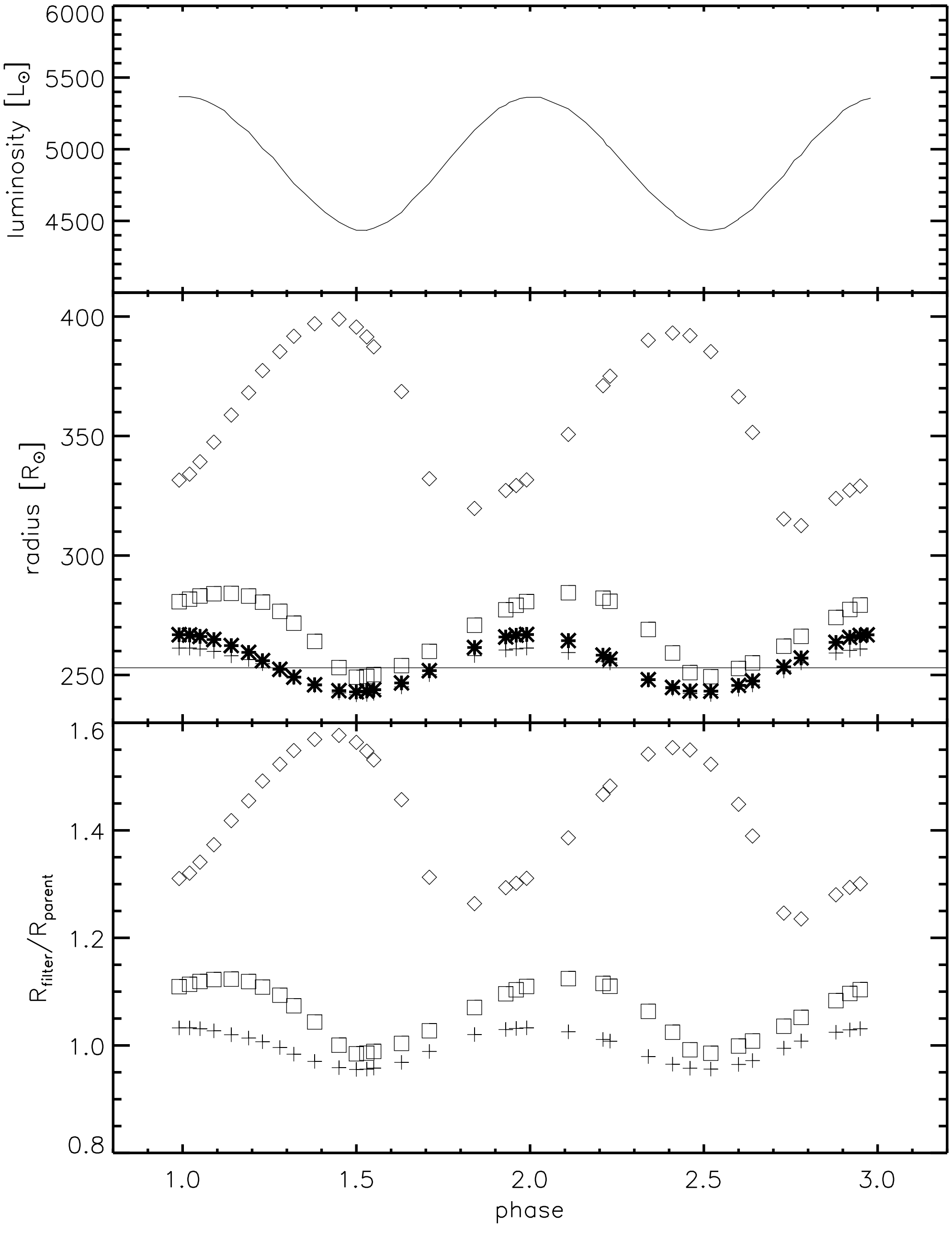

Figure 5.9: Same as Fig. 5.8 but for the oxygen-rich dynamical model. Crosses denote the K filter, diamonds the 623 filter and squares the 830 filter.

the sky. Jørgensen et al. (2000) showed that model C3000 describes the star's spectrum quite well between 0.5 and 10 μm. Therefore, we will compare in the following the results from angular diameter measurements with this particular model.

Quirrenbach et al. (1994) used for their study of TX Psc filters with central wavelengths at 712, 754 and 800 nm. For carbon stars, all these filters give access to the atmosphere to about the same depth (see Fig. 5.3). Therefore, observations through the three filters should all result in about the same diameters. This is indeed what was reported by Quirrenbach et al. (1994). These authors also obtained visual magnitudes at the epochs of the angular diameter measurements. The data showed TX Psc's diameter to be larger when it is brighter. Our carbon-rich dynamic model shows a similar behaviour, in the 800 filter it reaches the largest diameter around phase 0.2.

Model atmospheres and the resulting synthetic spectra describing the spectra of TX Psc well have effective temperatures between 3000 and 3100 K (see Jørgensen et al. 2000 for a summary). The effective temperature derived by Quirrenbach et al. (1994) was about 200 K lower; this is probably due to their measurement being the mean of two arbitrarily taken ones with correspondingly large errors. Quirrenbach et al. did not correct for the CN absorption which contaminates their measurements. Therefore, their derived radii should be slightly too large and the resulting effective temperature somewhat too low. Nevertheless, "measured" and model effective temperature lie essentially within the uncertainty limits.

Semi-regular and irregular variables appear to be the best candidates for radius determinations: Van Belle et al. (1997) found irregular and semi-regular variables to have smaller sizes than Mira variables which means that they are more compact and therefore less prone to large errors due to variable transparency within the atmosphere. They also found that oxygen-rich variables are systematically smaller and hotter than carbon-rich ones. In carbon stars, we generally come slightly closer to the Rosseland radius when observing in the visual spectral range.

It is not further surprising that the measured angular diameters and the claimed effective temperatures of irregular or only moderately varying semi-regular variable stars agree reasonably well with the corresponding quantities derived from detailed model atmospheres. Besides the fact that the measured radii are still slightly too large if the measurements are not corrected carefully for molecular absorption with the help of model atmospheres, it is the distance determination to assess linear dimensions which is the major source of error. Therefore, we are unfortunately confronted with the fact that the most suitable AGB variables for a radius determination are almost useless to settle the pulsation-mode debate because very long continuous observations are necessary to identify the rather long (and multiple) periods of these stars.

5.5 Conclusions

We discussed problems of assigning radii and eventually pulsation modes to LPVs by focusing on two well observed specimen, the O-rich Mira R Leo and the C-rich irregular variable TX Psc. We used synthetic spectra and model atmosphere simulations to understand the observational findings and the frequently encountered seemingly discrepant results between different authors.

We found that the inclusion of dust formation in the calculations altered the filter radii in the visual and near-infrared range down to about 1 μm. Radii derived from models with dust differed from dustless ones by about 10 % in this spectral range. The J, H and K filter radii are not affected. However, it should be noted that our approach only took into account the absorption of the dust. Dust also causes emission and this might influence the K filter much more than the V filter.

Based on the synthetic spectra presented in this work we can say that in most attempts to attribute radii to LPVs, the dimensions seem to be systematically overestimated, the amount depends on the chosen filter passband. Therefore, the first-overtone pulsation mode is favored in the final interpretations.

A further complication in the determination of the equilibrium radius of an LPV is its temporal variability. Figure 5.8 shows that a simple arithmetic averaging is reasonable only for small pulsation amplitudes. The asymmetry between expansion and compression grows with velocity amplitude (cf. Gautschy 1987). The restriction to phases of minimum radii of Miras yields generally a more satisfactory approximation to the equilibrium radius (see also Gautschy 1999). We finish this discussion with a recipe to optimize the pulsation-relevant radius measurement of LPVs, some ingredients are self-evident but they are mentioned nevertheless since they are a must for a successful result:

1. Only in the H and K filter we see deep enough into the cool stars' atmospheres to measure the radius at which $\tau_{\rm Ross} = 1$. This is the radius which enters in the theoretical determination of the pulsation constant Q. Notice that in the H and K filters, it can happen that one sees deeper than where $\tau_{\rm Ross}$ reaches unity. This is clearly preferable over getting stuck in regions with $\tau_{\rm Ross} < 1$. Due to the density rise at about the photosphere, the relative error in radius of going deeper is much less than getting caught higher up in the atmosphere.

2. The variability, and in particular the considerable radial displacements of the large-amplitude AGB stars make the determination of the "equilibrium" radius problematic. Except for small amplitude pulsators, the minimum radius is a better approximation of the equilibrium radius than the arithmetic mean over the phases of pulsation cycle. Averaging random-phase obser-

vations tends to overestimate the equilibrium radius. The deviation grows with velocity amplitude.

3. To minimize the errors in the effective-temperature determination, the visual and near-infrared photometry used for the calculation of the bolometric flux must be taken at the same epoch as the radius measurement. Additionally, fluxes longwards of $5\,\mu$m (e.g. IRAS fluxes) should also be included whenever possible. And again, averaging over epochs tends to introduce significant errors.

Keeping all of the above in mind, we suggest to select only well studied Miras, devoid of warm dust to determine radii and pulsation modes. If spectra of such a chosen star are available at different phases, model atmospheres can contribute substantially to optimise the quality of effective temperatures and possible corrections to the radii at the various phases.

5.6 Dependencies of radii on other parameters

Van Belle et al. (1999) obtained a sample of stars which is large enough to provide empirically determined dependencies of "effective temperature" and linear radius upon spectral type and V–K colour. The "effective temperatures" were calculated as explained in Sect. 5.4.2 and the distances of the stars, necessary to compute linear diameters, were derived with the help of HIPPARCOS parallaxes. The stellar radius is then given by

$$R = 0.1076\,\theta_{\mathrm{R}}\,d$$

where the units of R are $\mathrm{R}_\odot$, d is in parsecs, and θ_{R} is the Rosseland diameter. We selected the K and M giant stars from the paper of Van Belle et al. (1999) and compared the results with our models. Additionally, we used the data of carbon-rich Miras and S-type stars from Van Belle et al. (1997). In the work of Dyck et al. (1996a), Dyck et al. (1996b) and Dyck et al. (1998) only the "effective temperatures" and the measured diameters are given. In order to obtain linear diameters for these observations we used HIPPARCOS parallaxes to compute the distances. V and K data were collected from the SIMBAD data base. Van Belle et al. (1996) published linear radii for oxygen-rich Mira stars observed around minimum and maximum light. Correspondingly, we chose the minimum and maximum V values for the computation of V–K. It should be stated, however, that especially the V–K values of the Mira stars can be considerably uncertain. The K magnitude itself can vary about 1^m in Miras.

In a second attempt we derived the distances of the Miras and semi-regular variables differently: Using the period-luminosity relation derived by Barthés et al. (1999) for their Group 1 stars for our Mira stars in the sample,

$$M_K = -5.04\,(\log P - 2.48) - 7.26,$$

and their period-luminosity relation for their Group 2 stars for our semiregular variables in the sample,

$$M_K = -1.13\,(\log P - 2.00) - 6.41,$$

we calculated M_K and in the following the distance d and the linear radius. This excluded the K stars and irregular AGB stars from the sample because in those cases no periods were available. Originally we intended to use the period-luminosity-colour relations given in Barthés et al. (1999), but it turned out that we introduced an artificial effect due to the coulour term. Therefore, we decided to use the period-luminosity relations only. In the following we will discuss the results of both the HIPPARCOS and the P-L investigations and compare the results.

Figure 5.10 shows effective temperature versus V–K (upper left panel) for the observations and for models and observations (upper right panel), radius versus V–K (lower left panel) for observations and radius versus effective temperatures (lower right panel) for the observations; the linear radiii were calculated using the distances obtained from the HIPPARCOS data. The red asterisks denote models with C/O = 1.1, the green asterisks models with C/O = 1.4 and the blue asterisks models with C/O = 0.48. The black line and the crosses show the positions of blackbodies with temperatures between 5000 and 1800 K. The red sample are data from Van Belle et al. (1999; oxygen-rich, K stars and moderately variable stars), the green sample from Van Belle et al. (1997; carbon-rich Miras and S Miras, semiregular and irregular variables), the dark blue sample from Dyck et al. (1996a; carbon-rich, semiregular and irregular variables), the turquoise sample from Dyck et al. (1998; oxygen-rich, semiregular and irregular variables), and the magenta sample from Van Belle et al. (1996; oxygen-rich Miras). Different symbols denote different types of variability as labeled in the plot. Most reliable should be the red, turquoise and the dark blue samples, as most of the stars in these samples are only moderately variable stars, i.e. the errors introduced by using photometry taken at other epochs should be smaller than in the case of Miras. As a consequence also the derived "effective temperatures" are much more uncertain for the Miras. For all types of stars except probably the K giants the problems of determining the Rosseland radius which have been discussed in detail in Sect. 5.4.2 apply. However, Van Belle et al. (1999) were able to show the following with their data set:

- Looking at the oxygen-rich non-Mira stars (red and turquoise data points) in the upper left panel of Fig. 5.10 it is obvious that they deviate from the blackbody curve significantly at V–K values redder than 6.0. Also our oxygen-rich models (blue asterisks in upper right panel) show this behaviour

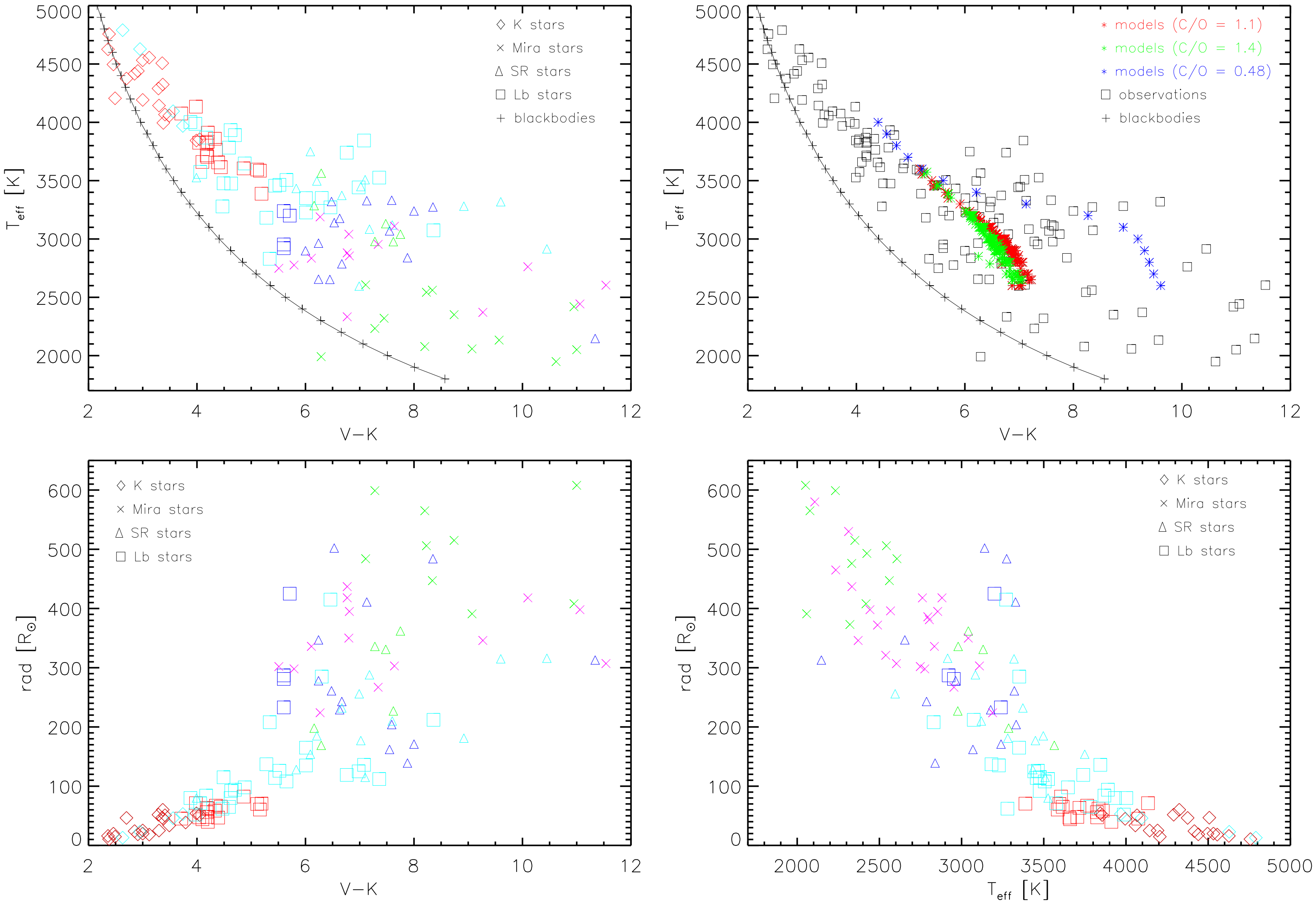

Figure 5.10: Effective temperature versus V–K (upper panel), radius versus V–K (lower left panel) and radius versus effective temperature (lower right panel) for observations. Different colours denote samples of stars with different variability types and chemistry. For details of the colour coding see the text. The distances of the stars, necessary for the computation of the linear radius, were calculated using HIPPARCOS data.

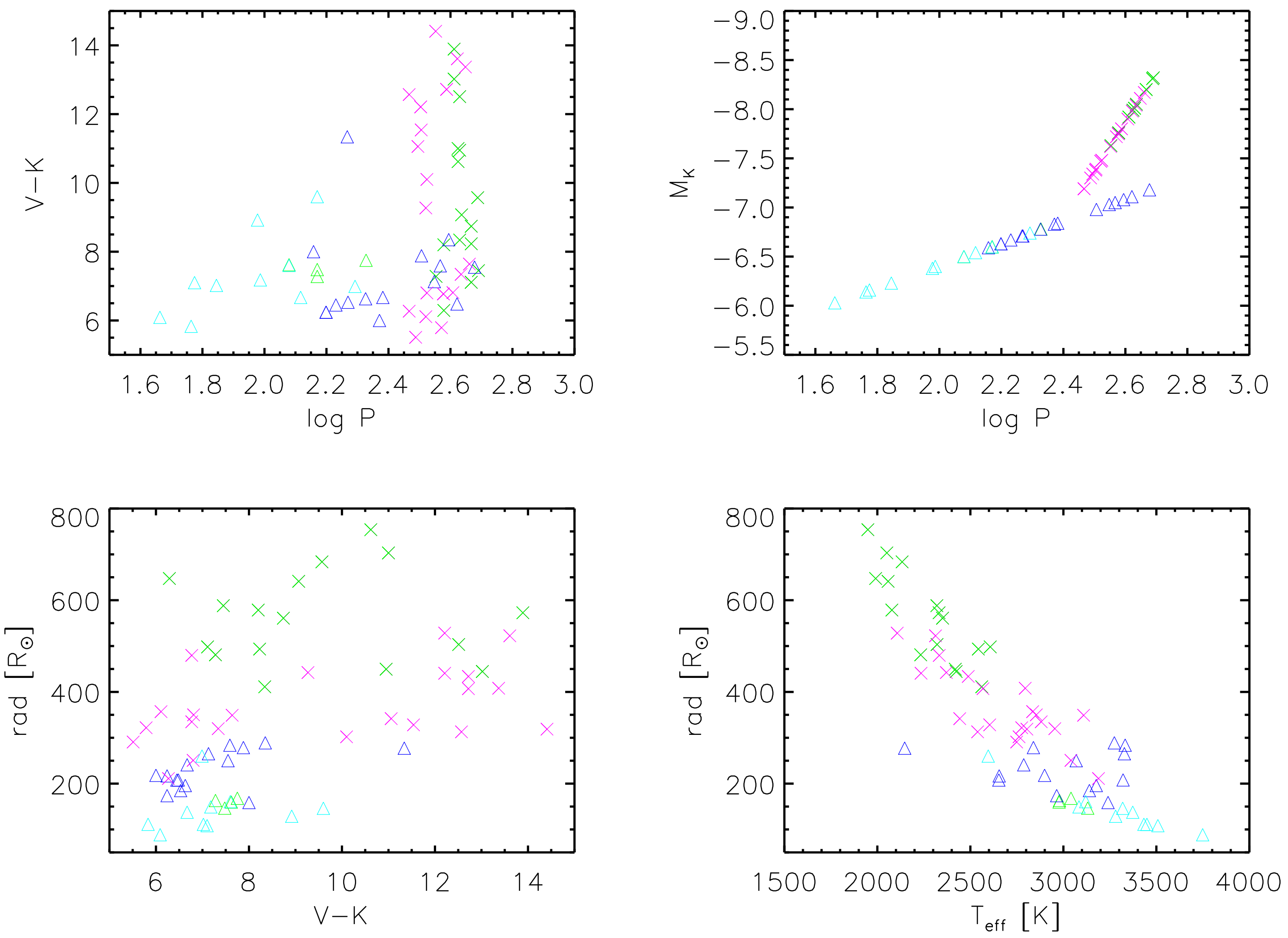

Figure 5.11: V−K plotted versus log$P$ (upper left panel), M_K versus log$P$ (upper right panel), linear radius versus V−K (lower left panel), and linear radius versus effective temperature (lower right panel). The denotations are the same as in Fig. 5.10. The distances of the stars, necessary for the computation of the linear radius, were calculated using a period-luminosity relation.

which is due to strong H_2O absorption. For carbon stars the effect is less pronounced (dark blue data points). The carbon-rich models (red and green asterisks in upper right panel) lie parallel to the blackbody curve.

- They found relations between the radius of a star and its spectral type and between radius and V–K (lower left panel of Fig. 5.10).

$$R = 1.76\,(V - K)^{2.36}\,R_{\odot}$$

- They found a relation between radius and effective temperature (lower right panel of Fig. 5.10). However, one has to keep in mind, that these effective temperatures were calculated via eq. 5.2, i.e. this result is therefore not surprising.

Figure 5.11 shows V−K plotted versus log$P$ (upper left panel), M_K versus log$P$ (upper right panel), linear radius versus V−K (lower left panel), and linear radius versus effective temperature (lower right panel). The denotation and colour coding is the same as in Fig. 5.10. The distances of the stars, necessary for the computation of the linear radius, were calculated using period-luminosity relations of Group 1 (for Miras) and Group 2 (for semiregular variables) stars of Barthés et al. (1999). A comparison of the linear radii versus V−K plots in Figs. 5.10 and 5.11 (lower left panels) yields the following:

- In both cases there is no clear correlation visible between linear radii and V−K for V−K values larger than 6.

- Miras (crosses) occupy a complete different region in the radius versus V−K diagram than semiregular variables (triangles) in Fig. 5.11. This is not the case in Fig. 5.10. The behaviour in the case where the linear distances were calculated with the help of a P–L relation may be artificial and caused by the fact that the largest M_K values of the semiregular variables are still smaller than the smallest M_K values of the Miras in our sample.

- Fig. 5.11 nicely illustrates that 1) Miras with a certain V−K value are larger than semiregular variables with the same V−K colour; 2) oxygen-rich semiregular variables (turquoise triangles) with a certain V−K value are smaller than carbon-rich semiregular variables (dark blue triangles) with the same V−K colour; 3) oxygen-rich Miras (magenta crosses) with a certain V−K value are smaller than carbon-rich Miras (green crosses) with the same V−K colour. Fig. 5.10 gives the same results, although less pronounced.

In Fig. 5.12 we show the ratio of linear radii determined with HIPPARCOS parallaxes and of linear radii derived from a P-L relation versus V−K (left panel)

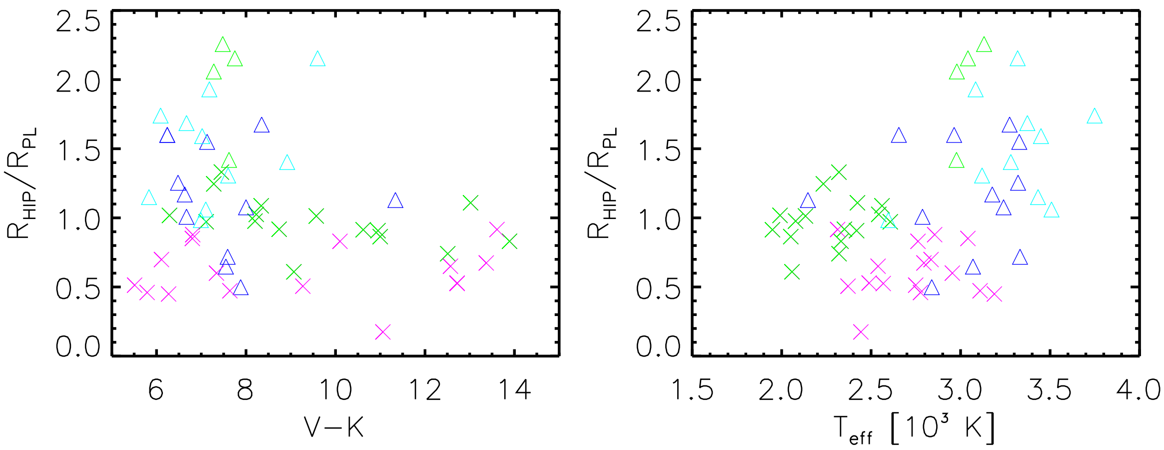

Figure 5.12: Ratio of linear radii determined with HIPPARCOS parallaxes and of linear radii derived from a P-L relation versus V−K (left panel) and versus the effective temperature (right panel). The symbols are the same as in Fig. 5.11.

and versus the effective temperature (right panel). We see that the linear radii of semiregular variables are basically all *smaller* if the distances of the stars were calculated using a period-luminosity relation. Most of the semiregular variables lie in the radius regime (see Fig. 5.11) being compatible with the loci of fundamental mode pulsators ($220 \leq R/R_\odot \leq 270$). On the contrary to the semiregular variables, Mira stars are basically all *larger* if the distances were computed using a period-luminosity relation. For oxygen-rich Miras the discrepancy between the results of both methods is larger than for carbon-rich ones. The loci of the Miras in the lower left panel of Fig. 5.11 are in accordance with the ones of overtone pulsators ($R \geq 350\,R_\odot$).

The fact that all semiregular variables become smaller and all Miras larger if the linear radii are calculated with the help of P–L relations suspiciously hints at a problem with the adopted P–L relations. We explicitely warn to conclude from our investigations that semiregular variables are fundamental mode and Miras overtone pulsators. Instead we conclude that at present the derived linear radii are very much dependent on the method used to compute the distances of the stars. Various available period-luminosity relations give already quite different linear radii with possible deviations of up to 100 %. The uncertainties are too high to conclude anything reasonable about the pulsation mode based on the observations currently. The smaller range occupied by semiregular variables in the linear radii versus V−K diagram probably reflects nothing else than that the "correct" diameters of semiregular variables are easier to measure than the ones of Miras due to their smaller variability and due to their less extended atmospheres (see discussion in Sect. 5.4.2).

Chapter 6

Conclusions and future aspects

6.1 Conclusions

We showed that the stellar parameters $T_{\rm eff}$, ^{12}C/^{13}C and C/O can in principle be determined from broad- and narrow-band colour indices. We have been able to find indices for which no or small systematic differences exist between the loci of models and observations. Spectrophotometry in the 3 and 5 μm region (L and M band) appears to be the most promising tool to determine $T_{\rm eff}$ and C/O of an AGB star.

Detailed investigations of the synthetic spectra of the presently available dynamical models calculated with a frequency-dependent radiative transfer yielded the following results:

- The spectra of the hydrostatic initial models of the dynamical computations calculated with only 51 frequency points resemble already very closely the spectrum of a classical hydrostatic model calculated with about 10 000 frequency points.

- The intensity of the CO feature around 4.6 μm, the intensity of the C_3 feature around 5.1 μm, and the intensity of the C_2H_2 feature at 3 μm decreased in the models that developed a stellar wind and where dust formed.

- Two strong emission features around 7 and 14 μm occured in our synthetic spectra if the model showed a pronounced mass loss and dust formed. The emission originated in layers cooler than ≈ 1000 K.

- Dynamical models are able to reproduce a spectral feature around 1.53 μm which is observed in cool carbon stars. The origin of this band is still debated; in our models it could be attributed to a contribution of C_2H_2 and HCN at the same wavelengths where a band of C_2 is present.

A comparison of various observational data in the wavelength range between 0.5 and 45 μm with plane parallel and spherical hydrostatic model spectra, as well as with dynamical model spectra showed that the spectra of relatively hot and only moderately variable stars with low C/O ratios as TX Psc can be fitted very well with synthetic spectra based on hydrostatic model atmospheres in the wavelength range between 0.7 and 10 μm. At wavelengths shorter than 0.7 μm we lack the contribution of the atomic lines in our calculations, at wavelengths longer than 10 μm we do not see the pure photospheric spectrum anymore. Hydrostatic and dynamic model spectra are able to reproduce the correct trends of colour indices in the wavelength range between 0.7 and 1.1 μm. The model colour indices lie in the correct regions. Depending on the index, the range of the observed colour indices can be reproduced to different extents. A discussion of various broad-band colours in the optical and infrared range showed that hydrostatic and dynamic models are able to reproduce the observed I−J, J−K, and I−K colours of carbon-rich stars in the LMC. The observed ranges of other colours can be described only partly. Generally speaking, the locations of very cool Miras in the two-colour diagrams cannot be reproduced currently. This may well be due to the choice of parameters of the four dynamical models discussed here which were designed to describe stars with moderately thick dust shells. Dynamical model spectra predict that the 7 and 14 μm feature is filled up with emission, but the amount of emission is much too strong. However, these models suggested that it is likely that we see emission in the 5.5 to 7 μm region in the spectra of cool carbon stars. Proper self-consistent modelling of the 14 μm region of carbon stars will be one of the challenging topics in the future. It will only be possible to describe it if the structure of the photosphere as well as of the envelope are modelled correctly. Our dynamical models show that the contribution of the dust as well as emission due to the molecules C_2H_2 and HCN fill up the strong photospheric absorption feature predicted by hydrostatic models.

We discussed problems of assigning radii and eventually pulsation modes to LPVs by focusing on two well observed specimen, the O-rich Mira R Leo and the C-rich irregular variable TX Psc. We conclude that in most attempts to attribute radii to LPVs, the dimensions seem to be systematically overestimated, the amount depends on the chosen filter passband. Therefore, the first-overtone pulsation mode is favored in the final interpretations. A further complication in the determination of the equilibrium radius of an LPV (which is the necessary input for a proper determination of the pulsation mode) is its temporal variability. The restriction to phases of minimum radii of Miras yields generally a more satisfactory approximation to the equilibrium radius than measurements taken at other pulsational phases. We suggest to select only well studied Miras, devoid of warm dust to determine radii and pulsation modes. If spectra of such a chosen star are available at different phases, model atmospheres can contribute substantially to optimise the quality of effective temperatures and possible corrections to the radii at the various phases.

6.2 Future aspects

Modelling of carbon stars has reached a level where the quality of the opacity data starts to become the crucial limitation. Unfortunately, considerable uncertainties in the C_2, C_3, C_2H_2, and HCN opacities exist. These uncertainties have strong implications on the determination of the C/O ratio of a star as well as on the amount of emission produced in dynamical model spectra. Spherical model atmospheres and spectra are much more susceptible to the effects introduced by uncertain opacity data than plane parallel ones; in the plane parallel case the features become saturated, in the spherical case emission can occur. In principle one could try to find the "best" opacity data by trying to fit a star which should have the following properties: 1) it should show a pronounced 3 μm feature, hence its effective temperature has to be lower than 3100 K; 2) it should not be surrounded by large amounts of dust, otherwise hydrostatic models are not able to describe it; 3) it should have a C/O ratio which is high enough that the spectra are susceptible to different sets of C_2 opacities and $K_p(C_3)$ values. The third point unfortunately excludes TX Psc as a candidate. Most promising for such an detective attempt seems to be T Lyr. However, it is a very unsatisfactory and annoying situation to determine the "correct" opacities by fitting observed spectra. We definitely need better laboratory measurements and hopefully they will be done in the near future. Otherwise it will not be possible to disentangle effects of missing physics in the models from artificial effects caused by badly determined equilibrium constants. For a better description of the optical spectra of carbon stars atomic lines will be included in our spectrum calculations in the near future.

Concerning dynamical models very promising results could be obtained already: the occurence of the 1.53 μm feature in dynamical models with a stellar outflow and the filling up of the strong photospheric absorption feature at 14 μm with emission shows that they are powerful tools. The next steps will be to successively eliminate or improve the models concerning the treatments which we proposed as reasons for the unrealistic strong emission; namely to extend the model structures to even lower temperatures, to test other model parameters, and on long sight to incorporate another equilibrium chemistry.

Appendix A

Model parameters of selected models

Model	$T_{\rm eff}$ [K]	$M_*/M_\odot$	$\log(g)$ [cm/s^2]	$L_*/L_\odot$	$R_*/R_\odot$	C/O	$\log(Z/Z_\odot)$	pp/sph
m001pp	2800	1.0	+0.00	1509	166	1.01	0.00	pp
m002pp	2900	1.0	+0.00	1736	166	1.01	0.00	pp
m003pp	3000	1.0	+0.00	1988	166	1.01	0.00	pp
m004pp	3200	1.0	+0.00	2574	166	1.01	0.00	pp
m005pp	2700	1.0	-0.20	2068	208	1.02	0.00	pp
m006pp	2800	1.0	-0.20	2391	208	1.02	0.00	pp
m007pp	2900	1.0	-0.10	2186	186	1.02	0.00	pp
m008pp	3000	1.0	+0.00	1988	166	1.02	0.00	pp
m009pp	3100	1.0	+0.00	2267	166	1.02	0.00	pp
m010pp	3200	1.0	+0.00	2574	166	1.02	0.00	pp
m011pp	3300	1.0	+0.00	2911	166	1.02	0.00	pp
m012pp	3400	1.0	+0.00	3281	166	1.02	0.00	pp
m013pp	2600	1.0	-0.43	3019	272	1.10	0.00	pp
m014pp	2650	1.0	-0.76	7000	397	1.10	0.00	pp
m015pp	2700	1.0	-0.36	3000	250	1.10	0.00	pp
m016pp	2700	1.0	-0.58	5000	323	1.10	0.00	pp
m017pp	2700	1.0	-0.73	7000	384	1.10	0.00	pp
m018pp	2800	1.0	-0.30	3000	234	1.10	0.00	pp
m019pp	2800	1.0	-0.52	5000	301	1.10	0.00	pp
m020pp	2800	1.0	-0.67	7000	358	1.10	0.00	pp
m021pp	2900	1.0	-0.24	3000	218	1.10	0.00	pp
m022pp	2900	1.0	-0.46	5000	281	1.10	0.00	pp
m023pp	2900	1.0	-0.61	7000	334	1.10	0.00	pp
m024pp	3000	1.0	-0.18	3000	204	1.10	0.00	pp
m025pp	3000	1.0	-0.40	5000	262	1.10	0.00	pp
m026pp	3000	1.0	-0.55	7000	312	1.10	0.00	pp
m027pp	3100	1.0	-0.12	3000	190	1.10	0.00	pp
m028pp	3100	1.0	-0.34	5000	245	1.10	0.00	pp
m029pp	3100	1.0	-0.49	7000	291	1.10	0.00	pp
m030pp	3200	1.0	-0.07	3000	179	1.10	0.00	pp
m031pp	3200	1.0	-0.29	5000	231	1.10	0.00	pp
m032pp	3200	1.0	-0.43	7000	272	1.10	0.00	pp
m033pp	3300	1.0	+0.00	2911	166	1.10	0.00	pp
m034pp	3400	1.0	+0.00	3281	166	1.10	0.00	pp
m035pp	3500	1.0	+0.00	3684	166	1.10	0.00	pp
m036pp	3600	1.0	+0.00	4123	166	1.10	0.00	pp
m037pp	2944	1.5	+0.00	2766	203	1.10	0.00	pp
m038pp	3184	1.5	+0.23	2229	156	1.10	0.00	pp
m039pp	3388	1.5	+0.53	1432	110	1.10	0.00	pp

Model	$T_{\rm eff}$ [K]	$M_*/{\rm M}_\odot$	$\log(g)$ [cm/s^2]	$L_*/{\rm L}_\odot$	$R_*/{\rm R}_\odot$	C/O	$\log(Z/{\rm Z}_\odot)$	pp/sph
m040pp	2972	1.5	-0.08	3454	222	1.10	0.00	pp
m041pp	2999	1.5	-0.15	4208	241	1.10	0.00	pp
m042pp	2831	1.5	-0.17	3499	247	1.10	0.00	pp
m043pp	2864	1.5	-0.27	4613	277	1.10	0.00	pp
m044pp	2786	1.5	-0.39	5446	318	1.10	0.00	pp
m045pp	2812	1.5	-0.46	6640	344	1.10	0.00	pp
m046pp	2958	2.0	+0.16	5433	281	1.10	0.00	pp
m047pp	2999	2.25	+0.00	4468	248	1.10	0.00	pp
m048pp	3236	2.25	+0.22	3650	193	1.10	0.00	pp
m049pp	3467	2.25	+0.56	2198	130	1.10	0.00	pp
m050pp	3467	2.25	-0.03	5062	257	1.10	0.00	pp
m051pp	3062	2.25	-0.05	5448	263	1.10	0.00	pp
m052pp	2877	2.25	-0.12	4989	285	1.10	0.00	pp
m053pp	3126	2.25	-0.22	8753	320	1.10	0.00	pp
m054pp	2838	2.25	-0.31	7316	355	1.10	0.00	pp
m055pp	2985	2.25	-0.38	10520	385	1.10	0.00	pp
m056pp	2951	2.25	-0.50	13246	442	1.10	0.00	pp
m057pp	3236	4.1	+0.10	8767	299	1.10	0.00	pp
m058pp	3459	4.3	+0.44	5487	207	1.10	0.00	pp
m059pp	3177	5.0	+0.00	12505	370	1.10	0.00	pp
m060pp	3388	5.0	+0.25	9095	278	1.10	0.00	pp
m061pp	3573	5.0	+0.56	5510	194	1.10	0.00	pp
m062pp	3020	5.0	-0.09	12561	411	1.10	0.00	pp
m063pp	2938	5.0	-0.22	15178	477	1.10	0.00	pp
m064pp	2967	5.0	-0.39	23350	580	1.10	0.00	pp
m065pp	3556	2.25	+0.32	4246	172	1.10	-0.30	pp
m066pp	3459	2.25	+0.16	5495	192	1.10	-0.30	pp
m067pp	3350	2.25	+0.00	6918	248	1.10	-0.30	pp
m068pp	3236	2.25	-0.16	8870	300	1.10	-0.30	pp
m069pp	3041	2.25	-0.49	14454	434	1.10	-0.30	pp
m070pp	2965	2.25	-0.67	19953	537	1.10	-0.30	pp
m071pp	2958	2.0	+0.16	5495	283	1.10	-0.30	pp
m072pp	3451	1.0	+0.24	1995	125	1.10	-0.30	pp
m073pp	3221	1.0	-0.04	2897	173	1.10	-0.30	pp
m074pp	3020	1.0	-0.33	4365	242	1.10	-0.30	pp
m075pp	2958	1.0	-0.46	5495	283	1.10	-0.30	pp
m076pp	2917	1.0	-0.55	6310	312	1.10	-0.30	pp
m077pp	2858	1.0	-0.72	8596	379	1.10	-0.30	pp
m078pp	2600	1.0	-0.43	3019	272	1.20	0.00	pp
m079pp	2650	1.0	-0.39	3000	259	1.20	0.00	pp
m080pp	2650	1.0	-0.62	5000	338	1.20	0.00	pp
m081pp	2650	1.0	-0.76	7000	397	1.20	0.00	pp
m082pp	2700	1.0	-0.36	3000	250	1.20	0.00	pp
m083pp	2700	1.0	-0.58	5000	323	1.20	0.00	pp
m084pp	2700	1.0	-0.73	7000	384	1.20	0.00	pp
m085pp	2800	1.0	-0.30	3000	234	1.20	0.00	pp
m086pp	2800	1.0	-0.52	5000	301	1.20	0.00	pp
m087pp	2800	1.0	-0.67	7000	358	1.20	0.00	pp
m088pp	2900	1.0	-0.24	3000	218	1.20	0.00	pp
m089pp	2900	1.0	-0.46	5000	281	1.20	0.00	pp
m090pp	2900	1.0	-0.61	7000	334	1.20	0.00	pp
m091pp	3000	1.0	-0.18	3000	204	1.20	0.00	pp
m092pp	3000	1.0	-0.40	5000	262	1.20	0.00	pp
m093pp	3000	1.0	-0.55	7000	312	1.20	0.00	pp
m094pp	3100	1.0	-0.12	3000	190	1.20	0.00	pp
m095pp	3100	1.0	-0.34	5000	245	1.20	0.00	pp
m096pp	3100	1.0	-0.49	7000	291	1.20	0.00	pp
m097pp	3200	1.0	-0.07	3000	179	1.20	0.00	pp
m098pp	3200	1.0	-0.29	5000	231	1.20	0.00	pp
m099pp	3200	1.0	-0.43	7000	272	1.20	0.00	pp
m100pp	2944	1.5	+0.00	2766	203	1.20	0.00	pp

Model	$T_{\rm eff}$ [K]	$M_*/\mathrm{M}_\odot$	$\log(g)$ [cm/s^2]	$L_*/\mathrm{L}_\odot$	$R_*/\mathrm{R}_\odot$	C/O	$\log(Z/\mathrm{Z}_\odot)$	pp/sph
m101pp	3184	1.5	+0.23	2229	156	1.20	0.00	pp
m103pp	3388	1.5	+0.53	1432	110	1.20	0.00	pp
m104pp	2972	1.5	-0.08	3454	222	1.20	0.00	pp
m105pp	2999	1.5	-0.15	4208	241	1.20	0.00	pp
m106pp	2831	1.5	-0.17	3499	247	1.20	0.00	pp
m107pp	2786	1.5	-0.39	5446	318	1.20	0.00	pp
m108pp	2812	1.5	-0.46	6640	344	1.20	0.00	pp
m109pp	2999	2.25	+0.00	4468	248	1.20	0.00	pp
m110pp	3236	2.25	+0.22	3650	193	1.20	0.00	pp
m111pp	3467	2.25	+0.56	2198	130	1.20	0.00	pp
m112pp	3467	2.25	-0.03	5062	257	1.20	0.00	pp
m113pp	3062	2.25	-0.05	5448	263	1.20	0.00	pp
m114pp	3104	2.25	-0.15	7243	295	1.20	0.00	pp
m115pp	3126	2.25	-0.22	8753	320	1.20	0.00	pp
m116pp	2838	2.25	-0.31	7316	355	1.20	0.00	pp
m117pp	2985	2.25	-0.38	10520	385	1.20	0.00	pp
m118pp	2951	2.25	-0.50	13246	442	1.20	0.00	pp
m119pp	3177	5.0	+0.00	12505	370	1.20	0.00	pp
m120pp	3388	5.0	+0.25	9095	278	1.20	0.00	pp
m121pp	3573	5.0	+0.56	5510	194	1.20	0.00	pp
m122pp	3020	5.0	-0.09	12561	411	1.20	0.00	pp
m123pp	2938	5.0	-0.22	15178	477	1.20	0.00	pp
m124pp	2967	5.0	-0.39	23350	580	1.20	0.00	pp
m125pp	3556	2.25	+0.32	4246	172	1.20	-0.30	pp
m126pp	3459	2.25	+0.16	5495	192	1.20	-0.30	pp
m127pp	3350	2.25	+0.00	6918	248	1.20	-0.30	pp
m128pp	3236	2.25	-0.16	8870	300	1.20	-0.30	pp
m129pp	3041	2.25	-0.49	14454	434	1.20	-0.30	pp
m130pp	2965	2.25	-0.67	19953	537	1.20	-0.30	pp
m131pp	2958	2.0	+0.16	5495	283	1.20	-0.30	pp
m132pp	3451	1.0	+0.24	1995	125	1.20	-0.30	pp
m133pp	3221	1.0	-0.04	2897	173	1.20	-0.30	pp
m134pp	3020	1.0	-0.33	4365	242	1.20	-0.30	pp
m135pp	2958	1.0	-0.46	5495	283	1.20	-0.30	pp
m136pp	2917	1.0	-0.55	6310	312	1.20	-0.30	pp
m137pp	2650	1.0	-0.39	3000	259	1.30	0.00	pp
m138pp	2650	1.0	-0.62	5000	338	1.30	0.00	pp
m139pp	2650	1.0	-0.76	7000	397	1.30	0.00	pp
m140pp	2700	1.0	-0.36	3000	250	1.30	0.00	pp
m141pp	2700	1.0	-0.58	5000	323	1.30	0.00	pp
m142pp	2700	1.0	-0.73	7000	384	1.30	0.00	pp
m143pp	2800	1.0	-0.30	3000	234	1.30	0.00	pp
m144pp	2800	1.0	-0.52	5000	301	1.30	0.00	pp
m145pp	2800	1.0	-0.67	7000	358	1.30	0.00	pp
m146pp	2900	1.0	-0.24	3000	218	1.30	0.00	pp
m147pp	2900	1.0	-0.46	5000	281	1.30	0.00	pp
m148pp	2900	1.0	-0.61	7000	334	1.30	0.00	pp
m149pp	3000	1.0	-0.18	3000	204	1.30	0.00	pp
m150pp	3000	1.0	-0.20	3152	208	1.30	0.00	pp
m151pp	3000	1.0	-0.40	5000	262	1.30	0.00	pp
m152pp	3000	1.0	-0.55	7000	312	1.30	0.00	pp
m153pp	3100	1.0	-0.12	3000	190	1.30	0.00	pp
m154pp	3100	1.0	-0.34	5000	245	1.30	0.00	pp
m155pp	3100	1.0	-0.49	7000	291	1.30	0.00	pp
m156pp	3200	1.0	-0.07	3000	179	1.30	0.00	pp
m157pp	3200	1.0	-0.29	5000	231	1.30	0.00	pp
m158pp	3200	1.0	-0.43	7000	272	1.30	0.00	pp
m159pp	2944	1.5	+0.00	2766	203	1.30	0.00	pp
m160pp	3184	1.5	+0.23	2229	156	1.30	0.00	pp
m161pp	3388	1.5	+0.53	1432	110	1.30	0.00	pp

Model	$T_{\rm eff}$ [K]	$M_*/\rm M_\odot$	$\log(g)$ [cm/s^2]	$L_*/\rm L_\odot$	$R_*/\rm R_\odot$	C/O	$\log(Z/\rm Z_\odot)$	pp/sph
m162pp	2972	1.5	-0.08	3454	222	1.30	0.00	pp
m163pp	2999	1.5	-0.15	4208	241	1.30	0.00	pp
m164pp	2831	1.5	-0.17	3499	247	1.30	0.00	pp
m165pp	2786	1.5	-0.39	5446	318	1.30	0.00	pp
m166pp	2812	1.5	-0.46	6640	344	1.30	0.00	pp
m167pp	2999	2.25	+0.00	4468	248	1.30	0.00	pp
m168pp	3236	2.25	+0.22	3650	193	1.30	0.00	pp
m169pp	3467	2.25	+0.56	2198	130	1.30	0.00	pp
m170pp	3467	2.25	-0.03	5062	257	1.30	0.00	pp
m171pp	3062	2.25	-0.05	5448	263	1.30	0.00	pp
m172pp	2877	2.25	-0.12	4989	285	1.30	0.00	pp
m173pp	3126	2.25	-0.22	8753	320	1.30	0.00	pp
m174pp	2838	2.25	-0.31	7316	355	1.30	0.00	pp
m175pp	2985	2.25	-0.38	10520	385	1.30	0.00	pp
m176pp	2951	2.25	-0.50	13246	442	1.30	0.00	pp
m177pp	3177	5.0	+0.00	12505	370	1.30	0.00	pp
m178pp	3388	5.0	+0.25	9095	278	1.30	0.00	pp
m179pp	3573	5.0	+0.56	5510	194	1.30	0.00	pp
m180pp	3020	5.0	-0.09	12561	411	1.30	0.00	pp
m181pp	2938	5.0	-0.22	15178	477	1.30	0.00	pp
m182pp	2967	5.0	-0.39	23350	580	1.30	0.00	pp
m183pp	3556	2.25	+0.32	4246	172	1.30	-0.30	pp
m184pp	3459	2.25	+0.16	5495	192	1.30	-0.30	pp
m185pp	3350	2.25	+0.00	6918	248	1.30	-0.30	pp
m186pp	3236	2.25	-0.16	8870	300	1.30	-0.30	pp
m187pp	3041	2.25	-0.49	14454	434	1.30	-0.30	pp
m188pp	2965	2.25	-0.67	19953	537	1.30	-0.30	pp
m189pp	2958	2.0	+0.16	5495	283	1.30	-0.30	pp
m190pp	3451	1.0	+0.24	1995	125	1.30	-0.30	pp
m191pp	3221	1.0	-0.04	2897	173	1.30	-0.30	pp
m192pp	3020	1.0	-0.33	4365	242	1.30	-0.30	pp
m193pp	2958	1.0	-0.46	5495	283	1.30	-0.30	pp
m194pp	2917	1.0	-0.55	6310	312	1.30	-0.30	pp
m195pp	2650	1.0	-0.39	3000	259	1.40	0.00	pp
m196pp	2650	1.0	-0.62	5000	338	1.40	0.00	pp
m197pp	2650	1.0	-0.76	7000	397	1.40	0.00	pp
m198pp	2700	1.0	-0.36	3000	250	1.40	0.00	pp
m199pp	2700	1.0	-0.58	5000	323	1.40	0.00	pp
m200pp	2700	1.0	-0.73	7000	384	1.40	0.00	pp
m201pp	2800	1.0	-0.30	3000	234	1.40	0.00	pp
m202pp	2800	1.0	-0.52	5000	301	1.40	0.00	pp
m203pp	2800	1.0	-0.67	7000	358	1.40	0.00	pp
m204pp	2900	1.0	-0.24	3000	218	1.40	0.00	pp
m205pp	2900	1.0	-0.46	5000	281	1.40	0.00	pp
m206pp	2900	1.0	-0.61	7000	334	1.40	0.00	pp
m207pp	3000	1.0	-0.18	3000	204	1.40	0.00	pp
m208pp	3000	1.0	-0.40	5000	262	1.40	0.00	pp
m209pp	3000	1.0	-0.55	7000	312	1.40	0.00	pp
m210pp	3100	1.0	-0.12	3000	190	1.40	0.00	pp
m211pp	3100	1.0	-0.34	5000	245	1.40	0.00	pp
m212pp	3100	1.0	-0.49	7000	291	1.40	0.00	pp
m213pp	3200	1.0	-0.07	3000	179	1.40	0.00	pp
m214pp	3200	1.0	-0.29	5000	231	1.40	0.00	pp
m215pp	3200	1.0	-0.43	7000	272	1.40	0.00	pp
m216pp	2944	1.5	+0.00	2766	203	1.40	0.00	pp
m217pp	3184	1.5	+0.23	2229	156	1.40	0.00	pp
m218pp	3388	1.5	+0.53	1432	110	1.40	0.00	pp
m219pp	2972	1.5	-0.08	3454	222	1.40	0.00	pp
m220pp	2999	1.5	-0.15	4208	241	1.40	0.00	pp
m221pp	2831	1.5	-0.17	3499	247	1.40	0.00	pp

Model	$T_{\rm eff}$ [K]	$M_*/\mathrm{M}_\odot$	$\log(g)$ [cm/s^2]	$L_*/\mathrm{L}_\odot$	$R_*/\mathrm{R}_\odot$	C/O	$\log(Z/\mathrm{Z}_\odot)$	pp/sph
m222pp	2786	1.5	-0.39	5446	318	1.40	0.00	pp
m223pp	2812	1.5	-0.46	6640	344	1.40	0.00	pp
m224pp	2999	2.25	+0.00	4468	248	1.40	0.00	pp
m225pp	3236	2.25	+0.22	3650	193	1.40	0.00	pp
m226pp	3467	2.25	+0.56	2198	130	1.40	0.00	pp
m227pp	3467	2.25	-0.03	5062	257	1.40	0.00	pp
m228pp	3062	2.25	-0.05	5448	263	1.40	0.00	pp
m229pp	3126	2.25	-0.22	8753	320	1.40	0.00	pp
m230pp	2838	2.25	-0.31	7316	355	1.40	0.00	pp
m231pp	2985	2.25	-0.38	10520	385	1.40	0.00	pp
m232pp	2951	2.25	-0.50	13246	442	1.40	0.00	pp
m233pp	3177	5.0	+0.00	12505	370	1.40	0.00	pp
m234pp	3388	5.0	+0.25	9095	278	1.40	0.00	pp
m235pp	3573	5.0	+0.56	5510	194	1.40	0.00	pp
m236pp	3020	5.0	-0.09	12561	411	1.40	0.00	pp
m237pp	2938	5.0	-0.22	15178	477	1.40	0.00	pp
m238pp	2967	5.0	-0.39	23350	580	1.40	0.00	pp
m239pp	3556	2.25	+0.32	4246	172	1.40	-0.30	pp
m240pp	3459	2.25	+0.16	5495	192	1.40	-0.30	pp
m241pp	3350	2.25	+0.00	6918	248	1.40	-0.30	pp
m242pp	3236	2.25	-0.16	8870	300	1.40	-0.30	pp
m243pp	3041	2.25	-0.49	14454	434	1.40	-0.30	pp
m244pp	2965	2.25	-0.67	19953	537	1.40	-0.30	pp
m245pp	2958	2.0	+0.16	5495	283	1.40	-0.30	pp
m255pp	3451	1.0	+0.24	1995	125	1.40	-0.30	pp
m256pp	3221	1.0	-0.04	2897	173	1.40	-0.30	pp
m257pp	3020	1.0	-0.33	4365	242	1.40	-0.30	pp
m258pp	2958	1.0	-0.46	5495	283	1.40	-0.30	pp
m259pp	2917	1.0	-0.55	6310	312	1.40	-0.30	pp
m260pp	2750	1.0	-0.20	2225	208	1.50	0.00	pp
m261pp	2800	1.0	-0.20	2391	208	1.50	0.00	pp
m262pp	2900	1.0	-0.10	2186	186	1.50	0.00	pp
m263pp	3000	1.0	+0.00	1988	166	1.50	0.00	pp
m264pp	3100	1.0	+0.00	2267	166	1.50	0.00	pp
m265pp	3200	1.0	+0.00	2574	166	1.50	0.00	pp
m266pp	2750	1.0	-0.20	2225	208	1.60	0.00	pp
m267pp	2800	1.0	-0.20	2391	208	1.60	0.00	pp
m268pp	2900	1.0	-0.10	2186	186	1.60	0.00	pp
m269pp	3000	1.0	+0.00	1988	166	1.60	0.00	pp
m270pp	3100	1.0	+0.00	2267	166	1.60	0.00	pp
m271pp	3200	1.0	+0.00	2574	166	1.60	0.00	pp
m272pp	2800	1.0	-0.20	2391	208	1.70	0.00	pp
m273pp	2900	1.0	-0.10	2186	186	1.70	0.00	pp
m274pp	3000	1.0	+0.00	1988	166	1.70	0.00	pp
m275pp	3100	1.0	+0.00	2267	166	1.70	0.00	pp
m276pp	3200	1.0	+0.00	2574	166	1.70	0.00	pp
m277pp	2800	1.0	-0.20	2391	208	1.80	0.00	pp
m278pp	2900	1.0	-0.10	2186	186	1.80	0.00	pp
m279pp	3000	1.0	+0.00	1988	166	1.80	0.00	pp
m280pp	3100	1.0	+0.00	2267	166	1.80	0.00	pp
m281pp	3200	1.0	+0.00	2574	166	1.80	0.00	pp
m282pp	2800	1.0	-0.20	2391	208	2.00	0.00	pp
m283pp	2800	1.0	-0.20	2391	208	2.40	0.00	pp
m284pp	2800	1.0	-0.20	2391	208	2.80	0.00	pp
m285pp	2800	1.0	-0.20	2391	208	3.00	0.00	pp

Model	$T_{\rm eff}$ [K]	$M_*/{\rm M}_\odot$	$\log(g)$ [cm/s^2]	$L_*/{\rm L}_\odot$	$R_*/{\rm R}_\odot$	C/O	$\log(Z/{\rm Z}_\odot)$	pp/sph
m001sph	2650	1.0	-0.39	3000	259	1.02	0.00	sph
m002sph	2700	1.0	-0.36	3000	250	1.02	0.00	sph
m003sph	2800	1.0	-0.30	3000	234	1.02	0.00	sph
m004sph	2900	1.0	-0.24	3000	218	1.02	0.00	sph
m005sph	3000	1.0	-0.18	3000	204	1.02	0.00	sph
m006sph	3100	1.0	-0.12	3000	190	1.02	0.00	sph
m007sph	3200	1.0	+0.00	2574	166	1.02	0.00	sph
m008sph	3300	1.0	-0.01	3000	167	1.02	0.00	sph
m009sph	3400	1.0	+0.04	3000	158	1.02	0.00	sph
m010sph	3500	1.0	+0.09	3000	149	1.02	0.00	sph
m011sph	3600	1.0	+0.14	3000	141	1.02	0.00	sph
m012sph	2650	1.0	-0.39	3000	259	1.10	0.00	sph
m013sph	2650	1.0	-0.62	5000	338	1.10	0.00	sph
m014sph	2650	1.0	-0.76	7000	397	1.10	0.00	sph
m015sph	2700	1.0	-0.36	3000	250	1.10	0.00	sph
m016sph	2700	1.0	-0.58	5000	323	1.10	0.00	sph
m017sph	2700	1.0	-0.73	7000	384	1.10	0.00	sph
m018sph	2800	1.0	-0.30	3000	234	1.10	0.00	sph
m019sph	2800	1.0	-0.52	5000	301	1.10	0.00	sph
m020sph	2800	1.0	-0.67	7000	358	1.10	0.00	sph
m021sph	2925	1.0	-0.24	3123	218	1.10	0.00	sph
m022sph	2925	1.0	-0.45	5065	278	1.10	0.00	sph
m023sph	2925	1.0	-0.57	6676	319	1.10	0.00	sph
m024sph	3000	1.0	-0.18	3000	204	1.10	0.00	sph
m025sph	3000	1.0	-0.40	5000	262	1.10	0.00	sph
m026sph	3000	1.0	-0.55	7000	312	1.10	0.00	sph
m027sph	3100	1.0	-0.12	3000	190	1.10	0.00	sph
m028sph	3100	1.0	-0.34	5000	245	1.10	0.00	sph
m029sph	3100	1.0	-0.49	7000	291	1.10	0.00	sph
m030sph	3200	1.0	-0.07	3000	179	1.10	0.00	sph
m031sph	3200	1.0	-0.29	5000	231	1.10	0.00	sph
m032sph	3200	1.0	-0.43	7000	272	1.10	0.00	sph
m033sph	3300	1.0	-0.01	3000	167	1.10	0.00	sph
m034sph	3300	1.0	-0.23	5000	216	1.10	0.00	sph
m035sph	3300	1.0	-0.38	7000	256	1.10	0.00	sph
m036sph	3400	1.0	+0.04	3000	158	1.10	0.00	sph
m037sph	3400	1.0	-0.18	5000	204	1.10	0.00	sph
m038sph	3400	1.0	-0.33	7000	242	1.10	0.00	sph
m039sph	3500	1.0	+0.09	3000	149	1.10	0.00	sph
m040sph	3500	1.0	-0.13	5000	192	1.10	0.00	sph
m041sph	3500	1.0	-0.28	7000	228	1.10	0.00	sph
m042sph	3600	1.0	+0.14	3000	141	1.10	0.00	sph
m043sph	3600	1.0	-0.08	3000	181	1.10	0.00	sph
m044sph	3600	1.0	-0.23	3000	216	1.10	0.00	sph
m045sph	2958	2.0	+0.16	5433	281	1.10	0.00	sph
m046sph	3062	2.25	-0.05	5448	263	1.10	0.00	sph
m047sph	3236	4.1	+0.10	8767	299	1.10	0.00	sph
m048sph	3459	4.3	+0.44	5487	207	1.10	0.00	sph
m049sph	3388	5.0	+0.25	9095	278	1.10	0.00	sph
m050sph	3573	5.0	+0.56	5510	194	1.10	0.00	sph
m051sph	3191	5.0	-0.04	13955	388	1.10	0.00	sph
m052sph	3459	2.25	+0.16	5495	192	1.10	-0.30	sph
m053sph	3236	2.25	-0.16	8870	300	1.10	-0.30	sph
m054sph	2958	2.0	+0.16	5495	283	1.10	-0.30	sph
m055sph	2650	1.0	-0.39	3000	259	1.20	0.00	sph
m056sph	2650	1.0	-0.62	5000	338	1.20	0.00	sph
m057sph	2650	1.0	-0.76	7000	397	1.20	0.00	sph
m058sph	2700	1.0	-0.36	3000	250	1.20	0.00	sph
m059sph	2700	1.0	-0.58	5000	323	1.20	0.00	sph
m060sph	2700	1.0	-0.69	6390	366	1.20	0.00	sph

Model	T_{eff} [K]	$M_*/\text{M}_\odot$	$\log(g)$ [cm/s^2]	$L_*/\text{L}_\odot$	$R_*/\text{R}_\odot$	C/O	$\log(Z/\text{Z}_\odot)$	pp/sph
m061sph	2795	1.0	-0.30	2989	234	1.20	0.00	sph
m062sph	2790	1.0	-0.52	4926	301	1.20	0.00	sph
m063sph	2775	1.0	-0.67	6809	358	1.20	0.00	sph
m064sph	3000	1.0	-0.18	3000	204	1.20	0.00	sph
m065sph	3000	1.0	-0.40	5000	262	1.20	0.00	sph
m066sph	3000	1.0	-0.55	7000	312	1.20	0.00	sph
m067sph	3100	1.0	-0.12	3000	190	1.20	0.00	sph
m068sph	3090	1.0	-0.34	4896	245	1.20	0.00	sph
m069sph	3200	1.0	-0.07	3000	179	1.20	0.00	sph
m070sph	3300	1.0	-0.01	3000	167	1.20	0.00	sph
m071sph	3400	1.0	+0.04	3000	158	1.20	0.00	sph
m072sph	3400	1.0	-0.18	5000	204	1.20	0.00	sph
m073sph	3500	1.0	+0.09	3000	149	1.20	0.00	sph
m074sph	3500	1.0	-0.13	5000	192	1.20	0.00	sph
m075sph	3500	1.0	-0.28	7000	228	1.20	0.00	sph
m076sph	3600	1.0	+0.14	3000	141	1.20	0.00	sph
m077sph	3600	1.0	-0.08	3000	181	1.20	0.00	sph
m078sph	3600	1.0	-0.23	3000	216	1.20	0.00	sph
m079sph	3062	2.25	-0.05	5448	263	1.20	0.00	sph
m080sph	3236	4.1	+0.10	8767	299	1.20	0.00	sph
m081sph	3459	4.3	+0.44	5487	207	1.20	0.00	sph
m082sph	3388	5.0	+0.25	9095	278	1.20	0.00	sph
m083sph	3573	5.0	+0.56	5510	194	1.20	0.00	sph
m084sph	3191	5.0	-0.04	13955	388	1.20	0.00	sph
m085sph	3459	2.25	+0.16	5495	192	1.20	-0.30	sph
m086sph	3236	2.25	-0.16	8870	300	1.20	-0.30	sph
m089sph	2650	1.0	-0.39	3000	259	1.30	0.00	sph
m090sph	2650	1.0	-0.62	5000	338	1.30	0.00	sph
m091sph	2650	1.0	-0.76	7000	397	1.30	0.00	sph
m092sph	2700	1.0	-0.36	3000	250	1.30	0.00	sph
m093sph	2700	1.0	-0.58	5000	323	1.30	0.00	sph
m094sph	2700	1.0	-0.73	7000	384	1.30	0.00	sph
m095sph	2775	1.0	-0.30	2905	234	1.30	0.00	sph
m096sph	2750	1.0	-0.52	4649	301	1.30	0.00	sph
m097sph	2750	1.0	-0.67	6567	358	1.30	0.00	sph
m098sph	3000	1.0	-0.18	3000	204	1.30	0.00	sph
m099sph	3000	1.0	-0.40	5000	262	1.30	0.00	sph
m100sph	3000	1.0	-0.55	7000	312	1.30	0.00	sph
m101sph	3090	1.0	-0.12	2950	190	1.30	0.00	sph
m102sph	3095	1.0	-0.34	4928	245	1.30	0.00	sph
m103sph	3400	1.0	+0.04	3000	158	1.30	0.00	sph
m104sph	3500	1.0	+0.09	3000	149	1.30	0.00	sph
m105sph	3500	1.0	-0.13	5000	192	1.30	0.00	sph
m106sph	3500	1.0	-0.28	7000	228	1.30	0.00	sph
m107sph	3600	1.0	+0.14	3000	141	1.30	0.00	sph
m108sph	3600	1.0	-0.08	3000	181	1.30	0.00	sph
m109sph	3600	1.0	-0.23	3000	216	1.30	0.00	sph
m110sph	3062	2.25	-0.05	5448	263	1.30	0.00	sph
m111sph	3236	4.1	+0.10	8767	299	1.30	0.00	sph
m112sph	3459	4.3	+0.44	5487	207	1.30	0.00	sph
m113sph	3388	5.0	+0.25	9095	278	1.30	0.00	sph
m114sph	3573	5.0	+0.56	5510	194	1.30	0.00	sph
m115sph	3191	5.0	-0.04	13955	388	1.30	0.00	sph
m116sph	3459	2.25	+0.16	5495	192	1.30	-0.30	sph
m117sph	3236	2.25	-0.16	8870	300	1.30	-0.30	sph
m118sph	2650	1.0	-0.39	3000	259	1.40	0.00	sph
m119sph	2650	1.0	-0.62	5000	338	1.40	0.00	sph
m120sph	2650	1.0	-0.76	7000	397	1.40	0.00	sph

Model	$T_{\rm eff}$ [K]	$M_*/\mathrm{M}_\odot$	$\log(g)$ [cm/s^2]	$L_*/\mathrm{L}_\odot$	$R_*/\mathrm{R}_\odot$	C/O	$\log(Z/\mathrm{Z}_\odot)$	pp/sph
m121sph	2700	1.0	-0.36	3000	250	1.40	0.00	sph
m122sph	2700	1.0	-0.58	5000	323	1.40	0.00	sph
m123sph	2700	1.0	-0.73	7000	384	1.40	0.00	sph
m124sph	3000	1.0	-0.18	3000	204	1.40	0.00	sph
m125sph	3000	1.0	-0.40	5000	262	1.40	0.00	sph
m126sph	3000	1.0	-0.55	7000	312	1.40	0.00	sph
m127sph	3400	1.0	+0.04	3000	158	1.40	0.00	sph
m128sph	3500	1.0	+0.09	3000	149	1.40	0.00	sph
m129sph	3500	1.0	-0.13	5000	192	1.40	0.00	sph
m130sph	3500	1.0	-0.28	7000	228	1.40	0.00	sph
m131sph	3600	1.0	+0.14	3000	141	1.40	0.00	sph
m132sph	3600	1.0	-0.08	3000	181	1.40	0.00	sph
m133sph	3600	1.0	-0.23	3000	216	1.40	0.00	sph
m134sph	3236	4.1	+0.10	8767	299	1.40	0.00	sph
m135sph	3459	4.3	+0.44	5487	207	1.40	0.00	sph
m136sph	3388	5.0	+0.25	9095	278	1.40	0.00	sph
m137sph	3573	5.0	+0.56	5510	194	1.40	0.00	sph
m138sph	3191	5.0	-0.04	13955	388	1.40	0.00	sph
m139sph	3459	2.25	+0.16	5495	192	1.40	-0.30	sph
m140sph	3236	2.25	-0.16	8870	300	1.40	-0.30	sph

Bibliography

Abia C., Isern J. 1997, MNRAS 289, L11

Abia C., Wallerstein G. 1998, MNRAS 293, 89

Alvarez R., Plez B. 1998, A&A 330, 1109

Anders E., Grevesse N. 1989, Geochimica et Cosmochimica Acta 53, 197

Andersen A.C., Jäger C., Mutschke H., et al. 1999b, A&A 343, 933

Andersen A.C., Loidl R., Höfner S. 1999a, A&A 349, 243

Aringer B. 2000, PhD thesis at the University of Vienna

Aoki W., Tsuji T., Ohnaka K. 1999, A&A 350, 945

Barthés D., Luri X., Alvarez R., Mennessier M.O. 1999, A&AS 140, 55

Baumert J.H. 1972, PhD thesis at The Ohio State University

Bedding T.R., Conn B.C., Zijlstra A.A. 2000, in: "The Impact of Large-Scale Surveys on Pulsating Star Research", eds. L.Szabados & D.Kurtz, ASP Conf. Ser. 203, 96

Bessell M.S. 1990, PASP 102, 1181

Bessell M.S., Brett J.M. 1988, PASP 100, 1134

Bessell M.S., Brett J.M., Scholz M., Wood P.R. 1989, A&AS 77, 1

Bessell M.S., Scholz M., Wood P.R. 1996, A&A 307, 481

Borghesi A., Bussoletti E., Colangeli L., De Blasi C. 1985, A&A 153, 1

Bowen G.H. 1988, ApJ 329, 299

Burns D., Baldwin J.E., Boysen R.C., et al. 1998, MNRAS 297, 462

Bussoletti E., Colangeli L., Borghesi A., Orofino V. 1987, A&AS 70, 257

Campbell M.F., Elias J.H., Gezari D.Y., et al. 1976, ApJ 208, 396

Carbon D.F. 1984, in: "Methods in Radiative Transfer", ed. W. Kalkofen, Cambridge Univ. Press, p. 395

Catchpole R.M., Feast M.W. 1971, MNRAS 154, 197

Catchpole R.M., Robertson B.S.C., Lloyd Evans T.H.H., et al. 1979, SAAO Circulars Nr. 4, Vol.1, 61

Chan S.J. 1994, MNRAS 268, 113

Chandra S., Kegel W.H., Le Roy R.J., Hertenstein T. 1995, A&AS 114, 175

Claussen M.J., Kleinmann S.G., Joyce R.R., Jura M. 1987, ApJS 65, 385

Colangeli L., Menella V., Palumbo P., et al. 1995, A&AS 113, 561

de Graauw T., Haser L.N., Beintema D.A., et al. 1996, A&A 315, L49

Di Giacomo A., Richichi A., Lisi F., Calamai G. 1991, A&A 249, 397

Draine B.T., Lee H.M. 1984, ApJ 285, 89

Dreiling L.A., Bell R.A. 1980, ApJ 241, 736

Dyck H.M., Benson J.A., Van Belle G.T., Ridgway S.T. 1996b, AJ 111, 1705

Dyck H.M., Van Belle G.T., Benson J.A. 1996a, AJ 112, 294

Dyck H.M., Van Belle G.T., Thompson R.R. 1998, AJ 116, 981

Eglitis I., Eglite M. 1995, Ap&SS 229, 63

Ekberg U., Eriksson K., Gustafsson B. 1986, A&A 167, 304

Eriksson K., Gustafsson B., Jørgensen U.G., Nordlund Å. 1984, A&A 132, 37

Fischel D., Sparks W.M. 1971, ApJ 164, 359

Fleischer A.J., Gauger A., Sedlmayr E. 1992, A&A 266, 321

Fluks M.A., Plez B., Thé P.S., et al. 1994, A&AS 105, 311

Fouqué P., Chevallier L., Cohen M., et al. 2000, A&AS 141, 313

Fox M.W., Wood P.R. 1982, ApJ 259, 198

Friedemann C. 1969a, Physica 41, 139

Friedemann C. 1969b, Astron. Nach. 291, 177

Frogel J.A., Mould J.R., Blanco V.M. 1990, ApJ 352, 96

Gail H.P., Sedlmayr E. 1988, A&A 206, 153

Gauger A., Gail H.P., Sedlmayr E. 1990, A&A 235, 345

Gautschy A. 1987, Vistas in Astron. 30, 197

Gautschy A. 1999, A&A 349, 209

Gautschy A., Ludwig H.G., Freytag B. 1996, A&A 311, 493

Gautschy A., Saio H. 1995, ARAA 33, 75

Gilman R.C. 1969, ApJ 155, L185

Goebel J.H., Bregman J.D., Cooper D.M., et al. 1983, ApJ 270, 190

Goebel J.H., Bregman J.D., Witteborn F.C., Taylor B.J. 1981, ApJ 246, 455

Goorvitch D. 1990, ApJS 74, 769

Goorvitch D., Chackerian C.Jr. 1994, ApJS 91, 483

Grevesse N., Sauval A.J. 1994, in: "Molecules in the Stellar Environment", IAU Colloquium 146, ed. U.G. Jørgensen, Springer-Verlag (Lecture Notes in Physics 428), p. 196

Gürtler J., Kömpe C., Henning Th. 1996, A&A 305, 878

Gustafsson B. 1973, Uppsala Astron. Obs. Ann. 5, No. 6

Gustafsson B., Bell R.A., Eriksson K., Nordlund Å. 1975, A&A 42, 407

Hackwell J.A. 1972, A&A 21, 239

Haniff C.A., Scholz M., Tuthill P.G. 1995, MNRAS 276, 640

Helling Ch., Jørgensen U.G. 1998, A&A 337, 477

Helling Ch., Jørgensen U.G., Plez B., Johnson H.R. 1996, A&A 315, 194

Herwig F., Blöcker T., Schönberner D., El Eid M.F. 1997, A&A 324, L81

Herzberg G. 1988, The Spectra and Structures of Simple Free Radicals, Dover Publications

Hofmann K.H., Balega Y., Scholz M., Weigelt G. 2000, A&A 353, 1016

Hofmann K.H., Scholz M. 1998a, A&A 335, 637

Hofmann K.H., Scholz M., Wood P.R. 1998b, A&A 339, 846

Höfner S. 1999, A&A 346, L9

Höfner S., Dorfi E.A. 1997, A&A, 319, 648

Höfner S., Feuchtinger M.U., Dorfi E.A. 1995, A&A 279, 815

Höfner S., Jørgensen U.G., Loidl R., Aringer B. 1998, A&A 340, 497

Hron J., Loidl R., Höfner S., et al. 1998, A&A 335, L69

Huffman D.R. 1988, in: "Experiments on Cosmic Dust Analogues", eds. E. Bussoletti, C. Fusco, G. Longo, Kluwer Academic Publishers, p. 25

Iben I.Jr. 1981, ApJ 246, 278

Iben I.Jr., Renzini A. 1983, Ann. Rev. Astron. Astrophys. 21, 271

Irwin A.W. 1981, ApJS 45, 621

Jäger C., Mutschke H., Henning Th. 1998, A&A 332, 291

Jeong K.S., Winters J.M., Sedlmayr E. 1999, in: "Asymptotic giant branch stars", IAU Symp. 191, eds. T. Le Bertre, A. Lèbre and C. Waelkens, ASP Conf. Ser., p. 233

Johnson H.R. 1982, ApJ 260, 254

Johnson H.R., Luttermoser D.G., Faulkner D.R. 1988, ApJ 332, 421

Johnson H.R., Querci F. 1986, The M-type stars, Monograph Series on nonthermal phenomena in stellar atmospheres, NASA SP-492

Jørgensen U.G. 1988, Nat 332, 702

Jørgensen U.G. 1990, A&A 232, 420

Jørgensen U.G. 1995, in: "Astrophysical Applications of Powerful New Databases", eds. W.L. Wiese & S.J. Adelman, ASP Conf. Ser. 78, p. 179

Jørgensen U.G. 1997, in: "Molecules in Astrophysics: Probes and Processes", Proc. IAU Symp. 178, ed. E.F. van Dishoeck, Kluwer, p. 441

Jørgensen U.G., Almlöf J., Gustafsson B., Larsson M., Siegbahn P.E.M. 1985, J. Chem. Phys. 83, 3034

Jørgensen U.G., Almlöf J., Siegbahn P.E.M. 1989, ApJ 343, 554

Jørgensen U.G., Hron J., Loidl R. 2000, A&A 356, 253

Jørgensen U.G., Johnson H.R., Nordlund Å. 1992, A&A 261, 263

Jørgensen U.G., Larsson M. 1990, A&A 238, 424

Jørgensen U.G., Larsson M., Iwamae A., Yu B. 1996, A&A 315, 204

Joyce R.R. 1998, AJ 115, 2059

Keenan P.C. 1993, PASP 105, 905

Keenan P.C., Boeshaar P. 1980, ApJS 43, 379

Kerschbaum F., Hron J. 1996, A&A 308, 489

Kholopov P.N., Samus' N.N., Frolov M.S., et al. 1988, *General Catalogue of Variable Stars*, 4th Edition, Nauka Publ. House, Moscow

Kipper T., Wallerstein G. 1990, PASP 102, 574

Kleinmann S.G., Hall D.N.B. 1986, ApJS 62, 501

Kozasa T., Dorschner J., Henning T., Stognienko R. 1996, A&A 307, 551

Kurucz R.F. 1970, Smithsonian Ap. Obs. Spec. Rept., No. 309

Kurucz R.F. 1994, in: "Molecules in the Stellar Environment", ed. U.G.Jørgensen, Springer LNP vol.428, p.282

Labeyrie A., Koechlin L., Bonneau D., Blazit A., Foy R. 1977, ApJ 218, L75

Lambert D.L., Gustafsson B., Eriksson K., Hinkle K.H. 1986, ApJS 62, 373

Lambert D.L., Hinkle K.H., Smith V.V. 1990, AJ 99, 1612

Lançon A., Wood P. 2000, A&AS 146, 217

Lázaro C., Hammersley P.L., Clegg R.E.S., et al. 1994, MNRAS 269, 365

Leech K., et al. 1998, SWS Instrument Data Users Manual Issue 1.0, SAI/98-195/Dc, ESA

Lewis R.S., Tang M., Wacker J.F., et al. 1987, Nat 326, 160

Lloyd Evans T. 1985, in: "Cool stars with Excess of Heavy Elements", eds. M. Jaschek & P.C. Keenan, Reidel, p. 163

Loidl R., Aringer B., Hron J., et al. 1999b, ESA SP-427, 365

Loidl R., Höfner S., Jørgensen U.G., Aringer B. 1999a, A&A 342, 531

Loidl R., Lançon A., Jørgensen U.G. 2001, A&A, submitted

Loidl R., Gautschy A. 2001 A&A, submitted

Maron N. 1990, Ap&SS 172, 21

Martin P.G., Rogers C. 1987, ApJ 322, 374

Michelson A.A., Pease F. 1921, ApJ 53, 249

Mowlavi N. 1999, A&A 344, 617

Mutschke H., Andersen A.C., Clément D., et al. 1999, A&A 345, 187

Nordlund Å. 1984, in: "Methods in Radiative Transfer", ed. W. Kalkofen, Cambridge Univ. Press, p. 211

Ohnaka K., Tsuji T. 1996, A&A 310, 933

Ostlie D.A., Cox A.N. 1986, ApJ 311, 864

Papoular R., Cauchetier M., Begin S., LeCaer G. 1998, A&A 329, 1035

Perrin G., Coudé du Foresto V., Ridgway S.T., et al. 1999, A&A 345, 221

Peytremann E. 1974, A&A 33, 203

Preibisch Th., Ossenkopf V., Yorke H. W., Henning Th. 1993, A&A 279, 577

Querci F., Querci M. 1975, A&A 39, 113

Querci F., Querci M., Kunde V.G. 1971, A&A 15, 256

Querci F., Querci M., Tsuji T. 1974, A&A 31, 265

Quirrenbach A., Mozurkewich D., Armstrong J.T., Buscher D.F., Hummel C.A. 1993, ApJ 406, 215

Quirrenbach A., Mozurkewich D., Hummel C.A., Buscher D.F., Armstrong J.T. 1994, A&A 285, 541

Ridgway S.T., Wells D.C., Joyce R.R. 1977, AJ 82, 414

Ridgway S.T., Jacoby G.H., Joyce R.R., Wells D.C. 1980, AJ 85, 1496

Ridgway S.T., Jacoby G.H., Joyce R.R., Siegel M.J., Wells D.C. 1982, AJ 87, 808

Rosario L. 1998, "Spectral Resolution of SWS AOT 1", *http://www.iso.vilspa.esa.es/users/expl_lib/SWS_list.html*

Rouleau F., Martin P.G. 1991, ApJ 377, 526

Scholz M., Takeda Y. 1987, A&A 186, 200

Scholz M., Tsuji T. 1984, A&A 130, 11

Smith V.V., Lambert D.L., McWilliam A. 1987, ApJ 320, 862

Sopka R.J., Hildebrand R.H., Jaffe D.T., et al. 1985, ApJ 294, 242

Sørensen G.O., Jørgensen U.G. 1992, J.Chem.Phys. 97, 4616

Speck A.K., Hofmeister A.M., Barlow M.J. 1999, ApJ 513, L87

Spitzer W.G., Kleinman D.A., Frosch C.J. 1959b, Phys. Rev. 113(1), 133

Spitzer W.G., Kleinman D.A., Walsh D. 1959a, Phys. Rev. 113(1), 127

Tanaka W., Hashimoto O., Nakada Y., et al. 1990, NAOJ 1,3

Tanaka W., Hashimoto O., Tanabe T., et al. 1992, NAOJ 2,3

Tanaka W., Okada T., Hashimoto O., et al. 1996, NAOJ 4,3

Taylor B.J. 1999, A&AS 134, 523

Traving G., Baschek B., Holweger H. 1966, Astron. Abh. Hamburg Sternw. Bergedorf VIII, 3

Treffers R., Cohen M. 1974, ApJ 188, 545

Tsuji T. 1973, A&A 23, 411

Tsuji T., Ohnaka K., Aoki W., Yamamura I. 1997, A&A 320, L1

Turnshek D.E., Turnshek D.A., Craine E.R., Boeshaar P.C. 1985, An Atlas of digital spectra of cool stars, Astronomy and astrophysics series vol. 1

Tuthill P.G., Haniff C.A., Baldwin J.E., Feast M.W. 1994, MNRAS 266, 745

Van Belle G.T., Dyck H.M., Benson J.A., Lacasse M.G. 1996, AJ 112, 2147

Van Belle G.T., Dyck H.M., Thompson R.R., Benson J.A., Kannappan S.J. 1997, AJ 114, 2150

Van Belle G.T., Lane B.F., Thompson R.R., et al. 1999, AJ 117, 521

Van Leeuven F., Feast M.W., Whitelock P.A., Yudin B. 1997, MNRAS 287, 995

Vardya M.S. 1965, MNRAS 129, 205

White N.M., Feierman B.H. 1987, AJ 94, 751

Whitelock P.A., Feast M.W., Marang F., Overbeck M.D. 1997, MNRAS 288, 512

Windsteig W., Dorfi E.A., Höfner S., Hron J., Kerschbaum F. 1997, A&A 324, 617

Wing R.F. 1967, PhD thesis at the University of California, Berkeley

Wing R.F. 1971, Proceedings of the Conference on Late-Type Stars, ed. Lockwood G.W. and Dyck H.M., Kitt Peak Nat. Obs. Contr. 554, 145

Wood P.R. 1975, MNRAS 171, 15

Wood P.R. 1979, ApJ 227, 220

Wood P.R. 1989, in: “From Miras to Planetary Nebulae”, ed. M.O. Mennessier, Editions Frontières, p.67

Ya’ari A., Tuchman Y. 1996, ApJ 456, 350

Yamamura I., de Jong T., Onaka T., Cami J., Waters L.B.F.M. 1999, A&A 341, L9

Zubko V.G., Menella V., Colangeli L., Bussoletti E. 1996, MNRAS 282, 1321

Danksagung/Acknowledgement

Ich möchte mich bei Josef Hron für die Betreuung und Förderung meiner Arbeit bedanken. Er hat im Rahmen etlicher Diskussionen wesentlich zur Entstehung der wissenschaftlichen Resultate und des Textes beigetragen.

Mein ganz besonderer Dank gilt auch Susanne Höfner, die mir ihre dynamischen Modelle zur Verfügung gestellt hat. Sie und Bernhard Aringer sind mir immer mit Rat und Tat zur Seite gestanden und haben mir ihre Programme zur Verfügung gestellt.

I want to thank Uffe G. Jørgensen for his support. He made his version of the MARCS code and his molecular data available to me.

Ein herzliches Dankeschön an Josef Hron, Alfred Gautschy, Uffe G. Jørgensen, Susanne Höfner und Ernst Dorfi für die Durchsicht des Manuskripts und die wertvollen Anregungen bei der Erstellung der Dissertation.

I want to thank Anja Andersen, Bernhard Aringer, Alfred Gautschy, Susanne Höfner, Josef Hron, Uffe G. Jørgensen, and Ariane Lançon for very good colaboration. Thomas Lebzelter sei für hilfreiche Diskussionen bzgl. FTS-Daten gedankt und Franz Kerschbaum für die Erlaubnis zur Benützung seiner AGB-Datenbank.

Many thanks to: Martin Cohen for digging in archives looking for KAO spectra; Osamu Hashimoto for recompiling their FTS near infrared spectra; Tom Lloyd Evans for sending his R Scl observations and for helpful discussions; Dick Joyce and Carlos Lázaro for sending their near-infrared spectra; Ariane Lançon for making her spectra available to me prior to publication; and last but not least Bob Wing for copying Baumerts' thesis and sending it.

This work made extensive use of the SIMBAD data base maintained by the Centre de Données (CDS) de Strasbourg, of the Astrophysics Data System (ADS) hosted by NASA, and of data provided by the American Association of Variable Star Observers (AAVSO). Without their services and continuous efforts, life of an astronomer would be even more laborious; I can barely imagine writing this thesis otherwise.

Meinem Mann, Alfred Gautschy, danke ich für die gute Zeit, die ich mit ihm verbringen darf, und für viele nützliche Kommentare, die dazu beitragen, den Text auch für Leute verständlich zu machen, die sich nicht täglich mit AGB Sternen beschäftigen.

Ein abschließendes Dankeschön an alle meine Freunde im In- und Ausland, die sich während der Entstehung dieser Arbeit um mein Wohlergehen gekümmert haben.

Nicht unerwähnt bleiben sollen auch die edlen Geldgeber. Das ist in meinem Fall einerseits die Österreichische Akademie der Wissenschaften, die meine Arbeit zwei Jahre lang im Rahmen eines Doktorandenstipendiums (APART-DOC 571) unterstützt hat. Die übrige Zeit wurde ich vom Fonds zur Förderung der wissenschaftlichen Forschung unterstützt, der meine Arbeit im Rahmen des Projekts S7308-AST finanziert hat.

Curriculum Vitae

Persönliches:

Mag. Rita Gautschy, geb. Loidl
geboren am 9. Mai 1973 in Bad Ischl
verheiratet seit 2001 mit Dr. Alfred Gautschy
Eltern: Brigitte Loidl, geb. Preinerstorfer, VS-Lehrerin
Dr. Wolfgang A. Passath, Arzt
österreichische Staatsbürgerin
wohnhaft in Wien 16, Thaliastraße 11/19

Schulbildung:

1979 – 1983 Volksschule Ost Bad Ischl
1983 – 1991 Bundesrealgymnasium Bad Ischl
Juni 1991 Matura mit ausgezeichnetem Erfolg

Studium:

1991 – 1997 Studium der Astronomie und Physik an der Universität Wien
SS 1993 Abschluss des 1. Studienabschnitts Astronomie
SS 1993 Abschluss des 1. Studienabschnitts Physik
SS 1997 Abschluss des Astronomiestudiums
Diplomarbeit: Synthetic Spectra and Colours of Carbon-Rich Long-Period-Variables
1997 – 2001 Doktoratsstudium Astronomie
ab WS 1993/94 Kurzstudium Versicherungsmathematik an der TU Wien
ab WS 1995/96 Studium Archäologie & Fächerkombination an der Universität Wien
1995 – 1997 Vorsitzende der Studienrichtungsvertretung Astronomie

Stipendien und Anstellungen:

1996–Oktober 1998: Anstellung über Forschungsprojekt FWF (S7308-AST)
Oktober 1998 – Oktober 2000: Doktorandenstipendium der Österreichischen Akademie der Wissenschaften (APART-DOC 571)
seit Oktober 2000: Anstellung über Forschungsprojekt FWF (S7308-AST)

Beobachtungs- und Forschungsaufenthalte:

1996 einmonatiger Aufenthalt am Niels Bohr Institut in Kopenhagen, Dänemark
1997 Kurzaufenthalt bei ESTEC in Nordwijk, Niederlande
seit 1997 wiederholte Aufenthalte am Astronomischen Institut der Universität Basel, Schweiz
1999 Aufenthalt am Niels Bohr Institut in Kopenhagen, Dänemark
1999 Beobachtungsaufenthalt ESO, Chile (DENIS)

Tagungsteilnahmen:

1996 IAU Symposium 177, "The Carbon Star Phenomenon", Antalya, Türkei
1996 EADN Sommerschule IX, "Stellar Atmospheres", Brüssel, Belgien
1997 CCP7/UMIST Workshop, "Dust and Molecules in Evolved Stars", Manchester, UK
1997 1. Österreichischer ISO Workshop, Innsbruck, Österreich
1997 "ISO's View on Stellar Evolution", Noordwijkerhout, Niederlande
1998 Les Houches Workshop, "Solid Interstellar Matter: The ISO Revolution", Les Houches, Frankreich
1998 Faraday Discussion 109, "Chemistry and Physics of Molecules and Grains in Space", Nottingham, UK
1998 IAU Symposium 191, "Asymptotic Giant Branch Stars", Montpellier, Frankreich
1999 2nd Austrian ISO Workshop, "Atmospheres of M, S and C giants", Wien, Österreich
2000 ISO beyond the peaks, "The second ISO workshop on analytical spectroscopy", Vilspa, Spanien